Data Bank
ISBN 978-92-64-99056-2
NEA/DB/DOC(2008)1

Analytical Benchmarks for Nuclear Engineering Applications

Case Studies in Neutron Transport Theory

B.D. Ganapol
Department of Aerospace and Mechanical Engineering
University of Arizona

with Forewords by

Paul F. Zweifel
Richard Sanchez and Norman J. McCormick

NEA No. 6292

NUCLEAR ENERGY AGENCY
ORGANISATION FOR ECONOMIC CO-OPERATION AND DEVELOPMENT

ORGANISATION FOR ECONOMIC CO-OPERATION AND DEVELOPMENT

The OECD is a unique forum where the governments of 30 democracies work together to address the economic, social and environmental challenges of globalisation. The OECD is also at the forefront of efforts to understand and to help governments respond to new developments and concerns, such as corporate governance, the information economy and the challenges of an ageing population. The Organisation provides a setting where governments can compare policy experiences, seek answers to common problems, identify good practice and work to co-ordinate domestic and international policies.

The OECD member countries are: Australia, Austria, Belgium, Canada, the Czech Republic, Denmark, Finland, France, Germany, Greece, Hungary, Iceland, Ireland, Italy, Japan, Korea, Luxembourg, Mexico, the Netherlands, New Zealand, Norway, Poland, Portugal, the Slovak Republic, Spain, Sweden, Switzerland, Turkey, the United Kingdom and the United States. The Commission of the European Communities takes part in the work of the OECD.

OECD Publishing disseminates widely the results of the Organisation's statistics gathering and research on economic, social and environmental issues, as well as the conventions, guidelines and standards agreed by its members.

* * *

NUCLEAR ENERGY AGENCY

The OECD Nuclear Energy Agency (NEA) was established on 1st February 1958 under the name of the OEEC European Nuclear Energy Agency. It received its present designation on 20th April 1972, when Japan became its first non-European full member. NEA membership today consists of 28 OECD member countries: Australia, Austria, Belgium, Canada, the Czech Republic, Denmark, Finland, France, Germany, Greece, Hungary, Iceland, Ireland, Italy, Japan, Luxembourg, Mexico, the Netherlands, Norway, Portugal, Republic of Korea, the Slovak Republic, Spain, Sweden, Switzerland, Turkey, the United Kingdom and the United States. The Commission of the European Communities also takes part in the work of the Agency.

The mission of the NEA is:

- to assist its member countries in maintaining and further developing, through international co-operation, the scientific, technological and legal bases required for a safe, environmentally friendly and economical use of nuclear energy for peaceful purposes, as well as
- to provide authoritative assessments and to forge common understandings on key issues, as input to government decisions on nuclear energy policy and to broader OECD policy analyses in areas such as energy and sustainable development.

Specific areas of competence of the NEA include safety and regulation of nuclear activities, radioactive waste management, radiological protection, nuclear science, economic and technical analyses of the nuclear fuel cycle, nuclear law and liability, and public information. The NEA Data Bank provides nuclear data and computer program services for participating countries.

In these and related tasks, the NEA works in close collaboration with the International Atomic Energy Agency in Vienna, with which it has a Co-operation Agreement, as well as with other international organisations in the nuclear field.

FOREWORD

P.F. Zweifel

Forty years ago, Kenneth Case and I wrote our treatise on transport theory[1] which dealt with a very idealized set of problems, basically one-speed transport in one-dimension, models that were amenable to exact solution. We gave a rationale for treating such idealized models on page 2 of our book:

1) In some special situations these [models] may be a good approximation to physical reality. [Let us admit that these special situations are indeed few and far between.]
2) The results are of (exploratory) mathematical interest in that knowledge is gained of the structure of solutions of linear transport boundary-value problems. [This aim was indeed fulfilled, as exemplified by an explosion of papers in linear transport in the years following book's publication, not to mention the birth, in 1969, of the bi-annual series of International Conferences in Transport Theory still very much alive, a series in which Professor Ganapol has been an active and important participant. The aim of this series, as stated in the manifesto of its founders, Charles Siewert, Robert Erdmann and myself, was to bring together researchers in the several fields of engineering and science who used similar – or even identical – mathematical methods in their studies, meaning those which evolved from the methods described in Ref. 1.]
3) *Of greatest importance*[2] is probably the fact that these exact solutions provide a sample set of problems against which approximate methods may be tested…

This last item is precisely that which Professor Ganapol has seized upon in his search for benchmark solutions to nuclear reactor physics problems. He has been a true pioneer in the exploitation of exact solutions as benchmarks. Although some tentative, earlier work had been carried out in the days immediately after the publication of Ref. 1 (by Dale Metcalf) an intensive program never got underway until Professor Ganapol began his studies, in the 1970s and 80s. His benchmarks have gone far beyond the simplified problems treated in Ref. 1; for example he has considered multi-speed (aka multigroup) models of transport as well as two-dimensional and even three-dimensional transport. He has also studied zero-dimensional transport, i.e. slowing down problems using methods originated in 1955[3] for calculating the neutron spectrum in water-moderated reactors with the aim of evaluating few-group cross sections by spectral averaging.

The Ganapol treatise which follows gives derivations of the benchmark equations which are then studied numerically, so it is complete in itself and could be the text for a graduate course in nuclear engineering. Or, if I may be permitted an anagram, in unclear engineering, since Professor Ganapol has his own unique methods in transport theory; for example, he is (in)famous as the creator of a multiple collision solution of the collisionless Vlasov equation. But all roads lead to Rome, and the material contained in this book offers a wealth of useful information and data to the practical engineer who wants to be assured that the numerical approximations being used have some correspondence to physical reality.

---

[1] Case, K.M., P.F. Zweifel, *Linear Transport Theory,* Addison-Wesley, Reading, MA (1967).

[2] Italics not in the original.

[3] Hurwitz, H., Jr., P.F. Zweifel, *J. Appl. Phys.*, **26**, 923 (1955).

FOREWORD

Richard Sanchez and N.J. McCormick

In this book on analytical benchmarks Professor Ganapol presents twelve reference calculations in transport theory. The material in the book is presented in order of progressive complexity, from problems in only the energy or only the spatial variables to problems with both variables.

Chapter 1 contains a detailed introduction to the different forms of the transport equation that are solved. Chapter 2 covers slowing down and thermalization in an infinite medium, Chapter 3 deals with one-group space dependent problems, including the classical Green's function, albedo and Milne problems, and Chapter 4 presents two multigroup space-dependent applications. True, the problems that are treated are mostly for homogeneous media in an infinite space, a half-space and the one-dimensional geometries. However, as one of us told Professor Ganapol a long time ago, it is much more difficult to accurately solve a simple transport problem than to carry out a transport calculation in a complicated geometry for reactor physics applications.

The treatment of the problems presented in this book excels by the rigor of both the mathematical and the numerical analysis. To solve these problems, the author has applied and further developed a number of classical transport methods, including Caseology (i.e. singular eigenfunction expansions), *H*-functions and invariant embedding, the *FN* method. In addition, he develops Green's functions and the mathematical relationships between solutions in elementary one-dimensional geometries, via pseudo fluxes. However, it is not enough to write down an analytical or semi-analytical explicit solution for a transport problem, there is still the problem of obtaining an accurate numerical solution.

Professor Ganapol has analyzed and developed numerical techniques to control the convergence and accuracy of all the steps involved in the numerical calculations needed to achieve a benchmark-quality solution. Romberg quadratures, numerical Fourier and Laplace inversion and extrapolation techniques are elegantly put to work to obtain the final results with several digits accuracy. Another aspect of this book is the pedagogical effort put into the presentation that makes for instructive reading, even for the non-specialist. The book should be useful for the specialist as well as for students that want to learn about transport theory.

With this book, Barry Ganapol, also known in our community as the transport cowboy, has given us a treat in transport theory applications.

Abstract

The developers of computer codes involving neutron transport theory for nuclear engineering applications seldom apply analytical benchmarking strategies to ensure the quality of their programs. A major reason for this is the lack of analytical benchmarks and their documentation in the literature. The few such benchmarks that do exist are difficult to locate, as they are scattered throughout the neutron transport and radiative transfer literature. The motivation for this benchmark compendium, therefore, is to gather several analytical benchmarks appropriate for nuclear engineering applications under one cover. We consider the following three subject areas: neutron slowing down and thermalization without spatial dependence, one-dimensional neutron transport in infinite and finite media, and multidimensional neutron transport in a half-space and an infinite medium. Each benchmark is briefly described, followed by a detailed derivation of the analytical solution representation. Finally, a demonstration of the evaluation of the solution representation includes qualified numerical benchmark results. All accompanying computer codes are suitable for the PC computational environment and can serve as educational tools for courses in nuclear engineering. While this benchmark compilation does not contain all possible benchmarks, by any means, it does include some of the most prominent ones and should serve as a valuable reference.

The set of FORTRAN programs for the benchmarks included in the study is available upon request from the OECD/NEA Data Bank (programs@nea.fr).

Acknowledgements

As with any creative inspirational endeavor, inspiration comes from many sources. For me, my parents, Manny and Mimi Ganapol, were inspirational in their encouragement to do my best and by emphasizing the excitement of learning. Also, my Aunt Gert, in her inspirational way, gave me the confidence to succeed at anything I set out to accomplish. To my brother David and sister-in-law Cheryl, who supported me with their continued loving kindness and encouragement, I am eternally grateful. Finally, Professor Larry Grossman, through his inspirational teaching of reactor physics and transport theory, gave me the tools and unique style that has become my professional signature.

I am sincerely indebted to all my colleagues and to the institutions that have encouraged and supported me over the 25 years of preparation of my benchmark compilation. The support came in several forms – through grants such as the DoE NEER Grant and summer appointments at DoE national laboratories (ANL, INL, LANL and ORNL). In addition, from time to time, colleagues would request specific benchmarks for testing a method and thus unknowingly collaborate in my analytical benchmarking enterprise. Many of my closest colleagues served as sounding boards for my various solution methods, which have proved to be both correct and incorrect; and I certainly appreciate their constructive, though sometimes harsh, criticism. To all these individuals, I express my sincere thanks for standing by me through the years. In particular, I acknowledge the many helpful discussions I had with Dave Nigg and thank him for his suggestions and guidance, and to Paul Zweifel, Richard Sanchez and Norm McCormick, who have encouraged me throughout our nearly 40 years of friendship – I say thanks for your critical eye which has resulted in a much better product.

My thanks go to the typists of my first INL report and subsequent versions through the years leading to my book – especially J. McManus and Connie Spencer, for putting up with all my many equations. Also thanks go to Mary Harris who so competently generated the figures but unfortunately did not live to see her final product. I am grateful to Amanda Costa for having devoted her competence and skills to finalizing my manuscript for publication.

Special thanks go to Enrico Sartori who had enough faith in me and my work to risk publishing the benchmark collection through the OECD/NEA Data Bank. Finally, I thank my wife Mary, for her continued encouragement and tender love during the completion of this work and for having the courage to marry me anyway.

My Apologies

While I have made every attempt to find all typographical errors in the text and equations, I am quite certain some will remain. I would appreciate any corrections, suggestions for additional benchmarks or criticism of the presentation as frank as that might be. I can be contacted at Ganapol@cowboy.ame.arizona.edu.

TABLE OF CONTENTS

List of tables

List of figures

PREFACE

Background

The notion of this analytical benchmark compilation originated in Switzerland in 1971 during my first paid job as a nuclear engineer at the Swiss Federal Institute for Reactor Research (EIR). At that time, I was full of the energy that “fresh outs” have when they want to change the world. In completing my thesis, I had become quite familiar with the Case, De Hoffmann and Placezk’s 1953 monograph (CdH&P) *Introduction to Neutron Diffusion* [1], along with what was supposed to be the second volume of CdH&P, *Linear Transport Theory* [2] by Case and Zweifel (C&Z). CdH&P had tabular benchmark solutions for infinite media and half-space problems but little else in the way of transport benchmarks. C&Z had similar tables and, of course, presented the theory of singular eigenfunction solutions from which benchmarks could be (and have been) obtained. I therefore sensed a need for readily accessible numerical solutions to the transport equation available to transport methods developers, not only in tables, but also through specialized computer codes.

On completion of my PhD dissertation, I had become quite skilful at numerically evaluating the analytical solution representation of the time-dependent transport equation in an infinite medium, bringing together a blend of mathematical techniques and numerical methods [3]. The challenge was to find new, innovative ways to achieve high-accuracy benchmark quality, which transport theorists later defined as four- or five- place accuracy. For instance, I had to evaluate an infinite series of neutron fluxes, each term representing a number of collisions. By following standard quadrature methods, I was able to establish only about 15 terms in the series before round off error destroyed the computation. However, drawing upon mathematics and reformulating the collided fluxes as contour integrations, I was able to overcome round off error by a straightforward change of variable – a very satisfying accomplishment indeed. For my effort, I became known as the “four-place transport theorist” (however, my late colleague, Bill Filippone later changed my title to “The Transport Cowboy” when he moved to Tucson). This experience demonstrated to me that highly accurate numerical solutions are possible, not only by “throwing” more digits at the problem, but also by applying mathematics to reformulate a numerical method in a clever way. This became my challenge.

I then happened upon Romberg integration [4], which taught me how to evaluate integrals to any desired accuracy. At about the same time, I discovered the Euler-Knopp (*EK*) acceleration, enabling efficient and accurate evaluation of alternating series. With these discoveries, I produced my first stationary benchmark by applying *EK* acceleration to evaluate the Fourier transform inversion integral, reformulated as a series of integrals, each obtained through Romberg integration. Thus, I reproduced CdH&P results for the flux in an isotropically scattering infinite medium. The lesson of that exercise was that analytical representations could reliably be evaluated to high accuracy through iteration and convergence acceleration, and standards could be established. All this was occurring against a backdrop of increasing CPU speeds and new computer architectures spawning new numerical methods, making the computational environment ideal for benchmark development.

With encouragement and support from Dave Nigg at (then) Idaho National Engineering Laboratory (INEL) during my sabbatical of 1989, I created the first benchmark compilation focused on the INEL PC/workstation-based code system which included the PC versions of COMBINE, ANISN, DORT, VENTURE, KENO and NESTLE. The original benchmark collection contained the four slowing down benchmarks of Chapter 2 (Benchmarks 2.1-2.4), the first three one-group benchmarks of Chapter 3 (Benchmarks 3.1-3.3), the first multigroup benchmark of Chapter 4 (Benchmark 4.1) and the 2-D searchlight problem of Chapter 5 (Benchmark 5.1). In addition, we began a reactor kinetics benchmark, which is not yet ready for publication. The published benchmarks proved invaluable in uncovering bugs in COMBINE and PC/ANISN and were helpful in transport methods development for the Boron Neutron Capture Therapy (BNCT) program.

I have recently added the cylindrical geometry benchmark of Chapter 3 (Benchmark 3.4), the multigroup slab benchmark of Chapter 4 (Benchmark 4.2) and the 3-D infinite medium multigroup benchmark of Chapter 5 (Benchmark 5.2). These benchmarks represent a more complete strategy of analytical benchmarking. In particular, we perform iteration on nearly all numerical approximations to guarantee benchmark performance. This is a strategy that I currently use, and that will become standard in the future.

While my original intent was to give transport code developers easy access to meaningful numerical solutions to the transport equation, the scope of benchmarking has widened over the years. We can now solve more complex transport equations to obtain the required analytical solution representations than was possible in the early 90s. The benchmarks included in this suite, however, are of the most basic variety, dealing with homogeneous media. One can, however, establish benchmarks for far more complex cases, such as for heterogeneous media, based on what I present here.

Benchmarking has slowly become a recognized part of accountability and continuous improvement of transport methods design. For this reason, benchmarking activity has increased in importance in the nuclear community. During the same period, Monte Carlo has dominated the computational transport landscape owing to its simplicity and versatility. For this reason, analytical transport methods are in danger of being lost altogether. Thus, the methods collected here also serve as a not – all-inclusive archive of analytical techniques to solve the neutron transport equation as well as a legacy of solution methodology for future transport theorists.

The presentation

This work represents only a fraction of the benchmarks I have developed over the past 25 years. In addition to those presented here, I have developed analytical benchmarks with time dependence, highly anisotropic scattering, and for heterogeneous media in such diverse applications as radiative transfer in participating media and in vegetation canopies as well as for galactic cosmic ray cascades. The benchmark technology presented is representative of what was available in the mid-90s. More sophisticated techniques have been developed since but are not contained in this volume and, hopefully, will appear in a future compilation.

We consider twelve well-defined analytical benchmarks covering a spectrum of nuclear reactor physics including neutron moderation through neutron/nucleus elastic and inelastic scattering, criticality and spatial neutron diffusion. We solve the transport equation, primarily for the scalar flux, with a host of mathematical transport methods. These methods include Laplace and Fourier transformations, continuous analytical continuation, invariant embedding, pseudo transport theory, spectral representation, Green’s function and the point kernel formulations. My aim is to establish analytical solution representations that one can evaluate to a high degree of accuracy. We loosely call these numerical evaluations “analytical” benchmarks. However, as explained in the Introduction, they are more precisely called “semi-analytical” benchmarks since the representations are not all in closed form and therefore will themselves contain numerical error. To evaluate these representations, we apply well-established numerical methods such as Romberg integration, Gauss quadrature, Euler-Knopp acceleration, Wynn-epsilon acceleration, rational interpolation and bisection zero search. By controlling numerical error, we anticipate results correct to four- or five- digits.

Chapter 1 is devoted to the heuristic derivation of the integro-differential neutron Boltzmann equation, also called the neutron transport equation. This is the most popular form of transport equation and is the origin of all other forms found in this volume. The derivation follows the standard format except for the treatment of leakage where we apply the divergence theorem to the volume integrated neutron balance in a reduced phase space. Several fundamental forms of the six variable stationary transport equation then follow. Of course, the full transport equation in all phase space variables plus time is much too difficult to solve analytically. Thus, we must mathematically reduce the number of variables through physical/mathematical assumptions like time independence in an infinite medium or monoenergetic and multigroup transport in one spatial dimension. The particular transport equations for these approximations then find use in subsequent chapters as the origin of the solution representations we evaluate.

The four benchmarks of Chapter 2 are concerned with neutron slowing down for increasingly wide-ranging physical assumptions. We begin with the constant cross section approximation for the scalar collision density and move to higher moments in the second benchmark. We then consider the general multigroup approximation with fast reactor criticality as prime example. The last of this series treats neutron thermalization. The next series, in Chapter 3, is for spatial transport in the monoenergetic approximation in one spatial dimension. We begin with the standard plane infinite medium case and end with radial transport in an infinitely long cylinder. In between, the half-space and slab are considered. In the third series of Chapter 4, we take energy (or lethargy) into account through the multigroup description in one spatial dimension. The first is for an infinite medium and the next for a finite medium. The final series, in Chapter 5, is for multidimensional transport in the one-group and multigroup formulations. The first of these is the 2-D searchlight problem and the second is for finite 3-D wire source configurations in an infinite medium.

The compendium is, in large part, patterned after CdH&P; however, I concentrate more on accurate numerical evaluation than on transport approximations and general transport theory. Each chapter begins with a brief description of the reactor physics context into which the benchmarks of that chapter fit. This description is by no means meant to be exhaustive, but rather to motive the reader as to why the particular series of benchmarks has been chosen. We follow this by a classification according to Table A of the Introduction, a general description and the analytical derivation of the appropriate solution representation. The derivation is self-contained in that the reader (with admittedly some effort) can derive any of the analytical solutions from the information provided in the section with minimal reference to the literature. Many of the derivations may be quite involved and require some mathematical insight, however. The chapter continues with a section on the algorithms required to implement the numerical evaluation of the solution representation. Finally, the chapter concludes with a demonstration of the numerical evaluation and a brief description of observed trends. In addition, for the majority of the benchmarks, I provide a table showing the convergence of the flux or reflectance and transmittance, with requested error. I call this section “benchmark qualification”, included to give the reader confidence that the benchmark is indeed accurate to the digits quoted. The tables then serve as standards for comparison to numerical neutron transport algorithms under development. The compendium format is such as to make those in the nuclear engineering and radiative transfer communities aware of the sophistication of current analytical benchmarks and their availability.

All numerical evaluations included in this compilation are available on CD or electronically from the OECD/NEA upon request. The disk contains the FORTRAN source code with the input to all but a few of the figures and tables. For convenience, the input and output descriptions are included in Appendix D. To further aid the reader, Appendix A includes a brief review of the primary numerical methods used, and Appendix B provides descriptions of the numerical transform inversions.

The equations are numbered per each section. For example, the reference Eq. (3.2.8) denotes Eq. (8) of Benchmark 3.2. Some of the fundamental transport equations derived in Chapter 1 are numbered with capital Roman numerals and quoted, for example as, Eq. (1.VII.1) referring to transport equation Eq. (VII.1) of Chapter 1. For convenience, I list all transport equations derived at the end of Chapter 1.

Reader preparation

I have aimed the level of the presentation at advanced undergraduates, first year graduates and professional transport methods developers. Obviously, a mastery of calculus and a modest knowledge of complex variables are required to get the most from this work. However, intimate knowledge of neutron transport theory and reactor physics is not a prerequisite for a thorough understanding. The reader interested in, but not necessarily an expert in, neutron transport theory should be able to gain considerable insight into the topic. However, for in-depth coverage of the overarching reactor physics context, an additional text (or texts) is (are) necessary. Since my primary focus is on the methods of transport theory and the numerical implementation of transport solution representations and not on reactor physics or reactor design, I provide the following list of some well known reactor physics texts, in chronological order of appearance.

Reactor physics texts

1) Glasstone, S., *Principles of Nuclear Reactor Engineering*, D. Van Norstrand Company, Princeton, NJ (1955).

2) Weinberg, A.M., E.P Wigner, *The Physical Theory of Neutron Chain Reactors*, University of Chicago Press, London, UK (1958).

3) Megrhreblian, R.V., D.K. Holmes, *Reactor Analysis*, McGraw-Hill, NY (1960).

4) Galanin, A.D., *Thermal Reactor Theory*, Pergamon Press, NY (1960).

5) Isbin, H.S., *Introductory Nuclear Reactor Theory*, Reinhold, NY (1963).

6) Lamarsh, J.R., *Introduction to Nuclear Reactor Theory*, Addison-Wesley Pub. Co./ANS, La Grange Park, IL (1966/2002).

7) Ferziger, J.H., P.F. Zweifel, *The Theory of Neutron Slowing Down*, The MIT Press, Cambridge, MA (1966).

8) Glasstone, S., A. Sesonske, *Nuclear Reactor Engineering*, Van Nostrand Reinhold, NY (1967).

9) Bell, G., S. Glasstone, *Nuclear Reactor Theory*, Van Nostrand, NY (1970).

10) Zweifel, P.F., *Reactor Physics*, McGraw-Hill, NY (1973).

11) Henry, A.F., *Nuclear-Reactor Analysis*, The MIT Press, Cambridge, MA (1975).

12) Duderstadt, J.J., L.J. Hamilton, *Nuclear Reactor Analysis*, John Wiley and Sons, Inc., NY (1976).

13) Lamarsh, J.R., *Introduction to Nuclear Engineering*, Addison-Wesley, NY (1983).

14) Larmash, J.R., A.J. Baratta, *Introduction to Nuclear Engineering,* 3rd ed., Prentice Hall, Upper Saddle River, NJ (2001).

15) Stacy, W.M., *Nuclear Reactor Physics*, Academic Press, NY (2001).

I also do not claim to have included the full spectrum of possible analytical transport solution methods. I include only the methods I consider most appropriate for numerical evaluation of transport solutions to high accuracy. For example, the method of singular eigenfunctions is not included, although, it is closely related to the pseudo and Fourier transform formulations [5]. In addition, the *Pn* method is not included. For this reason, I provide the following list of neutron transport texts where the reader can find these and other mathematical transport methods. Note however, I only list neutron transport texts and none on radiative transfer where many of the methods of neutron transport theory originated.

Transport texts

1) Glasstone, S., M.C. Edlund, *The Elements of Nuclear Reactor Theory*, D. Van Norstrand Company, Princeton, NJ (1952).

2) Case, K.M., F. De Hoffman, G. Placzek, *Introduction to the Theory of Neutron Diffusion*, Los Alamos Scientific Laboratory, Los Alamos, NM (1953).

3) Davison, B., *Neutron Transport Theory*, Oxford University Press, NY (1957).

4) Williams, M.M.R., *The Slowing Down and Thermalization of Neutrons,* North Holland, Amsterdam (1966).

5) Case, K.M., P.F. Zweifel, *Linerar Transport Theory,* Addison-Wesley, MA (1967).

6) Inonu, E., P.F. Zweifel, *Developments in Transport Theory*, Academic Press, London (1967).

7) Williams, M.M.R, *Mathematical Methods in Particle Transport Theory,* John Wiley & Sons, NY (1971).

8) Duderstadt, J.J., W.R. Martin, *Transport Theory*, John Wiley & Sons, NY (1979).

The most problematic concern associated with your (the reader's) preparation is in the area of mathematics. In the presentation, I use a variety of mathematical concepts including:

- divergence theorem;
- orthogonal polynomials;
- solutions to first and second order ODEs;
- Fourier and Laplace transforms;
- contour integration;
- Cauchy principal value integration;

- solution to linear equations;
- special functions.

A reader who is about to begin, or has completed, graduate studies in engineering or applied mathematics should be familiar with most of the above mathematical concepts. In addition, advanced undergraduates, who have taken courses in applied mathematics and complex variables should have little difficulty.

The reader should be able to derive nearly all the analytical solutions from the material presented. It is only through the derivation of these solutions that one ultimately learns the mathematical methods of transport theory and appreciates the beauty of the subject. If it were not for the struggle that I endured to obtain the representations as presented, this compilation would never have materialized. In addition, I sincerely believe that it is through struggle that real learning takes place. For this reason, the benchmark compilation can be an effective learning tool. Indeed, in compiling these benchmarks, I have been able to discover some of the connections between the various forms of the transport equation and, furthermore, exploit these connections for numerical advantage.

With this said, I urge the reader to fill in the steps of the derivations and to exercise the programs. I guarantee that you will be rewarded with self-satisfaction and at the same time increase your mathematical acuity. Who knows, you may uncover some of the secrets of the transport equation yourself, as I have.

It is my sincere hope that this benchmark compendium adds new knowledge and is, above all, an inspiration.

REFERENCES

[1] Case, K.M., F. De Hoffman, G. Placzek, *Introduction to the Theory of Neutron Diffusion*, Los Alamos Scientific Laboratory, Los Alamos, NM (1953).

[2] Case, K.M., P.F. Zweifel, *Linerar Transport Theory,* Addison-Wesley, MA (1967).

[3] Ganapol, B.D., L.M. Grossman, “The Collided Flux Expansion Method for Time dependent Neutron Transport”, *Nucl. Sci. Eng.*, **52,** 454 (1973).

[4] Miller, A.R., *FORTRAN Programs for Scientists and Engineers*, SYBEX, Inc. (1982).

[5] Ganapol, B.D., “From Fourier Transforms to Singular Eigenfunctions: Multigroup Transport”, *Nucl. Sci. Eng.*, **137**, 400-410 (2001).

INTRODUCTION

Nuclear engineers routinely design nuclear power reactors, including safety analysis and fuel burnup prediction, in today's large-scale computational environments. In particular, methods developers have perfected computational algorithms for cross section generation, neutron transport and diffusion, and Monte Carlo simulations in order to take full advantage of emerging computational architectures. Reactor physicists can accommodate ever larger reactor design calculations as computational capacity increases with microchip efficiency according to Moore's law. With our dependence on large-scale computing comes increased reliance on numerical methods, which in turn encourages development of more powerful and sophisticated numerical tools. Specifically, finite difference, finite element, nodal, discrete ordinates (*Sn*) and *Pn* methods are among today's most effective multidimensional numerical neutron transport algorithms. While these algorithms enable more comprehensive investigations of reactor physics and neutron transport theory, they all generally possess an inherent shortcoming, i.e. some degree of numerical discretization error. This error is a result of the finiteness, though large by past standards, of computer storage. Of course, for some algorithms, we are able to estimate numerical error; but usually this estimate is only approximate and quite often misleading. For this reason, the mathematical and numerical complexity of current schemes raises serious concerns regarding inaccuracy and improper coding. In these times of accountability and continuous improvement, users demand assurance of acceptable error and proper programming.

To address this issue, code verification, including one or all of the following tests, should routinely be a part of transport methods development:

- monitoring conservation of quantities such as particle number, total energy and momentum;
- comparison to known physical trends usually involving simplified problems with predictive behavior;
- comparison to algorithms designed for similar applications;
- construction of manufactured solutions by assuming a solution, generating the corresponding source for that solution, then numerically confirming the assumed solution;
- comparison to standards obtained through analytical benchmarks.

It should be emphasized that there is no guaranteed method of verifying that a particular computational algorithm performs correctly for all cases envisioned since, if there were, there would be no need for the algorithm in the first place. The value of the tests mentioned is in indicating algorithmic inconsistencies through their failure. Note that comparison to experiment is not included as one of them since such a comparison measures how faithful a particular physical model is and says nothing about the quality of the numerical results. For this reason, experimental comparison is model *validation* rather than code *verification*. Both verification and validation are elements of the more general category called *confirmation*.

We develop the present collection of analytical benchmarks, more appropriately called semi-analytical benchmarks, with the primary goal of providing standards of comparison. Currently, the literature lacks such standards, thus, the establishment of a library of transport solutions for code (solution) verification in nuclear engineering applications seems appropriate. A secondary, but just as significant, application is in education. Benchmark development requires a firm understanding of analytical solution techniques as well as numerical methods and computational strategies. One can therefore enhance student perception of how neutrons interact with matter in nuclear engineering courses through study of the theory that accompanies each benchmark. I hope to encourage this by presenting the benchmarks in a reactor physics context. Thus, with some additional material on the physical setting and on the approximations used in practice, we cover the majority of reactor physics taught in a nuclear engineering curriculum. In addition, the study of benchmarks introduces students to standard numerical methods (briefly described in Appendix A) such as iteration/convergence strategies and numerical integration. Thus, the learning experience provided by this benchmark collection serves as the basis for an introductory senior or graduate college course in the methods of reactor physics. Finally, the benchmarks developed here can also provide a first prediction for fluxes and/or reaction rates in a real application.

The benchmarks presented are semi-analytical benchmarks, not to be confused with (purely) numerical benchmarks. A semi-analytical benchmark is an accurate numerical evaluation (usually to four or five correct digits) of an analytical solution representation. A numerical benchmark, on the other hand, is a fine mesh application of a numerical algorithm and, though usually quite accurate, contains numerical discretization error nevertheless. As will become evident, evaluation of a semi-analytical benchmark itself possesses numerical error. The distinction between this error and that in a purely numerical solution is the level in the solution process at which they occur. For numerical benchmarks, the error, usually unmonitored, occurs at the level of the transport equation through direct discretization. While for a semi-analytical benchmark, the error occurs in the evaluation of a solution representation, which also includes discretization or iteration error, but is generally closer to the true analytical solution. By monitoring this error, numerical accountability is therefore possible. However, with this said, accountability of purely numerical solutions, has now also become possible using convergence acceleration [1].

Unfortunately, the requirement of an analytical solution representation limits our considerations to relatively simple transport problems. Thus, analytical benchmarks provide limited verification of isolated portions of comprehensive algorithms. Even with limited verification of the components of an algorithm, our goal is to achieve some degree of confidence in the entire operation of a code. Inconsistencies and inaccuracies may remain, however, from interfacing of components and unexercised portions of an algorithm.

In the past, methods developers have criticized analytical benchmarks because of their idealized nature and have remarked that they are far too idealized to give meaningful diagnostics. We emphasized, however, that even though the type of problem lending itself to analytical solution is usually much less sophisticated than the comprehensive problem for which a code has originally been designed, an analytical benchmark still has diagnostic value. Indeed, it makes perfectly good sense that transport codes designed for sophisticated reactor analyses should also perform well for the simple, idealized cases as well.

The benchmarks we consider describe neutrons of a particular energy moving in space in a certain direction in homogeneous media with and without boundaries. The theory of neutron slowing down addresses the energy loss neutrons experience as they collide with stationary nuclei on their way to thermal energies (thermalization). In the first series, we assume elastic scattering as neutrons slow down in an infinite medium. From a practical point of view, the resulting fluxes provide weighting spectra to generate multigroup cross sections. After sufficient loss of energy, and having passed through the resonance region, the neutrons reach the thermal energy range where they sense the thermal motion of nuclei and therefore gain as well as lose energy upon collision.

When neutrons encounter only heavy nuclei, they lose negligibly small amounts of energy through elastic collisions, giving rise to the monoenergetic (one-group) approximation. For this case, we conveniently apply 1-D transport theory to characterize monoenergetic neutron motion. We shall consider infinite, semi-infinite and finite homogeneous media in the monoenergetic approximation. In addition, 1-D transport theory can describe neutron motion in infinite and finite media in the multigroup approximation. Two-dimensional monoenergetic transport in a semi-infinite medium and 3-D multigroup transport from isotropically emitting finite wire sources in an infinite medium round out this benchmark collection.

We obtain each transport equation, solved for a particular physical setting in a mathematically consistent way from the fundamental integro-differential transport equation derived in Chapter 1. In addition to the description of the theory and numerical implementation, we discuss trends when apparent. A FORTRAN program, suitable for most computational platforms, accompanies each benchmark.

Analytical benchmark hierarchy

When solving the neutron transport equation, a hierarchy of analytical solutions, representing decreasing numerical accuracy, is possible. We characterize this hierarchy as

- exact-analytical;
- near-analytical;
- semi-analytical;
- purely-numerical.

A closed-form *exact-analytical* solution is the perfect solution one strives toward when numerically solving any equation. For this case, we have an explicit solution representation in terms of elementary functions. The most accurate numerical evaluation of this closed form representation is through infinite precision arithmetic, thus avoiding numerical truncation error altogether. Unfortunately, the solutions to particle transport equations do not generally lend themselves to simple closed form representations. With the increased use of symbolic manipulation for numerical evaluation, however, the ideal of the *exact-analytical* solution will become possible in the near future (see Ref. 2). A *near-analytical* solution is an evaluation of a closed form solution representation in terms of special functions using standard numerical approximations with high precision arithmetic. Such an evaluation may use numerical quadrature and infinite series for which error estimates are available. *Semi-analytical* solutions, on the other hand, are finite precision numerical evaluations of a continuous variable solution representation, which, for example, may be in the form of an integral or integral equation. These solutions generally require iterative evaluation with inherent error control and the potential for acceleration toward convergence. All benchmarks presented are examples of *semi-analytical* solutions. Finally, the most common solutions to the transport equation involve full numerical discretization of the transport operator with respect to particle position, direction, time and energy. These *purely-numerical* solutions, while containing discretization error, are nevertheless the most comprehensive transport solutions available today and are the foundation of numerical transport methods. Algorithms such as the discrete ordinates or *Pn* approximations can generate ultra-fine-mesh benchmark solutions that are as accurate as *semi-analytical* benchmarks [1].

There are several important distinctions between the classes of (*exact*-, *near*-, *semi*-) "*analytical*" and *purely*-*numerical* solutions. First, like any numerical solution, *analytical* benchmarks (with the exception of "*exact*") contain unavoidable numerical error resulting from finite precision arithmetic and numerical approximation. Unlike *purely*-*numerical* solutions, however, the error associated with *analytical* benchmarks occurs at a level theoretically closer to the true analytical solution. For this reason, *analytical* benchmarks represent a higher standard of quality than *purely*-*numerical* solutions. Comparison to *analytical* benchmarks can uncover unknown numerical vagaries and coding errors, and can provide an assessment of the accuracy of *purely*-*numerical* transport algorithms as well as confirm proper algorithm performance. The series of *semi*-*analytical* benchmarks we consider, therefore, serve as convenient standards to which to compare the numerical transport algorithms of neutron transport. This is not to say that fine-mesh numerical benchmarks cannot be as accurate as *analytical* benchmarks, but ultimate confidence in their accuracy only comes from comparisons with *semi*-*analytical* benchmarks (or possibly manufactured solutions).

Benchmark classification

Since many benchmarks are possible, I have established a classification scheme for reference purposes. We classify each benchmark according to the eight categories listed in Table A.

The first category (C1) specifies the type of all particles considered including neutrons, photons, electrons, ions and molecules. In future efforts, the benchmark suite will (hopefully) include most of the particles indicated. Here, we consider only neutrons. Category 2 (C2) specifies the medium geometry of the field particles with which neutrons interact. In this case study, we present benchmarks in one-, two- and three- dimensions. In general, the geometry can be infinite (without surfaces), 1-D or 2-D half-spaces with one surface or a 1-D finite medium with one or two surfaces. C3 gives the type of scattering kernel (isotropic, anisotropic or general) with the neutron energy spectrum approximation (one-group, multigroup or continuous) given in C4. Categories C5 and C6 indicate the angular and spatial source distributions, respectively. Information concerning the numerical method is given in C7 and C8, with C7 specifying which independent variables are treated either continuously (C) or discretely (D) with the numerical method designated in C8.

Table A. Benchmark classification

C1. SPECIFIC TRANSPORT FIELD	
NT	Neutron transport
ND	Neutron diffusion
RT	Radiative transfer
EIT	Electron and ion transport
RGD	Rarefied gas dynamics

C2. GEOMETRY	
P	Plane geometry (1-D,2-D)
SP	Spherical geometry (1-D)
CY	Cylindrical geometry (1-D,2-D)

SPECIFIC GEOMETRY QUALIFIERS	
I	Infinite medium
H	Half-space
2H	2 Half-spaces
S	Slab geometry
HE	Heterogeneous slab geometry

C3. ANISOTROPY OF SCATTERING KERNEL	
I	Isotropic
LE(*L*)	Legendre expansion of order *L*
G	General

C4. ENERGY SPECTRUM APPROXIMATION	
OG	One-group
MG	Multigroup
C	Continuous

C5. ANGULAR SOURCE DISTRIBUTION	
I	Isotropic
B	Beam
D	Distributed
LE(*L*)	Legendre expansion of order *L*

C6. SPATIAL AND/OR TEMPORAL SOURCE DISTRIBUTION	
L	Localized (delta function)
D	Distributed
PT	Pulsed in time
CT	Continuous in time
U	Uniform spatially

C7. NUMERICAL TREATMENT OF INDEPENDENT VARIABLES	
X(C,D)	Position (continuous, discrete)
A(C,D)	Angle (continuous, discrete)
T(C,D)	Time (continuous, discrete)
E(C,D)	Energy (continuous, discrete)

C8. NUMERICAL METHOD	
NLTI	Numerical Laplace transform inversion
NFTI	Numerical Fourier transform inversion
FN	FN method
IT	Integral transport
GFM	Green’s function method
RM	Reconstruction from moments
MC	Multiple collision
RR	Recurrence relation
CAC	Continuous analytical continuation
EE	Eigenfunction expansion
PKM	Point kernel method

REFERENCES

[1] Ganapol, B.D., “Mining the Multigroup Discrete Ordinates Algorithm for High Quality Solution”, *ANS M&C Topical*, Avignon, France (2005).

[2] Ganapol, B.D., *et al.*, “Multigroup Diffusion Kinetics Benchmark of an ADS System in Slab Geometry”, *Proc. PHYSOR’02*, Seoul, Korea (2002).

Chapter 1

THE NEUTRON BOLTZMANN EQUATION

Several choices are possible for describing neutron behavior in a medium filled with nuclei. A neutron is a subatomic particle called a baryon having the characteristic strong nuclear force of the standard model. Thus, a quantum mechanical description seems appropriate, leading to an involved system of Schrödinger equations describing neutron motion between and within nuclei. A neutron is also a relativistic particle with variation of its mass over time when travelling near the speed of light. Finally, a neutron possesses wave and classical particle properties simultaneously and therefore a collective description like that of Maxwell's equations also seems appropriate. In reality, a neutron displays all of the above characteristics at one time or another. When a neutron collides with a nucleus, its strong force interacts with all of the individual nucleons. However, between nuclear collisions, neutrons move ballistically. Neutrons with energies above 20 MeV with speeds of more than 20% the speed of light (c), exhibit relativistic motion, but most in a reactor are rarely above $0.17c$. The neutron wavelength is most important for ultra-low-energy neutrons mainly existing in the laboratory. Fortunately, the classical neutral particle description with quantum mechanics describing collisions emerges as the most appropriate for the investigation of neutron motion within a nuclear reactor.

We now derive the neutron Boltzmann equation, also called the neutron transport equation, to characterize a relatively small number of neutrons colliding in a vast sea of nuclei. Mathematically, a neutron is a neutral point particle, experiencing deflection from or capture by a nucleus at the center of an atom. If conditions are just right, the captured neutron causes a fissile nucleus to fission producing more neutrons. The statistically large number of neutrons interacting in a reactor allows for a continuum-like description through averaging resulting in the linear Boltzmann equation. Also, a statistical mechanical formulation, first attempted by Boltzmann [1] for interacting gases, provides an appropriate description. Boltzmann's equation, based on physical arguments, such as finite particle size, gives a more physically precise picture of particle-particle interaction than is presented here. In his description, all particles, including nuclei, are in motion with like particle collisions allowed. Because of the low density of neutrons in comparison to nuclei in a reactor however, these collisions are infrequent enabling a simplified physical/mathematical theory.

Several forms of the neutron transport equation exist. The integro-differential formulation, arguably the most popular form in neutron transport and reactor physics applications, is presented in §1.1. However, other forms of the transport equation may more appropriately establish the analytical solution representations required for an analytical benchmark. Therefore, §1.2 suggests eight additional forms, all originating from the integro-differential neutron Boltzmann equation. In §1.3, we present "derivative forms" of the Boltzmann equation leading to the benchmarks, such as for the multigroup transport equation, considered in the chapters to follow.

1.1 Integro-differential neutron Boltzmann equation

A primary goal of nuclear reactor design is the reliable prediction of neutron production and loss rates. Predictions come from the solution of the neutron conservation equation – hence, the importance of the neutron Boltzmann equation. Of the several possible physical descriptions, we consider the neutron as a classical interacting particle and formulate neutron conservation in a medium.

1.1.1 Independent variables

Figure 1.1(a) shows a neutron moving at the position denoted by the vector $\boldsymbol{r}$. Figure 1.1(b) shows a second vector $\boldsymbol{\Omega}$ in a coordinate system (dotted axes) superimposed on the neutron itself to indicate neutron direction. The $\boldsymbol{\Omega}$-vector specifies a point on the surface of a fictitious sphere of unit radius surrounding the neutron and pointing in its direction of travel. The neutron velocity is therefore, $\boldsymbol{V} \equiv \mathrm{v}\boldsymbol{\Omega}$, where v is the neutron speed giving the classical neutron kinetic energy:

$$E \equiv \frac{1}{2} m\mathrm{v}^2$$

for a neutron of mass m. Along with time, represented by t and measured from a reference time, $\boldsymbol{r},\boldsymbol{\Omega},E$ symbolize the six independent variables of the classical description of neutron motion.

1.1.2 Dependent variables

For convenience, we combine the position and velocity vectors into a single generalized six-dimensional vector $\boldsymbol{P} \equiv (\boldsymbol{r},\boldsymbol{V})$ defining the neutron phase space. Furthermore, decomposing the velocity vector into speed and direction gives the equivalent representations, $\boldsymbol{P} = (\boldsymbol{r},\boldsymbol{\Omega},\mathrm{v}) = (\boldsymbol{r},\boldsymbol{\Omega},E)$. Note that a Jacobian transformation is required between the various phase space transitions. The following derivation uses the latter representation exclusively. The derivation will be a purely heuristic one, i.e. coming from physical intuition rather than from precise mathematical rigor. In this regard, we largely follow the approach of Boltzmann.

The key element of the derivation is to maintain the point particle nature of a neutron while taking advantage of the statistics of large numbers. Thus, point collisions occur in a statistically averaged phase space continuum realized by defining the phase volume element $\Delta\boldsymbol{P} \equiv \Delta\boldsymbol{r}\Delta\boldsymbol{\Omega}\Delta E$ about $\boldsymbol{P}$ as shown in Figure 1.2. Note that the unit of solid angle, $\Delta\boldsymbol{\Omega}$**,** is the steradian (*sr*), and that 4π steradians account for all possible directions on a unit sphere.

The volume element of phase space $\Delta\boldsymbol{P}$ plays a central part in the overall neutron balance. One physically accounts for neutrons entering or leaving through the boundaries of $\Delta\boldsymbol{r}$ or that are lost or gained within $\Delta\boldsymbol{r}$. In addition, neutrons enter or leave the phase element through deflection into or out of the direction range $\Delta\boldsymbol{\Omega}$, or by slowing down or speeding up through the energy boundaries of ΔE.

Let $N(\boldsymbol{r},\boldsymbol{\Omega},E,t)$ be the neutron density distribution:

$$N(\boldsymbol{r},\boldsymbol{\Omega},E,t)\Delta\boldsymbol{P} \equiv \text{Number of neutrons in } \Delta\boldsymbol{P} \text{ at time } t$$

Since $\mathrm{v}\Delta t$ is the distance travelled per neutron of speed v, called the neutron track length, the total track length of all neutrons in $\Delta\boldsymbol{P}$ is:

$$\mathrm{v}N(\boldsymbol{r},\boldsymbol{\Omega},E,t)\Delta\boldsymbol{P}\Delta t \equiv \text{Total track length in } \Delta\boldsymbol{P} \text{ at time } t \text{ for neutrons of speed v}$$

As shown, the track length serves as the bridge between point-like and continuum particle behavior when characterizing collisions.

In the above definition, it is convenient to define the following quantity as the neutron angular flux at time t:

$$\phi(\boldsymbol{r},\Omega,E,t) \equiv \mathrm{v}N(\boldsymbol{r},\Omega,E,t)$$

representing the total track length per second of all neutrons in $\Delta\boldsymbol{P}$ per unit of phase space.

While the neutron density and flux are associated with a phase space volume element, the neutron angular current vector, $\boldsymbol{J}(\boldsymbol{r},\Omega,E,t)$, is associated with an area. The magnitude of the angular current vector is the rate of neutrons per steradian, energy and area, in the direction $\boldsymbol{\Omega}$ that pass through an area perpendicular to $\boldsymbol{\Omega}$ at time t. Neutrons, passing through the area A oriented with the unit normal $\hat{\boldsymbol{n}}$, as shown in Figure 1.3, during Δt, enter the volume element $\Delta\boldsymbol{r} = \hat{\boldsymbol{n}} \bullet \Omega A \mathrm{v}\Delta t$. Thus, the total number of neutrons in the phase volume element $\Delta\boldsymbol{P} = [\hat{\boldsymbol{n}} \bullet \Omega A \mathrm{v}\Delta t]\Delta\Omega\Delta E$ is:

$$N(\boldsymbol{r},\Omega,E,t)[\hat{\boldsymbol{n}} \bullet \Omega A \mathrm{v}\Delta t]\Delta\Omega\Delta E$$

We then conveniently define the angular current vector to be:

$$\boldsymbol{J}(\boldsymbol{r},\Omega,E,t) \equiv \mathrm{v}\Omega N(\boldsymbol{r},\Omega,E,t)$$

such that $\hat{\boldsymbol{n}} \bullet \boldsymbol{J}(\boldsymbol{r},\Omega,E,t)\Delta\Omega\Delta E$ is the rate of neutrons per area passing through an area of orientation $\hat{\boldsymbol{n}}$.

N, ϕ and $\boldsymbol{J}$ are called *dependent* variables since they *depend* on the *independent* variables of phase space and time.

1.1.3 Nuclear data

Neutrons primarily experience scattering, capture and fission characterized through probabilities represented by microscopic and macroscopic cross sections. In the following, we assume neutrons interact with inert stationary nuclei. The macroscopic cross section for interaction of type i with the nucleus of nuclide j is:

$$\Sigma_{ij}(\boldsymbol{r},E,t) \equiv \text{Fractional probability of neutron interactions } i \text{ with nuclide } j \text{ per path length travelled}$$

where $i = s_{catter}, c_{apture}, f_{ission}, a_{bsorption}(= c + f)$. $\Sigma_{ij}(\boldsymbol{r},E,t)$ is a product of a microscopic cross section $\sigma_{ij}(E)$ which depends on the nuclide j and reaction type i and the nuclear atomic density, $N_j(\boldsymbol{r},t)$, which can vary spatially. The microscopic cross section nominally represents the area presented to the neutron for an interaction to occur and is a measure of the probability of occurrence. The cross section is fundamental to neutron transport theory and provides the essential element in the continuum characterization of point collisions. Since, as previously shown, the total path length of all neutrons in the element $\Delta\boldsymbol{P}$ is $\phi(\boldsymbol{r},\Omega,E,t)\Delta\boldsymbol{P}\Delta t$, the number of interactions of type i per time, or the reaction rate for interaction i in $\Delta\boldsymbol{P}$ with nuclide j is simply from the definition of cross section:

$$\text{Reaction rate for interaction } i \text{ with nuclide } j \equiv \Sigma_{ij}(\boldsymbol{r},E,t)\phi(\boldsymbol{r},\Omega,E,t)\Delta\boldsymbol{P}$$

If we assume individual interactions to be independent events, the total interaction rate of type i is the sum over all J participating nuclear species giving the total macroscopic cross section:

$$\Sigma_i(\boldsymbol{r},E,t) = \sum_{j=1}^{J}\Sigma_{ij}(\boldsymbol{r},E,t) = \sum_{j=1}^{J}N_j(\boldsymbol{r},t)\sigma_{ij}(E)$$

Note that the macroscopic interaction rate is independent of neutron direction and depends only on neutron motion amongst interaction centers (the nuclei). When we next consider neutron deflection or scattering, directional information is essential, however.

The law of deflection, or the differential scattering kernel, is:

$$f_s(\mathbf{\Omega}' \bullet \mathbf{\Omega}, E' \to E)\Delta\Omega\Delta E \equiv \text{Fractional probability of scattering from direction } \mathbf{\Omega}' \text{ and energy } E' \text{ to direction range } \Delta\mathbf{\Omega} \text{ and energy range } \Delta E$$

We mostly require, however, the differential scattering cross section for the *j*th nuclide:

$$\Sigma_{sj}\left(\boldsymbol{r}, \Omega' \bullet \Omega, E' \to E, t\right) \equiv \Sigma_{sj}\left(\boldsymbol{r}, E', t\right) f_{sj}\left(\Omega' \bullet \Omega, E' \to E\right)$$

Scattering, assumed rotationally invariant, depends only on the cosine of the angle between the incoming $\mathbf{\Omega}'$ and scattered $\mathbf{\Omega}$ neutron directions, $\mathbf{\Omega}'\bullet\mathbf{\Omega}$. We normalize the scattering kernel such that neutrons must appear in some direction and energy range:

$$\int_0^\infty dE \int_{4\pi} d\Omega f_s\left(\Omega' \bullet \Omega, E' \to E\right) \equiv 1$$

Assuming that the speed of light is an upper limit, the integration is actually over a finite range $[0,E_0]$.

The scattering law f_{sj} is generally independent of time and position. The scattering cross section for an individual nuclide, however, includes the atomic density, which can provide a time variation of the differential scattering cross section.

Neutrons from fission are either prompt or delayed through subsequent nuclear decay and emission. Here, we consider only prompt neutrons. The neutrons, produced isotropically, appear in an energy and direction range according to the distribution $\chi(E)$:

$$\frac{\chi(E)}{4\pi}\Delta\Omega\Delta E \equiv \text{Fractional probability of a fission neutron appearing in the direction range } \Delta\mathbf{\Omega} \text{ and energy range } \Delta E$$

with normalization:

$$\int_0^\infty dE \chi(E) \equiv 1$$

In addition, we shall require the average number of neutrons produced per fission, $\nu(E)$.

With the notation now in place, an accounting of the total number of neutrons in the phase space volume element $\Delta\boldsymbol{P}$ becomes our focus.

1.1.4 Contributions to the total neutron balance

We now account for the net number of neutrons within an arbitrary volume *V* (shown in Figure 1.4) and in the partial phase space element $\Delta\mathbf{\Omega}\Delta E$ during a time Δt. In words, the neutron balance in the entire volume *V* and partial element $\Delta\mathbf{\Omega}\Delta E$ is:

$$\boxed{\begin{array}{c}\text{Number}\\ \text{at time } t+\Delta t\end{array}} = \boxed{\begin{array}{c}\text{Number}\\ \text{at time } t\end{array}} +$$

$$+ \boxed{\begin{array}{c}\text{Number gained}\\ \text{during}\,\Delta t\end{array}} - \boxed{\begin{array}{c}\text{Number lost}\\ \text{during}\,\Delta t\end{array}}$$

All contributions to the neutron balance, which we now consider separately, are in terms of the dependent variables.

1.1.4.1 *Total number of neutrons*

The total number of neutrons in $V\Delta\Omega\Delta E$ at times t and $t + \Delta t$ is:

$$\Delta\Omega\Delta E \int_V d\boldsymbol{r} N\left(\boldsymbol{r},\Omega,E,t\right)$$

$$\Delta\Omega\Delta E \int_V d\boldsymbol{r} N\left(\boldsymbol{r},\Omega,E,t+\Delta t\right)$$

1.1.4.2 *Scattering gain*

Neutrons from all points within V are scattered into the element $\Delta\Omega\Delta E$. The total number scattered during Δt from any element $dE'd\Omega'$ (at time t) is therefore the total scattering rate in V multiplied by Δt:

$$\Delta t \int_V d\boldsymbol{r} \Sigma_s\left(\boldsymbol{r},E',t\right)\phi\left(\boldsymbol{r},\Omega',E',t\right)dE'd\Omega'$$

and of these:

$$f_s\left(\Omega'\bullet\Omega,E'\to E\right)\Delta\Omega\Delta E$$

reach $\Delta\Omega\Delta E$. Thus, the total number scattering into $\Delta\Omega\Delta E$ during Δt within V is the integration over all possible contributions from all differential phase space elements $dE'd\Omega'$:

$$\Delta\Omega\Delta E\Delta t\int_V d\boldsymbol{r}\int_0^\infty dE'\int_{4\pi} d\Omega' f_s\left(\Omega'\bullet\Omega,E'\to E\right)\Sigma_s\left(\boldsymbol{r},E',t\right)\phi\left(\boldsymbol{r},\Omega',E',t\right)$$

1.1.4.3 *Fission production*

The number of fissions occurring within V during Δt in any differential element $dE'd\Omega'$ is:

$$\Delta t \int_V d\boldsymbol{r} \Sigma_f\left(\boldsymbol{r},E',t\right)\phi\left(\boldsymbol{r},\Omega',E',t\right)dE'd\Omega'$$

For each fission, $\frac{\chi(E)}{4\pi}\nu(E')\Delta\Omega\Delta E$ neutrons appear in $\Delta\Omega\Delta E$ giving a total gain from fission in $V\Delta\Omega\Delta E$ of:

$$\Delta\Omega\Delta E\Delta t\int_V d\boldsymbol{r}\frac{\chi(E)}{4\pi}\int_0^\infty dE'\int_{4\pi} d\Omega'\nu(E')\Sigma_f(\boldsymbol{r},E',t)\phi(\boldsymbol{r},\Omega',E',t)$$

1.1.4.4 Losses from absorption and scattering

The number of neutrons lost due to absorption in $V\Delta\Omega\Delta E$ is:

$$\Delta\Omega\Delta E\Delta t\int_V d\boldsymbol{r}\Sigma_a(\boldsymbol{r},E,t)\phi(\boldsymbol{r},\Omega,E,t)$$

Here, absorption refers to loss independently of whether a neutron causes a fission or not.

In addition, a neutron is lost when it scatters out of the direction range $\Delta\Omega$ or energy range ΔE. The number lost from scattering out of $V\Delta\Omega\Delta E$ is therefore:

$$\Delta\Omega\Delta E\Delta t\int_V d\boldsymbol{r}\left[\int_0^\infty dE'\int_{4\pi} d\Omega' f_s(\Omega'\bullet\Omega,E\to E')\right]\Sigma_s(\boldsymbol{r},E,t)\phi(\boldsymbol{r},\Omega,E,t)$$

or, from the scattering kernel normalization:

$$\Delta\Omega\Delta E\Delta t\int_V d\boldsymbol{r}\Sigma_s(\boldsymbol{r},E,t)\phi(\boldsymbol{r},\Omega,E,t)$$

Note that scattering from the element $\Delta\Omega\Delta E$ to itself is a loss since it is also a gain as per §1.1.4.2.

1.1.4.5 Losses from streaming out of V

Consider the elemental area dA on the surface of V with outward normal $\hat{\boldsymbol{n}}_s$ (see Figure 1.4). By definition of the current vector, the number of neutrons "leaking out" of dA from the element $\Delta\Omega\Delta E$ during Δt is:

$$\Delta\Omega\Delta E\Delta t\ \hat{\boldsymbol{n}}_s\bullet\boldsymbol{J}(\boldsymbol{r},\Omega,E,t)dA$$

Thus, over the entire surface of V, the total leakage is:

$$\Delta\Omega\Delta E\Delta t\int_A dA\hat{\boldsymbol{n}}_s\bullet\boldsymbol{J}(\boldsymbol{r}_s,\Omega,E,t)=\Delta\Omega\Delta E\Delta t\int_V d\boldsymbol{r}\nabla\bullet\boldsymbol{J}(\boldsymbol{r},\Omega,E,t)$$

where the divergence theorem [2] has transformed the surface integration into a volume integration.

1.1.5 Total balance: the neutron Boltzmann equation

Putting all contributions together, dividing by $\Delta t\Delta\Omega\Delta E$ and taking the limit as Δt, $\Delta\Omega$, ΔE approach 0 gives the overall balance in any partial element $d\Omega dE$ over the entire volume at time t:

$$\int_V d\boldsymbol{r}\left\{\begin{array}{l}\left[\frac{1}{\mathrm{v}}\frac{\partial}{\partial t}+\boldsymbol{\Omega}\bullet\nabla+\Sigma(\boldsymbol{r},E,t)\right]\phi(\boldsymbol{r},\Omega,E,t)- \\ -\int_0^\infty dE'\int_{4\pi}d\Omega'\Sigma_s(\boldsymbol{r},\Omega'\bullet\Omega,E'\to E)\phi(\boldsymbol{r},\Omega',E',t)- \\ -\frac{\chi(E)}{4\pi}\int_0^\infty dE'\int_{4\pi}d\Omega'\nu(E')\Sigma_f(\boldsymbol{r},E',t)\phi(\boldsymbol{r},\Omega',E',t)\end{array}\right\}=0$$

where the total macroscopic and the differential scattering cross sections are:

$$\Sigma(\boldsymbol{r},E,t)\equiv\Sigma_a(\boldsymbol{r},E,t)+\Sigma_s(\boldsymbol{r},E,t)$$

$$\Sigma_s(\boldsymbol{r},\Omega'\bullet\Omega,E'\to E,t)\equiv\Sigma_s(\boldsymbol{r},E',t)\,f_s(\Omega'\bullet\Omega,E'\to E)$$

Finally, because the volume is arbitrary and assuming a continuous integrand, the above integral is zero only if the integrand is zero yielding the following neutron Boltzmann equation:

$$\begin{array}{l}\left[\frac{1}{\mathrm{v}}\frac{\partial}{\partial t}+\boldsymbol{\Omega}\bullet\nabla+\Sigma(\boldsymbol{r},E,t)\right]\phi(\boldsymbol{r},\Omega,E,t)= \\ =\int_0^\infty dE'\int_{4\pi}d\Omega'\Sigma_s(\boldsymbol{r},\Omega'\bullet\Omega,E'\to E)\phi(\boldsymbol{r},\Omega',E',t)+ \\ +\frac{\chi(E)}{4\pi}\int_0^\infty dE'\int_{4\pi}d\Omega'\nu(E')\Sigma_f(\boldsymbol{r},E',t)\phi(\boldsymbol{r},\Omega',E',t)+Q(\boldsymbol{r},\Omega,E,t)\end{array}\qquad\text{(I)}$$

We include an external volume source rate of emission from non-flux related events, $Q(\boldsymbol{r},\Omega,E,t)$, for completeness.

Equation (I) is a linear integro-differential equation and as such requires boundary and initial conditions. We will fashion these conditions after the particular benchmark considered.

The benchmarks in this compilation are steady state benchmarks obtained by assuming all nuclear data to be time independent and:

$$\lim_{t\to\infty}\phi(\boldsymbol{r},\Omega,E,t)=0$$

Then through integration over all time, the steady state form of Eq. (I) becomes:

$$\begin{array}{l}\left[\boldsymbol{\Omega}\bullet\nabla+\Sigma(\boldsymbol{r},E)\right]\phi(\boldsymbol{r},\Omega,E)= \\ =\int_0^\infty dE'\int_{4\pi}d\Omega'\Sigma_s(\boldsymbol{r},\Omega'\bullet\Omega,E'\to E)\phi(\boldsymbol{r},\Omega',E')+ \\ +\frac{\chi(E)}{4\pi}\int_0^\infty dE'\int_{4\pi}d\Omega'\nu(E')\Sigma_f(\boldsymbol{r},E')\phi(\boldsymbol{r},\Omega',E')+Q(\boldsymbol{r},\Omega,E)\end{array}\qquad\text{(II)}$$

where:

$$\phi(\boldsymbol{r},\Omega,E) \equiv \int_0^\infty dt\phi(\boldsymbol{r},\Omega,E,t)$$

The steady state source distribution $Q(\boldsymbol{r},\Omega,E)$ now incorporates the initial condition.

The neutron transport equation given by Eq. (II) is the source of all the other transport equations in this compendium. Obviously, Eq. (II), being an integro-differential equation in six independent variables, does not lend itself to simple analytical solutions. Therefore, we require further simplification to enable analytical solution representations for eventual numerical evaluation.

Monte Carlo and other sophisticated deterministic methods solve Eq. (II) numerically; but, as we discussed in the Introduction, these methods contain numerical and sampling errors and will not be our focus. Our objective is to solve Eq. (II) in the most analytically pure way possible. In the chapters to follow, we present examples of analytical solutions of zero to three dimensions and continuous to multigroup in energy. Most of the solutions come from other forms of Eq. (II) that provide the necessary simplicity for further analytical and numerical investigation. We now consider these forms.

1.2 Additional forms of the neutron transport equation

Before defining the benchmarks inspired by Eq. (II), it is of interest to reformulate Eq. (II) in the various versions used to define these benchmarks. At last count, there are at least eight (and probably more) equivalent forms of Eq. (II) not counting Monte Carlo including:

- integral;
- even/odd parity;
- slowing down kernel;
- multiple collision;
- invariant embedding;
- singular integral;
- Green's function;
- pseudo flux.

Each form has a particular mathematical property facilitating a class of solutions. For example, the multiple collision form is appropriate for highly absorbing media. Invariant embedding is useful for half-space problems, whereas the pseudo flux form is appropriate for isotropic scattering in multidimensions. The Green's function representation is best suited for highly heterogeneous 1-D plane media in the multigroup approximation.

In the following sections, we consider the integral transport equation, the pseudo flux equations and the Green's function forms only. We also derive the monoenergetic and multigroup approximations in 3-D and specifically in 1-D geometies, as they enable analytical solutions and are ubiquitous in the literature.

1.2.1 The integral equation

The integral transport equation is essentially an integration along the characteristic defining the neutron path. If a neutron travels in direction **Ω**, shown in Figure 1.5, between the points specified by vectors $\boldsymbol{r}'$ and $\boldsymbol{r}$, the following relationship holds:

$$\boldsymbol{r} = \boldsymbol{r}' + s\boldsymbol{\Omega}$$

where s is the magnitude of the vector $\boldsymbol{r} - \boldsymbol{r}'$. Since the derivative along the neutron path is:

$$\frac{d}{ds} = \frac{\partial \boldsymbol{r}'}{\partial s} \bullet \nabla_{r'}$$

where the gradient is with respect to $\boldsymbol{r}'$, evaluation of Eq. (II) at $\boldsymbol{r}'$ gives:

$$\left[\frac{d}{ds} - \Sigma(\boldsymbol{r}', E)\right]\phi(\boldsymbol{r}', \Omega, E) = -q(\boldsymbol{r}', \Omega, E) \tag{1a}$$

where and collision source is

$$q(\boldsymbol{r}, \Omega, E) = \int_0^\infty dE' \int_{4\pi} d\Omega' \Sigma_s(\boldsymbol{r}, \Omega' \bullet \Omega, E' \to E)\phi(\boldsymbol{r}, \Omega', E') + \\ + \frac{\chi(E)}{4\pi}\int_0^\infty dE' \int_{4\pi} d\Omega' \nu(E')\Sigma_f(\boldsymbol{r}, E')\phi(\boldsymbol{r}, \Omega', E') + Q(\boldsymbol{r}, \Omega, E) \tag{1b}$$

Further, if we define the optical depth, or mean free path, as:

$$\tau(\boldsymbol{r}, \boldsymbol{r}', E) \equiv \int_0^{|\boldsymbol{r}-\boldsymbol{r}'|} ds' \Sigma(\boldsymbol{r}'(s'), E)$$

and assume we know $q(\boldsymbol{r},\Omega,E)$, the solution to Eq. (1a), viewed as a first order ordinary differential equations, is:

$$\phi(\boldsymbol{r}, \Omega, E) = \phi(\boldsymbol{r}', \Omega, E)e^{-\tau(\boldsymbol{r}, \boldsymbol{r}', E)} + \int_0^s ds' e^{-\tau(\boldsymbol{r}, \boldsymbol{r}'(s'), E)} q(\boldsymbol{r}'(s'), \Omega, E) \tag{2}$$

and becomes:

$$\phi(\boldsymbol{r}, \Omega, E) = \phi(\boldsymbol{r}_s(\Omega), \Omega, E)e^{-\tau(\boldsymbol{r}, \boldsymbol{r}_s(\Omega), E)}\Theta(-\hat{\boldsymbol{n}}_s \bullet \Omega) + \\ + \int_0^{|\boldsymbol{r}-\boldsymbol{r}_s|} ds' e^{-\tau(\boldsymbol{r}, \boldsymbol{r}-s'\Omega, E)} q(\boldsymbol{r} - s'\Omega, \Omega, E) \tag{3}$$

for $\boldsymbol{r}' = \boldsymbol{r}_s$ on the boundary of the medium with outward normal surface $\hat{\boldsymbol{n}}_s$ shown in Figure 1.6. Note that the distance to the point on the surface from the origin, $\boldsymbol{r}_s(\Omega)$, depends on the neutron direction. $\Theta(-\hat{\boldsymbol{n}}_s \bullet \Omega)$ is the Heaviside step function representing only incoming neutrons where $\phi(\boldsymbol{r}_s,\Omega,E)$ is known for all incoming directions. We do not consider re-entrant boundaries. Therefore, Eqs. (3) and (1b) constitute a Fredholm integral equation of the second kind for the angular flux. We obtain the scalar, or angularly integrated, flux:

$$\phi(\boldsymbol{r},E)=\int\limits_{4\pi}d\Omega\phi(\boldsymbol{r},\Omega,E) \tag{4}$$

through integration of Eq. (2):

$$\begin{aligned}&\phi(\boldsymbol{r},E)= \\ &=\int\limits_{\hat{\boldsymbol{n}}_s\bullet\boldsymbol{\Omega}<0}d\Omega\phi\left(\boldsymbol{r}_s(\Omega),\Omega,E\right)e^{-\tau(\boldsymbol{r},\boldsymbol{r}_s(\Omega),E)}+\int\limits_{4\pi}d\Omega\int\limits_{0}^{|\boldsymbol{r}-\boldsymbol{r}_s|}ds'e^{-\tau(\boldsymbol{r},\boldsymbol{r}',E)}q\left(\boldsymbol{r}'(s'),\Omega,E\right)\end{aligned} \tag{5}$$

By substitution of the differential volume element, $d\boldsymbol{r}'=s'^2d\Omega\ ds'$, Eq. (5) becomes:

$$\begin{aligned}&\phi(\boldsymbol{r},E)= \\ &=\int\limits_{\hat{\boldsymbol{n}}_s\bullet\boldsymbol{\Omega}<0}d\Omega\phi\left(\boldsymbol{r}_s(\Omega),\Omega,E\right)e^{-\tau(\boldsymbol{r},\boldsymbol{r}_s(\Omega),E)}+\int\limits_{V}d\boldsymbol{r}'\frac{e^{-\tau(\boldsymbol{r},\boldsymbol{r}',E)}}{|\boldsymbol{r}-\boldsymbol{r}'|^2}q\left(\boldsymbol{r}',\frac{\boldsymbol{r}-\boldsymbol{r}'}{|\boldsymbol{r}-\boldsymbol{r}'|},E\right)\end{aligned} \tag{6}$$

Note that Eq. (6) is not an integral equation for the scalar flux since the scalar flux does not generally appear under the integral. However, we can find an integral equation for the scalar flux under certain circumstances. If scattering is isotropic and the source is isotropically emitting, then:

$$f_s(\Omega'\bullet\Omega,E'\rightarrow E)=\frac{1}{4\pi}f_s(E'\rightarrow E)$$

$$Q(\boldsymbol{r},\Omega,E)=\frac{1}{4\pi}Q(\boldsymbol{r},E)$$

and Eq. (6) reduces to:

$$\begin{aligned}\phi(\boldsymbol{r},E)=&\int\limits_{\hat{\boldsymbol{n}}_s\bullet\boldsymbol{\Omega}<0}d\Omega\phi\left(\boldsymbol{r}_s(\Omega),\Omega,E\right)e^{-\tau(\boldsymbol{r},\boldsymbol{r}_s(\Omega),E)}+ \\ &+\int\limits_{V}d\boldsymbol{r}'\frac{e^{-\tau(\boldsymbol{r},\boldsymbol{r}',E)}}{4\pi|\boldsymbol{r}-\boldsymbol{r}'|^2}\left[\int\limits_{0}^{\infty}dE'\Sigma(\boldsymbol{r}',E'\rightarrow E)\phi(\boldsymbol{r}',E')+Q(\boldsymbol{r}',E)\right]\end{aligned} \tag{7a}$$

with:

$$\Sigma(\boldsymbol{r},E'\rightarrow E)\equiv\Sigma(\boldsymbol{r},E')f_s(E'\rightarrow E)+\nu(E')\Sigma_f(\boldsymbol{r},E')\chi(E)$$

and:

$$Q(\boldsymbol{r},E)=\int\limits_{4\pi}d\Omega Q(\boldsymbol{r},\Omega,E)$$

Equation (1b) then gives the angular flux for the collision source:

$$q(\boldsymbol{r},\Omega,E)=\frac{1}{4\pi}\left\{\int\limits_{0}^{\infty}dE'\Sigma(\boldsymbol{r}',E'\rightarrow E)\phi(\boldsymbol{r},E')+Q(\boldsymbol{r},E)\right\} \tag{7b}$$

If there is no flux passing through the boundary from the vacuum into the medium, $\phi(\boldsymbol{r}_s,\Omega,E) \equiv 0$, for $\hat{\boldsymbol{n}}_s \bullet \boldsymbol{\Omega} < 0$ and if the nuclear properties are uniform, Eq. (7a) further simplifies to:

$$\phi(\boldsymbol{r},E) = \int_V d\boldsymbol{r}' \frac{e^{-\Sigma(E)|\boldsymbol{r}-\boldsymbol{r}'|}}{4\pi|\boldsymbol{r}-\boldsymbol{r}'|^2}\left[\int_0^\infty dE'\Sigma(E' \to E)\phi(\boldsymbol{r}',E') + Q(\boldsymbol{r}',E)\right] \tag{III}$$

This equation represents the fundamental neutron transport equation for a 3-D medium with energy dependence and is especially appealing in the multiple collision approximation when absorption dominates. One can also numerically solve Eq. (III) through collision probability methods to find fluxes for cross section homogenization. However, there seems to be a more basic formulation, which we now investigate.

1.2.2 The pseudo equation

Here, we derive the relatively uncommon pseudo flux equation, which is limited to the determination of the scalar flux for the case of isotropic scattering and spatially uniform cross sections only. Of course, knowledge of the scalar flux then gives the angular flux from Eqs. (3) and (7b).

Through the identity:

$$\frac{e^{-\Sigma(E)|\boldsymbol{r}-\boldsymbol{r}'|}}{4\pi|\boldsymbol{r}-\boldsymbol{r}'|^2} = \int_0^{1/\Sigma(E)} d\nu \frac{e^{-|\boldsymbol{r}-\boldsymbol{r}'|/\nu}}{4\pi|\boldsymbol{r}-\boldsymbol{r}'|\nu^2} = \int_0^{1/\Sigma(E)} \frac{d\nu}{\nu^2} K_\nu\left(|\boldsymbol{r}-\boldsymbol{r}'|\right)$$

where:

$$K_\nu(r) \equiv \frac{e^{-r/\nu}}{4\pi r}$$

Eq. (III) becomes:

$$\phi(\boldsymbol{r},E) = \int_0^{1/\Sigma(E)} \frac{d\nu}{\nu^2} \int_V d\boldsymbol{r}' K_\nu\left(|\boldsymbol{r}-\boldsymbol{r}'|\right) q(\boldsymbol{r}',E) \tag{8}$$

with:

$$q(\boldsymbol{r},E) \equiv \int_0^\infty dE'\Sigma(E' \to E)\phi(\boldsymbol{r},E') + Q(\boldsymbol{r},E)$$

If one defines the pseudo flux $\phi(\boldsymbol{r},\nu,E)$ as part of the integrand of the outer integral in Eq. (8):

$$\phi(\boldsymbol{r},\nu,E) = \int_V d\boldsymbol{r}' K_\nu\left(|\boldsymbol{r}-\boldsymbol{r}'|\right) q(\boldsymbol{r}',E) \tag{9a}$$

then the scalar flux is:

$$\phi(\boldsymbol{r},E) = \int_0^{1/\Sigma(E)} \frac{d\nu}{\nu^2} \phi(\boldsymbol{r},\nu,E) \tag{9b}$$

By operating on $\phi(\boldsymbol{r},\nu,E)$ with ∇^2, we therefore have:

$$\nabla^2\phi(\boldsymbol{r},\nu,E)=\int_V d\boldsymbol{r}'\nabla^2 K_\nu\left(|\boldsymbol{r}-\boldsymbol{r}'|\right)q(\boldsymbol{r}',E) \tag{10}$$

However, we know that [3]:

$$\left[\nabla^2-\frac{1}{\nu^2}\right]K_\nu\left(|\boldsymbol{r}|\right)=-\delta(\boldsymbol{r}) \tag{11}$$

and substitution of:

$$\nabla^2 K_\nu\left(|\boldsymbol{r}-\boldsymbol{r}'|\right)=\frac{1}{\nu^2}K_\nu\left(|\boldsymbol{r}-\boldsymbol{r}'|\right)-\delta(\boldsymbol{r}-\boldsymbol{r}')$$

into Eq. (10) gives the second order form of the transport equation for the pseudo flux:

$$\begin{gathered}\left[\nabla^2-\frac{1}{\nu^2}\right]\phi(\boldsymbol{r},\nu,E)=\\ -\int_0^\infty dE'\Sigma(E'\to E)\int_0^{1/\Sigma(E')}\frac{d\nu'}{\nu'^2}\phi(\boldsymbol{r},\nu',E')-Q(\boldsymbol{r},E)\end{gathered} \tag{IV}$$

Note that the pseudo flux resembles an angular flux but in general is not. Only in plane geometry will this be true. Also note that two boundary conditions are now required. Once we find the pseudo flux, Eq. (9b) gives the scalar flux, which is our primary objective.

Equation (IV) has the potential to generate benchmarks in any geometry that admits separable solutions to the Helmholtz equation [4]. Thus, this formulation presents several possibilities for new analytical solutions, which, unfortunately, we cannot pursue here.

1.2.3 The Green's function form

The solution of the neutron Boltzmann in terms of the Green's function is a particularly elegant representation. The solution within a volume V of area A, based on Plazcek's lemma [5], mathematically forces the solution outside the medium to zero by constructing consistent, though unknown, boundary fluxes. We know the incoming boundary flux but not the outgoing flux. From the Green's function of the integro-differential transport equation given by Eq. (II) with:

$$Q(\boldsymbol{r},\Omega,E)=\delta(\boldsymbol{r}-\boldsymbol{r}')\delta(\Omega-\Omega')\delta(E-E')$$

or explicitly:

$$\begin{aligned}&\left[\Omega\bullet\nabla+\Sigma(\boldsymbol{r},E)\right]G(\boldsymbol{r},\Omega,E;\boldsymbol{r}',\Omega',E')=\\&=\int_0^\infty dE''\int_{4\pi}d\Omega''\Sigma_s(\boldsymbol{r},\Omega''\bullet\Omega,E''\to E)G(\boldsymbol{r},\Omega'',E'';\boldsymbol{r}',\Omega',E')+\\&+\frac{\chi(E)}{4\pi}\int_0^\infty dE''\int_{4\pi}d\Omega''\nu(E'')\Sigma_f(\boldsymbol{r},E'')G(\boldsymbol{r},\Omega'',E'';\boldsymbol{r}',\Omega',E')+\\&\qquad\qquad+\delta(\boldsymbol{r}-\boldsymbol{r}')\delta(\Omega-\Omega')\delta(E-E')\end{aligned}\tag{V.1}$$

we obtain the solution in the form of an integral equation over the boundary fluxes. The unknown boundary flux comes from the solution to a Fredholm integral equation as will be shown.

Let the characteristic function of the volume V be:

$$\Theta_s(\boldsymbol{r})\equiv\begin{cases}1, & \boldsymbol{r}\in V\\0, & \boldsymbol{r}\notin V\end{cases}\tag{12}$$

Then, if we require the flux inside V to remain unchanged, but the flux outside the medium to be zero (since it is not of interest) the extended angular flux is:

$$\psi(\boldsymbol{r},\Omega,E)\equiv\phi(\boldsymbol{r},\Omega,E)\Theta_s(\boldsymbol{r})\tag{13}$$

The streaming (or gradient) term now becomes:

$$\begin{aligned}&\Omega\bullet\nabla\psi(\boldsymbol{r},\Omega,E)=\\&\quad=\left[\Omega\bullet\nabla\phi(\boldsymbol{r},\Omega,E)\right]\Theta_s(\boldsymbol{r})+\phi(\boldsymbol{r},\Omega,E)\Omega\bullet\nabla\Theta_s(\boldsymbol{r})\end{aligned}\tag{14}$$

By solving for $\Omega\bullet\nabla\phi(\boldsymbol{r},\Omega,E)$ from Eq. (II) and substituting the result into Eq. (14), we find:

$$\begin{aligned}&\Omega\bullet\nabla\psi(\boldsymbol{r},\Omega,E)=\\&=\begin{bmatrix}-\Sigma(\boldsymbol{r},E)\phi(\boldsymbol{r},\Omega,E)+\\+\int_0^\infty dE'\int_{4\pi}d\Omega'\Sigma_s(\boldsymbol{r},\Omega'\bullet\Omega,E'\to E)\phi(\boldsymbol{r},\Omega',E')+\\+\frac{\chi(E)}{4\pi}\int_0^\infty dE'\int_{4\pi}d\Omega'\nu(E')\Sigma_f(\boldsymbol{r},E')\phi(\boldsymbol{r},\Omega',E')+\\+Q(\boldsymbol{r},\Omega,E)\end{bmatrix}\Theta_s(\boldsymbol{r})+\\&\qquad\qquad+\phi(\boldsymbol{r},\Omega,E)\Omega\bullet\nabla\Theta_s(\boldsymbol{r})\end{aligned}\tag{15}$$

This equation therefore is the following transport equation for the extended solution $\psi(\boldsymbol{r},\Omega,E)$:

$$\begin{aligned}&\left[\Omega\bullet\nabla+\Sigma(\boldsymbol{r},E)\right]\psi(\boldsymbol{r},\Omega,E)=\\&=\int_0^\infty dE'\int_{4\pi}d\Omega'\Sigma_s(\boldsymbol{r},\Omega'\bullet\Omega,E'\to E)\psi(\boldsymbol{r},\Omega',E')+\\&+\frac{\chi(E)}{4\pi}\int_0^\infty dE'\int_{4\pi}d\Omega'\nu(E')\Sigma_f(\boldsymbol{r},E')\psi(\boldsymbol{r},\Omega',E')+S(\boldsymbol{r},\Omega,E)\end{aligned}\tag{16a}$$

where:

$$S\left(\boldsymbol{r},\Omega,E\right)\equiv Q\left(\boldsymbol{r},\Omega,E\right)\Theta_{s}\left(\boldsymbol{r}\right)+\phi\left(\boldsymbol{r},\Omega,E\right)\Omega\bullet\nabla\Theta_{s}\left(\boldsymbol{r}\right) \tag{16b}$$

Note that the source is composed of the original volume source and an additional artificial flux component multiplied by the gradient of the characteristic function. We momentarily leave $\nabla\Theta_s(\boldsymbol{r})$ as is rather than attempting to find a formal interpretation as it is a discontinuous function at the volume surface and would lead to technical difficulties.

In terms of the Green's function, the extended solution representation is therefore:

$$\psi\left(\boldsymbol{r},\Omega,E\right)=\int_{V_\infty}d\boldsymbol{r}'\int_{0}^{\infty}dE'\int_{4\pi}d\Omega' S\left(\boldsymbol{r}',\Omega',E'\right)G\left(\boldsymbol{r},\Omega,E;\boldsymbol{r}',\Omega',E'\right) \tag{17}$$

and explicitly introducing the source, we have:

$$\begin{aligned}\psi\left(\boldsymbol{r},\Omega,E\right)=&\int_{V}d\boldsymbol{r}'\int_{0}^{\infty}dE'\int_{4\pi}d\Omega' Q\left(\boldsymbol{r}',\Omega',E'\right)G\left(\boldsymbol{r},\Omega,E;\boldsymbol{r}',\Omega',E'\right)+\\&+\int_{0}^{\infty}dE'\int_{4\pi}d\Omega'\int_{V_\infty}d\boldsymbol{r}' G\left(\boldsymbol{r},\Omega,E;\boldsymbol{r}',\Omega',E'\right)\phi\left(\boldsymbol{r}',\Omega',E'\right)\Omega'\bullet\nabla_{\boldsymbol{r}'}\Theta_{s}\left(\boldsymbol{r}'\right)\end{aligned} \tag{18}$$

To evaluate the spatial integration in the second integral, let:

$$f\left(\boldsymbol{r}'\right)\equiv G\left(\boldsymbol{r},\Omega,E;\boldsymbol{r}',\Omega',E'\right)\phi\left(\boldsymbol{r}',\Omega',E'\right)$$

(retaining only $\boldsymbol{r}'$ dependence). Therefore, from the gradient chain rule:

$$f\left(\boldsymbol{r}'\right)\Omega'\bullet\nabla_{\boldsymbol{r}'}\Theta_{s}\left(\boldsymbol{r}'\right)=\Omega'\bullet\nabla_{\boldsymbol{r}'}\left[f\left(\boldsymbol{r}'\right)\Theta_{s}\left(\boldsymbol{r}'\right)\right]-\Theta_{s}\left(\boldsymbol{r}'\right)\Omega'\bullet\nabla_{\boldsymbol{r}'}f\left(\boldsymbol{r}'\right)$$

and the divergence theorem, the spatial integration (over all space) becomes:

$$\begin{aligned}&\int_{V_\infty}d\boldsymbol{r}' f\left(\boldsymbol{r}'\right)\Omega'\bullet\nabla\Theta_{s}\left(\boldsymbol{r}'\right)=\\&=\int_{A_\infty}dA_{s'}\hat{\boldsymbol{n}}_{s'}\bullet\Omega' f\left(\boldsymbol{r}_{s'}\right)\Theta_{s}\left(\boldsymbol{r}_{s'}\right)-\int_{V}d\boldsymbol{r}'\Omega'\bullet\nabla_{\boldsymbol{r}'}f\left(\boldsymbol{r}'\right)\end{aligned} \tag{19}$$

Since:

$$\lim_{r_{s'}\ on\ A_\infty}\left[\Theta_{s}\left(\boldsymbol{r}_{s'}\right)\right]\equiv 0$$

the first integral vanishes; and again from the divergence theorem, the second integral is:

$$\int_{V}d\boldsymbol{r}'\Omega'\bullet\nabla_{\boldsymbol{r}'}f\left(\boldsymbol{r}'\right)=\int_{A}dA_{s}\hat{\boldsymbol{n}}_{s}\bullet\Omega' f\left(\boldsymbol{r}_{s}\right)$$

The final form of Eq. (18) is therefore:

$$\begin{aligned}\psi(\boldsymbol{r},\Omega,E) &= \int_V d\boldsymbol{r}' \int_0^\infty dE' \int_{4\pi} d\Omega' Q(\boldsymbol{r}',\Omega',E')\, G(\boldsymbol{r},\Omega,E;\boldsymbol{r}',\Omega',E') - \\ &- \int_0^\infty dE' \int_{4\pi} d\Omega' \int_A dA_s \hat{\boldsymbol{n}}_s \bullet \Omega' G(\boldsymbol{r},\Omega,E;\boldsymbol{r}_s,\Omega',E')\,\phi(\boldsymbol{r}_s,\Omega',E')\end{aligned} \tag{V.2}$$

where $\phi(\boldsymbol{r}_s,\Omega,E)$, for $\hat{\boldsymbol{n}}_s \bullet \Omega < 0$, is assumed known. To find the unknown outgoing flux required in Eq. (V.2), $\boldsymbol{r}$ is set to $\boldsymbol{r}_s^+$ just inside the medium boundary to give:

$$\begin{aligned}\phi(\boldsymbol{r}_s^+,\Omega,E) &= \int_V d\boldsymbol{r}' \int_0^\infty dE' \int_{4\pi} d\Omega' Q(\boldsymbol{r}',\Omega',E')\, G(\boldsymbol{r}_s^+,\Omega,E;\boldsymbol{r}',\Omega',E') - \\ &- \int_0^\infty dE' \int_{4\pi} d\Omega' \int_A dA_s \hat{\boldsymbol{n}}_s \bullet \Omega' G(\boldsymbol{r}_s^+,\Omega,E;\boldsymbol{r}_s,\Omega',E')\,\phi(\boldsymbol{r}_s,\Omega',E')\end{aligned}$$

and considering only outgoing directions $\hat{\boldsymbol{n}}_s \bullet \Omega \geq \boldsymbol{0}$, we have:

$$\begin{aligned}\phi(\boldsymbol{r}_s^+,\Omega,E) &= \int_V d\boldsymbol{r}' \int_0^\infty dE' \int_{4\pi} d\Omega' Q(\boldsymbol{r}',\Omega',E')\, G(\boldsymbol{r}_s^+,\Omega,E;\boldsymbol{r}',\Omega',E') - \\ &- \int_0^\infty dE' \int_{\hat{\boldsymbol{n}}_s \bullet \boldsymbol{\Omega}' \geq 0} d\Omega' \int_A dA_s \hat{\boldsymbol{n}}_s \bullet \Omega' G(\boldsymbol{r}_s^+,\Omega,E;\boldsymbol{r}_s,\Omega',E')\,\phi(\boldsymbol{r}_s^+,\Omega',E') + \\ &+ \int_0^\infty dE' \int_{\hat{\boldsymbol{n}}_s \bullet \boldsymbol{\Omega}' < 0} d\Omega' \int_A dA_s \left|\hat{\boldsymbol{n}}_s \bullet \Omega'\right| G(\boldsymbol{r}_s^+,\Omega,E;\boldsymbol{r}_s,\Omega',E')\,\phi(\boldsymbol{r}_s,\Omega',E')\end{aligned} \tag{V.3}$$

Equation (V.3) is a Fredholm integral equation for the outgoing boundary flux, $\phi(\boldsymbol{r}_s^+,\Omega,E)$, which along with Eqs. (V.2) and Eq. (V.1) for the (infinite domain) Green's function constitute the Green's function form of the transport equation.

This form of the transport equation is especially convenient in that the spatial variable is just a parameter. In addition, Eq. (V.3) is independent of the scattering anisotropy since the Green's function contains this information.

1.3 Derivative forms of the neutron transport equation

Mathematical tractability is the key to generating analytical benchmarks. In its six-dimensional space, the steady state transport equation is anything but mathematically tractable. To make it so, we must reduce the number of independent variables leading to the two approximations in the energy variable to follow. The monoenergetic, or one-group, approximation is a special case of the multigroup approximation but is so ubiquitous in the literature and particularly physically instructive, we consider it separately.

1.3.1 Monoenergetic approximation

Because of its simplicity, the monoenergetic approximation, also called one-group approximation, is the most widely considered neutron transport model both analytically and numerically. The model serves as a relatively simple test case to observe the efficiency of new mathematical and numerical methods. The one-group approximation retains the fundamental features of the neutron transport process yet lends itself to theoretical consideration.

As with all approximations, we begin with Eq. (II) rewritten here:

$$\begin{aligned}&\left[\Omega\bullet\nabla+\Sigma(\boldsymbol{r},E)\right]\phi(\boldsymbol{r},\Omega,E)=\\&=\int_0^\infty dE'\int_{4\pi}d\Omega'\Sigma_s(\boldsymbol{r},\Omega'\bullet\Omega,E'\to E)\phi(\boldsymbol{r},\Omega',E')+\\&+\frac{\chi(E)}{4\pi}\int_0^\infty dE'\int_{4\pi}d\Omega'\nu(E')\Sigma_f(\boldsymbol{r},E')\phi(\boldsymbol{r},\Omega',E')+Q(\boldsymbol{r},\Omega,E)\end{aligned}\tag{II}$$

A physically based derivation gives the one-group form directly, while the multigroup form of the next section straightforwardly produces the same result as a degenerate multigroup approximation.

To obtain the one-group form, we assume neutrons scatter elastically from a nucleus of infinite mass, and therefore do not lose energy. The details of elastic scattering are found in nearly every reactor physics text; however, the derivation provided here [6] is more mathematically and physically intuitive than most.

An elastic collision between a neutron and nucleus of masses m and M respectively is one that leaves the internal (binding) energy of the nucleus unchanged. The collision occurs instantaneously between two mathematical point particles as shown in Figure 1.7(a) in the physical laboratory (**L**) reference frame. In what follows, a primed quantity refers to before collision and unprimed after collision. The vectors $\boldsymbol{r}'(t)$ and $\boldsymbol{R}'(t)$ define the neutron and nucleus positions at time t and the vector $\boldsymbol{R}_{cm}(t)$:

$$\boldsymbol{R}_{cm}(t)\equiv\frac{1}{m+M}\left[m\boldsymbol{r}'(t)+M\boldsymbol{R}'(t)\right]=\frac{1}{1+A}\left[\boldsymbol{r}'(t)+A\boldsymbol{R}'(t)\right]\tag{20}$$

defines the position of the center of mass in **L** where A is the mass ratio M/m. To the colliding particles of constant velocity, the center of mass remains stationary before and after collision. For a nucleus initially at rest ($\mathbf{V}'\equiv\mathbf{0}$) and a neutron moving with velocity $\mathbf{v}'$ toward the nucleus, the velocity of the center of mass in the laboratory reference frame is the time derivative of $\boldsymbol{R}_{cm}(t)$:

$$\boldsymbol{V}_{cm}=\frac{1}{1+A}\boldsymbol{v}'\tag{21}$$

The most convenient view of elastic scattering is from the center of mass reference frame (**C**) created by imposing a velocity of $-\mathbf{V}_{cm}$ on the laboratory reference frame shown in Figure 1.7(b). The particle velocities in **C** before collision are therefore:

$$\boldsymbol{v}_c'=\boldsymbol{v}'-\boldsymbol{V}_{cm}=\frac{A}{1+A}\boldsymbol{v}',\ \boldsymbol{V}_c'=-\boldsymbol{V}_{cm}\tag{22}$$

respectively, and the total linear momentum in **C** is zero, since:

$$\boldsymbol{M}_c'=\boldsymbol{v}'-\boldsymbol{V}_{cm}-A\boldsymbol{V}_{cm}=\mathbf{0}$$

Figure 1.7(c) shows the particle velocity vectors **v**, and **V** in **L** after collision. Again, if we impose $-\mathbf{V}_{cm}$, also shown, the corresponding velocities in **C** after collision result. Since the total momentum after collision in **C** is also zero from conservation:

$$\mathbf{M}_c = \mathbf{v}_c + A\mathbf{V}_c = \mathbf{0}$$

the velocity of the nucleus in **C** after collision therefore is:

$$\mathbf{V}_c = -\frac{1}{A}\mathbf{v}_c \tag{23}$$

which is in the exact opposite direction of the neutron. Conservation of kinetic energy in **C** requires:

$$\frac{1}{2}v_c'^2 + \frac{A}{2}V_c'^2 = \frac{1}{2}v_c^2 + \frac{A}{2}V_c^2$$

and since $\mathbf{M}'_c = \mathbf{v}'_c + A\mathbf{V}'_c = 0$, implies $\mathbf{V}'_c = -\mathbf{v}'_c / A$, we have:

$$v_c = v'_c,\ V_c = V'_c \tag{24}$$

Thus, the particles' speed before and after collision remain unchanged in **C**.

The scattering angles made by the velocity vectors with respect to the incident neutron direction in **L** and **C**, θ_0 and θ_c, and their corresponding cosines, μ_0, μ_c are also shown in Figure 1.7(c). For future reference, in terms of the neutron direction before $\mathbf{\Omega}'$ and after collision $\mathbf{\Omega}$, we define:

$$\mu_0 \equiv \mathbf{\Omega}' \bullet \mathbf{\Omega} \tag{25}$$

Because of the rotational invariance experienced by scattering of perfectly spherical point particles, the collision dynamics will depend only on μ_0.

To obtain a fundamental relationship between the energy before and after collision and the scattering angle in **C**, we form the following expression:

$$v^2 \equiv \mathbf{v} \bullet \mathbf{v} = \left(\mathbf{v}_c + \mathbf{V}_{cm}\right) \bullet \left(\mathbf{v}_c + \mathbf{V}_{cm}\right) = v_c^2 + 2V_{cm}v_c\mu_c + V_{cm}^2$$

to give using Eq. (21):

$$E = \frac{1}{2}\left[\left(1+\alpha\right) + \left(1-\alpha\right)\mu_c\right]E' \tag{26a}$$

where the collision parameter α is:

$$\alpha \equiv \left[\frac{A-1}{A+1}\right]^2 \tag{26b}$$

Since from Figure 1.7(c), we deduce that:

$$V_{cm} = -v_c\mu_c + v\mu_0$$

and using Eqs. (21) and (24), we can relate the scattering angle in the laboratory and center of mass frames:

$$\mu_0 = \frac{A\mu_c + 1}{\left(A^2 + 2A\mu_c + 1\right)^{1/2}} \tag{27a}$$

or rearranging:

$$\mu_c\left(\mu_0\right) = \frac{1}{A}\left[\sqrt{\left(A^2+1\right)\mu_0^2 + \left(1-\mu_0^2\right)^2 - 1} - \left(1-\mu_0^2\right)\right] \tag{27b}$$

Now recall the differential scattering kernel [defined just prior to Eq. (I)]:

$$\Sigma_s\left(\boldsymbol{r}, \Omega' \bullet \Omega, E' \to E\right) = \Sigma_s\left(\boldsymbol{r}, E'\right) f_s\left(\Omega' \bullet \Omega, E' \to E\right) \tag{28a}$$

with normalization:

$$\int_0^\infty dE \int_{4\pi} d\Omega f_s\left(\Omega' \bullet \Omega, E' \to E\right) \equiv 1 \tag{28b}$$

Based on energy and momentum conservation, we express the law for scattering through an angle θ_0 in the laboratory frame, and correspondingly through angle θ_c in the center of mass frame as:

$$f_s\left(\Omega' \bullet \Omega, E' \to E\right) \equiv p_s\left(\mu_0, E'\right) \delta\left(E - \frac{1}{2}\left[\left(1+\alpha\right) + \left(1-\alpha\right)\mu_c\right]E'\right) \tag{29a}$$

where the delta function enforces the correct kinematics for a given scattering angle. The first factor maintains the normalization with:

$$\int_{4\pi} d\Omega p_s\left(\mu_0, E'\right) \equiv 1 \tag{29b}$$

From conservation of probability between the two reference frames:

$$p_s\left(\mu_0, E'\right) = p_s^c\left(\mu_c, E'\right)\left|\frac{d\mu_c}{d\mu_0}\right| \tag{30}$$

the scattering kernel then becomes:

$$\begin{aligned} &\Sigma_s\left(\boldsymbol{r}, \Omega' \bullet \Omega, E' \to E\right) = \\ &= \Sigma_s\left(\boldsymbol{r}, E'\right) p_s^c\left(\mu_c, E'\right)\left|\frac{d\mu_c}{d\mu_0}\right| \delta\left(E - \frac{1}{2}\left[\left(1+\alpha\right) + \left(1-\alpha\right)\mu_c\right]E'\right); \end{aligned} \tag{31}$$

where, from Eq. (27b):

$$\frac{d\mu_c}{d\mu_0} = \frac{\mu_0}{A}\left[\frac{A^2+1-2\left(1-\mu_0^2\right)}{\sqrt{\left(A^2+1\right)\mu_0^2+\left(1-\mu_0^2\right)^2-1}}+2\right]$$

Note that we introduce angular dependence in the laboratory representation through the transformation between **C** and **L** coordinates.

Finally, when $A \to \infty$, $\alpha \to 1$, Eq. (31) gives:

$$\Sigma_s\left(\boldsymbol{r},\Omega'\bullet\Omega,E'\to E\right)\to\Sigma_s\left(\boldsymbol{r},\Omega'\bullet\Omega,E\right)\delta\left(E-E'\right) \tag{32a}$$

with:

$$\Sigma_s\left(\boldsymbol{r},\Omega'\bullet\Omega,E\right)\equiv\Sigma_s\left(\boldsymbol{r},E\right)p_s^c\left(\mu_c\left(\mu_0\right),E\right) \tag{32b}$$

Equation (32a) confirms the intuitive notion that a neutron scatters elastically without energy loss on collision with an infinite mass.

If, in addition, neutrons from fission and the external source appear only at energy E_0, then:

$$\begin{aligned} &Q\left(\boldsymbol{r},\Omega,E\right)\equiv Q\left(\boldsymbol{r},\Omega\right)\delta\left(E-E_0\right) \\ &\chi\left(E\right)\equiv\delta\left(E-E_0\right) \end{aligned} \tag{33}$$

When we introduce Eqs. (32a) and (33) into Eq. (II) after integrating over the delta function in the collision term, there results:

$$\begin{aligned} &\left[\Omega\bullet\nabla+\Sigma\left(\boldsymbol{r},E\right)\right]\phi\left(\boldsymbol{r},\Omega,E\right)= \\ &=\int_{4\pi} d\Omega'\Sigma_s\left(\boldsymbol{r},\Omega'\bullet\Omega,E'\right)\phi\left(\boldsymbol{r},\Omega',E\right)+ \\ &+\left[\frac{1}{4\pi}\int_0^\infty dE'\int_{4\pi} d\Omega'\nu\left(E'\right)\Sigma_f\left(\boldsymbol{r},E'\right)\phi\left(\boldsymbol{r},\Omega',E'\right)+Q\left(\boldsymbol{r},\Omega\right)\right]\delta\left(E-E_0\right) \end{aligned} \tag{34}$$

Since all scattered and fission source neutrons appear at a single energy E_0, physical consistency requires neutrons to be at that energy or expressed formally:

$$\phi\left(\boldsymbol{r},\Omega,E\right)=\phi\left(\boldsymbol{r},\Omega\right)\delta\left(E-E_0\right) \tag{35}$$

where mathematical consistency requires:

$$\phi\left(\boldsymbol{r},\Omega\right)\equiv\int_0^\infty dE\phi\left(\boldsymbol{r},\Omega,E\right)$$

When we introduced Eq. (35) into Eq. (34), the one-group approximation emerges:

$$\begin{aligned}&\left[\Omega\bullet\nabla+\Sigma(\boldsymbol{r},E_0)\right]\phi(\boldsymbol{r},\Omega)= \\ &=\int_{4\pi}d\Omega'\Sigma_s(\boldsymbol{r},\Omega'\bullet\Omega,E_0)\phi(\boldsymbol{r},\Omega')+ \\ &+\frac{1}{4\pi}\nu(E_0)\Sigma_f(\boldsymbol{r},E_0)\int_{4\pi}d\Omega'\phi(\boldsymbol{r},\Omega')+Q(\boldsymbol{r},\Omega)\end{aligned}\tag{VI}$$

Energy is now just a passive parameter, which we can ignore.

In three dimensions, Eq. (VI) is still mathematically intractable so we need to make additional simplifications to realize analytical solutions. An additional simplification, reduction to 1-D plane geometry, is considered in §1.3.3.

1.3.2 The multigroup approximation

We initiate the multigroup approximation to Eq. (II) by partitioning the total energy interval of interest into G energy groups:

$$\Delta E_g=\left[E_g,E_{g-1}\right],\ \ g=1,2,...,G$$

where g = 1 is the highest group. By expressing the energy integrals of the scattering and fission sources as sums over all groups, without loss of generality, the integrals in Eq. (II) become:

$$\begin{aligned}&\int_0^\infty dE'\int_{4\pi}d\Omega'\Sigma_s(\boldsymbol{r},\Omega'\bullet\Omega,E'\to E)\phi(\boldsymbol{r},\Omega',E')= \\ &=\sum_{g'=1}^{G}\int_{\Delta E_{g'}}dE'\int_{4\pi}d\Omega'\Sigma_s(\boldsymbol{r},E')\,f_s(\Omega'\bullet\Omega,E'\to E)\phi(\boldsymbol{r},\Omega',E')\end{aligned}$$

and:

$$\int_0^\infty dE'\nu(E')\Sigma_f(\boldsymbol{r},E')\phi(\boldsymbol{r},E')=\sum_{g'=1}^{G}\int_{\Delta E_{g'}}dE'\nu(E')\Sigma_f(\boldsymbol{r},E')\phi(\boldsymbol{r},E')$$

By integrating Eq. (II) over ΔE_g, we therefore have:

$$\begin{aligned}&\left[\Omega\bullet\nabla\int_{\Delta E_g}dE\phi(\boldsymbol{r},\Omega,E)+\int_{\Delta E_g}dE\Sigma(\boldsymbol{r},E)\phi(\boldsymbol{r},\Omega,E)\right]= \\ &=\sum_{g'=1}^{G}\int_{\Delta E_g}dE\int_{\Delta E_{g'}}dE'\int_{4\pi}d\Omega'\Sigma_s(\boldsymbol{r},\Omega'\bullet\Omega,E'\to E)\phi(\boldsymbol{r},\Omega',E')+ \\ &+\frac{1}{4\pi}\int_{\Delta E_g}dE\chi(E)\sum_{g'=1}^{G}\int_{\Delta E_{g'}}dE'\nu(E')\Sigma_f(\boldsymbol{r},E')\phi(\boldsymbol{r},E')+\int_{\Delta E_g}dEQ(\boldsymbol{r},\Omega,E)\end{aligned}\tag{36}$$

At this point, we introduce the multigroup approximation:

$$\begin{aligned}\phi(\boldsymbol{r},\Omega,E) &= f(E)\phi_g(\boldsymbol{r},\Omega)\\ Q(\boldsymbol{r},\Omega,E) &= g(E)Q_g(\boldsymbol{r},\Omega)\end{aligned}\tag{37a}$$

stating the flux and source within each group, $E \in \Delta E_g$ are separable functions of energy and $\boldsymbol{r}$,$\boldsymbol{\Omega}$. The following normalizations:

$$\int\limits_{\Delta E_g} dEf(E) \equiv 1, \quad \int\limits_{\Delta E_g} dEg(E) \equiv 1\tag{37b}$$

are also required with *f*(*E*) and *g*(*E*) assumed to be piecewise smooth functions of *E*. Then, with the multigroup approximation, Eq. (36) becomes:

$$\begin{aligned}&\left[\Omega \bullet \nabla\phi_g(\boldsymbol{r},\Omega) + \Sigma_g(\boldsymbol{r})\phi_g(\boldsymbol{r},\Omega)\right] =\\ &= \sum_{g'=1}^{G} \int\limits_{4\pi} d\Omega' \Sigma_{sgg'}(\boldsymbol{r},\Omega' \bullet \Omega)\phi_{g'}(\boldsymbol{r},\Omega') +\\ &\quad + \frac{1}{4\pi}\chi_g \sum_{g'=1}^{G} \nu_{g'}\Sigma_{fg'}(\boldsymbol{r})\phi_{g'}(\boldsymbol{r}) + Q_g(\boldsymbol{r},\Omega)\end{aligned}\tag{VII.1}$$

with the following definitions of the group parameters:

$$\begin{aligned}\Sigma_g(\boldsymbol{r}) &\equiv \int\limits_{\Delta E_g} dE\, f(E)\Sigma(\boldsymbol{r},E)\\ \Sigma_{sgg'}(\boldsymbol{r},\Omega' \bullet \Omega) &\equiv \int\limits_{\Delta E_g} dE \int\limits_{\Delta E_{g'}} dE' \Sigma_s(\boldsymbol{r},\Omega' \bullet \Omega, E' \to E)\, f(E')\\ \nu_g\Sigma_{fg}(\boldsymbol{r}) &\equiv \int\limits_{\Delta E_g} dEf(E)\nu(E)\Sigma_f(\boldsymbol{r},E)\\ \chi_g &\equiv \int\limits_{\Delta E_g} dE\chi(E)\end{aligned}\tag{VII.2}$$

In more convenient vector notation, Eq. (VII.1) is:

$$\begin{aligned}&\left[\Omega \bullet \nabla + \Sigma(\boldsymbol{r})\right]\boldsymbol{\phi}(\boldsymbol{r},\Omega) =\\ &= \int\limits_{4\pi} d\Omega' \Sigma_s(\boldsymbol{r},\Omega' \bullet \Omega)\boldsymbol{\phi}(\boldsymbol{r},\Omega') +\\ &\quad + \frac{1}{4\pi}\chi\left[\nu\Sigma_f(\boldsymbol{r})\right]^{\mathrm{T}}\boldsymbol{\phi}(\boldsymbol{r}) + \boldsymbol{Q}(\boldsymbol{r},\Omega)\end{aligned}\tag{VII.3}$$

with the group flux and source vectors:

$$\begin{aligned}\boldsymbol{\phi}(\boldsymbol{r},\Omega) &= \left\{\phi_g(\boldsymbol{r},\Omega),\ g = 1,\ldots,G\right\}\\ \boldsymbol{Q}(\boldsymbol{r},\Omega) &= \left\{Q_g(\boldsymbol{r},\Omega),\ g = 1,\ldots,G\right\}\end{aligned}$$

and the group "constants":

$$\begin{aligned}
&\Sigma(\boldsymbol{r}) \equiv diag\left\{\Sigma_g(\boldsymbol{r}),\ g=1,\ldots,G\right\} \\
&\nu\Sigma_f(\boldsymbol{r}) \equiv \left\{\nu_g\Sigma_{fg}(\boldsymbol{r}),\ g=1,\ldots,G\right\} \\
&\Sigma_s(\boldsymbol{r},\Omega'\bullet\Omega) \equiv \left\{\Sigma_{sgg'}(\boldsymbol{r},\Omega'\bullet\Omega),\ g,g'=1,\ldots,G\right\} \\
&\chi \equiv \left\{\chi_g,\ g=1,\ldots,G\right\}
\end{aligned} \tag{VII.4}$$

The multigroup approximation is the basis of nearly all reactor physics codes, making it one of most widely used approximations of neutron transport and diffusion theory. For inner/outer iterative numerical algorithms, one can reformulate the multigroup approximation as a series of one-group equations [7]. Thus, the one-group representation of §1.3.1 takes on added importance.

1.3.3 One-dimensional plane symmetry

We obtain the 1-D transport equation for plane symmetry when the medium is transversely infinite (in the *yz* plane) with cross section and source variation only in the *x* direction. For this case, Eq. (II) becomes:

$$\begin{aligned}
&\left[\Omega\bullet\nabla+\Sigma(x,E)\right]\phi(\boldsymbol{r},\Omega,E)= \\
&=\int_0^\infty dE'\int_{4\pi} d\Omega'\Sigma_s(x,\Omega'\bullet\Omega,E'\to E)\phi(\boldsymbol{r},\Omega',E')+ \\
&+\frac{\chi(E)}{4\pi}\int_0^\infty dE'\nu(E')\Sigma_f(x,E')\phi(\boldsymbol{r},E')+Q(x,\Omega,E)
\end{aligned} \tag{38}$$

When we integrate Eq. (38) over the transverse *yz* plane, there results:

$$\begin{aligned}
&\left[\mu\frac{\partial}{\partial x}+\Sigma(x,E)\right]\phi(x,\Omega,E)= \\
&=\int_0^\infty dE'\int_{4\pi} d\Omega'\Sigma_s(x,\Omega'\bullet\Omega,E'\to E)\phi(x,\Omega',E')+ \\
&\quad+\frac{\chi(E)}{4\pi}\int_0^\infty dE'\nu(E')\Sigma_f(x,E')\phi(x,E')+Q(x,\Omega,E)
\end{aligned} \tag{39}$$

Now:

$$\begin{aligned}
\phi(x,\Omega,E) &\equiv \int_{-\infty}^{\infty} dz\int_{-\infty}^{\infty} dy\phi(x,y,z,\Omega,E) \\
Q(x,\Omega,E) &\equiv \int_{-\infty}^{\infty} dz\int_{-\infty}^{\infty} dyQ(x,y,z,\Omega,E)
\end{aligned}$$

and the *x*-direction (cosine) μ is:

$$\mu \equiv \Omega\bullet\hat{\boldsymbol{x}}$$

Since the differential scattering cross section is rotationally invariant with respect to the angle of scattering:

$$\Sigma_s\left(x,\mathbf{\Omega}'(\mu',\vartheta')\bullet\mathbf{\Omega}(\mu,\vartheta),E'\to E\right)=\Sigma_s\left(x,\mu',\mu,\vartheta-\vartheta',E'\to E\right) \tag{40a}$$

where we explicitly show the dependence on the polar and azimuthal angles of the particle directions (see Figure 1.1). Upon integration over the azimuth ϑ of the scattered direction:

$$\Sigma_s\left(x,\mu',\mu,E'\to E\right)\equiv\int_0^{2\pi}d\vartheta\Sigma_s\left(x,\mathbf{\Omega}'\bullet\mathbf{\Omega},E'\to E\right) \tag{40b}$$

Eq. (39) becomes:

$$\begin{aligned}&\left[\mu\frac{\partial}{\partial x}+\Sigma(x,E)\right]\phi(x,\mu,E)=\\&=\int_0^\infty dE'\int_{-1}^{1}d\mu'\Sigma_s\left(x,\mu',\mu,E'\to E\right)\phi\left(x,\mu',E'\right)+\\&+\frac{1}{2}\chi(E)\int_0^\infty dE'\nu(E')\Sigma_f\left(x,E'\right)\phi\left(x,E'\right)+Q(x,\mu,E)\end{aligned} \tag{41}$$

with:

$$\phi(x,\mu,E)\equiv\frac{1}{2\pi}\int_0^{2\pi}d\vartheta\phi\left(x,\mathbf{\Omega}(\mu,\vartheta),E\right)$$

$$Q(x,\mu,E)\equiv\frac{1}{2\pi}\int_0^{2\pi}d\vartheta Q\left(x,\mathbf{\Omega}(\mu,\vartheta),E\right)$$

Commonly, we express the scattering kernel as in a Legendre expansion representation [7]:

$$\Sigma_s\left(x,\mathbf{\Omega}'\bullet\mathbf{\Omega},E'\to E\right)=\sum_{l=0}^{\infty}\frac{(2l+1)}{4\pi}\Sigma_{sl}\left(x,E'\to E\right)P_l\left(\mathbf{\Omega}'\bullet\mathbf{\Omega}\right) \tag{42a}$$

where the scattering coefficients are (from orthogonality):

$$\Sigma_{sl}\left(x,E'\to E\right)\equiv2\pi\int_{-1}^{1}d\mu_0P_l\left(\mu_0\right)\Sigma_s\left(x,\mu_0,E'\to E\right) \tag{42b}$$

Equation (40b) then becomes:

$$\Sigma_s\left(x,\mu',\mu,E'\to E\right)=\sum_{l=0}^{\infty}\frac{(2l+1)}{2}\Sigma_{sl}\left(x,E'\to E\right)P_l\left(\mu'\right)P_l\left(\mu\right) \tag{43}$$

We have applied the addition theorem for Legendre polynomials [7], in the form:

$$P_l\left(\mu'\right)P_l\left(\mu\right)=\frac{1}{2\pi}\int_0^{2\pi}d\vartheta P_l\left(\mathbf{\Omega}'\bullet\mathbf{\Omega}\right) \tag{44}$$

to obtain Eq. (43). With Eq. (43), Eq. (41) becomes:

$$\begin{aligned}&\left[\mu\frac{\partial}{\partial x}+\Sigma(x,E)\right]\phi(x,\mu,E)=\\&=\frac{1}{2}\sum_{l=0}^{\infty}(2l+1)\int_0^{\infty}dE'\Sigma_{sl}(x,E'\to E)P_l(\mu)\phi_l(x,E')+\\&+\frac{1}{2}\chi(E)\int_0^{\infty}dE'\nu(E')\Sigma_f(x,E')\phi_0(x,E')+Q(x,\mu,E)\end{aligned}\tag{VIII.1}$$

where the l^{th} Legendre moment of the angular flux is:

$$\phi_l(x,E)\equiv\int_{-1}^{1}d\mu P_l(\mu)\phi(x,\mu,E)$$

Similarly, the multigroup approximation [Eq. (VII.1)] for plane geometry is:

$$\begin{aligned}&\left[\mu\frac{\partial}{\partial x}+\Sigma_g(x)\right]\phi_g(x,\mu)=\\&=\frac{1}{2}\sum_{l=0}^{\infty}(2l+1)\sum_{g'=1}^{G}\Sigma_{slgg'}(x)P_l(\mu)\phi_{lg'}(x)+\\&+\frac{1}{2}\chi_g\sum_{g'=1}^{G}\nu_{g'}\Sigma_{fg'}(x)\phi_{0g'}(x)+Q_g(x,\mu)\end{aligned}\tag{VIII.2}$$

with:

$$\phi_{lg}(x)\equiv\int_{-1}^{1}d\mu P_l(\mu)\phi_g(x,\mu)$$

and:

$$\Sigma_{slgg'}(x)\equiv\int_{\Delta E_g}dE\int_{\Delta E_{g'}}dE'\Sigma_{sl}(x,E'\to E)f(E')$$

1.4 Transport equations for analytical benchmarking

Eqs. (II) to (VIII) form the collection of transport equations for the analytical solutions that define the benchmarks we next consider. Each chapter begins with a brief description of the reactor physics associated with the benchmarks of that chapter. The benchmark classification according to Table A and a general physical description follow. The next section contains the derivation of the specific transport equation to be solved beginning with one of Eqs. (II) to (VIII). In the final section, we outline the numerical implementation and provide a demonstration with some discussion. There, we qualify the benchmark by indicating its convergence behavior with desired error.

1.4.1 Summary of the transport equations

For convenience, we list the transport equations considered in the following chapters:

$$\begin{aligned}&\left[\Omega\bullet\nabla+\Sigma(\boldsymbol{r},E)\right]\phi(\boldsymbol{r},\Omega,E)=\\&=\int_0^\infty dE'\int_{4\pi}d\Omega'\Sigma_s(\boldsymbol{r},\Omega'\bullet\Omega,E'\to E)\phi(\boldsymbol{r},\Omega',E')+\\&+\frac{\chi(E)}{4\pi}\int_0^\infty dE'\int_{4\pi}d\Omega'\nu(E')\Sigma_f(\boldsymbol{r},E')\phi(\boldsymbol{r},\Omega',E')+Q(\boldsymbol{r},\Omega,E)\end{aligned}\tag{II}$$

$$\phi(\boldsymbol{r},E)=\int_V d\boldsymbol{r}'\frac{e^{-\Sigma(E)|\boldsymbol{r}-\boldsymbol{r}'|}}{4\pi|\boldsymbol{r}-\boldsymbol{r}'|^2}\left[\int_0^\infty dE'\Sigma(E'\to E)\phi(\boldsymbol{r}',E')+Q(\boldsymbol{r}',E)\right]\tag{III}$$

$$\begin{aligned}&\left[\nabla^2-\frac{1}{\nu^2}\right]\phi(\boldsymbol{r},\nu,E)=\\&-\int_0^\infty dE'\Sigma(E'\to E)\int_0^{1/\Sigma(E')}\frac{d\nu'}{\nu'^2}\phi(\boldsymbol{r},\nu',E')-Q(\boldsymbol{r},E)\end{aligned}\tag{IV}$$

$$\begin{aligned}&\left[\Omega\bullet\nabla+\Sigma(\boldsymbol{r},E)\right]G(\boldsymbol{r},\Omega,E;\boldsymbol{r}',\Omega',E')=\\&=\int_0^\infty dE''\int_{4\pi}d\Omega''\Sigma_s(\boldsymbol{r},\Omega''\bullet\Omega,E''\to E)G(\boldsymbol{r},\Omega'',E'';\boldsymbol{r}',\Omega',E')+\\&+\frac{\chi(E)}{4\pi}\int_0^\infty dE''\int_{4\pi}d\Omega''\nu(E'')\Sigma_f(\boldsymbol{r},E'')G(\boldsymbol{r},\Omega'',E'';\boldsymbol{r}',\Omega',E')+\\&\qquad+\delta(\boldsymbol{r}-\boldsymbol{r}')\delta(\Omega-\Omega')\delta(E-E')\end{aligned}\tag{V.1}$$

$$\begin{aligned}\psi(\boldsymbol{r},\Omega,E)&=\int_V d\boldsymbol{r}'\int_0^\infty dE'\int_{4\pi}d\Omega'Q(\boldsymbol{r}',\Omega',E')G(\boldsymbol{r},\Omega,E;\boldsymbol{r}',\Omega',E')-\\&-\int_0^\infty dE'\int_{4\pi}d\Omega'\int_A dA_s\hat{\boldsymbol{n}}_s\bullet\Omega'G(\boldsymbol{r},\Omega,E;\boldsymbol{r}_s,\Omega',E')\phi(\boldsymbol{r}_s,\Omega',E')\end{aligned}\tag{V.2}$$

$$\begin{aligned}&\phi(\boldsymbol{r}_s^+,\Omega,E)=\int_V d\boldsymbol{r}'\int_0^\infty dE'\int_{4\pi}d\Omega'Q(\boldsymbol{r}',\Omega',E')G(\boldsymbol{r}_s^+,\Omega,E;\boldsymbol{r}',\Omega',E')-\\&-\int_0^\infty dE'\int_{\hat{\boldsymbol{n}}_s\bullet\boldsymbol{\Omega}'\geq 0}d\Omega'\int_A dA_s\hat{\boldsymbol{n}}_s\bullet\Omega'G(\boldsymbol{r}_s^+,\Omega,E;\boldsymbol{r}_s,\Omega',E')\phi(\boldsymbol{r}_s^+,\Omega',E')+\\&+\int_0^\infty dE'\int_{\hat{\boldsymbol{n}}_s\bullet\boldsymbol{\Omega}'<0}d\Omega'\int_A dA_s\left|\hat{\boldsymbol{n}}_s\bullet\Omega'\right|G(\boldsymbol{r}_s^+,\Omega,E;\boldsymbol{r}_s,\Omega',E')\phi(\boldsymbol{r}_s,\Omega',E')\end{aligned}\tag{V.3}$$

$$\begin{aligned}&\left[\boldsymbol{\Omega}\bullet\nabla+\Sigma(\boldsymbol{r})\right]\phi(\boldsymbol{r},\Omega)=\\&=\int_{4\pi}d\Omega'\Sigma_s\left(\boldsymbol{r},\Omega'\bullet\Omega\right)\phi\left(\boldsymbol{r},\Omega'\right)+\\&+\frac{1}{4\pi}\nu\Sigma_f\left(\boldsymbol{r}\right)\int_{4\pi}d\Omega'\phi\left(\boldsymbol{r},\Omega'\right)+Q\left(\boldsymbol{r},\Omega\right)\end{aligned}\tag{VI}$$

$$\begin{aligned}&\left[\boldsymbol{\Omega}\bullet\nabla\phi_g\left(\boldsymbol{r},\Omega\right)+\Sigma_g\left(\boldsymbol{r}\right)\phi_g\left(\boldsymbol{r},\Omega\right)\right]=\\&=\sum_{g'=1}^{G}\int_{4\pi}d\Omega'\Sigma_{sgg'}\left(\boldsymbol{r},\Omega'\bullet\Omega\right)\phi_{g'}\left(\boldsymbol{r},\Omega'\right)+\\&\quad+\frac{1}{4\pi}\chi_g\sum_{g'=1}^{G}\nu_{g'}\Sigma_{fg'}\left(\boldsymbol{r}\right)\phi_{g'}\left(\boldsymbol{r}\right)+Q_g\left(\boldsymbol{r},\Omega\right)\end{aligned}\tag{VII.1}$$

$$\begin{aligned}&\left[\boldsymbol{\Omega}\bullet\nabla+\boldsymbol{\Sigma}(\boldsymbol{r})\right]\boldsymbol{\phi}(\boldsymbol{r},\Omega)=\\&=\int_{4\pi}d\Omega'\boldsymbol{\Sigma}_s\left(\boldsymbol{r},\Omega'\bullet\Omega\right)\boldsymbol{\phi}\left(\boldsymbol{r},\Omega'\right)+\\&\quad+\frac{1}{4\pi}\boldsymbol{\chi}\left[\boldsymbol{\nu\Sigma}_f\left(\boldsymbol{r}\right)\right]^{\mathrm{T}}\boldsymbol{\phi}\left(\boldsymbol{r}\right)+\boldsymbol{Q}\left(\boldsymbol{r},\Omega\right)\end{aligned}\tag{VII.3}$$

$$\begin{aligned}&\left[\mu\frac{\partial}{\partial x}+\Sigma\left(x,E\right)\right]\phi\left(x,\mu,E\right)=\\&=\frac{1}{2}\sum_{l=0}^{\infty}\left(2l+1\right)\int_0^{\infty}dE'\Sigma_{sl}\left(x,E'\to E\right)P_l\left(\mu\right)\phi_l\left(x,E'\right)+\\&\quad+\frac{1}{2}\chi\left(E\right)\int_0^{\infty}dE'\nu\left(E'\right)\Sigma_f\left(x,E'\right)\phi_0\left(x,E'\right)+Q\left(x,\mu,E\right)\end{aligned}\tag{VIII.1}$$

$$\begin{aligned}&\left[\mu\frac{\partial}{\partial x}+\Sigma_g\left(x\right)\right]\phi_g\left(x,\mu\right)=\\&=\frac{1}{2}\sum_{l=0}^{\infty}\left(2l+1\right)\sum_{g'=1}^{G}\Sigma_{slgg'}\left(x\right)P_l\left(\mu\right)\phi_{lg'}\left(x\right)+\\&\quad+\frac{1}{2}\chi_g\sum_{g'=1}^{G}\nu_{g'}\Sigma_{fg'}\left(x\right)\phi_{0g'}\left(x\right)+Q_g\left(x,\mu\right)\end{aligned}\tag{VIII.2}$$

REFERENCES

[1] Boltzmann, L., *Wissenschaftliche Abhandlungen*, Vol. I, II and III, F. Hasenöhrl (Ed.), Leipzig, Barth (1909); reissued New York, Chelsea (1969).

[2] Greenberg, M.D., *Advanced Engineering Mathematics*, Prentice Hall, New Jersey (1998).

[3] Case, K.M., P.F. Zweifel, *Linerar Transport Theory*, Addison-Wesley, MA (1967).

[4] Gibbs, A.G., Neutron Transport Theory Conference, USAEC/ORO-3858-1, 587-606, Jan. (1969).

[5] Case, K.M., F. De Hoffman, G. Placzek, *Introduction to the Theory of Neutron Diffusion*, Los Alamos Scientific Laboratory, Los Alamos, NM (1953).

[6] Megrhreblian, R.V., D.K. Holmes, *Reactor Analysis*, McGraw-Hill, NY (1960).

[7] Lewis, E.E., W.F. Miller, *Computational Methods of Neutron Transport*, ANS La Grange Park, IL (1993).

Figure 1.1

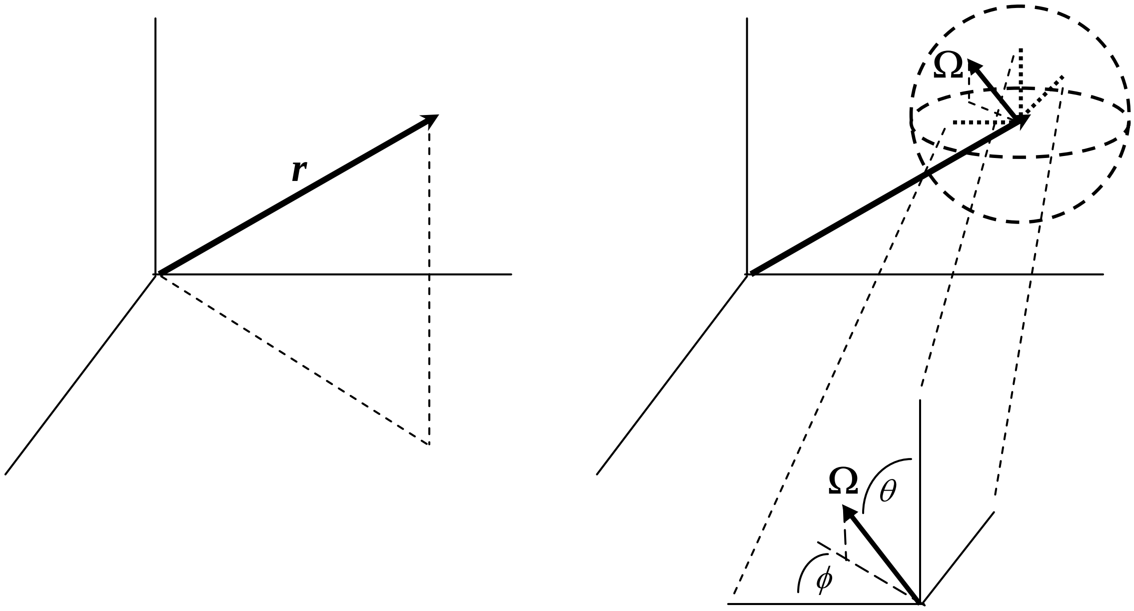

(a) Configuration coordinates

(b) Velocity coordinates

Figure 1.2. Phase space volume element $\Delta \boldsymbol{P} \equiv \Delta \boldsymbol{r} \Delta \Omega \Delta E$

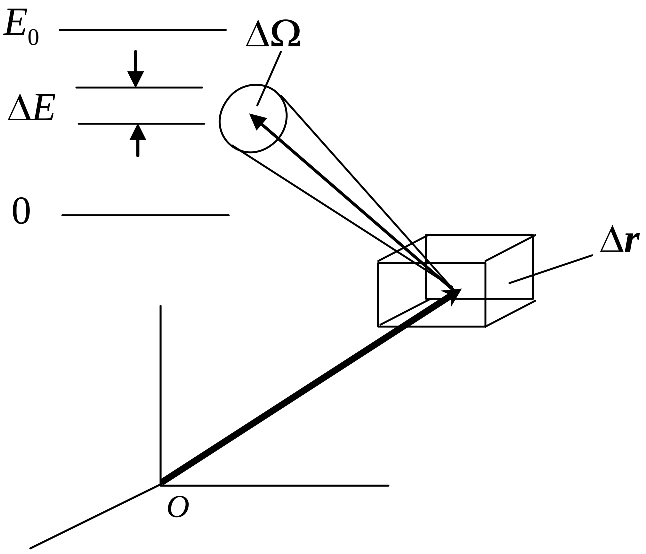

Figure 1.3. Neutrons passing through area *A* are moving into Δ*r* during Δ*t*

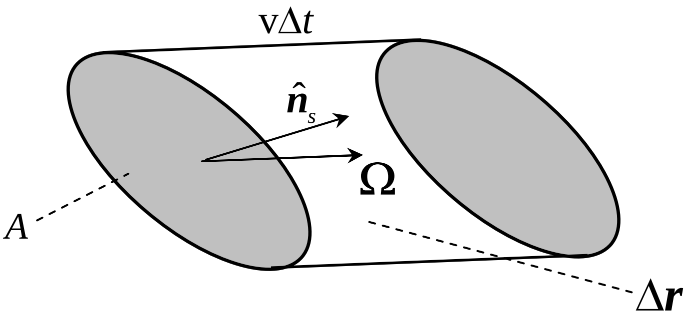

Figure 1.4. General transport medium

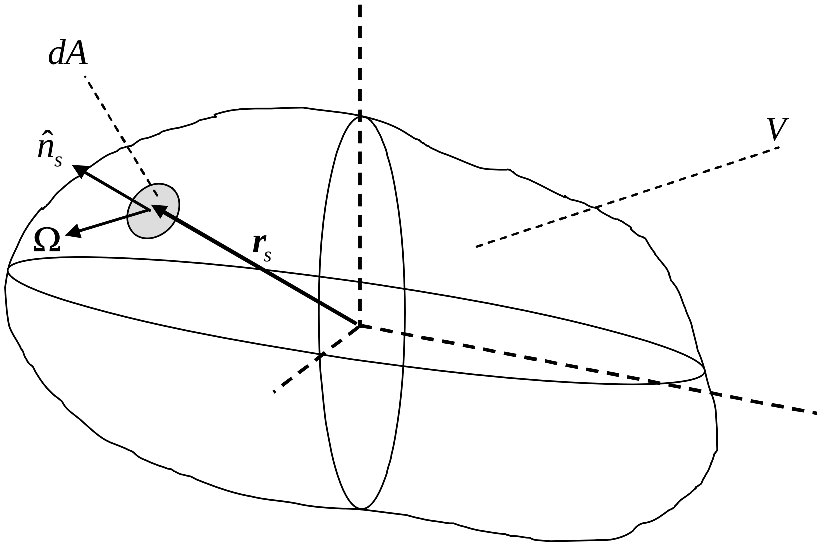

Figure 1.5. Neutron motion along direction Ω

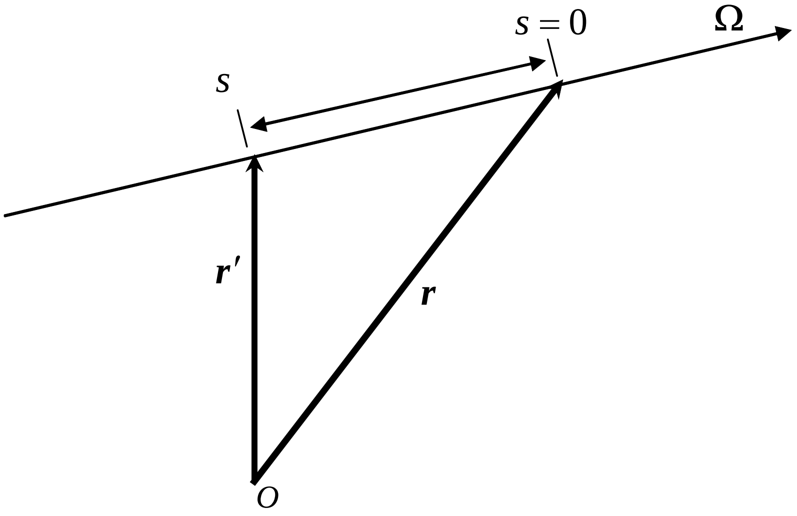

Figure 1.6. Transport along a neutron direction

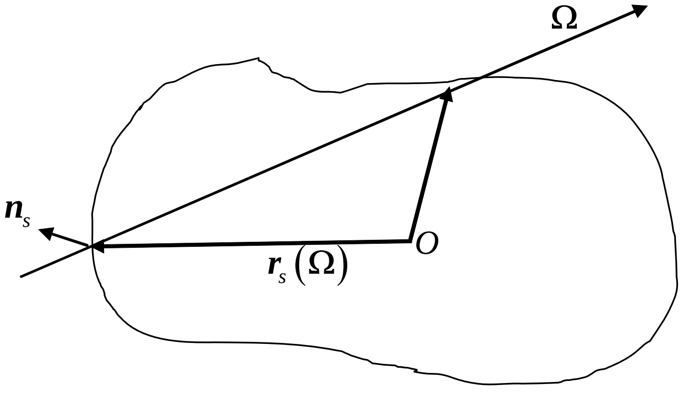

Figure 1.7(a). Laboratory (L) reference frame before collision

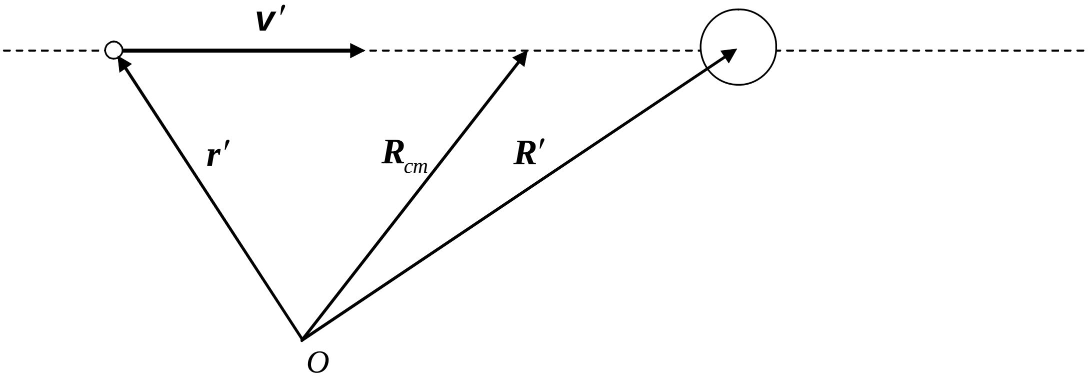

Figure 1.7(b). Center of mass (C) reference frame before collision

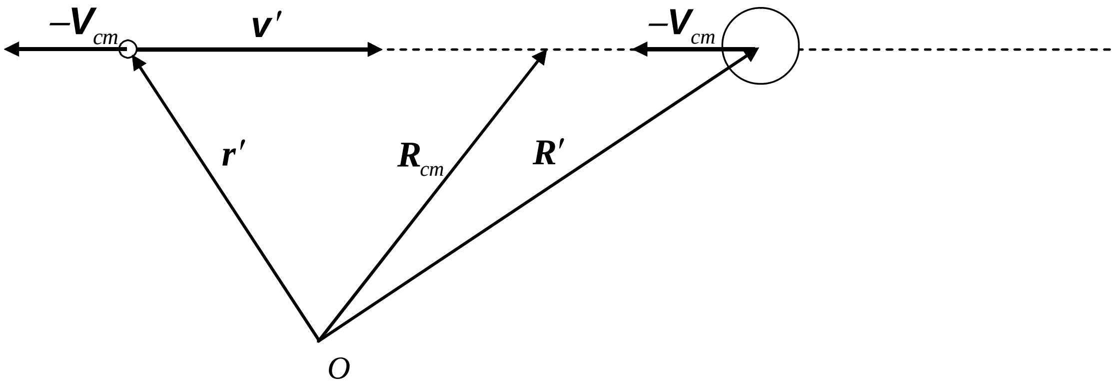

Figure 1.7(c). L and C after collision

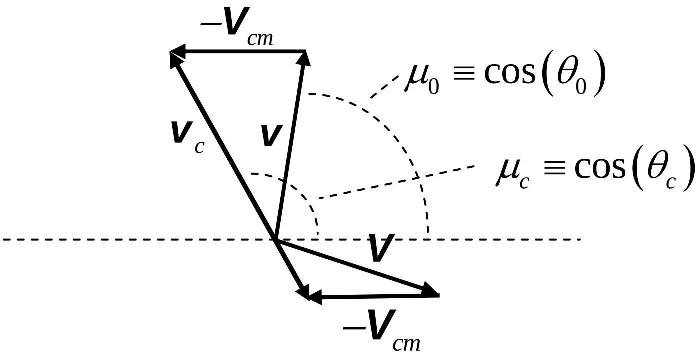

Chapter 2

NEUTRON SLOWING DOWN AND THERMALIZATION

The role of a nuclear reactor is to harvest potential energy stored within fissile nuclei. Nuclear potential energy is stored in the same way chemical potential energy is in conventional energy sources like oil, gasoline and wood. The nucleus is a collection of neutrons and protons (nucleons) held together by the strong nuclear force that acts only over nuclear distances. The dynamic motion of nucleons within the nucleus, a result of forces acting through a distance, creates the nuclear potential energy in the form of stored binding energy holding the nucleus together. For its release, a means to access the nuclear potential energy is therefore required. One way is to split, or fission, heavy nuclei, like uranium 235 (^{235}U), into several more stable nuclei, a process that releases excess binding energy in the form of kinetic energy of the fission fragments and accompanying radiation. The highly charged nuclear fragments quickly attract electrons and come to rest within 10^{-3} *cm* of their birth. They are radioactive and now become the waste product of the fission process. Waste production is invariably a consequence of any kind of energy generation, but in the case of nuclear energy generation, it is radioactive.

For the majority of commercial nuclear energy applications, ^{235}U is the nuclear fuel. ^{235}U is particularly advantageous since fission can occur with the addition of just the equivalent energy of the neutron mass and requires no additional neutron kinetic energy. Energy production, however, is possible only through a sustained fission process. Fortunately, fission typically produces two to three neutrons to continue the process. The neutrons from fission, however, are born at relatively high energies (>1 *MeV*), which, because of low probabilities, are not effective for continued ^{235}U fission. Sustained fission requires neutrons of kinetic energies characteristic of the thermal energies of the neighboring nuclei (~0.0253 *ev*) – a reduction of eight orders in magnitude. In the reactor core, the neutrons slow down (are moderated) through elastic and inelastic neutron-nucleus scattering collisions. The most effective moderation comes from nuclei of similar size to the neutron, like the hydrogen nuclei (protons) in water. Thus, in some sense, a nuclear reactor acts like a neutron pump, where high energy neutrons from fission trickle down to low energies and are “pumped up to” high energies by the fission process.

The focus of this chapter is on neutron slowing down and thermalization. The four benchmarks considered enable verification of transport algorithms or portions of algorithms, concerned with slowing down. In the following chapters, we will add spatial variables with all benchmarks originating from the transport equations of Chapter 1 [Eq. (II)]. Our primary objective is to determine, as accurately as possible, neutron collision densities or fluxes and hence reaction rates predictive of overall neutron balance and utilization.

The first two benchmarks describe neutron slowing down from high energy in an infinite medium without absorption. We initially assume constant cross sections in energy and the solution is through the Laplace transform and its inversion. The first benchmark is for an infinite medium for which the scalar collision density is the primary quantity of interest. The second is for the B_L approximation simulating spatial leakage thereby including limited anisotropic scattering in the laboratory system. The third benchmark is an example of the multigroup approximation characterizing neutron moderation and, as such, is not a true benchmark; however, the group parameters are determined analytically for elastic scattering. Therefore, this benchmark is appropriate for verification of group parameter generation, and assessment of how well the multigroup formulation captures the true continuous energy variation of the first two benchmarks. Also demonstrated is the use of benchmarks in a fast reactor application. The final benchmark treats neutrons after thermalization including a full scattering matrix.

Benchmark 2.1: Infinite medium slowing down/the Laplace transform solution

(a) Brief description

Neutron slowing down in an infinite medium without spatial dependence and with constant cross sections.

(b) Classification

NT/I/I/C/I/U/E(C)/NLTI

(c) Physical description

Neutrons slow down through elastic scattering with nuclei to thermal energies in an infinite medium. We obtain an analytical representation for the collision density of the slowing down equation in an infinite medium including multiple species and assuming constant cross sections.

(d) Analytical representations

(i) The collision density as a function of lethargy

The derivation of the neutron slowing down equation begins with Eq. (1.II) for *J* scattering and one fissioning species:

$$\begin{aligned}&\left[\Omega\bullet\nabla+\Sigma(E)\right]\phi(\boldsymbol{r},\Omega,E)=\\&=\sum_{j=1}^{J}\int_0^\infty dE'\int_{4\pi}d\Omega'\Sigma_{sj}(E')\,f_{sj}(\Omega'\bullet\Omega,E'\to E)\phi(\boldsymbol{r},\Omega',E')+\\&+\frac{\chi(E)}{4\pi}\int_0^\infty dE'\int_{4\pi}d\Omega'\nu(E')\Sigma_f(E')\phi(\boldsymbol{r},\Omega',E')+Q(\boldsymbol{r},\Omega,E)\end{aligned}\tag{1}$$

We assume all nuclear properties to be spatially uniform. Since each collision is an independent event, the scattering term is a summation over *J* nuclear species with a scattering law for each species *j*:

$$\Sigma_{sj}(\Omega'\bullet\Omega,E'\to E)\equiv\Sigma_{sj}(E')\,f_{sj}(\Omega'\bullet\Omega,E'\to E)$$

If we integrate Eq. (1) over the transport medium of volume *V* and surface area *A*, then from the divergence theorem [1]:

$$\begin{aligned}&\int_A dA\hat{\boldsymbol{n}}_s\bullet\boldsymbol{J}(r_s,\Omega,E)+\Sigma(E)\phi(\Omega,E)=\\&=\sum_{j=1}^{J}\int_0^\infty dE'\int_{4\pi}d\Omega' f_{sj}(\mu_0,E'\to E)\Sigma_{sj}(E')\phi(\Omega',E')+\\&+\frac{\chi(E)}{4\pi}\int_0^\infty dE'\int_{4\pi}d\Omega'\nu(E')\Sigma_f(E')\phi(\Omega',E')+Q(\Omega,E)\end{aligned}\tag{2}$$

where:

$$\mu_0 \equiv \mathbf{\Omega}' \bullet \mathbf{\Omega}$$

and:

$$\phi(\Omega,E) \equiv \int_V d\boldsymbol{r}\phi(\boldsymbol{r},\Omega,E)$$

$$Q(\Omega,E) \equiv \int_V d\boldsymbol{r}Q(\boldsymbol{r},\Omega,E)$$

The infinite medium assumption requires the total current on the bounding surface to vanish when we pass to the limit of an infinite medium yielding:

$$\begin{aligned}
&\Sigma(E)\phi(\Omega,E) = \\
&= \sum_{j=1}^{J} \int_0^{E_0} dE' \int_{4\pi} d\Omega' f_{sj}(\mu_0,E' \to E)\Sigma_{sj}(E')\phi(\Omega',E') + \\
&+ \frac{\chi(E)}{4\pi} \int_0^{E_0} dE' \int_{4\pi} d\Omega' \nu(E')\Sigma_f(E')\phi(\Omega',E') + Q(\Omega,E)
\end{aligned} \tag{3}$$

Each point in the medium is now identical. Note that spatial uniformity of the flux comes about from a vanishing current and not a vanishing flux. In addition, we have assumed the upper energy limit E_0.

The reduction of the number of variables continues as in §1.3.3, where we again note that:

$$f_{sj}(\mu_0,E' \to E) = f_{sj}(\mu',\mu,\vartheta-\vartheta',E' \to E)$$

and on integration over the azimuth ϑ, the integrated scattering probability:

$$f_{sj}(\mu',\mu,E' \to E) \equiv \int_0^{2\pi} d\vartheta'' f_{sj}(\mu_0(\mu',\mu,\vartheta''),E' \to E)$$

becomes independent of azimuth. Therefore, on integration of Eq. (3), we find:

$$\begin{aligned}
&\Sigma(E)\phi(\mu,E) = \\
&= \sum_{j=1}^{J} \int_0^{E_0} dE' \int_{-1}^{1} d\mu' f_{sj}(\mu',\mu,E' \to E)\Sigma_{sj}(E')\phi(\mu',E') + \\
&+ \frac{\chi(E)}{2} \int_0^{E_0} dE' \int_{-1}^{1} d\mu' \nu(E')\Sigma_f(E')\phi(\mu',E') + Q(\mu,E)
\end{aligned} \tag{4}$$

where the azimuthally averaged angular flux and source are:

$$\phi(\mu,E) \equiv \frac{1}{2\pi} \int_0^{2\pi} d\vartheta\phi(\Omega,E)$$

$$Q(\mu,E) \equiv \frac{1}{2\pi} \int_0^{2\pi} d\vartheta Q(\Omega,E)$$

By expressing $f_{sj}\left(\mu_0, E' \to E\right)$ as the usual Legendre series expansion [2]:

$$f_{sj}\left(\mu_0, E' \to E\right) = \sum_{l=0}^{\infty} \frac{2l+1}{4\pi} f_{slj}\left(E' \to E\right) P_l\left(\mu_0\right)$$

and introducing this expansion into Eq. (4), there results:

$$\begin{aligned}
&\Sigma(E)\phi(\mu,E) = \\
&= \sum_{j=1}^{J}\sum_{l=0}^{\infty} \frac{2l+1}{2} P_l(\mu) \int_0^{E_0} dE' \Sigma_{sj}(E') f_{slj}(E' \to E)\phi_l(E') + \\
&+ \frac{\chi(E)}{2} \int_0^{E_0} dE' \nu(E')\Sigma_f(E')\phi_0(E') + Q(\mu,E)
\end{aligned} \tag{5}$$

where the Legendre moments are [after application of the addition theorem for Legendre polynomials Eq. (1.44)]:

$$\phi_l(E) \equiv \int_{-1}^{1} d\mu' P_l(\mu')\phi(\mu,E)$$

In terms of the angular collision density:

$$F(\mu,E) \equiv \Sigma(E)\phi(\mu,E) \tag{6a}$$

Eq. (5) becomes:

$$\begin{aligned}
&F(\mu,E) = \\
&= \sum_{j=1}^{J}\sum_{l=0}^{\infty} \frac{2l+1}{2} P_l(\mu) \int_0^{E_0} dE' c_{slj}(E' \to E) F_l(E') + \\
&+ \frac{\chi(E)}{2} \int_0^{E_0} dE' c_f(E') F_0(E') + Q(\mu,E)
\end{aligned} \tag{6b}$$

where:

$$\begin{aligned}
&c_{slj}(E' \to E) \equiv c_{sj}(E') f_{slj}(E' \to E) \\
&c_{sj}(E) \equiv \Sigma_{sj}(E)/\Sigma(E) \\
&c_f(E) \equiv \nu(E)\Sigma_f(E)/\Sigma(E)
\end{aligned}$$

Finally, integrating $F(\mu,E)$ over μ, after noting orthogonality of Legendre polynomials, gives the well known slowing down equation for the collision density in an infinite medium [3]:

$$\begin{aligned}
F(E) = &\sum_{j=1}^{J} \int_0^{E_0} dE' c_{s0j}(E' \to E) F(E') + \\
&+ \chi(E) \int_0^{E_0} dE' c_f(E') F(E') + Q(E)
\end{aligned} \tag{7}$$

where $F(E)$ is the scalar collision density:

$$F(E) \equiv \int_{-1}^{1} d\mu F(\mu, E)$$

For convenience, we make the switch to the lethargy variable:

$$u = \ln\left(\frac{E_0}{E}\right) \tag{8}$$

where the reference energy is the highest neutron energy E_0. To accommodate the transformation to the lethargy unit (of energy), we must require:

$$\begin{aligned}
&F(E)|dE| = F(u)|du| \\
&Q(E)|dE| = Q(u)|du| \\
&f_{s0j}(E' \rightarrow E)|dE| = f_{s0j}(u' \rightarrow u)|du| \\
&\chi(E)|dE| = \chi(u)|du|
\end{aligned}$$

since a change of a unit in phase space does not change the absolute number of particles or fractional probabilities in the phase space volume element.

As will be shown in §2.2, the isotropic component of the elastic scattering cross section in lethargy is:

$$f_{s0j}(u' \rightarrow u) = \frac{e^{-(u-u')}}{1-\alpha_j} \Theta(u-u') \Theta\left(q_j - (u-u')\right) \tag{9a}$$

where Θ is the unit step function and:

$$q_j \equiv -\ln(\alpha_j)$$

α_j is the scattering parameter of the jth scattering species [I.26b]. We therefore recast Eq. (7) as:

$$\begin{aligned}
F(u) = \sum_{j=1}^{J} \frac{1}{1-\alpha_j} \int_{u-q_j}^{u} du' e^{-(u-u')} c_{sj}(u') F(u') + \\
+ \chi(u) \int_{0}^{\infty} du' c_f(u') F(u') + Q(u)
\end{aligned} \tag{10}$$

To proceed analytically, we assume the cross sections are constant in lethargy. This assumption allows the theoretical advantage of the Laplace transform. The constant cross section assumption, in general, limits our consideration to an approximate slowing down solution. However, the assumption of constant cross sections is exact for a single non-absorbing species, appropriate for neutrons in the energy range above resonances.

(ii) The solution via Laplace transform

After application of the Laplace transform to Eq. (10) with:

$$\bar{F}(p) \equiv \int_0^\infty du e^{-pu} F(u)$$

$$\bar{\chi}(p) \equiv \int_0^\infty du e^{-pu} \chi(u)$$

$$\bar{Q}(p) \equiv \int_0^\infty du e^{-pu} Q(u)$$

we find:

$$\left[1-\bar{Q}_s(p)\right]\bar{F}(p) = c_f \bar{\chi}(p)\bar{F}(0) + \bar{Q}(p) \tag{11a}$$

with:

$$\bar{Q}_s(p) \equiv \sum_{j=1}^{J} \frac{c_{sj}}{1-\alpha_j}\left[\frac{1-e^{-q_j(p+1)}}{p+1}\right] \tag{11b}$$

Note that the Laplace transform solution is possible only through the constant cross section assumption. Then, when p is zero in Eq. (11a) and since $\bar{\chi}(0)$ is unity by definition:

$$\bar{F}(0) = \frac{\bar{Q}(0)}{1-c}, \quad c \equiv c_s + c_f, \quad 0 \le c \le 1$$

where:

$$c_s \equiv \sum_{j=1}^{J} c_{sj}$$

and the image function $\bar{F}(p)$ becomes:

$$\bar{F}(p) = \frac{\bar{Q}(p) + c_f (1-c)^{-1} \bar{Q}(0)\bar{\chi}(p)}{1-\bar{Q}_s(p)} \tag{12a}$$

On inversion, we obtain the following analytical solution representation:

$$F(u) = \mathrm{L}_u^{-1}\left[\frac{\bar{Q}(p) + c_f (1-c)^{-1} \bar{Q}(0)\bar{\chi}(p)}{1-\bar{Q}_s(p)}\right] \tag{12b}$$

L_u^{-1} is the inverse Laplace transform operator (on the Bromwich contour):

$$\mathrm{L}_u^{-1} \equiv \frac{1}{2\pi i}\int_{\gamma-i\infty}^{\gamma+i\infty} dp e^{pu}\left(\bullet\right)$$

γ is the real part of p to the right of all singularities in the complex p-plane with the largest real part γ_S.

For the special case of fission neutrons appearing only at E_0 (u = 0), the fission spectrum is the delta function distribution:

$$\chi\left(u\right) \equiv \delta\left(u\right),\ \bar{\chi}\left(p\right) = 1 \tag{13a}$$

which applies in the following unless otherwise stated. Also, we assume the source to emit neutrons at u = 0:

$$Q\left(u\right) \equiv Q_0\delta\left(u\right),\ \bar{Q}\left(p\right) = Q_0 \tag{13b}$$

It is numerically advantageous to separate collision densities for neutrons coming directly from the source and having had at most three collisions from those with more than three collisions. The collision density transforms for neutrons with up to three collisions are:

$$\bar{F}_n\left(p\right) = Q_0\left[1+\frac{c_f}{1-c}\right]\left[\bar{Q}_s\left(p\right)\right]^n,\ n = 0,1,2,3 \tag{14}$$

which upon inversion become:

$$F_0\left(u\right) = Q_0\left[1+\frac{c_f}{1-c}\right]\delta\left(u\right)$$

$$F_1\left(u\right) = Q_0\left[1+\frac{c_f}{1-c}\right]e^{-u}\sum_{j=1}^{J}\frac{c_{sj}}{1-\alpha_j}\left[1-\Theta\left(u-q_j\right)\right]$$

$$F_2\left(u\right) =$$

$$= Q_0\left[1+\frac{c_f}{1-c}\right]e^{-u}\sum_{j=1}^{J}\frac{c_{sj}}{1-\alpha_j}\sum_{k=1}^{J}\frac{c_{sk}}{1-\alpha_k}\left[\begin{array}{l} u-\left(u-q_k\right)\Theta\left(u-q_k\right)- \\ -\left(u-q_j\right)\Theta\left(u-q_j\right)+ \\ +\left(u-q_k-q_j\right)\Theta\left(u-q_k-q_j\right)\end{array}\right]$$

$$F_3\left(u\right) = Q_0\left[1+\frac{c_f}{1-c}\right]e^{-u}\sum_{j=1}^{J}\frac{c_{sj}}{1-\alpha_j}\sum_{k=1}^{J}\frac{c_{sk}}{1-\alpha_k}\sum_{l=1}^{J}\frac{c_{sl}}{1-\alpha_l}\chi_{jkl}\left(u\right)$$

with:

$$\chi_{jkl}(u) \equiv \left\{ \begin{array}{l} f(u) - f\left(u-q_j\right) - f\left(u-q_k\right) - f\left(u-q_l\right) + \\ + f\left(u-q_j-q_k\right) + f\left(u-q_k-q_l\right) + f\left(u-q_l-q_j\right) - \\ - f\left(u-q_j-q_k-q_l\right) \end{array} \right\}$$

$$f(u) \equiv \frac{u^2}{2}\Theta(u)$$

For more than three collisions, the analytical forms are prohibitively complicated. The desired inversion [Eq. (12b)], then becomes:

$$F(u) = \sum_{n=0}^{3} F_n(u) + Q_0\left[1+\frac{c_f}{1-c}\right] \mathrm{L}_u^{-1}\left[\frac{1}{1-\bar{Q}_s(p)} - \sum_{n=0}^{3}\left[\bar{Q}_s(p)\right]^n\right] \tag{15}$$

For a general source and a delta function fission spectrum, we only evaluate the uncollided contribution analytically:

$$\begin{aligned} F(u) &= Q(u) + \frac{c_f}{1-c}Q_0\delta(u) + \\ &+ \mathrm{L}_u^{-1}\left\{\left[\bar{Q}(p) + \frac{c_f}{1-c}Q_0\right]\left[\frac{1}{1-\bar{Q}_s(p)} - 1\right]\right\} \end{aligned} \tag{16}$$

where Q_0 is the source normalization:

$$Q_0 \equiv \int_0^\infty du Q(u)$$

In his classic work, Marshak [4] analytically evaluated the inversion of Eq. (12b) for a single non-fissioning, non-absorbing species by analytically continuing $\overline{F}$ (p) from the Bromwich contour into the left half of the complex p-plane. Using his method, even the simplest case becomes difficult to evaluate. For $J = 1$, Marshak found the following closed form representation:

$$F(u) = \frac{e^{-u}}{1-\alpha}\sum_{k=0}^{[u/q]} \frac{(-1)^k}{k!}\left[\frac{u-kq}{1-\alpha}\right]^{(k-1)}\left[\frac{u-kq}{1-\alpha} + k\right] e^{-(u-kq)/(1-\alpha)} \tag{17}$$

where $[u/q]$ is the greatest integer contained in u/q. This expression has its numerical shortcomings however, as we shall soon see. The two scattering species case ($J = 2$) has similarly been treated [5], but the analysis becomes hopelessly complicated for $J \geq 3$, making a general analytical inversion virtually impossible. For this reason, we have developed a numerical inversion outlined in Appendix B.1, complete with comparison to other numerical inversions.

(iii) Criticality

A critical nuclear system of infinite extent is in perfect balance, i.e. the number of neutrons produced from fission is the same as the number lost from non-productive capture and from producing fission. There is no external source, thus the reaction is self-sustaining. Equation (12b) remains the appropriate solution for the case of constant cross sections and criticality:

$$F(u) = \lim_{Q_0 \to 0} \left\{ \mathrm{L}_u^{-1} \left[\frac{\bar{Q}(p) + c_f (1-c)^{-1} Q_0 \bar{\chi}(p)}{1 - \bar{Q}_s(p)} \right] \right\} \tag{18}$$

however for $Q(u) \equiv 0$, implying both Q_0 and $\bar{Q}(p)$ are zero. At the same time, the collision density must be non-zero (and positive) for all u in order to be a physical solution. The only way this can occur is for the ratio:

$$\frac{Q_0}{1-c}$$

to remain finite, implying the well known condition that for criticality in an infinite system, $c = 1$ or:

$$k_\infty \equiv \frac{\nu \Sigma_f}{\Sigma_a} = 1 \tag{19}$$

where k_∞ is the infinite medium multiplication factor representing the balance between fission production and absorption. We shall say more concerning k_∞ later.

The critical distribution for a general fission spectrum is therefore:

$$F(u) \propto \mathrm{L}_u^{-1} \left\{ \frac{\bar{\chi}(p)}{1 - \bar{Q}_s(p)} \right\} = \int_0^u du' \chi(u') \mathrm{L}_{u-u'}^{-1} \left\{ \frac{1}{1 - \bar{Q}_s(p)} \right\} \tag{20}$$

The convolution integral indicates that the critical collision density distribution follows from a shift of the fission spectrum through the collision density. The most convenient normalized critical collision density distribution is:

$$F(u) \left[\nu \Sigma_f \int_0^\infty du' F(u') \right]^{-1} = \int_0^u du' \chi(u') \mathrm{L}_{u-u'}^{-1} \left\{ \frac{1}{1 - \bar{Q}_s(p)} \right\} \tag{21}$$

Section 2.3 contains a more general interpretation of criticality for non-constant cross sections.

(iv) The exact multigroup collision density

It is informative to note that from knowledge of the image function $\bar{F}(p)$ [Eq. (12a)], integrals of the collision density over arbitrary lethargy intervals are possible. In particular, by partitioning the lethargy range of interest $[0,u_L]$ into G groups:

$$\Delta u_g = u_g - u_{g-1},\ \ g = 1,2,...,G$$

the group collision density follows:

$$F_g \equiv \frac{1}{\Delta u_g}\int_{u_{g-1}}^{u_g} du F(u) \tag{22a}$$

or:

$$F_g \equiv \frac{1}{\Delta u_g}\left[\int_{0}^{u_g} du F(u) - \int_{0}^{u_{g-1}} du F(u)\right] \tag{22b}$$

In terms of the Laplace transform inversion, Eq. (22b) becomes:

$$F_g = \frac{1}{\Delta u_g}\left\{\mathrm{L}^{-1}_{u_g}\left[\frac{\bar{F}(p)}{p}\right] - \mathrm{L}^{-1}_{u_{g-1}}\left[\frac{\bar{F}(p)}{p}\right]\right\} \tag{23}$$

With numerical evaluation of the inversion, we therefore can determine the “exact” group collision density. As for the pointwise collision density with a delta function source, we treat the uncollided and first three collided contributions analytically:

$$F_g = \sum_{n=0}^{3} F_{ng} + \frac{1}{\Delta u_g}\left\{\mathrm{L}^{-1}_{u_g}\left[\hat{f}(p)\right] - \mathrm{L}^{-1}_{u_{g-1}}\left[\hat{f}(p)\right]\right\} \tag{24}$$

where:

$$\hat{f}(p) \equiv \frac{1}{p}\left[\bar{F}(p) - \sum_{n=0}^{3}\left[\bar{Q}_s(p)\right]^n\right]$$

and:

$$F_{0g} = \frac{Q_0}{\Delta u_1}\left[1 + \frac{c_f}{1-c}\right]\delta_{g1}$$

$$F_{1g} = \frac{Q_0}{\Delta u_g}\left[1 + \frac{c_f}{1-c}\right]\sum_{j=1}^{J}\frac{c_{sj}}{1-\alpha_j}\left\{\begin{array}{l} e^{-u_{g-1}} - e^{-u_g} - \Theta\left(q_j - u_g\right)\bullet \\ \bullet\left[\begin{array}{l}\left[e^{-q_j} - e^{-u_g}\right]\Theta\left(q_j - u_{g-1}\right) + \\ +\left[e^{-u_{g-1}} - e^{-u_g}\right]\Theta\left(u_{g-1} - q_j\right)\end{array}\right]\end{array}\right\} \tag{25a}$$

$$F_{2g} = \frac{Q_0}{\Delta u_g}\left[1 + \frac{c_f}{1-c}\right]\sum_{j=1}^{J}\frac{c_{sj}}{1-\alpha_j}\sum_{k=1}^{J}\frac{c_{sk}}{1-\alpha_k}\left[\chi_{2jk}\left(u_g\right) - \chi_{2jk}\left(u_{g-1}\right)\right] \tag{25b}$$

$$F_{3g} = \frac{Q_0}{\Delta u_g}\left[1 + \frac{c_f}{1-c}\right]\sum_{j=1}^{J}\frac{c_{sj}}{1-\alpha_j}\sum_{k=1}^{J}\frac{c_{sk}}{1-\alpha_k}\sum_{l=1}^{J}\frac{c_{sl}}{1-\alpha_l}\left[\chi_{3jkl}\left(u_g\right) - \chi_{3jkl}\left(u_{g-1}\right)\right] \tag{25c}$$

with:

$$\chi_{2jk}(u) \equiv \left\{ f_2(u) - f_2\left(u-q_j\right)e^{-q_j} - f_2\left(u-q_j\right)e^{-q_k} + f_2\left(u-q_j-q_k\right)e^{-\left(q_j+q_k\right)} \right\}$$

$$\chi_{3jkl}(u) \equiv \left\{ \begin{array}{l} f_3(u) - f_3\left(u-q_j\right)e^{-q_j} - f_3\left(u-q_k\right)e^{-q_k} - f_3\left(u-q_l\right)e^{-q_l} + \\ + f_3\left(u-q_j-q_k\right)e^{-\left(q_l+q_j\right)} + f_3\left(u-q_k-q_l\right)e^{-\left(q_k+q_l\right)} + \\ + f_3\left(u-q_l-q_j\right)e^{-\left(q_k+q_j\right)} - f_3\left(u-q_j-q_k-q_l\right)e^{-\left(q_j+q_k+q_l\right)} \end{array} \right\}$$

$$f_2(u) \equiv \left[1-(1+u)e^{-u}\right]\Theta(u)$$

$$f_3(u) \equiv \left[1-\left(1+u+\frac{u^2}{2}\right)e^{-u}\right]\Theta(u)$$

For a general source, $Q(u)$ and delta function fission spectrum:

$$F_g = \frac{1}{\Delta u_g}\left\{ \int_{u_{g-1}}^{u_g} du Q(u) + \frac{c_f}{1-c}Q_0\delta_{g1} + \mathrm{L}_{u_g}^{-1}\left[\bar{g}(p)\right] - \mathrm{L}_{u_{g-1}}^{-1}\left[\bar{g}(p)\right] \right\} \tag{26}$$

where:

$$\bar{g}(p) \equiv \frac{1}{p}\left[\bar{Q}(p) + \frac{c_f}{1-c}Q_0\right]\left[\frac{1}{1-\bar{Q}_s(p)} - 1\right]$$

(e) Numerical implementation and demonstration for Benchmark 2.1

(i) The numerical Laplace transform

We have developed a numerical Laplace transform inversion for evaluation of Eqs. (15), (16), (24) and (26). The success or failure of the numerical inversion rests on the convergence of the equivalent series representation given in Appendix B.1 by Eq. (B.1.2). As derived in Appendix A.1, Euler-Knopp (*EK*) convergence acceleration with the free parameter p_e can, in most cases, force convergence of an alternating series in fewer terms relative to the original series. Apparently, because discontinuities in the function or its derivatives induce oscillations in the transform, the series is most prone to poor performance near discontinuities. To see this, consider the numerical inversion of:

$$f_n(p) = \frac{\left(1-e^{-qp}\right)}{p^{n+1}} \tag{27a}$$

which corresponds to the n^{th} integral of $(1-\alpha)e^{-u}F_1(u)$ for a single species over $[0,u]$ and:

$$f_n(u) = \frac{1}{n!}\left[u^n - (u-q)^n\,\Theta(u-q)\right] \tag{27b}$$

Note that for $n = 0$, $f_0(u)$ is discontinuous at $u = q$. For $A = 12$, ($q = 0.3341$), Figure 2.1.1(a) clearly shows that as the discontinuity is uncovered (decreasing n), the inversion error increases. We performed these calculations for an acceleration parameter of $p_e = 0.45$, experimentally found to be the most efficient. As shown in Table 2.1.1, the fewest number of terms required for convergence of the inversion series for minimum error occurs near $p_e = 0.45$. Even without convergence to the desired accuracy, the result is inaccurate only near the discontinuity as shown in Figure 2.1.1(b). The reason for the difficulty near the singularity is that more terms are required for convergence as n approaches zero. For $n = 0$, the series fails to converge in 100 terms which is most likely a manifestation of the ill-conditioned nature of the inversion and seems, unfortunately, to be an unavoidable feature of numerical Laplace transform inversions. A successful inversion algorithm, however, is one in which failure is detected and flagged. In the algorithm described in Appendix B.1, we report a lack of convergence of the inversion series (relative error ε_T), the Romberg integration (relative error ε_R) and the contour iteration (relative error ε_γ). Note that in this compendium, convergence is always based on an “engineering estimate” of the relative error between the last two iterates. If the algorithm converges, then we are reasonably confident in a true result. This is, after all, the most one can demand of any numerical procedure.

As noted above, to avoid difficulty at the discontinuity induced by the delta function fission spectrum and/or source at $u = 0$ and $u = q_j$, the transforms of the uncollided and first collided components of the collision density are subtracted from the image function and analytically evaluated. To provide additional numerical margin, we also analytically evaluate the transforms of the second and third collided components of the collision density [Eq. (15)] and remove them from the image function. Thus, the inversion of the remaining image function should be a relatively smooth function of lethargy.

(ii) The first collision interval

Experience with the numerical inversion indicates that, in general, the inversion requires considerable computational effort near $u = 0$. For this reason, the solution for the collision density in the first collision interval:

$$0 \le u \le \min_j \left(q_j\right)$$

is analytically determined for the case of a monoenergetic source. We obtain the solution by evaluating the collision density in the first collision interval from its differential equation to give (see Ref. 3 for $J = 1$ only):

$$F\left(u\right) = Q_0\delta\left(u\right) + Q_0\left[1+\frac{c_f}{1-c}\right]\beta e^{(\beta-1)u} \tag{28a}$$

where:

$$\beta \equiv \sum_{j=1}^{J}\frac{c_{sj}}{1-\alpha_j}$$

and for the corresponding (exact) multigroup collision density:

$$F_g = Q_0\delta_{g1} + Q_0\left[1+\frac{c_f}{1-c}\right]\left[\frac{\beta}{\beta-1}\right]\left[e^{(\beta-1)u_g} - e^{(\beta-1)u_{g-1}}\right] \tag{28b}$$

(iii) Large lethargy and small c_{sj}

When absorption is significant and at large lethargies, the collision density is relatively small. Because the numerical Laplace transform inversion requires the evaluation of a series of both positive and negative terms, values only to machine accuracy (about 10^{-15} double precision) are attainable. Thus, in the following, we only trust collision densities larger than 10^{-12} by limiting the largest desired lethargy.

Since the asymptotic density is:

$$F(u) \approx r^* e^{\lambda^* u} \tag{29a}$$

where the residue from Eq. (16) is:

$$r^* = -\left[1 + \frac{c_f}{1-c}\right]\left[\left.\frac{d\bar{Q}_s(p)}{dp}\right|_{p=\lambda^*}\right]^{-1} \tag{29b}$$

and λ^* is the zero with largest real part of the solution to:

$$\bar{Q}_s(\lambda) = 1$$

for $F(u) < 10^{-z}$, we limit u to:

$$u < \frac{1}{|\lambda^*|}\ln\left(\frac{10^{-z}}{r^*}\right) \tag{29c}$$

for $z = 12$.

Of a similar concern, for absorption dominated media where $c_{sj} \leq 0.01$, the truncated multiple collision form given by Eq. (14):

$$F(u) \approx Q_0\left[1 + \frac{c_f}{1-c}\right]\sum_{n=0}^{N} \mathrm{L}_u^{-1}\left[\bar{Q}_s(p)\right]^n \tag{30}$$

seems to provide the most reliable evaluation when we increase N until convergence.

(iv) Demonstration for Benchmark 2.1

Note that all results in this section are for non-absorbing media.

We can assess the inversion accuracy of the collision density through a comparison with the analytical solution for a single scattering species given by Eq. (17). Figure 2.1.2 shows the relative error for $A = 4$ (helium), $A = 12$ (carbon) and $A = 56$ (iron). The numerical inversion parameters are $\varepsilon = \varepsilon_T = \varepsilon_R = \varepsilon_\gamma = 10^{-4}$. In general, for the lighter elements, the transform inversion is within the specified accuracy in comparison with the analytical solution. A noticeable exception however, occurs at large lethargy for carbon and iron, where the error increases with lethargy and in the case of iron saturates at one. This comes from a numerical instability in the analytical solution with respect to round off error and is an example of a numerical inversion outperforming the evaluation of an analytical representation. To see that this conjecture is true, Figure 2.1.3(a) shows the collision density for iron at large lethargy from the numerical inversion, which is stable. Figure 2.1.3(b) shows the detail of the Placzek discontinuity [3], exactly predicted by the numerical inversion.

It is interesting to reflect for a moment on the significance of the Placzek transient. The Placezk transient is a manifestation of a finite maximum lethargy gain allowable per neutron collision. For a (singular) delta function source distribution in a medium of a single species, all neutrons emitted are at zero lethargy. Since in a single collision, these neutrons can gain a maximum of q in lethargy, all neutrons having had one collision will be in the lethargy interval $[0,q]$. Thus, the collision density of once collided neutrons is non-zero in this region and therefore has a discontinuity at the interval boundaries. When the once collided neutrons have a collision in this interval, they serve as the source of second and higher collided neutrons which are able to reach the boundary of the next collision interval $[q,2q]$. There is no longer a discontinuity in the collision density in the second collision interval because their source was distributed in energy through first collisions. However, the derivative of the second collided collision density is discontinuous at lethargies q and $2q$ reflecting the strong discontinuity of the source. In this way, the initial delta function source discontinuity becomes more deeply embedded in higher derivatives of the collided flux collision densities in subsequent collision intervals extending to lethargy nq. Of course, the total collision density $F(u)$ inherits all discontinuities which are responsible for the oscillations observed in Figure 2.1.3(a). This is an excellent example of how collisions mathematically smooth distributions and illustrates how neutrons, starting from order become increasingly disordered through scattering, thus increasing their entropy.

Figure 2.1.4 gives the collision density for neutrons slowing down in a mixture of carbon and helium for a decreasing (increasing) volume fraction of carbon (helium). As He replaces carbon on depletion, its Placzek signature diminishes while the Placzek signature for helium emerges.

In Figure 2.1.5, the collision densities for a uniformly distributed source over lethargy of increasing lethargy widths, $\Delta = 0.5$, 1 and 2, in carbon are displayed. The Laplace transform for this source is:

$$\bar{Q}(p) = \frac{1 - e^{-\Delta p}}{\Delta}$$

Note that Placzek-like transients occur at the end of the source interval, and we obtain the same asymptotic density as a delta function source regardless of the source interval.

Figure 2.1.6 shows a comparison between the pointwise and multigroup flux in carbon, giving essentially identical results. Because the multigroup evaluation involves a subtraction, we require iteration on the accuracy of the Laplace transform inversion to avoid round off error.

The final figure, Figure 2.1.7, shows the collision density for a hypothetical equal mix of elements $A = 1(5)56$. Note that all 11 Placzek transients are clearly visible.

Finally, a benchmark would not be complete without a table of values to confirm that the benchmark claim is indeed a legitimate one. Table 2.1.2 gives the collision density distribution for slowing down in helium for decreasing desired relative error ε. The collision densities converge to the desired number of places. We expect the last column to be correct to the number of digits quoted.

Table 2.1.1. Choice of Euler-Knopp convergence parameter p_e based on $f_n(p)$ ($\varepsilon = \varepsilon_T = \varepsilon_R = \varepsilon_\gamma = 10^{-8}$, $\gamma u = 1$, $A = 12$, $u = 2$, $n = 1$)

p_e	*Number of terms*	*Relative error*
0.0	72	1.2e9
0.2	19	0.9e-9
0.4	16	0.2e-9
0.45	15	1.0e-9
0.6	14	1.0e-9
0.8	13	1.7e-9
1.0	14	1.5e-9

Table 2.1.2. Qualification of Benchmark 2.1

Collision density for slowing down in helium

$u \backslash \varepsilon$	10^{-3}	10^{-4}	10^{-5}	10^{-6}	10^{-7}
5.10826E-01	2.08262E+00	2.08262E+00	2.08262E+00	2.08262E+00	2.08262E+00
1.17057E+00	2.26412E+00	2.26443E+00	2.26446E+00	2.26445E+00	2.26445E+00
1.46840E+00	2.34079E+00	2.34088E+00	2.34088E+00	2.34089E+00	2.34089E+00
1.76624E+00	2.37001E+00	2.36992E+00	2.36988E+00	2.36989E+00	2.36989E+00
2.06407E+00	2.33776E+00	2.33822E+00	2.33832E+00	2.33836E+00	2.33836E+00
2.36191E+00	2.35150E+00	2.35110E+00	2.35109E+00	2.35115E+00	2.35114E+00
2.65974E+00	2.35259E+00	2.35275E+00	2.35285E+00	2.35282E+00	2.35282E+00
2.95758E+00	2.35040E+00	2.35038E+00	2.35025E+00	2.35025E+00	2.35025E+00
3.25541E+00	2.35134E+00	2.35122E+00	2.35117E+00	2.35126E+00	2.35126E+00
3.55325E+00	2.35102E+00	2.35125E+00	2.35133E+00	2.35130E+00	2.35130E+00
3.85108E+00	2.35109E+00	2.35120E+00	2.35107E+00	2.35108E+00	2.35108E+00

REFERENCES

[1] Greenberg, M.D., *Advanced Engineering Mathematics*, Prentice Hall, New Jersey (1998).

[2] Lewis, E.E., W.F. Miller, *Computational Methods of Neutron Transport*, ANS La Grange Park, IL (1993).

[3] Lamarsh, J.R., *Introduction to Nuclear Reactor Theory*, Addison-Wesley Pub Co/American Nuclear Society, LaGrange Park, IL (1966).

[4] Marshak, R.E., "Theory of Slowing Down of Neutrons by Elastic Collision with Atomic Nuclei", *Rev. Mod. Phys.*, **19**, 185 (1947).

[5] Teichman, T., "Slowing Down of Neutrons", *Nucl. Sci .& Eng.*, **7**, 292 (1960).

Figure 2.1.1(a). Relative error for numerical inversion of $f_n(p) = \left(1 - e^{-qp}\right) / p^{n+1}$

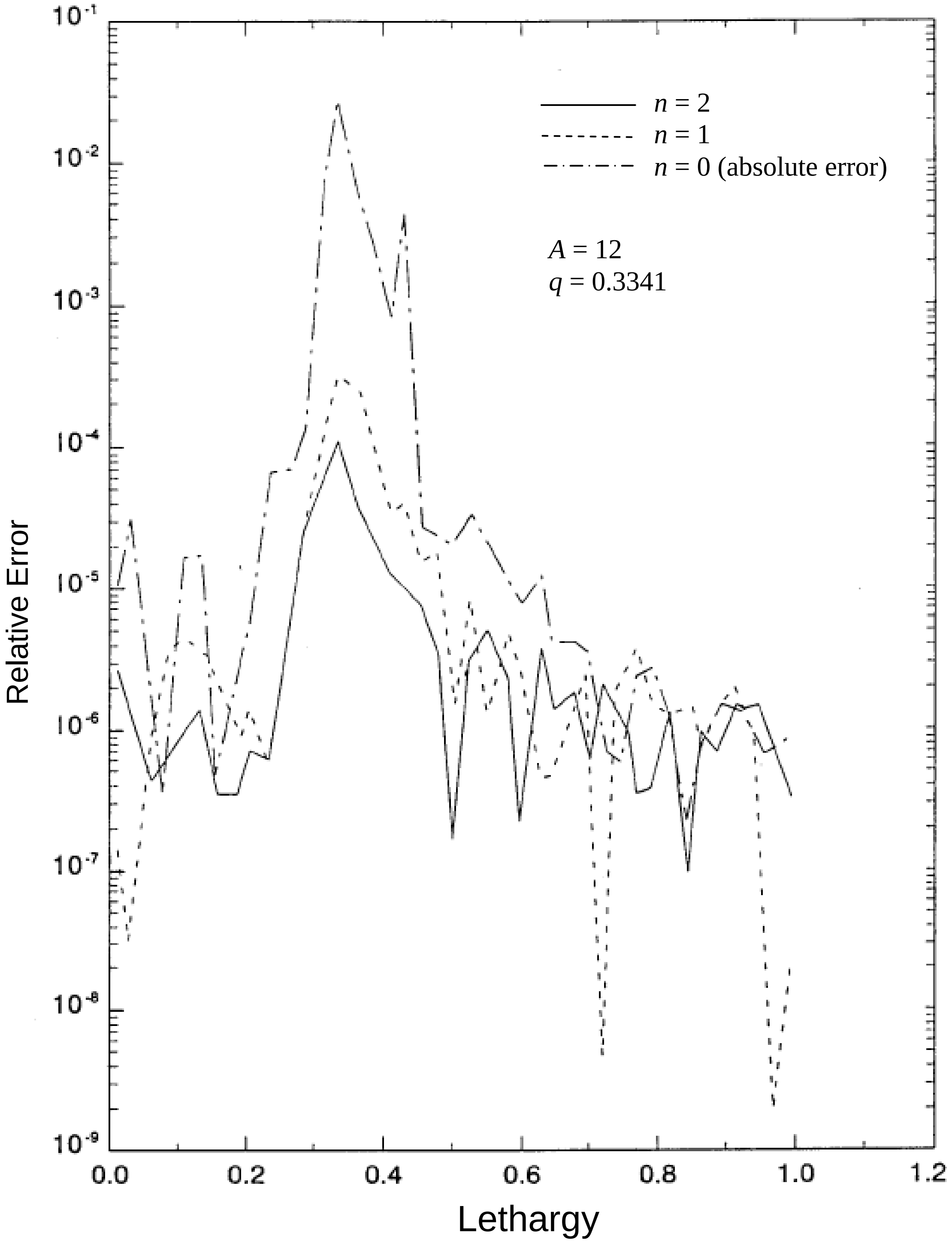

Figure 2.1.1(b). Numerical inversion near discontinuity for $f_0(u)$

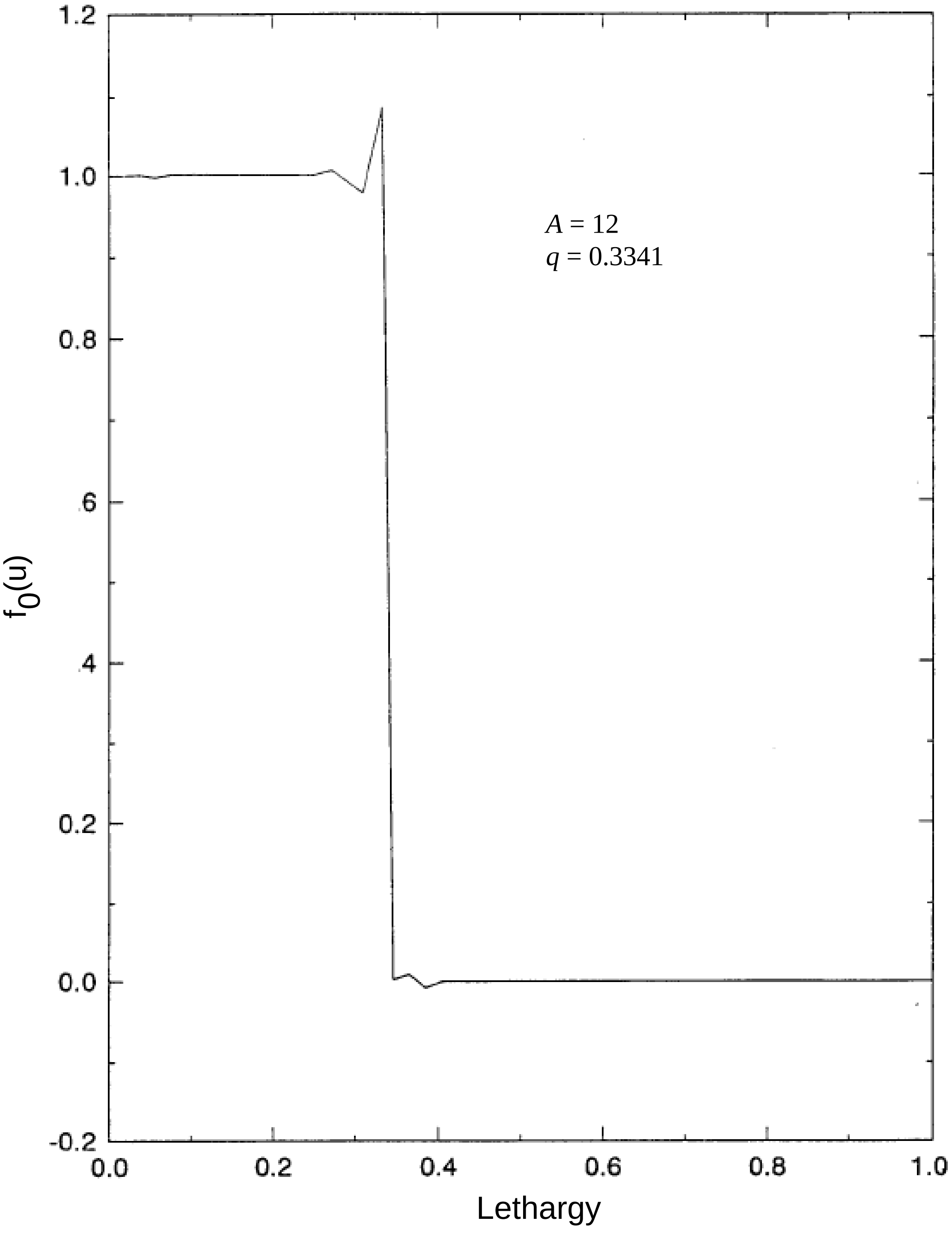

Figure 2.1.2. Relative error comparison to exact solution ($\varepsilon = 10^{-4}$)

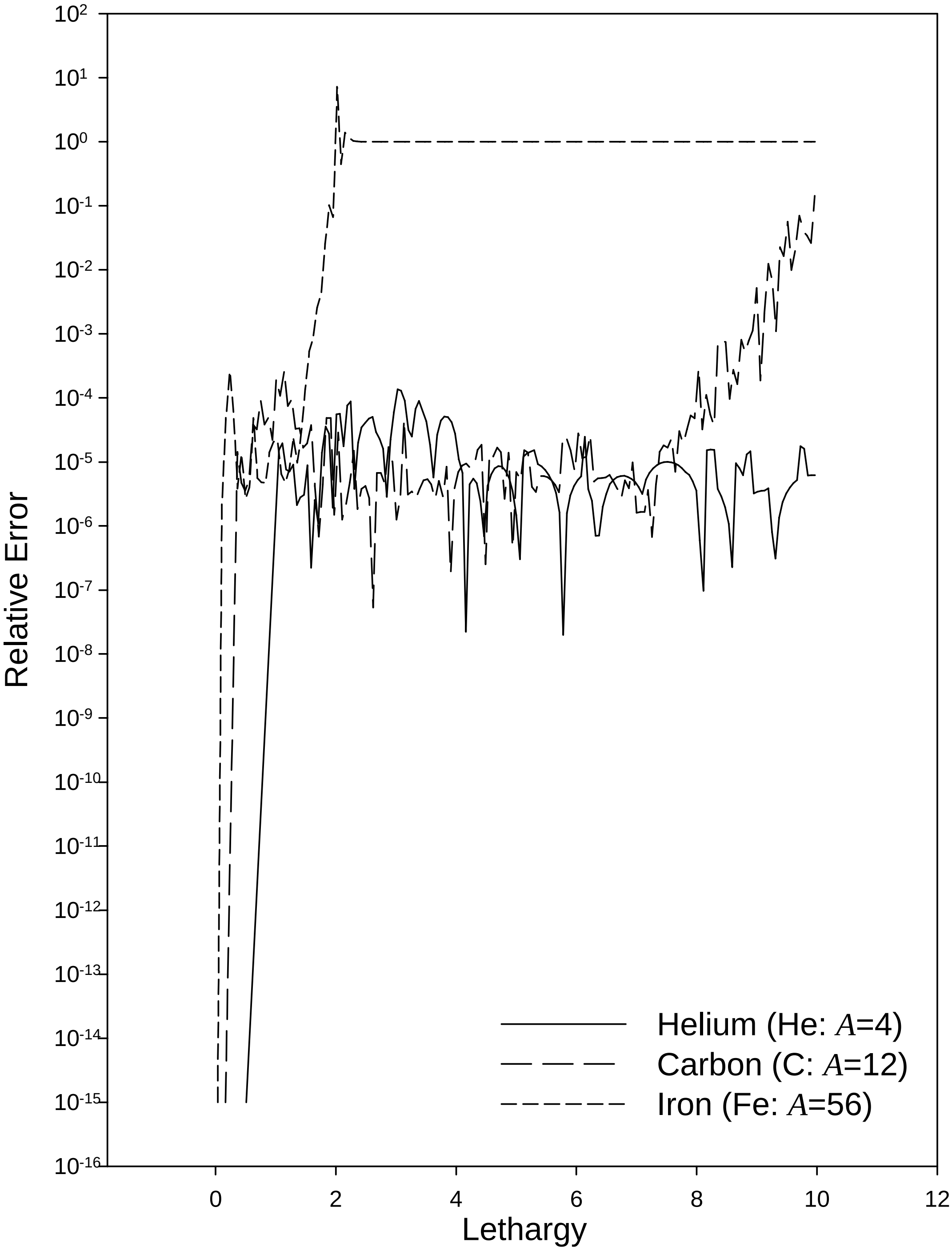

Figure 2.1.3(a). Stability of the inversion for iron at large lethargy

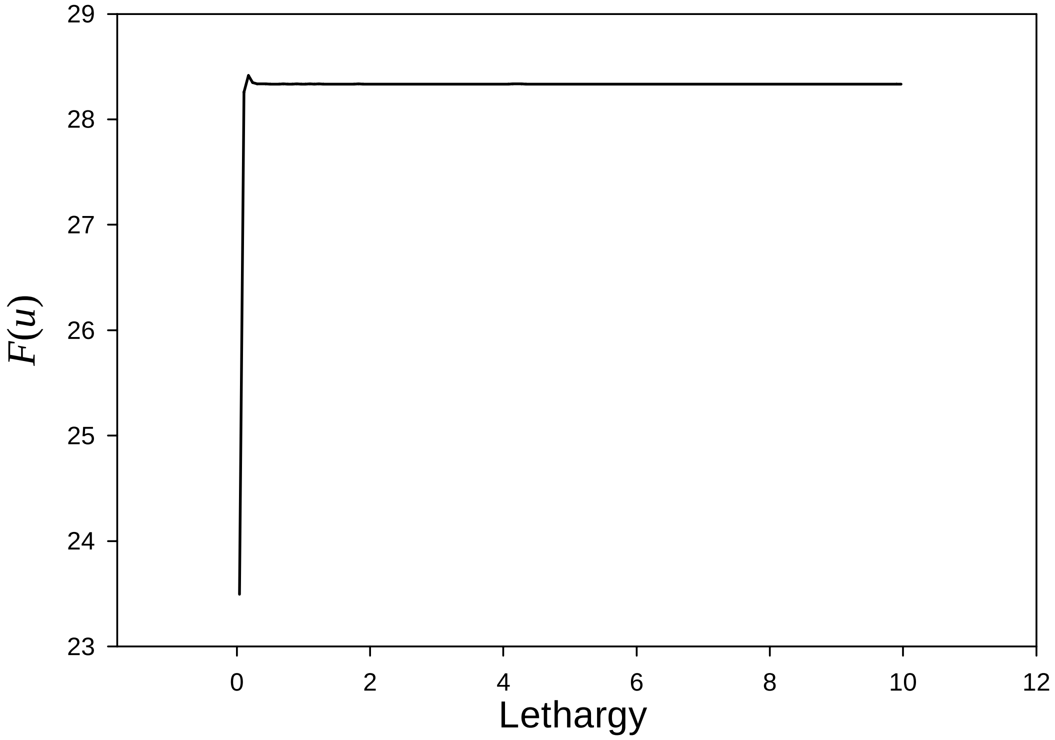

Figure 2.1.3(b). Placzek transient for iron

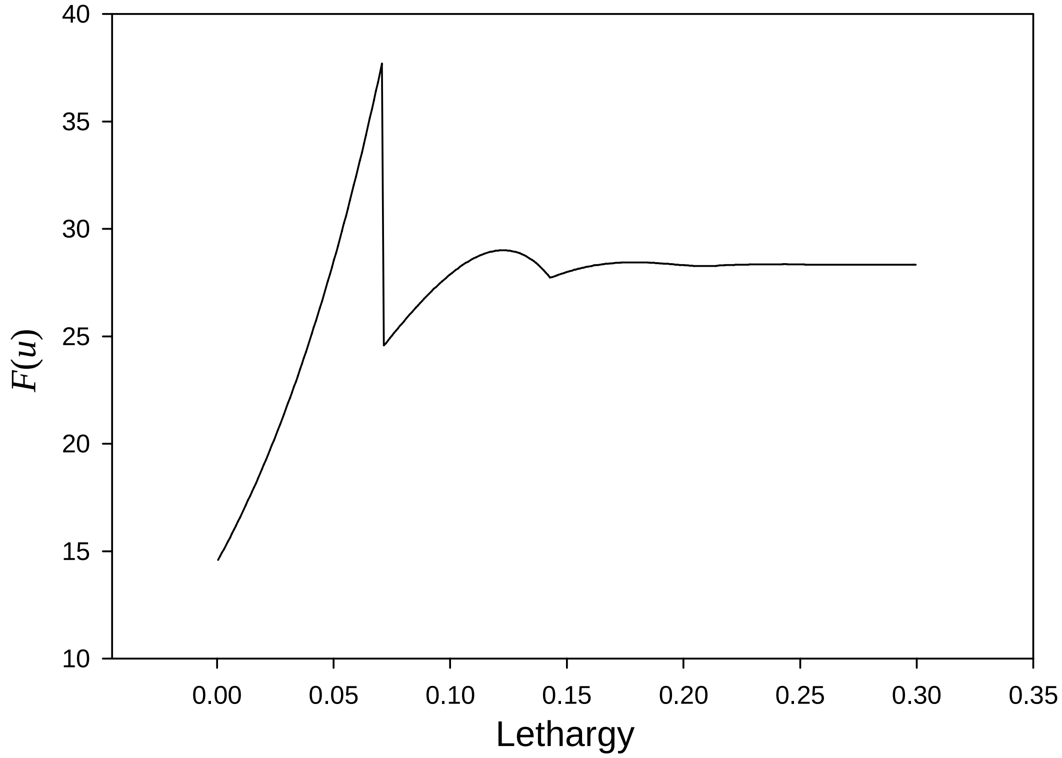

Figure 2.1.4. Slowing down in a mixture of C/He

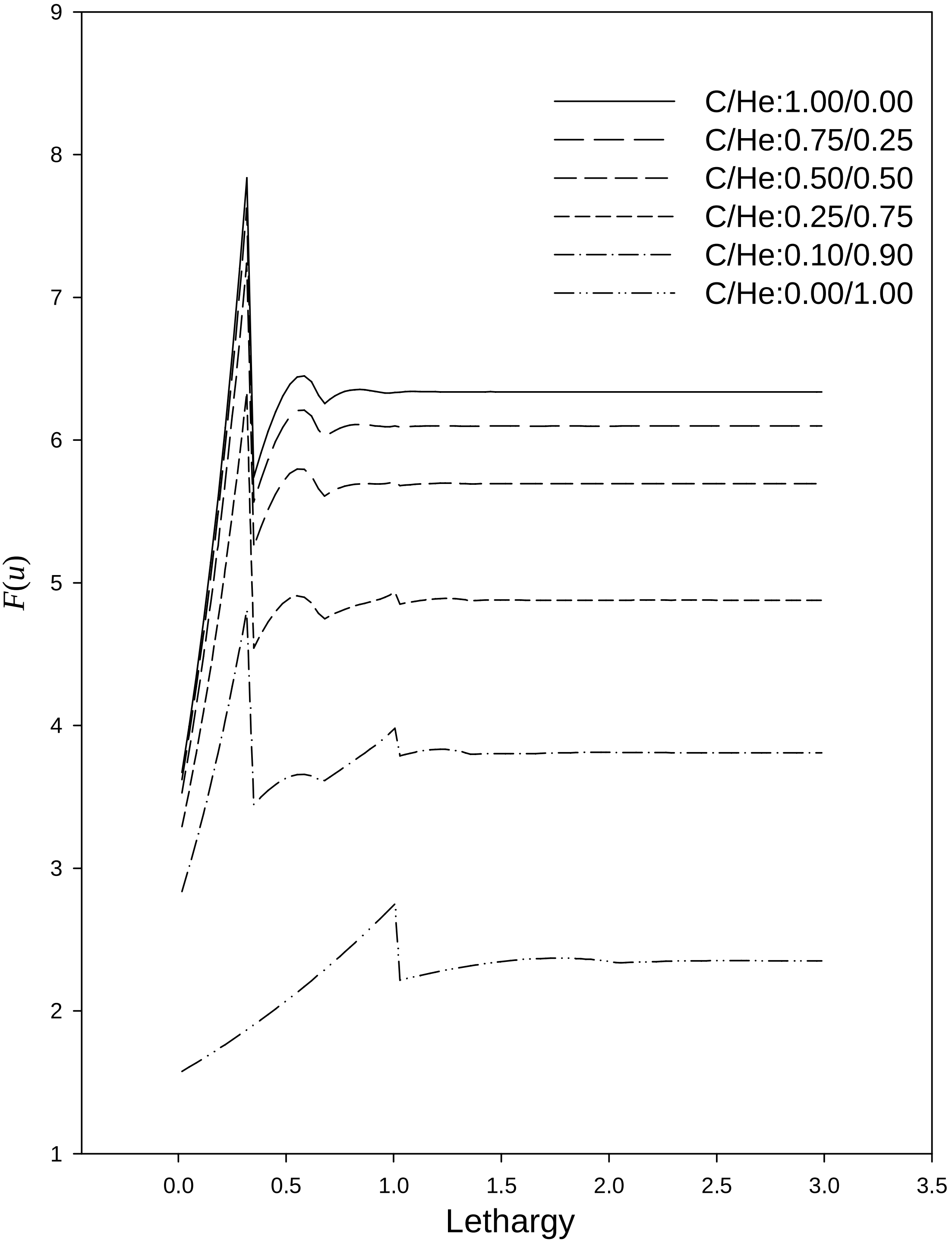

Figure 2.1.5. Slowing down in C for a constant source over an interval

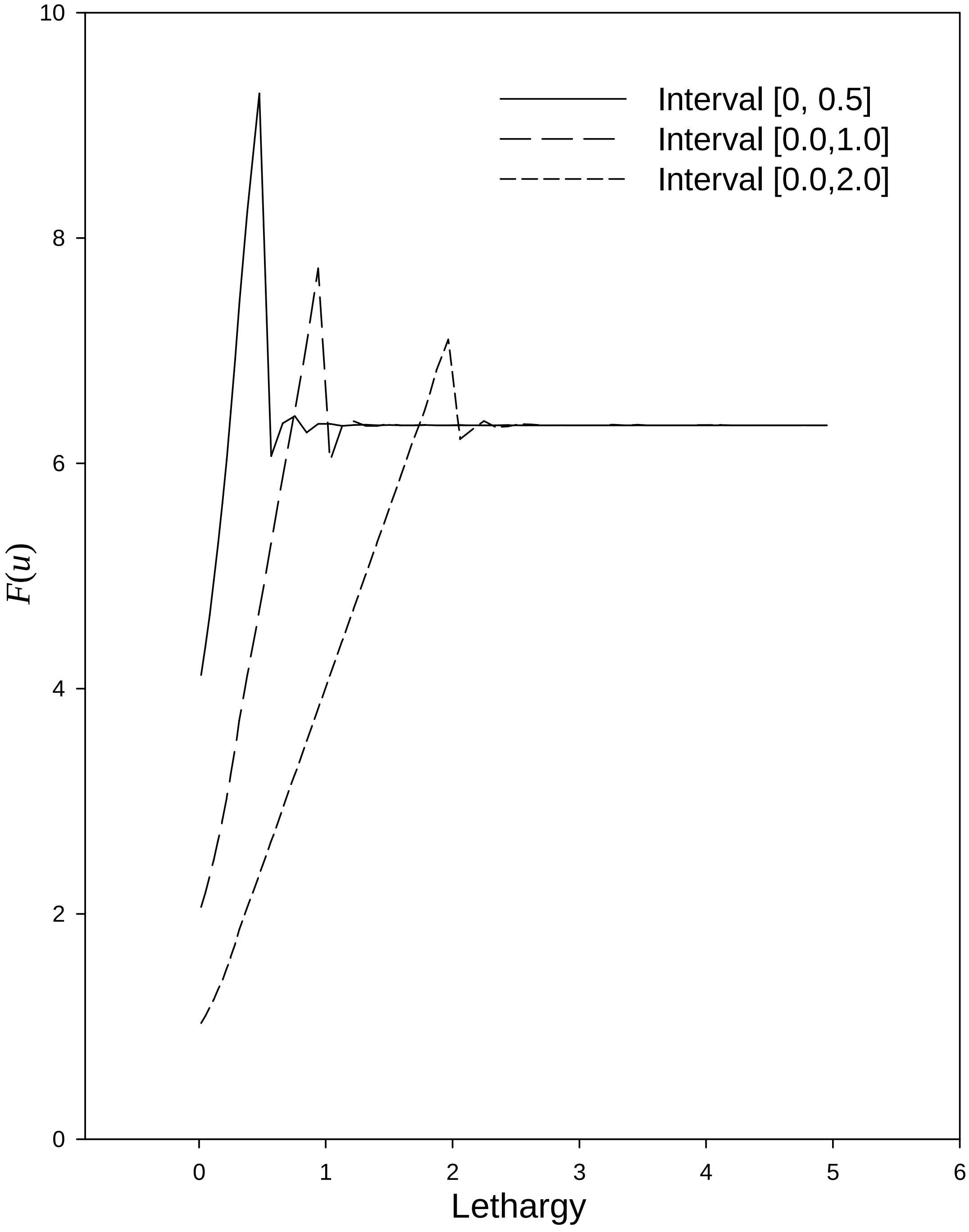

Figure 2.1.6. Comparison of pointwise and multigroup collision densities for slowing down in carbon

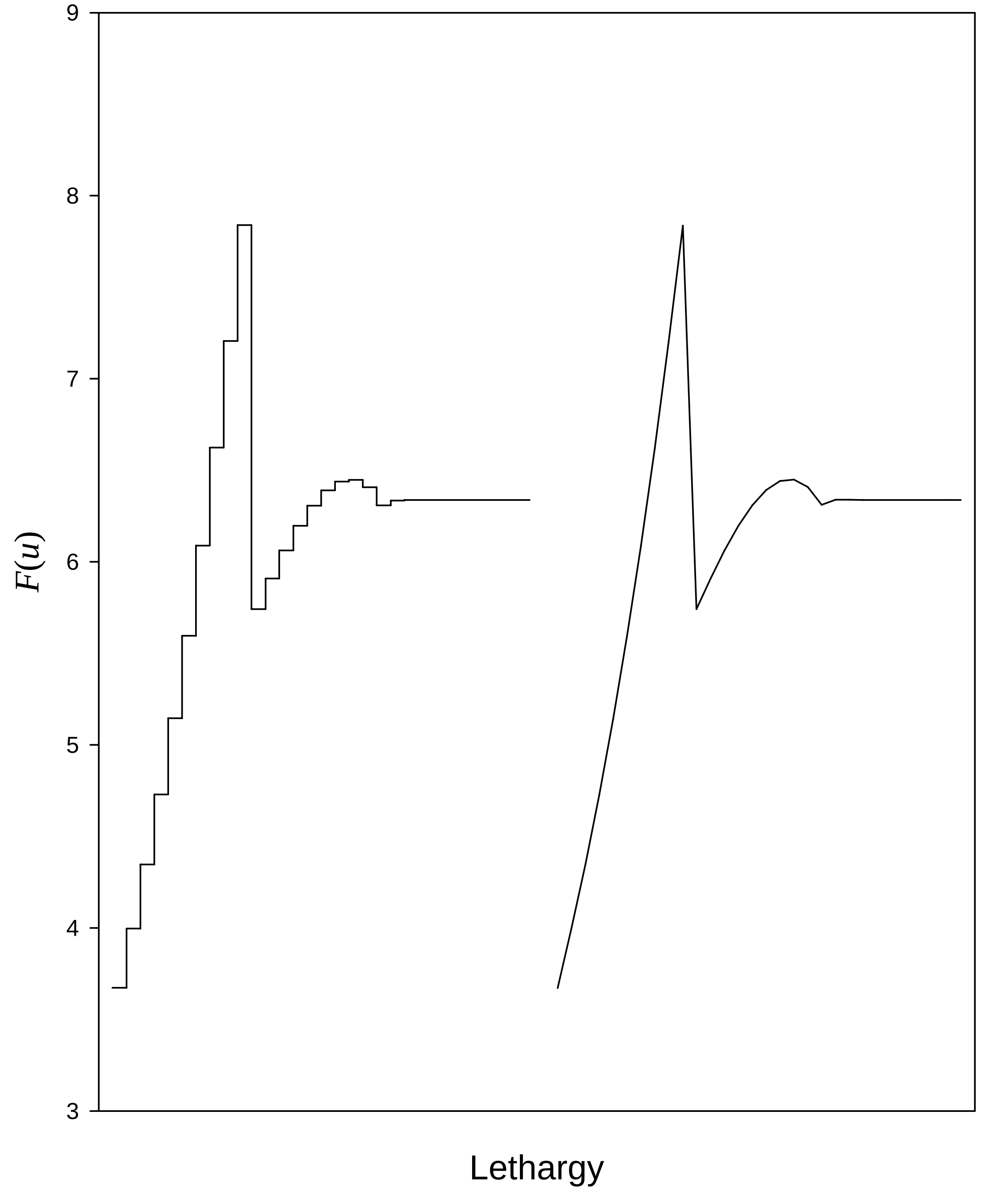

Figure 2.1.7. Hypothetical equal mix of elements *A* = 1(5)56

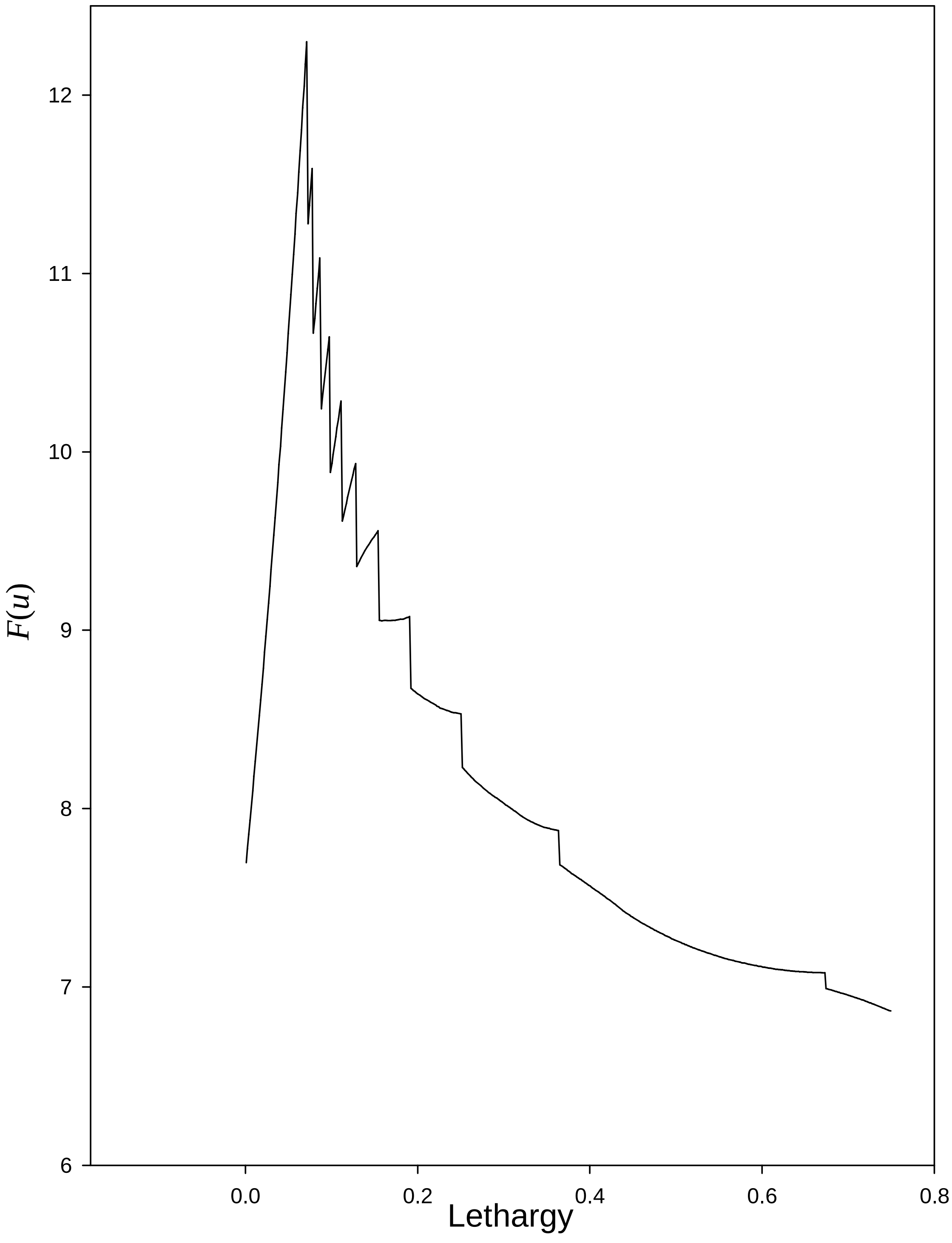

Benchmark 2.2: Slowing down/the Laplace transform solution in the B_L approximation

(a) Brief description

Stationary neutron slowing down in an infinite medium with non-zero buckling in the continuous lethargy B_L approximation with constant cross sections.

(b) Classification

NT/I/LE(3)/C/I/U/E(C)/NLTI

(c) Physical description

Neutrons slow down through elastic scattering with nuclei to thermal energies in an infinite medium. We obtain an analytical representation for the moments of the collision density of the slowing down equation in the B_L approximation with constant cross sections and multiple species scattering.

(d) Analytical representations

(i) The collision density as a function of lethargy

When treating the general slowing down case, now including neutron loss through volume leakage, the transport equation does not simplify as readily as it did for the preceding benchmark. By integrating the first term of Eq. (1.II) over an arbitrary volume with surface area A, the leakage rate out of the volume is:

$$\int_A dA\hat{\boldsymbol{n}}_s \bullet \boldsymbol{J}\left(r_s,\Omega,E\right) = \int_V d\boldsymbol{r}\Omega \bullet \nabla\phi\left(r,\Omega,E\right)$$

from the divergence theorem. Thus, if we assume that the flux is spatially separable in the form:

$$\phi\left(\boldsymbol{r},\Omega,E\right) \equiv \frac{1}{\left(2\pi\right)^3} e^{-i\boldsymbol{B}_L\bullet\left(\boldsymbol{r}-\boldsymbol{r}_0\right)}\Psi\left(\Omega,E\right) \tag{1a}$$

for $\boldsymbol{r}$, $\boldsymbol{r}_0 \in V$, the leakage out of the surface is:

$$\int_A dA\hat{\boldsymbol{n}}_s \bullet \boldsymbol{J}\left(r_s,\Omega,E\right) = -i\boldsymbol{B}_L \bullet \Omega\Psi\left(\Omega,E\right)\left[\frac{1}{\left(2\pi\right)^3}\int_V d\boldsymbol{r}e^{-i\boldsymbol{B}_L\bullet\left(\boldsymbol{r}-\boldsymbol{r}_0\right)}\right] \tag{2}$$

$\boldsymbol{r}_0$ is included to allow the last factor in Eq. (2) to make mathematical sense as a delta function in the infinite medium limit $V \to \infty$. The leakage integral given by Eq. (2) is a scalar whose magnitude is proportional to $B_L \equiv \left|\boldsymbol{B}_L\right|$. Thus, we retain a non-zero $\boldsymbol{B}_L$, called the "buckling", to simulate leakage from a finite medium but keep the simplicity of the infinite medium approximation [Eq. (1a)]. Each point in the medium now uniformly contributes to leakage out the surface.

When we introduce the separability condition of Eq. (1a) with corresponding source separability:

$$Q(\boldsymbol{r},\Omega,E) \equiv \frac{1}{(2\pi)^3} e^{-i\boldsymbol{B}_L \bullet (\boldsymbol{r}-\boldsymbol{r}_0)} S(\Omega,E) \tag{1b}$$

into Eq. (II) for *J* scattering species and assume spatially uniform nuclear properties, there results after volume integration:

$$\begin{aligned} &\left[\Sigma(E) - i\boldsymbol{B}_L \bullet \Omega\right]\Psi(\Omega,E) = \\ &= \sum_{j=1}^{J}\int_0^{\infty} dE' \int_{4\pi} d\Omega' f_{sj}\left(\mu_0, E' \to E\right)\Sigma_{sj}\left(E'\right)\Psi\left(\Omega',E'\right) + \\ &+ \frac{\chi(E)}{4\pi}\int_0^{\infty} dE' \int_{4\pi} d\Omega' \nu\left(E'\right)\Sigma_f\left(E'\right)\Psi\left(\Omega',E'\right) + S(\Omega,E) \end{aligned} \tag{3}$$

Note that *V* is still finite. For *V* infinite, the separability assumption is equivalent to the Fourier transform we consider in §3.1. Here, our concern is with slowing down only in the transform $\boldsymbol{B}_L$ space for a fixed value of B_L.

As in the previous benchmark, we reduce the number of variables in Eq. (3) by integrating over azimuthal direction ϕ in an arbitrary reference frame. Since $\mu_0 = \mu_0(\mu',\mu,\phi - \phi')$ and depends on the difference of the azimuths, upon integration over the azimuth, where $\boldsymbol{B}_L$ is oriented on the *z*-axis as shown in Figure 2.2.1, there results:

$$\begin{aligned} &\left[\Sigma(E) - iB_L\mu\right]\Psi(\mu,E) = \\ &= \sum_{j=1}^{J}\int_0^{\infty} dE' \int_{4\pi} d\Omega' f_{sj}\left(\mu', \mu, E' \to E\right)\Sigma_{sj}\left(E'\right)\Psi\left(\Omega',E'\right) + \\ &+ \frac{\chi(E)}{4\pi}\int_0^{\infty} dE' \int_{-1}^{1}\int_0^{2\pi} d\mu' d\phi' \nu\left(E'\right)\Sigma_f\left(E'\right)\Psi\left(\Omega',E'\right) + S(\mu,E) \end{aligned} \tag{4}$$

where the azimuthally integrated flux, source and scattering kernel are:

$$\begin{aligned} \Psi(\mu,E) &\equiv \frac{1}{2\pi}\int_0^{2\pi} d\phi \Psi(\Omega,E) \\ S(\mu,E) &\equiv \frac{1}{2\pi}\int_0^{2\pi} d\phi S(\Omega,E) \end{aligned} \tag{5}$$

$$f_{sj}\left(\mu',\mu,E' \to E\right) \equiv \int_0^{2\pi} d\phi' f_{sj}\left(\mu_0\left(\mu',\mu,\phi'\right), E' \to E\right)$$

When we introduce the azimuthally integrated flux and scattering kernel into the collision term of Eq. (4) and convert to lethargy by assuming and upper energy E_0, there results:

$$\begin{aligned}&\left[\Sigma(u)-iB_L\mu\right]\Psi(\mu,u)=\\&=\sum_{j=1}^{J}\int_0^{\infty}du'\int_{-1}^{1}d\mu' f_{sj}\left(\mu',\mu,u'\rightarrow u\right)\Sigma_{sj}\left(u'\right)\Psi\left(\mu',u'\right)+\\&+\frac{\chi(u)}{2}\int_0^{\infty}du'\int_{-1}^{1}d\mu'\nu\left(u'\right)\Sigma_f\left(u'\right)\Psi\left(\mu',u'\right)+S(\mu,u)\end{aligned} \tag{6}$$

Next, we expand the scattering kernel into:

$$f_{sj}\left(\mu_0,u'\rightarrow u\right)=\sum_{l=0}^{\infty}\frac{2l+1}{4\pi}f_{slj}\left(u'\rightarrow u\right)P_l\left(\mu_0\right) \tag{7a}$$

and after application of the addition theorem for Legendre polynomials as in §1.3.3, we have:

$$f_{sj}\left(\mu',\mu,u'\rightarrow u\right)=\sum_{l=0}^{\infty}\frac{2l+1}{2}f_{slj}\left(u'\rightarrow u\right)P_l\left(\mu'\right)P_l(\mu) \tag{7b}$$

By introducing this expansion into Eq. (6) along with the angular collision density:

$$F(\mu,u)\equiv\Sigma(u)\Psi(\mu,u) \tag{8a}$$

Eq. (6) becomes:

$$\begin{aligned}&\left[1-i\alpha_{B_L}(u)\mu\right]F(\mu,u)=\\&=\sum_{j=1}^{J}\sum_{l=0}^{\infty}\frac{2l+1}{2}P_l(\mu)\int_0^{\infty}du'c_{sj}\left(u'\right)f_{slj}\left(u'\rightarrow u\right)F_l\left(u'\right)+\\&+\frac{\chi(u)}{2}\int_0^{\infty}du'c_f\left(u'\right)F_0\left(u'\right)+S(\mu,u)\end{aligned} \tag{8b}$$

where the Legendre moments are:

$$F_l(u)\equiv\int_{-1}^{1}d\mu P_l(\mu)F(\mu,u) \tag{8c}$$

and:

$$\alpha_{B_L}(u)\equiv\frac{B_L}{\Sigma(u)} \tag{8d}$$

To continue analytically requires that we know the lethargy-to-lethargy scattering kernel since we will be interested in higher moments other than the zeroth; thus, we now assume elastic scattering.

The general elastic scattering kernel for the j^{th} species in lethargy and assuming isotropic scattering in the center of mass reference frame:

$$\begin{aligned} & f_{sj}\left(\mu_0, u' \to u\right) = \\ & = \frac{1}{2\pi} \frac{e^{-(u-u')}}{\left(1-\alpha_j\right)} \delta\left(\mu_0 - \mu_{sj}\left(u-u'\right)\right) \Theta\left(u-u'\right) \Theta\left(q_j - \left(u-u'\right)\right) \end{aligned} \tag{9a}$$

which is just the statement that for a neutron of lethargy u' scattering through an angle θ_0 with final lethargy u, μ_0 must be:

$$\mu_{sj}\left(u-u'\right) \equiv \left[\frac{A_j+1}{2}\right] e^{-(u-u')/2} - \left[\frac{A_j-1}{2}\right] e^{(u-u')/2} \tag{9b}$$

to conserve energy and momentum. Eq. (9a) corresponds to Eq. (I.29a) in the energy variable. When we formally express the delta function in Eq. (9a) in the Legendre series:

$$\delta\left(\mu_0 - \mu_{sj}\left(u-u'\right)\right) = \sum_{l=0}^{\infty} \frac{2l+1}{2} P_l\left(\mu_{sj}\left(u-u'\right)\right) P_l\left(\mu_0\right) \tag{9c}$$

the l^{th} scattering coefficient becomes:

$$f_{slj}\left(u' \to u\right) \equiv \frac{e^{-(u-u')}}{1-\alpha_j} P_l\left(\mu_{sj}\left(u-u'\right)\right) \Theta\left(u-u'\right) \Theta\left(q_j - \left(u-u'\right)\right) \tag{9d}$$

which, for $l = 0$, confirms Eq. (2.1.9a). With Eq. (9d) substituted into Eq. (8b), we have:

$$\begin{aligned} & \left[1 - i\alpha_{B_L}(u)\mu\right] F(\mu, u) = \\ & = \sum_{j=1}^{J} \frac{1}{1-\alpha_j} \sum_{l=0}^{\infty} \frac{2l+1}{2} P_l(\mu) \int_{u-q_j}^{u} du' e^{-(u-u')} c_{sj}(u') P_l\left(\mu_{sj}\left(u-u'\right)\right) F_l(u') + \\ & + \frac{\chi(u)}{2} \int_0^{\infty} du' c_f(u') F_0(u') + S(\mu, u) \end{aligned} \tag{10}$$

(ii) The solution for the Legendre moments via Laplace transform

Reformulating Eq. (10) in terms of moments by dividing by the coefficient on the LHS and projecting over the Legendre polynomials $P_m(\mu)$ gives:

$$\begin{aligned} F_m(u) = & \sum_{j=1}^{J} \frac{1}{1-\alpha_j} \sum_{l=0}^{\infty} \left(2l+1\right) T_{ml}\left(-\alpha_{B_L}(u)\right) \bullet \\ & \bullet \int_{u-q_j}^{u} du' e^{-(u-u')} c_{sj}(u') P_l\left(\mu_{sj}\left(u-u'\right)\right) F_l(u') + \\ & + T_{m0}\left(-\alpha_{B_L}(u)\right) \chi(u) \int_0^{\infty} du' c_f(u') F_0(u') + S_{m0}\left(-\alpha_{B_L}(u), u\right) \end{aligned} \tag{11a}$$

where:

$$T_{ml}\left(-z\right)\equiv\frac{1}{2}\int_{-1}^{1}d\mu\frac{P_m\left(\mu\right)P_l\left(\mu\right)}{1-iz\mu} \tag{11b}$$

$$S_{m0}\left(-z,u\right)\equiv\int_{-1}^{1}d\mu\frac{P_m\left(\mu\right)}{1-iz\mu}S\left(\mu,u\right)$$

Thus, unlike the previous benchmark (in which $B_L = 0$), we cannot isolate the $m = 0$ moment in a single equation and all moments now come into play.

With replacement $F_m(u) \to i^m F_m(u)$, a real valued set of equations results:

$$\begin{aligned}F_m\left(u\right)=\sum_{j=1}^{J}\frac{1}{1-\alpha_j}\sum_{l=0}^{\infty}\left(2l+1\right)A_{ml}\left(-\alpha_{B_L}\left(u\right)\right)\bullet\\ \bullet\int_{u-q_j}^{u}du'e^{-(u-u')}c_{sj}\left(u'\right)P_l\left(\mu_{sj}\left(u-u'\right)\right)F_l\left(u'\right)+\\ +A_{m0}\left(-\alpha_{B_L}\left(u\right)\right)\chi\left(u\right)\int_{0}^{\infty}du'c_f\left(u'\right)F_0\left(u'\right)+i^{-m}S_{m0}\left(-\alpha_{B_L}\left(u\right),u\right)\end{aligned} \tag{12a}$$

where:

$$A_{ml}\left(-z\right)\equiv i^{l-m}T_{ml}\left(-z\right) \tag{12b}$$

is a real function of z. Equations (12) are a coupled set of integral equations for the collision density moments. To proceed toward an analytical solution, we now assume constant nuclear properties and an isotropic source. A Laplace transform in lethargy then takes the integral equations into the following infinite set of algebraic equations for m = 0,1,… :

$$\sum_{l=0}^{\infty}\left[\delta_{lm}-\left(2l+1\right)\bar{Q}_{sl}\left(p\right)A_{ml}\left(-\alpha_{B_L}\right)\right]\bar{F}_l\left(p\right)=\bar{H}\left(p\right)A_{m0}\left(-\alpha_{B_L}\right) \tag{13a}$$

where:

$$\bar{H}\left(p\right)\equiv c_f\bar{\chi}\left(p\right)\bar{F}_0\left(0\right)+\bar{S}\left(p\right) \tag{13b}$$

and:

$$\bar{Q}_{sl}\left(p\right)=\sum_{j=1}^{J}\frac{c_{sj}}{1-\alpha_j}\int_{0}^{q_j}due^{-(p+1)u}P_l\left(\mu_{sj}\left(u\right)\right) \tag{13c}$$

which, after some algebra (see Appendix C), becomes:

$$\begin{aligned}\bar{Q}_{sl}\left(p\right)=\sum_{j=1}^{J}\frac{c_{sj}}{1-\alpha_j}\frac{1}{2^l}\sum_{m=0}^{[l/2]}\left(-1\right)^m\begin{pmatrix}l\\m\end{pmatrix}\begin{pmatrix}2l-2m\\l\end{pmatrix}\bullet\\ \bullet\sum_{k=0}^{l-2m}\left(-1\right)^k\begin{pmatrix}l-2m\\k\end{pmatrix}\frac{\alpha_{j+}^{l-2m-k}\alpha_{j-}^{k}}{\beta_{klm}}\left[1-\alpha_j^{\beta_{klm}}\right]\end{aligned} \tag{13d}$$

with binomial coefficients:

$$\binom{r}{s} \equiv \frac{r!}{s!(r-s)!}$$

and:

$$\alpha_{j+} \equiv \frac{A_j+1}{2}, \quad \alpha_{j-} \equiv \frac{A_j-1}{2}$$

$$\beta_{klm} \equiv p+1-\left[k-\frac{l-2m}{2}\right]$$

Note that [n/2] is the greatest integer contained in n/2. Equation (13a), written in the more compact vector form, is:

$$\boldsymbol{A}(p)\bar{\boldsymbol{F}}(p)=\bar{H}(p)\boldsymbol{B} \tag{14}$$

with the elements of $\boldsymbol{A}(p)$, $\bar{\boldsymbol{F}}$ (p) and $\boldsymbol{B}$ for m, l = 0,1,…

$$a_{ml} \equiv \delta_{ml}-(2l+1)\bar{Q}_{sl}(p)A_{ml}\left(-\alpha_{B_L}\right)$$

$$\bar{F}_l(p)$$

$$b_m \equiv A_{m0}\left(-\alpha_{B_L}\right)$$

Obviously, an infinite system is not numerically viable, thus we truncate the scattering order to L with l, m = 0,1,…,L – hence, the origin of the name B_L approximation.

$\bar{F}_0$ (0) is required *a priori* to specify $\bar{H}$ (p). By setting p to zero in Eq. (14), we find:

$$\boldsymbol{A}\bar{\boldsymbol{F}}(0)=S_0\boldsymbol{B} \tag{15}$$

where $S_0 \equiv \int_0^\infty du\,S(u)$ and the elements of $\boldsymbol{A}$ are:

$$\bar{a}_{ml} \equiv \delta_{ml}-(2l+1)\left[\bar{Q}_{sl}(0)+c_f\delta_{0l}\right]A_{ml}\left(-\alpha_{B_L}\right), \quad m,l=0,1,\dots,L$$

giving the formal solution of Eq. (15) as:

$$\bar{\boldsymbol{F}}(0)=S_0\boldsymbol{A}^{-1}\boldsymbol{B}$$

$\bar{F}_0$ (0) is the first component of $\bar{F}$ (0), thus completely determining $\bar{H}$ (p) from Eq. (13b).

From matrix inversion, the transformed solution of Eqs. (14) is:

$$\bar{\boldsymbol{F}}(p)=\bar{H}(p)\boldsymbol{A}(p)^{-1}\boldsymbol{B}$$

and from Laplace transform inversion, the moment vector $\boldsymbol{F}(u)$ is:

$$\boldsymbol{F}(u) = \mathrm{L}_u^{-1}\left[\bar{H}(p)\boldsymbol{A}(p)^{-1}\right]\boldsymbol{B}$$

By determining an analytical expression for the uncollided contribution (set $\bar{Q}_{sl}(p) \equiv 0$), a more numerically convenient form is:

$$\boldsymbol{F}(u) = \boldsymbol{F}_0(u) + \mathrm{L}_u^{-1}\left\{\bar{H}(p)\left[\boldsymbol{A}(p)^{-1} - \boldsymbol{I}\right]\right\}\boldsymbol{B} \tag{16a}$$

with:

$$\boldsymbol{F}_0(u) = \left[S(u) + c_f \bar{F}_0(0)\delta(u)\right]\boldsymbol{B} \tag{16b}$$

and the assumption:

$$\chi(u) \equiv \delta(u) \tag{16c}$$

For a delta function source $S(u) = S_0\delta(u)$, the first collided contribution, for $m = 0,1,\ldots,L$, is:

$$\begin{aligned} F_{1m}(u) &= \\ &= e^{-u}\sum_{j=1}^{J}\frac{c_{sj}}{1-\alpha_j}\Theta\left(q_j - u\right)\sum_{l=0}^{L}(2l+1)A_{ml}\left(-\alpha_{B_L}\right)A_{l0}\left(-\alpha_{B_L}\right)P_l\left(\mu_{sj}(u)\right) \end{aligned}$$

and Eq. (16a) becomes:

$$\boldsymbol{F}(u) = \boldsymbol{F}_0(u) + \boldsymbol{F}_1(u) + \mathrm{L}_u^{-1}\left[\boldsymbol{A}(p)^{-1} - \boldsymbol{I} - \bar{H}_0\boldsymbol{G}(p)\right]\boldsymbol{B} \tag{17a}$$

with:

$$\bar{H}_0 \equiv c_f \bar{F}_0(0) + S_0 \tag{17b}$$

and the elements of $\boldsymbol{G}(p)$ are:

$$g_{ml} \equiv (2l+1)A_{ml}\left(-\alpha_{B_L}\right)\bar{Q}_{sl}(p), \quad m,l = 0,1,\ldots,L$$

(iii) The exact multigroup collision density

For the m^{th} moment, Eqs. (2.1.22b) and (2.1.23) of Benchmark 2.1 also apply here. For a delta function source, where we know the uncollided and first collided contributions explicitly, we have:

$$\boldsymbol{F}_g(u) = \boldsymbol{F}_{0g}(u) + \boldsymbol{F}_{1g}(u) + \frac{1}{\Delta u_g}\left\{\mathrm{L}_{u_g}^{-1}\left[\hat{f}(p)\right] - \mathrm{L}_{u_{g-1}}^{-1}\left[\hat{f}(p)\right]\right\}\boldsymbol{B} \tag{18}$$

with:

$$\hat{f}(p) \equiv \frac{\bar{H}(p)}{p}\left[\boldsymbol{A}(p)^{-1} - \boldsymbol{I} - \boldsymbol{G}(p)\right]$$

For $m = 0,1,\ldots,L$, the elements of $\boldsymbol{F}_{0g}(u)$ and $\boldsymbol{F}_{1g}(u)$ are:

$$F_{0gm} = \frac{1}{\Delta u_g}\left[S_0 + c_f \bar{F}_0(0)\right] A_{m0}\left(-\alpha_{B_L}\right)\delta_{g1}$$

and:

$$F_{1gm} = \frac{1}{\Delta u_g}\sum_{j=1}^{J}\frac{c_{sj}}{1-\alpha_j}\sum_{l=0}^{L}(2l+1)A_{ml}\left(-\alpha_{B_L}\right)A_{0l}\left(-\alpha_{B_L}\right)\bullet$$
$$\bullet\left\{\begin{array}{l}\left[\Theta\left(u_g - q_j\right) - \Theta\left(u_{g-1} - q_j\right)\right]W_{lj}\left(0,q_j\right) + \\ +\Theta\left(q_j - u_g\right)W_{lj}\left(0,u_g\right) - \Theta\left(q_j - u_{g-1}\right)W_{lj}\left(0,u_{g-1}\right)\end{array}\right\}$$

with:

$$W_{lj}(0,u) \equiv \int_0^u du' e^{-u'} P_l\left(\mu_{sj}(u')\right)$$

and δ_{g1} is the Kronecker delta (1 for $g = 1$ and 0 otherwise).

For a general source, $S(u)$, the corresponding uncollided contribution is:

$$\boldsymbol{F}_{0g}(u) = \frac{1}{\Delta u_g}\left\{\begin{array}{l}\int_{u_{g-1}}^{u_g} du S(u)\boldsymbol{I} + c_f \boldsymbol{F}(0)\delta(u) + \\ +\left\{\mathrm{L}_{u_g}^{-1}\left[\hat{g}(p)\right] - \mathrm{L}_{u_{g-1}}^{-1}\left[\hat{g}(p)\right]\right\}\end{array}\right\}\boldsymbol{B} \tag{19}$$

with:

$$\hat{g}(p) \equiv \frac{\bar{H}(p)}{p}\left[\boldsymbol{A}(p)^{-1} - \boldsymbol{I}\right]$$

Here, we have removed only the uncollided contribution.

(e) Numerical implementation and demonstration for Benchmark 2.2

(i) Recurrence relation and matrix inversion

A_{ml}, (or T_{ml}) required for the matrix $\boldsymbol{A}$, is most straightforwardly determined from the Legendre polynomial recurrence formula [2] as the following recurrence for $l \geq 1$:

$$T_{ml}\left(z\right)=\frac{1}{m}\left[\frac{\left(2m-1\right)}{iz}T_{m-1,l}-\left(m-1\right)T_{m-2,l}\left(z\right)\right]-\frac{\delta_{m,l-1}}{izl} \tag{20a}$$

initiated by:

$$T_{-1l}\left(z\right)=0,\;\; T_{0l}\left(z\right)=\frac{\left(-1\right)^{l-1}}{iz}Q_l\left(\frac{1}{z}\right) \tag{20b}$$

where Q_l is the Legendre function of the second kind of order l also given recursively [2]:

$$Q_l\left(\frac{1}{z}\right)=\frac{1}{l}\left[\frac{\left(2l+1\right)}{z}Q_{l-1}\left(\frac{1}{z}\right)-\left(l-1\right)Q_{l-2}\left(\frac{1}{z}\right)\right],\;\; l\geq 1 \tag{20c}$$

and initiated by:

$$Q_{-1}\left(\frac{1}{z}\right)=0,\;\; Q_0\left(\frac{1}{z}\right)=\frac{tan^{-1}\left(1/z\right)}{z} \tag{20d}$$

An analytical representation for $T_{ml}(z)$ also exists which we do not use here.

The same numerical inversion procedure applies to Eqs. (16), (17), (18) and (19) as in Benchmark 2.1; however, the computational time increases because of the additional matrix inversion for the moments at each integration abscissa. Since we consider only $L \leq 3$, the most efficient method of inverting the set of equations represented in Eq. (16a) leading to the inverse $\boldsymbol{A}^{-1}$ is to use Cramer's rule implemented through symbolic algebra. Using the REDUCE [1] computer algebra language, we have generated a subroutine to calculate up to a 4 by 4 determinant. We then find the transform for each moment from the division of two determinants (Cramer's rule) and subtract the uncollided and first collided contributions as appropriate to obtain the image function we are to invert.

(ii) The first collision interval

To avoid numerical difficulties because of poor convergence properties of the Laplace transform inversion in the first collision interval:

$$0\leq u\leq \min_j\left(q_j\right)$$

we obtain the following analytical representation of the m^{th} moment in the form of the Taylor series around $u = 0$ for a delta function source:

$$F_m\left(u\right)=\overline{S}\left[A_{0m}\left(-\alpha_{B_L}\right)\delta\left(u\right)+e^{-u}\sum_{n=0}^{\infty}\frac{u^n}{n!}\psi_m^{(n)}\left(0\right)\right] \tag{21a}$$

where:

$$\overline{S}\equiv S_0+c_f\overline{F}\left(0\right) \tag{21b}$$

We find the derivatives, $\psi_m^{(n)}(0)$, starting with the following substitution into Eq. (11a):

$$F_m(u) = \bar{S}\left[A_{0m}\left(-\alpha_{B_L}\right)\delta(u) + e^{-u}\psi_k(u)\right]$$

to give in the first collision interval:

$$\psi_m(u) = \sum_{j=1}^{J}\frac{c_{sj}}{1-\alpha_j}\sum_{l=0}^{L}(2l+1)A_{ml}\left(-\alpha_{B_L}\right)\begin{bmatrix}\int_0^u du' P_l\left(\mu_{sj}(u-u')\right)\psi_l(u') + \\ +A_{l0}\left(-\alpha_{B_L}\right)P_l\left(\mu_{sj}(u)\right)\end{bmatrix} \tag{22a}$$

The n^{th} derivative at u = 0 then follows recursively from:

$$\psi_m^{(n)}(0) = \sum_{j=1}^{J}\frac{c_{sj}}{1-\alpha_j}\sum_{l=0}^{L}(2l+1)A_{ml}\left(-\alpha_{B_L}\right)\begin{bmatrix}\sum_{r=0}^{n-1}P_l^{(n-1-r)}\left(\mu_{sj}(0)\right)\psi_l^{(r)}(0) + \\ +A_{0l}\left(-\alpha_{B_L}\right)P_l^{(n)}\left(\mu_{sj}(0)\right)\end{bmatrix} \tag{22b}$$

with corresponding m^{th} multigroup moment density:

$$F_{mg}(u) = \frac{1}{\Delta u_g}\left[1 + \frac{c_{sf}}{1-c}\right]\begin{bmatrix}A_{m0}\left(-\alpha_{B_L}\right)\delta_{g1} + \\ +\sum_{n=0}^{\infty}\Gamma_{ng}(u)\psi_m^{(n)}(0)\end{bmatrix} \tag{23a}$$

where:

$$\Gamma_{ng}(u) \equiv \frac{1}{n!}\left[\int_0^{u_g} due^{-u}u^n - \int_0^{u_{g-1}} due^{-u}u^n\right] \tag{23b}$$

We truncate the series in Eqs. (21a) and (23a) when the relative truncation error estimate falls below a specified value.

(iii) Demonstration for Benchmark 2.2

Figure 2.2.2 provides an example of the B_L approximation for slowing down in carbon with L = 3. The buckling is B_L = 0.1 and the total cross section is 0.3814 (and $c \cong 1$, $\Sigma_a = 0.0034\ cm^{-1}$). As observed, each component inherits the Placzek transient; and in addition, because of simulated neutron leakage from the infinite medium, the density decreases as lethargy increases. Figure 2.2.3 shows a comparison of the pointwise and multigroup moments for a 70%/30% carbon/iron mixture by volume fraction, with B_L = 0.1. Again, as for Benchmark 2.1, we find excellent agreement.

Finally, we include Table 2.2.1 containing values of the first four moments for a more in-depth benchmark comparison to qualify Benchmark 2.2. We expect the last column to be accurate to all digits quoted.

Table 2.2.1. Qualification of Benchmark 2.2

Collision density moments m = 0,1,2,3 for 70%/30% C/Fe

$u\backslash\varepsilon$	10^{-3}	10^{-4}	10^{-5}	10^{-6}	10^{-7}
l = 0					
3.57181E-02	1.02543E+01	1.02543E+01	1.02543E+01	1.02543E+01	1.02543E+01
1.07154E-01	7.03271E+00	7.03064E+00	7.02990E+00	7.02985E+00	7.02983E+00
2.35729E-01	6.45487E+00	6.45430E+00	6.45461E+00	6.45465E+00	6.45463E+00
4.21441E-01	5.46187E+00	5.46454E+00	5.46847E+00	5.46994E+00	5.46965E+00
6.07154E-01	4.51126E+00	4.51119E+00	4.50966E+00	4.51003E+00	4.50998E+00
7.92867E-01	3.55271E+00	3.55401E+00	3.55336E+00	3.55361E+00	3.55356E+00
9.78580E-01	2.85019E+00	2.84842E+00	2.84865E+00	2.84861E+00	2.84862E+00
1.16429E+00	2.27173E+00	2.27406E+00	2.27404E+00	2.27404E+00	2.27404E+00
1.35001E+00	1.81699E+00	1.81629E+00	1.81635E+00	1.81633E+00	1.81633E+00
1.53572E+00	1.45037E+00	1.45095E+00	1.45088E+00	1.45088E+00	1.45088E+00
1.72143E+00	1.15884E+00	1.15887E+00	1.15887E+00	1.15887E+00	1.15887E+00
1.90714E+00	9.25660E-01	9.25632E-01	9.25650E-01	9.25652E-01	9.25652E-01
l = 1					
3.57181E-02	7.52707E-01	7.52707E-01	7.52707E-01	7.52707E-01	7.52704E-01
1.07154E-01	4.49530E-01	4.49477E-01	4.49446E-01	4.49447E-01	4.49447E-01
2.35729E-01	3.56287E-01	3.56459E-01	3.56458E-01	3.56459E-01	3.56458E-01
4.21441E-01	2.93841E-01	2.93794E-01	2.94454E-01	2.94354E-01	2.94323E-01
6.07154E-01	2.44251E-01	2.44217E-01	2.44175E-01	2.44176E-01	2.44172E-01
7.92867E-01	1.91833E-01	1.91821E-01	1.91811E-01	1.91817E-01	1.91818E-01
9.78580E-01	1.53441E-01	1.53514E-01	1.53500E-01	1.53501E-01	1.53501E-01
1.16429E+00	1.22575E-01	1.22621E-01	1.22617E-01	1.22617E-01	1.22617E-01
1.35001E+00	9.78814E-02	9.79254E-02	9.79275E-02	9.79275E-02	9.79275E-02
1.53572E+00	7.82345E-02	7.82241E-02	7.82209E-02	7.82207E-02	7.82207E-02
1.72143E+00	6.24801E-02	6.24822E-02	6.24788E-02	6.24789E-02	6.24789E-02
1.90714E+00	4.99073E-02	4.99037E-02	4.99054E-02	4.99052E-02	4.99052E-02
l = 2					
3.57181E-02	4.11505E-02	4.11501E-02	4.11501E-02	4.11501E-02	4.11501E-02
1.07154E-01	2.84011E-02	2.83838E-02	2.83807E-02	2.83811E-02	2.83811E-02
2.35729E-01	2.01714E-02	2.01629E-02	2.01623E-02	2.01629E-02	2.01628E-02
4.21441E-01	1.94463E-02	1.92971E-02	1.93312E-02	1.93412E-02	1.93373E-02
6.07154E-01	1.59452E-02	1.59291E-02	1.59346E-02	1.59347E-02	1.59344E-02
7.92867E-01	1.24647E-02	1.24634E-02	1.24676E-02	1.24672E-02	1.24671E-02
9.78580E-01	1.00148E-02	1.00159E-02	1.00148E-02	1.00150E-02	1.00150E-02
1.16429E+00	7.99008E-03	7.98972E-03	7.98967E-03	7.98976E-03	7.98974E-03
1.35001E+00	6.38122E-03	6.38239E-03	6.38250E-03	6.38254E-03	6.38255E-03
1.53572E+00	5.09624E-03	5.09773E-03	5.09815E-03	5.09813E-03	5.09813E-03
1.72143E+00	4.07226E-03	4.07211E-03	4.07208E-03	4.07208E-03	4.07208E-03
1.90714E+00	3.25277E-03	3.25270E-03	3.25263E-03	3.25260E-03	3.25260E-03
l = 3					
3.57181E-02	2.81199E-03	2.81199E-03	2.81200E-03	2.81200E-03	2.81200E-03
1.07154E-01	1.80357E-03	1.80321E-03	1.80320E-03	1.80322E-03	1.80322E-03
2.35729E-01	1.58589E-03	1.58695E-03	1.58672E-03	1.58672E-03	1.58672E-03
4.21441E-01	1.34239E-03	1.33166E-03	1.33459E-03	1.33490E-03	1.33507E-03
6.07154E-01	1.11564E-03	1.11490E-03	1.11444E-03	1.11437E-03	1.11439E-03
7.92867E-01	8.71472E-04	8.71031E-04	8.71204E-04	8.71162E-04	8.71170E-04
9.78580E-01	6.99094E-04	6.99371E-04	6.99252E-04	6.99239E-04	6.99236E-04
1.16429E+00	5.57722E-04	5.58167E-04	5.58174E-04	5.58166E-04	5.58168E-04
1.35001E+00	4.45837E-04	4.45820E-04	4.45815E-04	4.45820E-04	4.45821E-04
1.53572E+00	3.56225E-04	3.56126E-04	3.56113E-04	3.56116E-04	3.56115E-04
1.72143E+00	2.84468E-04	2.84434E-04	2.84444E-04	2.84443E-04	2.84443E-04
1.90714E+00	2.27202E-04	2.27208E-04	2.27200E-04	2.27200E-04	2.27200E-04

REFERENCES

[1] MacCallum, M.A.H., F.J. Wright, *Algebraic Computing with* ***REDUCE***, in Lecture Notes from the First Brazilian School on Computer Algebra, M.J. Reboucas (Ed.), Oxford Univ. Press, Oxford, UK (1991).

[2] Abramowitz, M.A. and I. Stegun, *Handbook of Mathematical Functions*, Dover, NY (1972).

Figure 2.2.1. Collision vector orientation

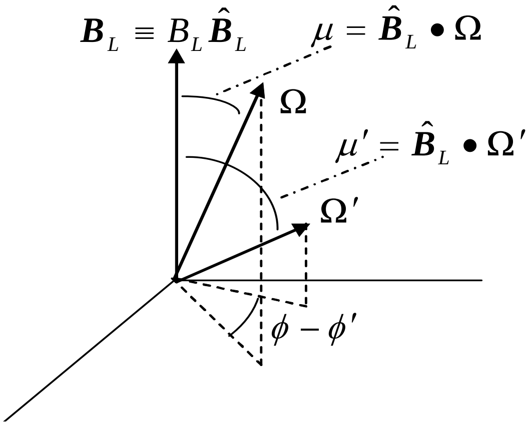

Figure 2.2.2. Collision density and moments for slowing down in carbon

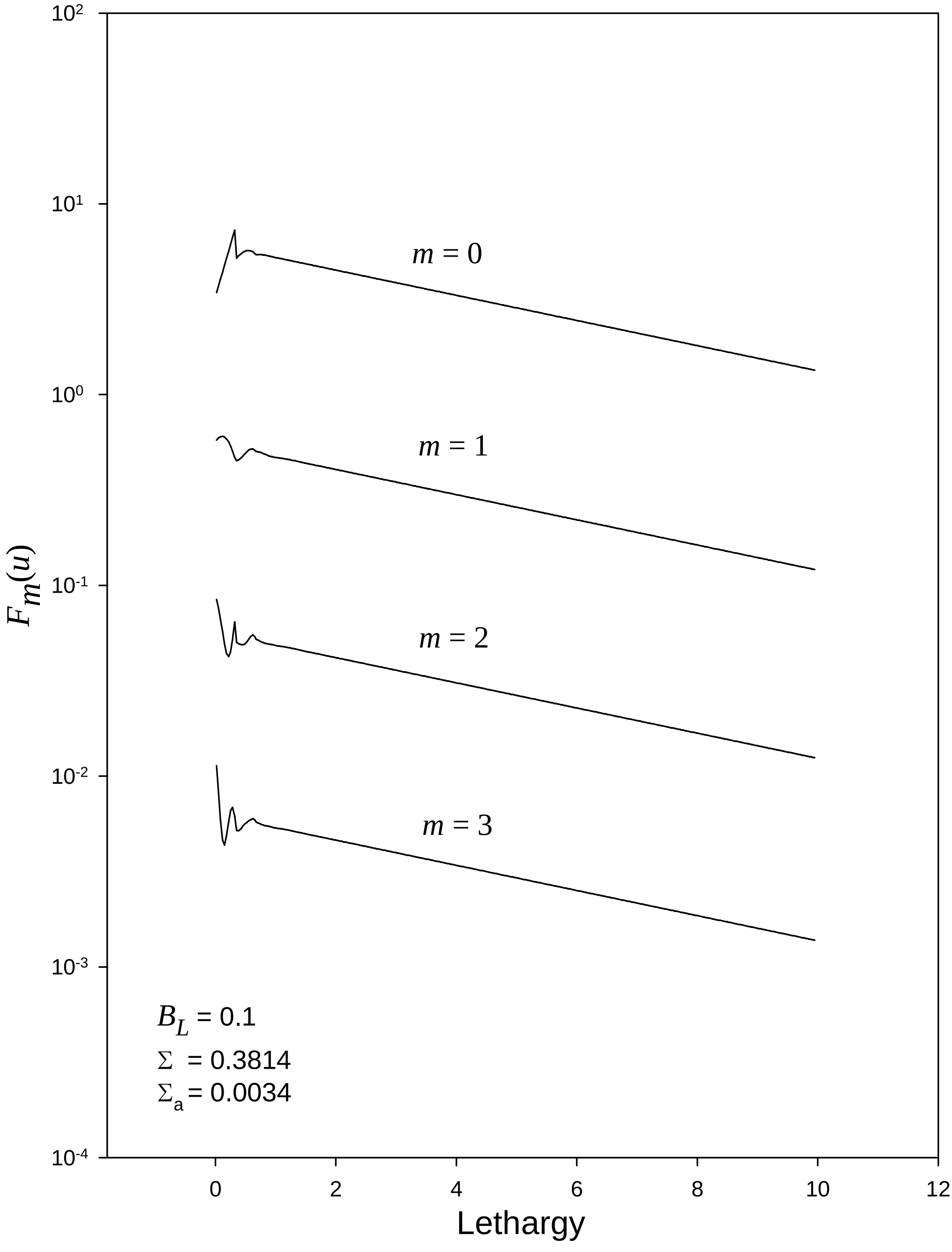

Figure 2.2.3. Comparison of pointwise and multigroup collision densities and moments for 70%/30% carbon/iron mixture

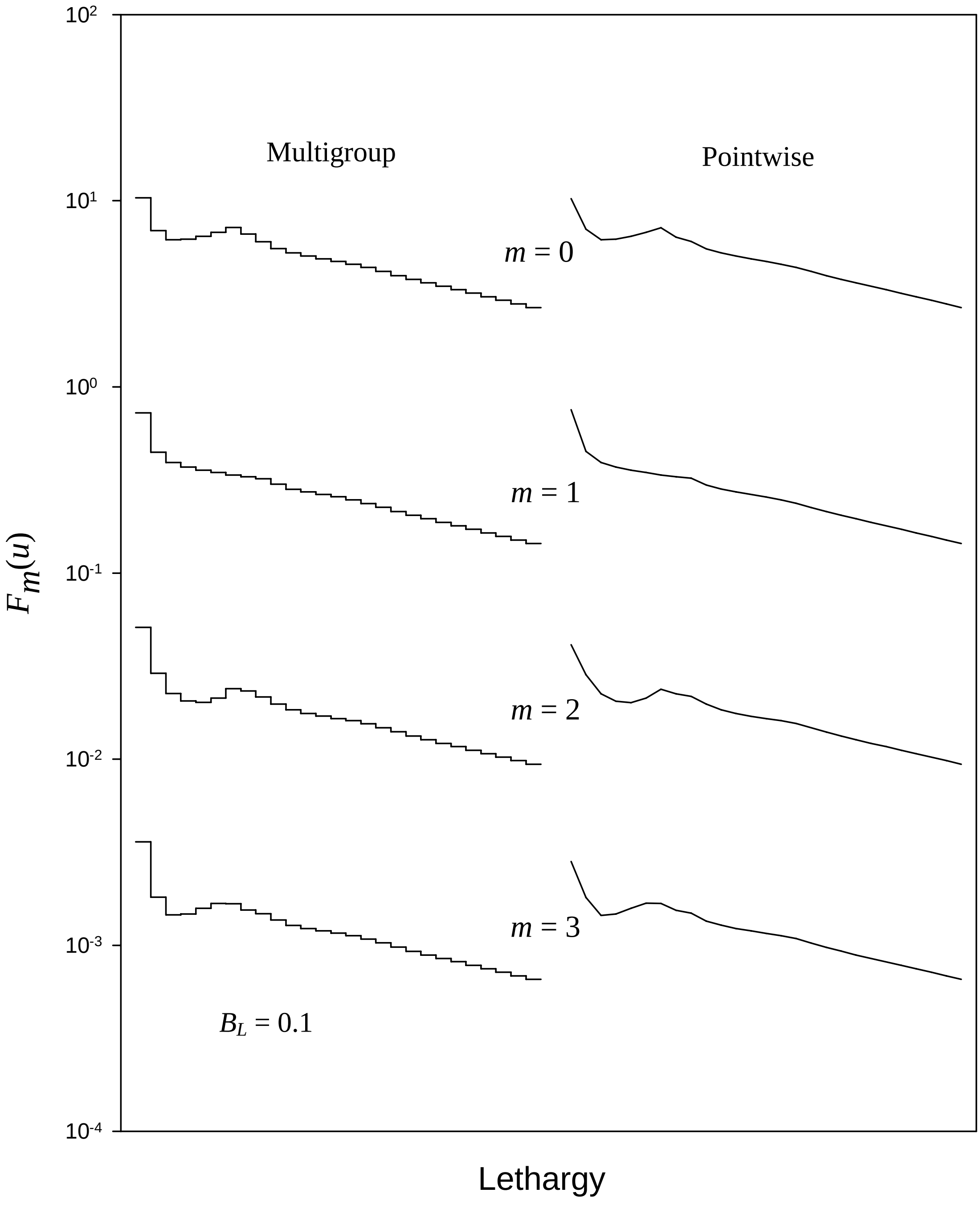

Benchmark 2.3: Slowing down/the multigroup solution in the B_L approximation

(a) Brief description

Stationary neutron slowing down in an infinite medium with non-zero buckling in the multigroup B_L approximation.

(b) Classification

NT/I/LE(3)/MG/I/U/E(D)/RR

(c) Physical description

Same as for Benchmark 2.2.

(d) Analytical representation

This benchmark differs from the previous benchmark in that we discretize the lethargy variable through the multigroup approximation, which is the most commonly used numerical approximation for treating the energy variable. In some sense, this is not a true benchmark since it is not continuous in all independent variables; nevertheless, it is a true *multigroup* benchmark. Since we determine the group parameters analytically for elastic scattering, this benchmark serves as a benchmark for multigroup parameter generation. In addition, we demonstrate benchmark accuracy for a sufficiently fine group structure.

(i) The multigroup formulation

We begin with the multigroup approximation in energy of Eq. (1.VII.1), repeated here for spatially uniform nuclear properties:

$$\left[\Omega\bullet\nabla\phi_g\left(\boldsymbol{r},\Omega\right)+\Sigma_g\phi_g\left(\boldsymbol{r},\Omega\right)\right]= \tag{1a}$$

$$=\sum_{g'=1}^{G}\int_{4\pi}d\Omega'\Sigma_{sgg'}\left(\Omega'\bullet\Omega\right)\phi_{g'}\left(\boldsymbol{r},\Omega'\right)+\frac{1}{4\pi}\chi_g\sum_{g'=1}^{G}\nu_{g'}\Sigma_{fg'}\phi_{g'}\left(\boldsymbol{r}\right)+Q_g\left(\boldsymbol{r},\Omega\right)$$

For J materials the transfer cross section is

$$\Sigma_{sgg'}\left(\Omega'\bullet\Omega\right)\equiv\sum_{j=1}^{J}\Sigma_{sjgg'}\left(\Omega'\bullet\Omega\right) \tag{1b}$$

Note that we now include full upscattering as well as elastic and inelastic scattering, denoted by superscripts u,e,i respectively, in the total scattering cross section and in the scattering law:

$$\Sigma_{sjgg'}\left(\Omega'\bullet\Omega\right)\equiv\Sigma^{e}_{sjgg'}\left(\Omega'\bullet\Omega\right)+\Sigma^{i}_{sjgg'}\left(\Omega'\bullet\Omega\right)+\Sigma^{u}_{sjgg'}\left(\Omega'\bullet\Omega\right)$$

.

Equivalently, Eq. (1a) holds in the multigroup approximation in lethargy. To see this, a lethargy group structure is first established:

$$[0,\infty] \to \left[u_{g-1}, u_g\right],\ g = 1,2,...,G$$

where g = 1 is the lowest (highest) lethargy (energy) group. The multigroup approximation in lethargy is therefore:

$$\begin{aligned}\phi(\boldsymbol{r},\Omega,u) &= f(u)\phi_g(\boldsymbol{r},\Omega)\\ Q(\boldsymbol{r},\Omega,u) &= g(u)Q_g(\boldsymbol{r},\Omega)\end{aligned}$$

for $u\in[u_{g-1},u_g]$ with normalizations:

$$\int\limits_{\Delta u_g} duf(u) \equiv 1,\quad \int\limits_{\Delta u_g} dug(u) \equiv 1$$

However, because equivalence between energy and lethargy in the differential phase space element requires the same number of particles in a phase element:

$$\begin{aligned}f(u)|du| &= f(E)|dE|\\ g(u)|du| &= g(E)|dE|\end{aligned}$$

With this correspondence, the group parameters are, from Eqs. (1.VII.2):

$$\Sigma_g \equiv \int\limits_{\Delta u_g} duf(u)\Sigma(u)$$

$$\Sigma_{sgg'}(\Omega'\bullet\Omega) \equiv \int\limits_{\Delta u_g} du \int\limits_{\Delta u_{g'}} du' f(u')\Sigma_s(\Omega'\bullet\Omega, u'\to u)$$

$$\nu_g\Sigma_{fg} \equiv \int\limits_{\Delta u_g} duf(u)\nu(u)\Sigma_f(u)$$

$$\chi_g \equiv \int\limits_{\Delta u_g} du\chi(u)$$

With the spatial decomposition of the previous benchmark:

$$\begin{aligned}\phi_g(\boldsymbol{r},\Omega) &\equiv \frac{1}{(2\pi)^3}e^{-i\boldsymbol{B}_L\bullet(\boldsymbol{r}-\boldsymbol{r}_0)}\Psi_g(\Omega)\\ Q_g(\boldsymbol{r},\Omega) &\equiv \frac{1}{(2\pi)^3}e^{-i\boldsymbol{B}_L\bullet(\boldsymbol{r}-\boldsymbol{r}_0)}S_g(\Omega)\end{aligned}$$

Eq. (1a) becomes:

$$\begin{aligned}&\left[\Sigma_g - i\boldsymbol{B}_L \bullet \Omega\right]\Psi_g(\Omega) = \\ &= \sum_{g'=1}^{G} \int_{4\pi} d\Omega' \Sigma_{sgg'}(\Omega' \bullet \Omega)\Psi_{g'}(\Omega') + \\ &+ \frac{1}{4\pi}\chi_g \sum_{g'=1}^{G} \nu_{g'}\Sigma_{fg'}(\boldsymbol{r}) \int_{4\pi} d\Omega' \Psi_{g'}(\Omega') + S_g(\Omega)\end{aligned} \tag{2}$$

When we follow the same steps to obtain Eq. (2.2.10) namely, expansion of the scattering kernel for species *j* in a Legendre series, Eq.(2) becomes:

$$\Sigma_{sgg'j}(\Omega' \bullet \Omega) = \Sigma_{g'} c_{sjgg'}(\Omega' \bullet \Omega) = \Sigma_{g'} \sum_{l=0}^{\infty} \frac{2l+1}{4\pi} c_{sljgg'} P_l(\mu_0)$$

By integration over azimuth and application of the Legendre polynomial addition theorem, we find:

$$\begin{aligned}\left[1 - i\alpha_{B_L g}\mu\right] F_g(\mu) = \sum_{l=0}^{\infty} \frac{2l+1}{2} P_l(\mu) \sum_{g'=1}^{G} c_{slgg'} F_{lg'} + \\ + \frac{1}{2}\chi_g \sum_{g'=1}^{G} c_{fg'} F_{0g'} + S_g(\mu)\end{aligned} \tag{3}$$

where:

$$F_g(\mu) \equiv \Sigma_g \Psi_g(\mu)$$

$$F_{lg} = \int_{-1}^{1} d\mu P_l(\mu) F_g(\mu)$$

$$\alpha_{B_L g} \equiv \frac{B_L}{\Sigma_g}$$

$$c_{fg} \equiv \frac{\nu_g \Sigma_{fg}}{\Sigma_g}$$

$$c_{slgg'} \equiv \sum_{j=1}^{J} c_{sljgg'}$$

$$c_{sljgg'} \equiv \frac{\Sigma_{sljgg'}}{\Sigma_{g'}}$$

The second to last quantity is the total group transfer cross section and represents scattering from group *g′* to *g* for all nuclides. Note that at this point scattering remains unrestricted.

(ii) The moments solution

With replacement $F_m(\mu) \to i^m F_m(\mu)$, we obtain the group moments directly from Eq. (3) by projection over the Legendre polynomials $P_m(\mu)$:

$$F_{mg} = \sum_{l=0}^{\infty}(2l+1)A_{mlg}\sum_{g'=1}^{G} c_{slgg'}F_{lg'} + \left[\chi_g \sum_{g'=1}^{G} c_{fg'}F_{0g'} + S_{0g}\right]A_{m0g}, \quad m = 0,1,... \tag{4}$$

The source, assumed isotropic, is:

$$S_g(\mu) \to \frac{1}{2}S_{0g}$$

and from Eq. (2.2.12b)

$$A_{mlg} \equiv i^{l-m}T_{ml}\left(-\alpha_{B_L g}\right)$$

For elastic scattering, with the scattering kernel truncated at L, and fission suppressed, Eq. (4) therefore becomes:

$$\begin{aligned}&\sum_{l=0}^{L}\left[\delta_{ml} - (2l+1)A_{mlg}c_{slgg}\right]F_{lg} = \\ &= \sum_{l=0}^{L}(2l+1)A_{mlg}\sum_{g'=1}^{g-1}c_{slgg'}F_{lg'} + S_{0g}A_{m0g}, \quad m = 0,1,2,...,L\end{aligned} \tag{5a}$$

Note, we now consider down scattering only since $g' \le g$ and no fission. Unrestricted scattering with fission is part of the next section.

With some rearrangement, we can express Eq. (5a) in the more compact vector form:

$$\boldsymbol{A}_g\boldsymbol{F}_g = \boldsymbol{S}_g \tag{5b}$$

with the moment vector:

$$\boldsymbol{F}_g \equiv \left\{F_{lg},\ l = 0,1,...,L\right\}$$

and for $m,l = 0,1,\ldots,L$:

$$\boldsymbol{A}_g \equiv \left\{\delta_{ml} - (2l+1)A_{mlg}c_{slgg}\right\}$$

$$\boldsymbol{S}_g \equiv \left\{\sum_{l=0}^{L}(2l+1)A_{mlg}\sum_{g'=1}^{g-1}c_{slgg'}F_{lg'} + S_{0g}A_{m0g}\right\}$$

Therefore, we obtain the L+1 group moments by matrix inversion of a matrix of rank L+1 for each group g. Specification of the moments allows the construction of the source $\boldsymbol{S}_g$ for the next group. We continue recursively in this fashion for all G groups.

Given the relatively simple nature of the recursive algorithm presented above, the generation of the group parameters now becomes the focus. In order to test the accuracy of the multigroup equations, a comparison to the slowing down solution of Benchmark 2.2 for elastic scattering with constant cross sections is appropriate. For this reason, we render the elastic scattering law analytically in multigroup form.

By analogy to Eq. (2.2.9d), the l^{th} moment of the elastic scattering cross section for material j is:

$$c_{slj}\left(u'\to u\right)\equiv c_{sj}\left(u'\right)\Theta\left(u-u'\right)\Theta\left(q_j-\left(u-u'\right)\right)f_{slj}\left(u'\to u\right) \tag{6}$$

where:

$$f_{slj}\left(u'\to u\right)\equiv\frac{e^{-\left(u-u'\right)}}{1-\alpha_j}P_l\left(\mu_{sj}\left(u-u'\right)\right)$$

By substitution of the piecewise constant energy approximation:

$$f\left(u\right)=g\left(u\right)\equiv\frac{1}{\Delta u_g},\quad u\in\Delta u_g$$

into the definition of the l^{th}-component of the group transfer cross section, we find:

$$\begin{aligned}&c_{sljgg'}=\\&=\frac{1}{\Delta u_{g'}}\int_{\Delta u_g}du\int_{\Delta u_{g'}}du'\Theta\left(u-u'\right)\Theta\left(u'-u+q_j\right)c_{sj}\left(u'\right)f_{slj}\left(u'\to u\right)\end{aligned} \tag{7}$$

Upon change of variables and assuming $c_{sj}(u')$ to be piecewise constant, it therefore follows that:

$$c_{sljgg'}=\frac{c_{sjg'}}{\Delta u_{g'}}\int_{\Delta u_g}du\,h_{lg'j}\left(u\right) \tag{8}$$

with:

$$h_{lg'j}\left(u\right)\equiv\int_{u-u_{g'}}^{u-u_{g'-1}}d\omega\,\Theta\left(\omega\right)\Theta\left(q_j-\omega\right)f_{slj}\left(\omega\right)$$

By performing integration by parts, Eq. (8) becomes:

$$c_{sljgg'}=\frac{c_{sjg'}}{\Delta u_{g'}}\left[u_g h_{lg'j}\left(u_g\right)-u_{g-1}h_{lg'j}\left(u_{g-1}\right)-\int_{u_{g-1}}^{u_g}du\,u\frac{dh_{lg'j}\left(u\right)}{du}\right] \tag{9a}$$

where:

$$\begin{aligned}\frac{dh_{lg'j}\left(u\right)}{du}=&\ f_{slj}\left(u-u_{g'-1}\right)\Theta\left(u-u_{g'-1}\right)\Theta\left(q_j-u+u_{g'-1}\right)-\\&-f_{slj}\left(u-u_{g'}\right)\Theta\left(u-u_{g'}\right)\Theta\left(q_j-u+u_{g'}\right)\end{aligned} \tag{9b}$$

Calling the last term in Eq. (9a) $I_{lg'gi}$:

$$I_{lg'gj} \equiv \int_{u_{g-1}}^{u_g} duu \frac{dh_{lg'j}(u)}{du} \tag{9c}$$

and performing some algebra, we find:

$$I_{lg'gj} = \bar{I}_{lg'-1gj} - \bar{I}_{lg'gj} \tag{10a}$$

where:

$$\bar{I}_{lg'gj} \equiv \int_{r_l}^{r_{uj}} d\omega\left(\omega + u_{g'}\right) f_{slj}(\omega) \tag{10b}$$

with the following limits depending on g and g':

$$r_l \equiv \max\left(u_{g-1} - u_{g'}, 0\right)$$

$$r_{uj} \equiv \min\left(u_g - u_{g'}, q_j\right)$$

We can find the last integral analytically to be:

$$\bar{I}_{lg'gj} = \frac{1}{2^l} \sum_{m=0}^{[l/2]} a_{lm} \sum_{k=0}^{l-2m} b_{klm} \alpha_{j+}^{l-2m-k} \alpha_{j-}^{k} \chi_{lmg'gkj} \tag{11}$$

where:

$$\chi_{lmg'gkj} \equiv \frac{1}{\hat{\beta}_{klm}} \left[r_{uj} e^{\hat{\beta}_{klm} r_{uj}} - r_l e^{\hat{\beta}_{klm} r_l} \right] + \frac{1}{\hat{\beta}_{klm}} \left[u_{g'} - \frac{1}{\hat{\beta}_{klm}} \right] \left[e^{\hat{\beta}_{klm} r_{uj}} - e^{\hat{\beta}_{klm} r_l} \right]$$

$$\hat{\beta}_{klm} \equiv k - \frac{l-2m}{2}$$

$$a_{lm} \equiv (-1)^m \binom{l}{m} \binom{2l-2m}{m}$$

$$b_{klm} \equiv (-1)^k \binom{l-2m}{k}$$

and $\binom{s}{r}$ is the binomial coefficient.

Similarly:

$$h_{lg'j}\left(u_g\right) = \frac{1}{2^l} \sum_{m=0}^{[l/2]} a_{lm} \sum_{k=0}^{l-2m} b_{klm} \alpha_{j+}^{l-2m-k} \alpha_{j-}^{k} y_{lmg'gkj} \tag{12}$$

with:

$$y_{lmg'gkj} \equiv \frac{1}{\hat{\beta}_{klm}} \left[e^{\hat{\beta}_{klm} r'_{uj}} - e^{\hat{\beta}_{klm} r'_{l}} \right]$$

$$r'_l \equiv \max\left(u_g - u_{g'}, 0\right)$$
$$r'_{uj} \equiv \min\left(u_g - u_{g'-1}, q_j\right)$$

Thus, we have evaluated all integrals analytically (as complicated as they are) for the multigroup transfer cross section giving the final expression:

$$c_{sljgg'} = \frac{c_{sjg'}}{\left(1-\alpha_j\right)\Delta u_{g'}} \left[u_g h_{lg'j}\left(u_g\right) - u_{g-1} h_{lg'j}\left(u_{g-1}\right) + \overline{I}_{lg'gj} - \overline{I}_{lg'-1gj} \right] \tag{13}$$

(iii) Criticality

In the design of a critical nuclear reactor to given dimensions, material selection and concentrations must be compatible or a steady state self-sustaining flux (or collision density) distribution will not be achieved. For this reason, the *k*-eigenvalue (also called k_{eff}) associated with a critical system, becomes uniquely important. k_{eff} is the divisor of the fission cross section that forces the system to be mathematically self-sustaining (an eigenstate). Essentially, knowing the buckling B_L, k_{eff} then adjusts the fission cross section (or neutron multiplication ν) to make the reactor critical for that buckling. It is a measure of how far from a critical system (when $k_{eff} = 1$) the B_L approximation actually is. Alternatively, we can choose the materials, their concentrations and the reactor size (related to B_L) to make $k_{eff} = 1$. We now consider such a critical system.

Assuming isotropic scattering only, Eq. (3) without a source, will give the critical flux from:

$$\left[\Sigma_g - iB_L\mu\right]\Psi_g\left(\mu\right) = \frac{1}{2}\sum_{g'=1}^{G}\Sigma_{s0gg'}\Psi_{0g'} + \frac{1}{2}\frac{1}{k_{eff}}\chi_g\sum_{g'=1}^{G}\nu_{g'}\Sigma_{fg'}\Psi_{0g'} \tag{14}$$

where we have divided the fission cross section by the eigenvalue k_{eff}. Recall that:

$$\Sigma_{s0gg'} \equiv \Sigma^{e}_{s0gg'} + \Sigma^{i}_{s0gg'} + \Sigma^{u}_{s0gg'}$$

Inelastic scattering is especially important in fast reactors because scattering against heavy nuclei degrades the energy (lethargy) spectrum, which is undesirable. Upscatter is important near the resonance/thermal energy boundary (~1 *eV*).

Through projection of Eq. (14) over Legendre polynomials, the following equation for the zeroth flux moment results:

$$\Sigma_g\Psi_{0g} = T_{Lg}\sum_{g'=1}^{G}\left[\Sigma_{s0gg'} + \frac{1}{k_{eff}}\chi_g\nu_{g'}\Sigma_{fg'}\right]\Psi_{0g'} \tag{15}$$

where:

$$T_{Lg} \equiv \frac{tan^{-1}\left(B_L / \Sigma_g\right)}{B_L / \Sigma_g}$$

and therefore:

$$\sum_{g'=1}^{G} \left\{ \Sigma_{g'} \delta_{gg'} - T_{Lg} \left[\Sigma_{s0gg'} + \frac{1}{k_{eff}} \chi_g \nu_{g'} \Sigma_{fg'} \right] \right\} \Psi_{0g'} = 0$$

We now solve this set of homogeneous equations in the form:

$$\boldsymbol{A\Psi} = \boldsymbol{0} \tag{16}$$

with:

$$\boldsymbol{A} \equiv \left\{ \Sigma_g \delta_{gg'} - T_{Lg} \left[\Sigma_{s0gg'} + \frac{1}{k_{eff}} \chi_g \nu_{g'} \Sigma_{fg'} \right] \right\}$$

where $\boldsymbol{\Psi}$ is the group scalar flux vector.

A non-trivial solution to Eq. (16) exists only if:

$$Det\left[\boldsymbol{A}\right] = 0 \tag{17}$$

The solution then determines k_{eff} for a given buckling. Once we know k_{eff}, the critical distribution for the normalization $\Psi_{00} \equiv 1$ comes from:

$$\begin{aligned} &\sum_{g'=2}^{G} \left\{ \Sigma_g \delta_{gg'} - T_{Lg} \left[\Sigma_{s0gg'} + \frac{1}{k_{eff}} \chi_g \nu_{g'} \Sigma_{fg'} \right] \right\} \Psi_{0g'} = \\ &= -\left\{ \Sigma_g \delta_{g1} - T_{Lg} \left[\Sigma_{s0g1} + \frac{1}{k_{eff}} \chi_g \nu_1 \Sigma_{f1} \right] \right\} \end{aligned} \tag{18}$$

We demonstrate criticality for a fast reactor in the next section.

(e) Numerical implementation and demonstration for Benchmark 2.3

Because of the simplicity of the recurrence relation and multigroup cross section generator, we require no special numerical methods other than matrix inversion. As with most recurrence relations, however, the calculation must be of sufficiently high precision to avoid round off error accumulation.

For routine core design, the generation of a collision density distribution is a two-step process. The first step is to generate the appropriate cross sections. Here, we first evaluate Eqs. (10a), (11), (12) and (13) for elastic scattering. To capture the detail of the Placzek transient at the discontinuity $u = q_j$ appropriately, we call for edits of groups adjacent to the discontinuity. In the second step, we input the cross sections into the multigroup slowing down equations given by Eqs. (5).

(i) Demonstration: elastic scattering

We first demonstrate the consistency of the multigroup formulation for the 70%/30% C/Fe mixture of benchmark 2,2. Figure 2.3.1(a) shows a collision density comparison for an increasing number of groups: G = 17, 77 and 167. The slowing down distribution looks very nearly continuous for the last case. We further demonstrate the accuracy of the multigroup calculation in Figures 2.3.1(b) and 2.3.1(c) by comparing the multigroup collision density distributions for $G = 17$ and 167 to that of the numerical Laplace transform inversion. The "exact solution", as determined from Benchmark 2.2, is virtually identical to the multigroup solution for $G = 167$.

(ii) Demonstration: inelastic scattering

The fast reactor data found in Ref. 1 provides an informative example featuring inelastic scattering. We will find the critical multiplication factor, k_{eff}, from the 18-group data set for the nominal volume fractions of the reactor components shown in Table 2.3.1. We obtain the elastic scattering transfer cross section from the above analytical multigroup generation procedure. ^{239}Pu is the reactor fuel along with depleted uranium (^{238}U) in the amounts indicated in the table. Figure 2.3.2(a) shows the variation of the total macroscopic cross sections and fission spectrum with lethargy for the nominal case. Figure 2.3.2(b) gives the variation of k_{eff} with B_L for three different fuel compositions. We observe that for an increase in the ^{239}Pu volume fraction or decrease in density over nominal, a larger reactor is necessary for criticality with the opposite true for a volume fraction decrease. The trend is intuitively correct for a fixed fuel mass. Figure 2.3.3 presents a comparison of the fission spectrum to the critical flux for $k_{eff} = 1.0004$ and $B_L = 0.003355$ and indicates how the flux spectrum shifts because of elastic and inelastic scattering. The buckling compares well with the buckling of 0.003243 of the original reference [1].

Table 2.3.1. Fast reactor composition

Material	**Vol. Frac.**				
Fuel	0.45	^{239}Pu	10.4%	^{238}U	89.6%
Na coolant	0.35				
Structure	0.20				

REFERENCE

[1] Bowden, R.L., M.C. Edlund, *Reactor Statics Module, RS-5, Multigroup Constants for Fast Reactors*, Virginia Polytechnic Institute and State University (1963).

Figure 2.3.1(a). Multigroup comparison for *G* = 17, 77, 167 for 70%/30% carbon/iron mixture

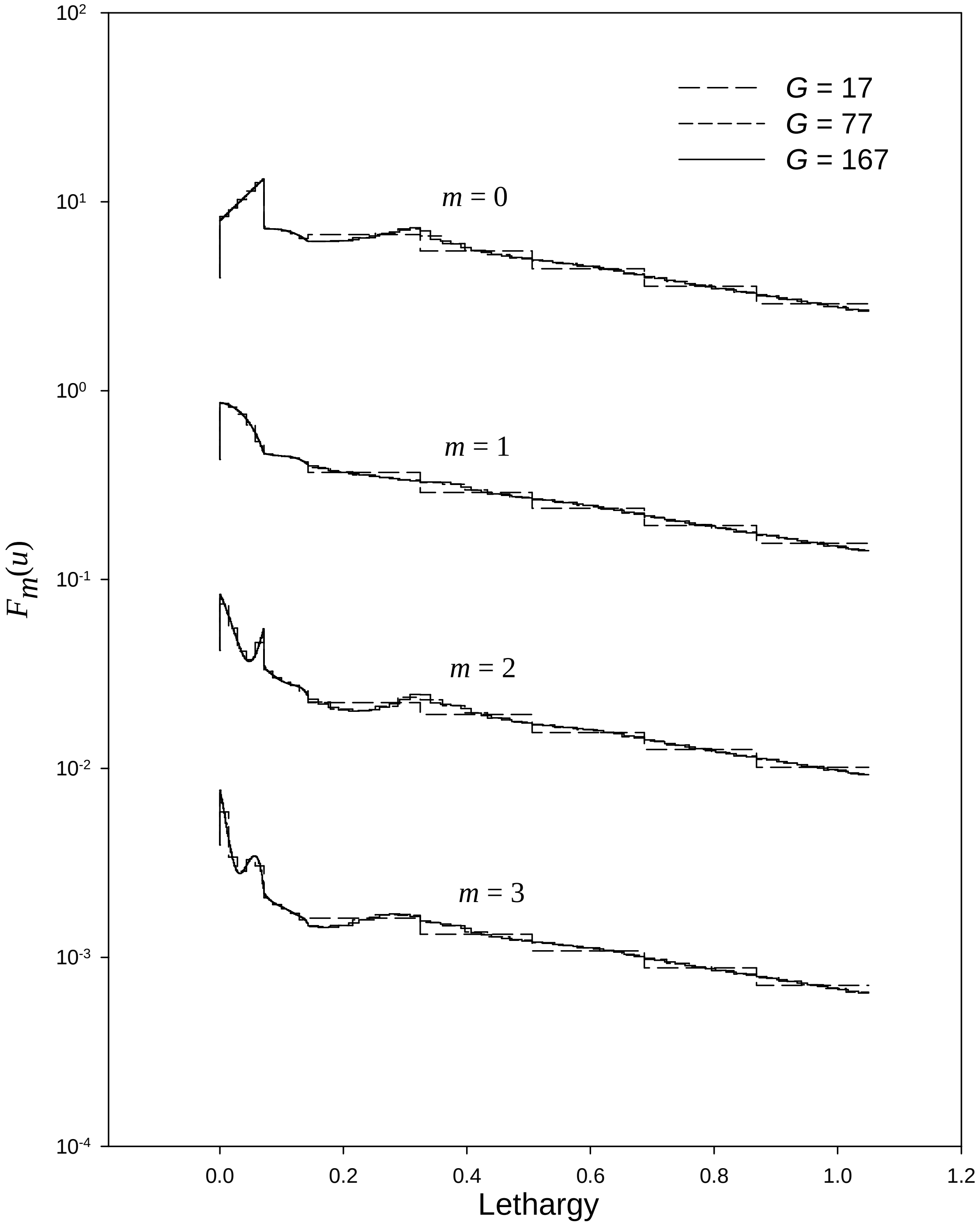

Figure 2.3.1(b). Comparison of multigroup for *G* = 17 and Laplace transform inversion

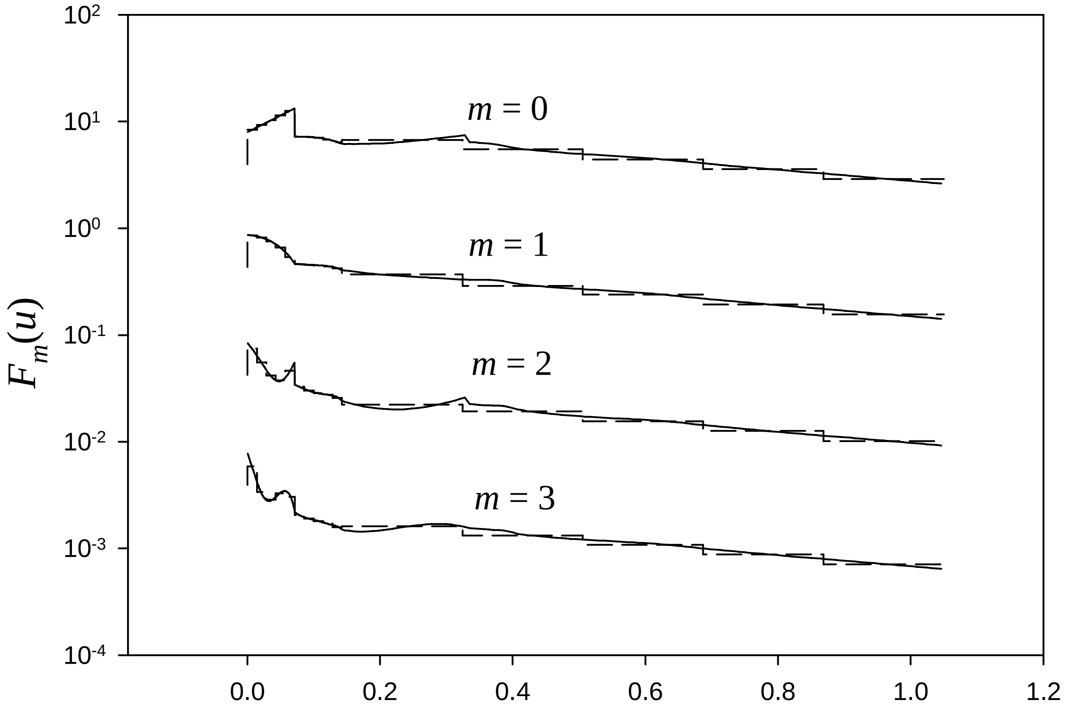

Figure 2.3.1(c). Comparison of multigroup with *G* = 167 and Laplace transform inversion

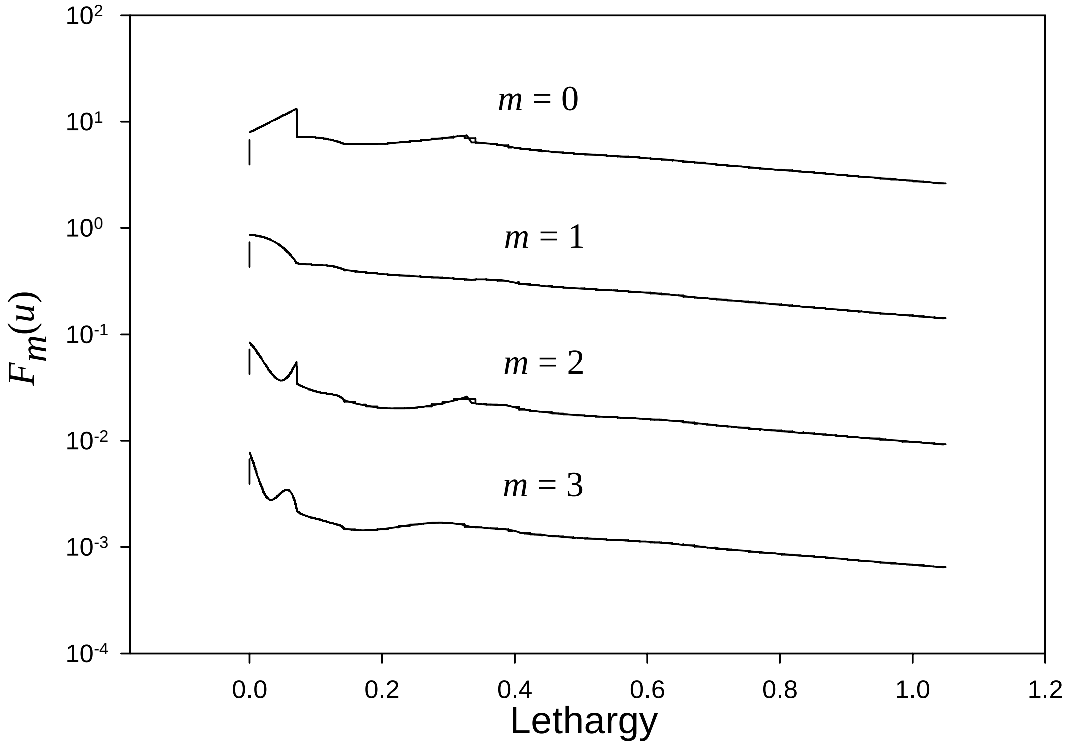

Figure 2.3.2(a). Nuclear data for fast reactor example from Ref. 1

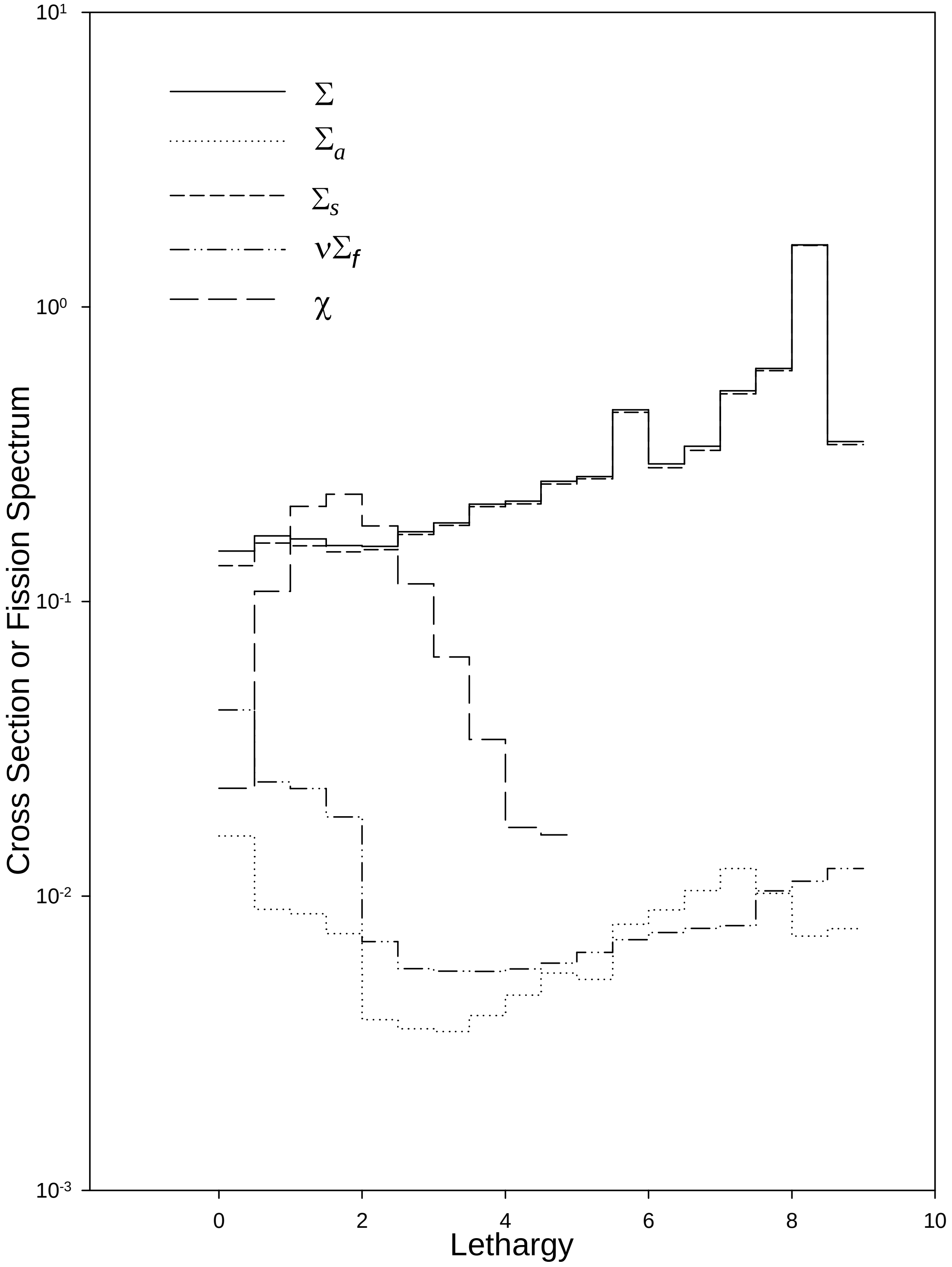

Figure 2.3.2(b). Variation of k_{eff} with B_L and fuel volume fractions

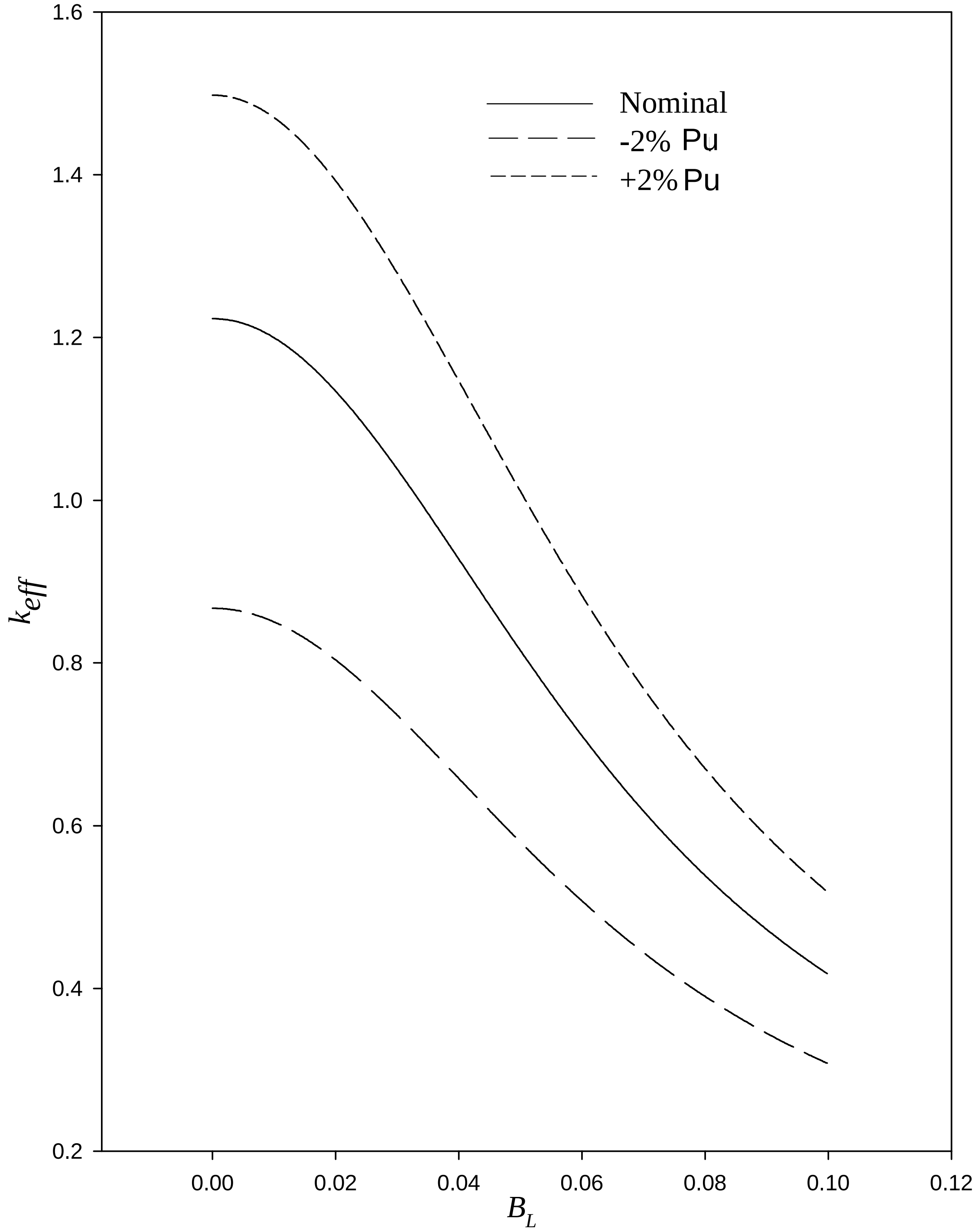

Figure 2.3.3. Comparison of fission spectrum and flux for k_{eff} = 1.0004 and $B_L = 3.8299 \times 10^{-2}$

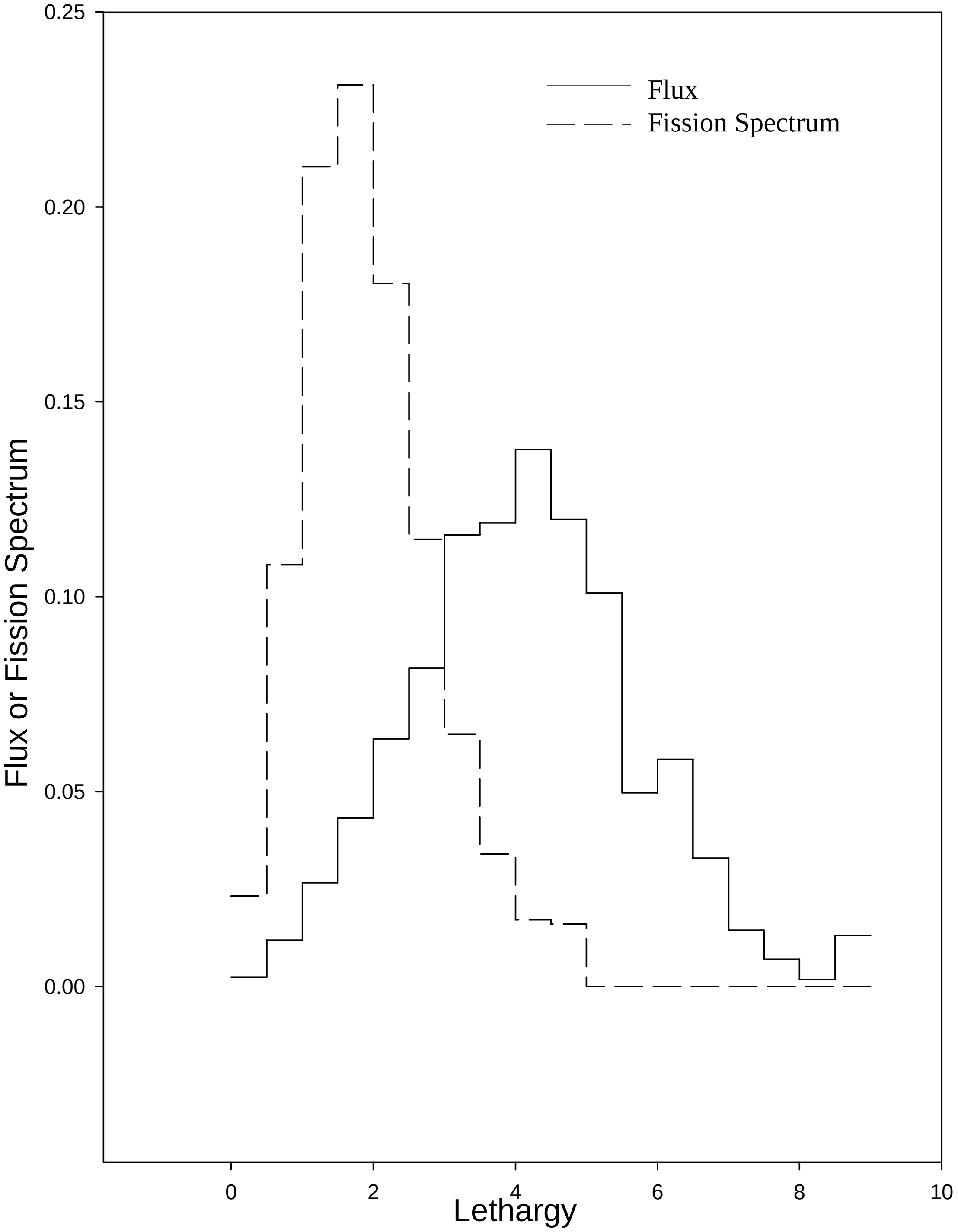

Benchmark 2.4: Slowing down and thermalization in an infinite medium/the embedded multigroup approximation

(a) Brief description

Neutrons scattering in the thermal energy region below the resonance region in an infinite medium with a non-zero buckling.

(b) Classification

NT/I/LE(1)/MG/I/U/E(D)/CAC

(c) Physical description

After neutrons have been slowed down in the fast energy region (5 *MeV* to 10 *KeV*) and have survived the resonance region (1 *KeV* to 1 *eV*), they enter the thermal region (~0.0253 *ev*). Here, the neutrons gain and lose energy upon collision depending on the thermal motion of interacting nuclei. Usually, we neglect thermal motion of the nucleus in the fast and resonance regions but cannot at thermal energies. In the multigroup approximation, the scattering matrix is full since each group communicates with all other groups. Neutron spatial redistribution is significant at thermal energies; therefore, buckling is included to simulate leakage. The thermalized flux represents a fine-group weighting spectrum, which is essential in producing representative homogenized cross sections.

(d) Analytical representation

The equations for the first two moments of the collision density in the thermal energy region from Eq. (2.3.4) for L = 1 are:

$$F_{mg} = \sum_{l=0}^{1}\left(2l+1\right)A_{mlg}\sum_{g'=1}^{G} c_{slgg'}F_{lg'} + S_{0g}A_{m0g}, \quad m = 0,1 \tag{1}$$

or written out:

$$F_{0g} = A_{00g}\sum_{g'=1}^{G} c_{s0gg'}F_{0g'} + 3A_{01g}\sum_{g'=1}^{G} c_{s1gg'}F_{1g'} + A_{00g}S_{0g} \tag{2a}$$

$$F_{1g} = A_{10g}\sum_{g'=1}^{G} c_{s0gg'}F_{0g'} + 3A_{11g}\sum_{g'=1}^{G} c_{s1gg'}F_{1g'} \tag{2b}$$

for g = 1,2,...,G, where the scattering matrix is full. Through manipulation, we can reformulate Eqs. (2) as:

$$\Sigma_g F_{0g} + B_L F_{1g} = \Sigma_g \sum_{g'=1}^{G} c_{s0gg'}F_{0g'} + \Sigma_g S_{0g} \tag{3a}$$

$$-\frac{B_L}{3}F_{0g} + \gamma_g \Sigma_g F_{1g} = \Sigma_g \sum_{g'=1}^{G} c_{s1gg'}F_{1g'} \tag{3b}$$

where:

$$\gamma_g \equiv \frac{T_g \alpha_{Lg}^2}{3\left(1-T_g\right)}, \quad \alpha_{Lg} \equiv \frac{B_L}{\Sigma_g}, \quad T_g \equiv \frac{tan^{-1}\left(\alpha_{Lg}\right)}{\alpha_{Lg}}$$

Equations (3) give the collision density moments as a vector found by matrix inversion for *G* on the order of 100 to 1000. Thus, for routine use in a limited computational environment, direct matrix inversion may quickly become prohibitive. Therefore, alternative methods other than direct inversion may prove more efficient for some applications. One alternative inversion technique is to solve a more general problem (with or without physical significance) within which the specific problem of interest is contained. We call this method mathematical embedding. One gains analytical advantage if the general problem lends itself to a straightforward solution. For the case at hand, we embed the stationary thermal spectrum equations in a fictitious time dependent formulation.

Arbitrarily adding fictitious "time derivatives" to Eqs. (3) gives:

$$\varepsilon_0 \frac{\partial F_{0g}\left(t\right)}{\partial t} + \Sigma_g F_{0g}\left(t\right) + B_L F_{1g}\left(t\right) = \Sigma_g \sum_{g'=1}^{G} c_{s0gg'} F_{0g'}\left(t\right) + \Sigma_g S_{0g} \tag{4a}$$

$$\varepsilon_1 \frac{\partial F_{1g}\left(t\right)}{\partial t} - \frac{B_L}{3} F_{0g}\left(t\right) + \gamma_g \Sigma_g F_{1g}\left(t\right) = \Sigma_g \sum_{g'=1}^{G} c_{s1gg'} F_{1g'}\left(t\right) \tag{4b}$$

Equations (4a) and (4b) do not necessarily represent a true physical transport scenario however. The addition of the derivatives is purely a numerical artifice to iterate straightforwardly to a solution. ε_0 and ε_1 are parameters to accelerate convergence of the iterative process if possible. It is evident that the desired solution is the "stationary distribution" associated with Eqs. (4) for a source uniform in time.

We obtain the solution to Eqs. (4) through a method called continuous analytical continuation (CAC) [1]. Let the time interval $[0,T_L]$ be partitioned into N_R uniform intervals:

$$\Delta t \equiv \frac{T_L}{N_R}$$

where N_R is an integer. By expressing $F_{mg}(t)$, $m = 0,1$ as the following Taylor series in the r^{th} interval, $t_{r-1} \le t \le t_r$, we have:

$$F_{mg}\left(t\right) = \sum_{k=0}^{\infty} h_{mk}^{rg} \left(t - t_{r-1}\right)^k, \quad r = 1,2,\ldots,N_R \tag{5}$$

where the coefficients are recursively determined. When we introduce Eq. (5) into Eqs. (4), the following recurrence obtains:

$$\varepsilon_0 k h_{0k}^{rg} = -B_L h_{1k-1}^{rg} - \Sigma_g h_{0k-1}^{rg} + \Sigma_g \sum_{g'=1}^{G} c_{s0gg'} h_{0k-1}^{rg'} + \Sigma_g S_{0g} \delta_{k1} \tag{6a}$$

$$\varepsilon_1 k h_{1k}^{rg} = -\gamma_g \Sigma_g h_{1k-1}^{rg} + \frac{B_L}{3} h_{0k-1}^{rg} + \Sigma_g \sum_{g'=1}^{G} c_{s1gg'} h_{1k-1}^{rg'} \tag{6b}$$

Eqs. (6a) and (6b) are initiated at each time interval with $F_{mg}(t_{r-1})$:

$$h_{m0}^{rg} = F_{mg}\left(t_{r-1}\right), \quad m = 0,1$$

and for the first interval ($r = 1$):

$$h_{m0}^{1g} = 0$$

Thus, the desired solution is the asymptotic value of F_{mg} as T_L (and therefore t) approaches infinity. In effect, each time interval represents an iteration with the collision density eventually converging to the stationary distribution.

(e) Numerical implementation and demonstration for Benchmark 2.4

Since the recurrence relations are exact, except for round off error, there are only two numerical errors associated with the CAC evaluation of F_{mg}. The first is the truncation error of the Taylor series. In the numerical evaluation, we truncate the series when the relative errors of three consecutive additional contributions fall below a specified tolerance. The second error relates how close the solution is to the converged "steady state" distribution. As an indication of convergence, we compare each moment to the last in "time". When the relative error is below a given tolerance for all energy groups, the moment has converged.

Figure 2.4.1 shows the iterative approach to steady state for $F_{0g}(t)$ assuming elastic scattering in carbon with $B_L = 10^{-6}$ and for 21 groups. $F_{0g}(t)$ is also plotted for $t = 10$, 20, 50 and 100 as is the semi-analytical solution from Benchmark 2.1. We observe that the distributions are graphically coincident at $t = 100$. It is interesting to note how the steady state comes about. The collision density in the region of the Placzek transient seems to reach steady state before the collision densities at large lethargies. Figure 2.4.2 shows traces ("time" evolution) of the collision densities in groups 5, 10 and 21. Clearly, the larger the lethargy, the longer it takes to reach steady state. Figure 2.4.3 shows the same case in comparison to the exact Laplace transform inversion but only for eight groups. Again, we see excellent agreement even for this rather coarse group structure. Figure 2.4.4 displays a comparison between the CAC and "exact collision densities" for slowing down in a 70%/30% carbon/iron medium with $B_L = 0.1$ and for an increasing number of groups. Apparently, with significant leakage and at large lethargies, one requires a relatively large number of groups for adequate accuracy. This is clear evidence of the discretization error of the multigroup approximation and how we can quantify this error through comparison with semi-analytical benchmarks.

A conclusion from these comparisons is that the multigroup formulation implemented through CAC provides highly accurate benchmark results for a sufficiently large number of groups – at least for neutron slowing down.

The final figure, Figure 2.4.5, shows the approach to equilibrium for the thermal neutron spectrum in water at room temperature obtained by CAC using actual cross section data. We compare the CAC results to those of the INL spectral code COMBINE/PC [2] indicating excellent agreement. This demonstration shows that the CAC numerical method is appropriate for a relatively meaningful case of a 100 groups.

REFERENCES

[1] Fairen, V., *et al*., “Power Series Approximation to Solutions of Nonlinear Systems of Differential Equations”, *Am J. Phys*., **56**, 1 (1988).

[2] Grimesey, R.A., D.W. Nigg, R.L. Curtis, *COMBINE/PC Manual*, EG&G Idaho, Inc. (1990).

Figure 2.4.1. Approach to stationary for F_0 moment in carbon

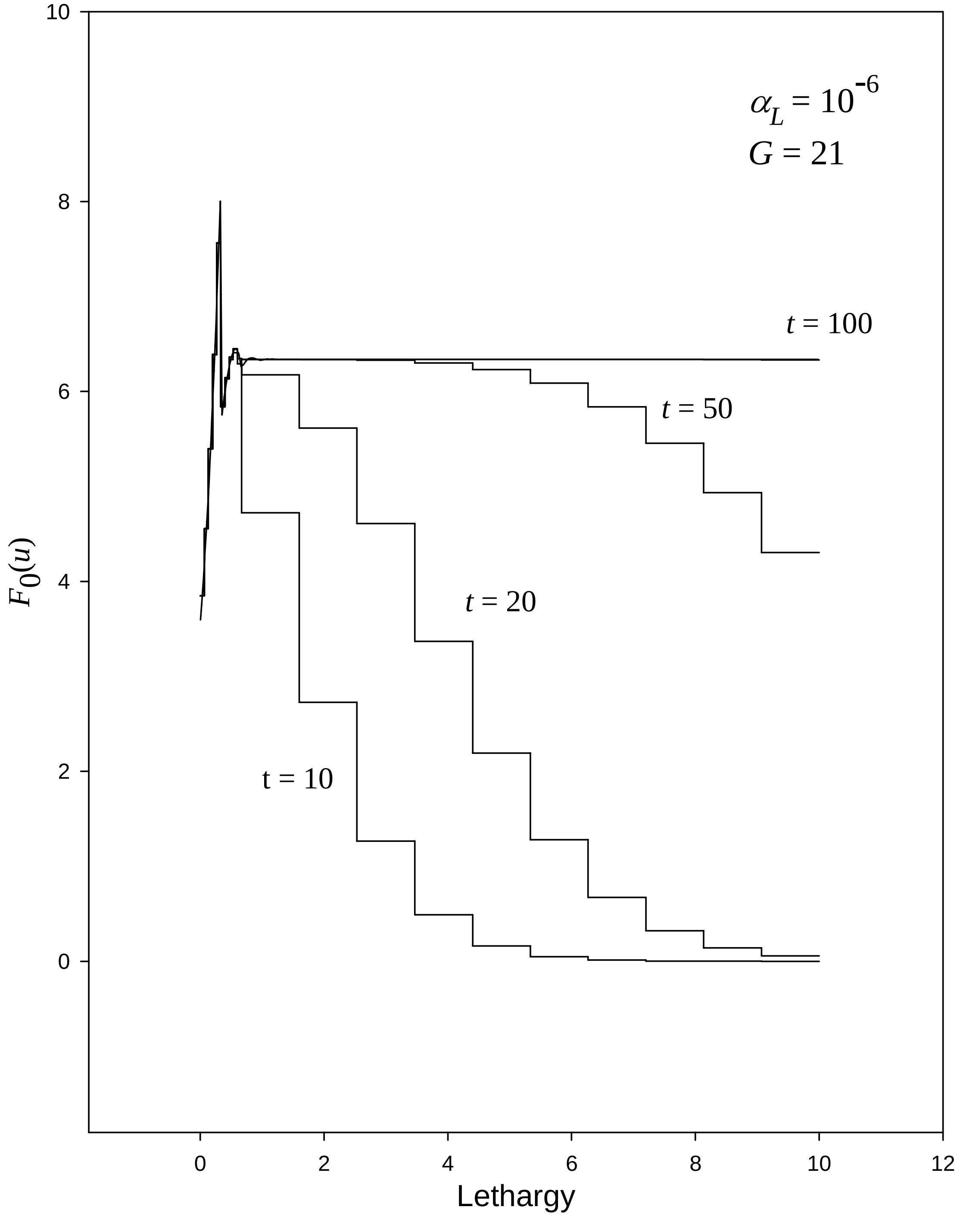

Figure 2.4.2. “Time” traces for *g* = 5, 10, 21 in carbon

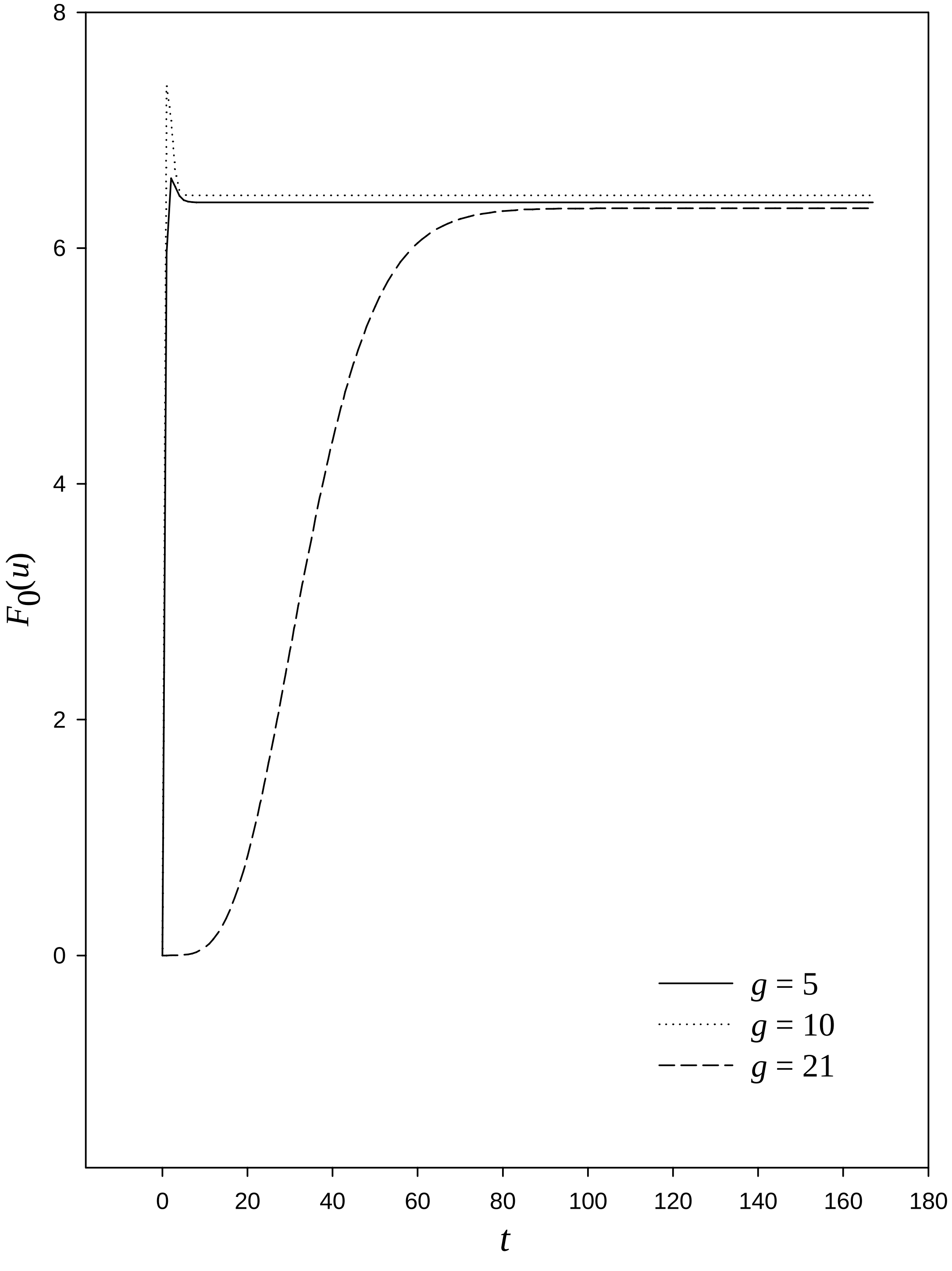

Figure 2.4.3. Collision density comparison to Laplace transform for *G* = 8 in carbon

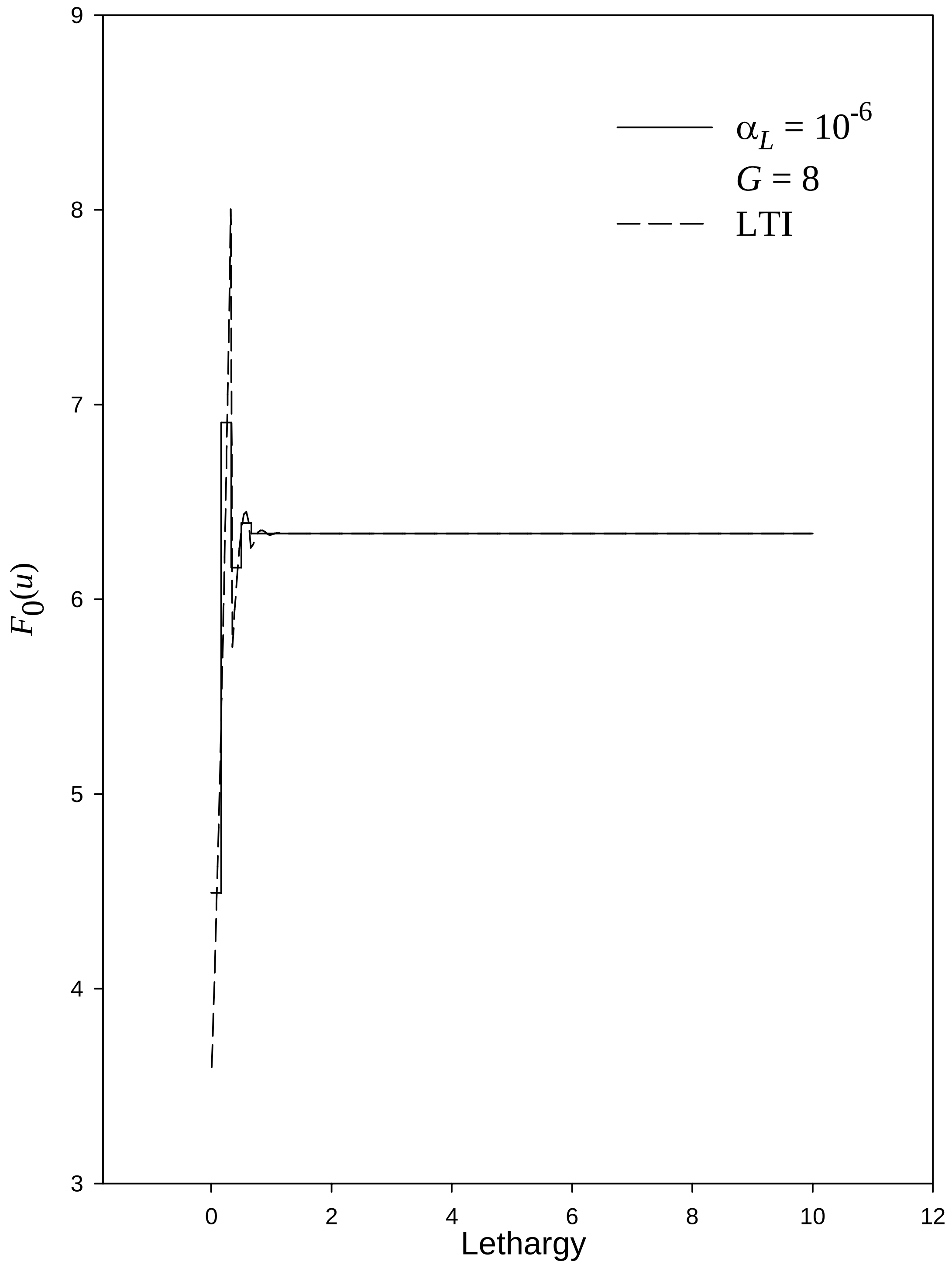

Figure 2.4.4. Approach to exact moment F_0 by increasing number of groups for slowing down in 70%/30% C/Fe mixture

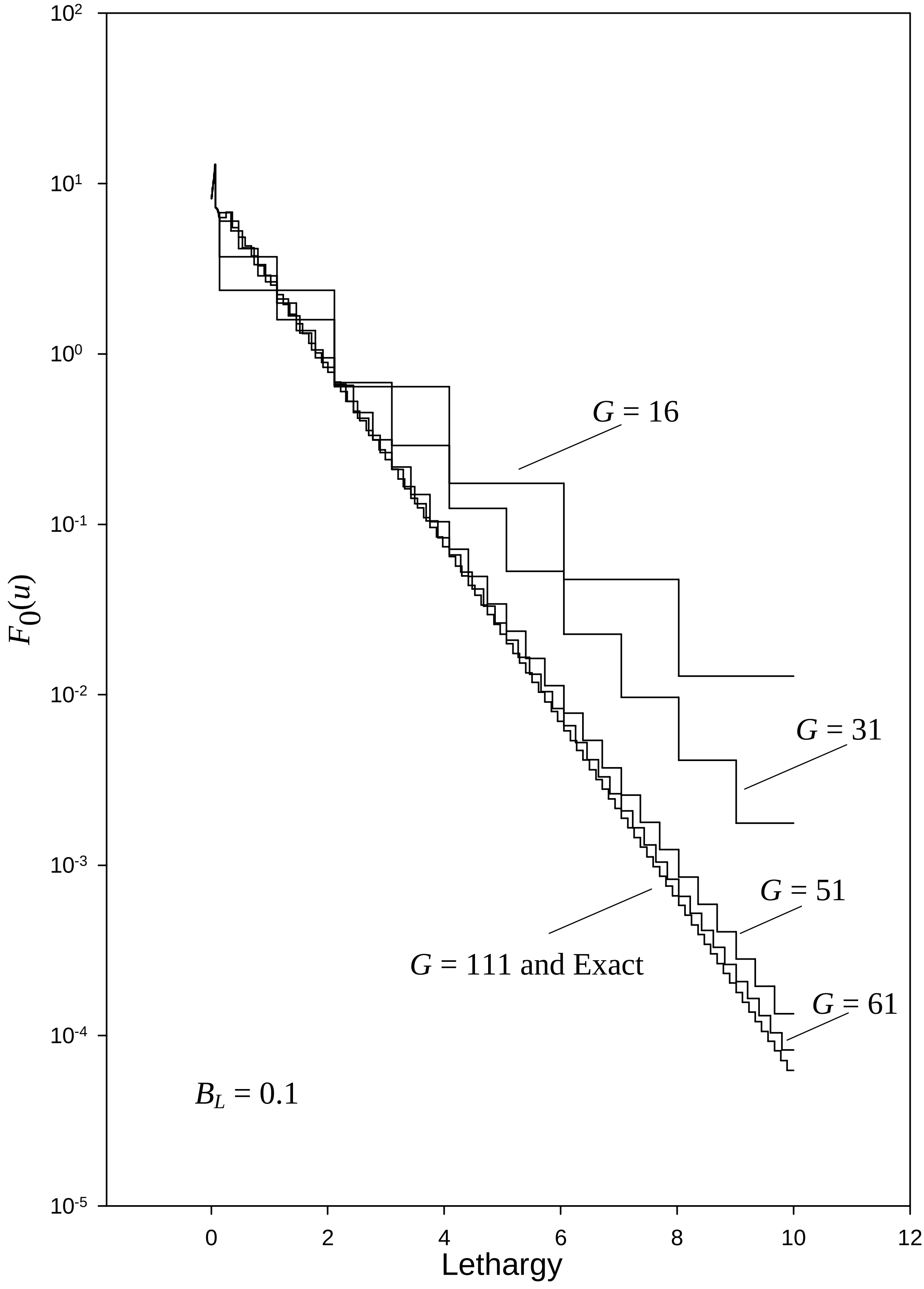

Figure 2.4.5. Thermalization in H_2O at room temperature

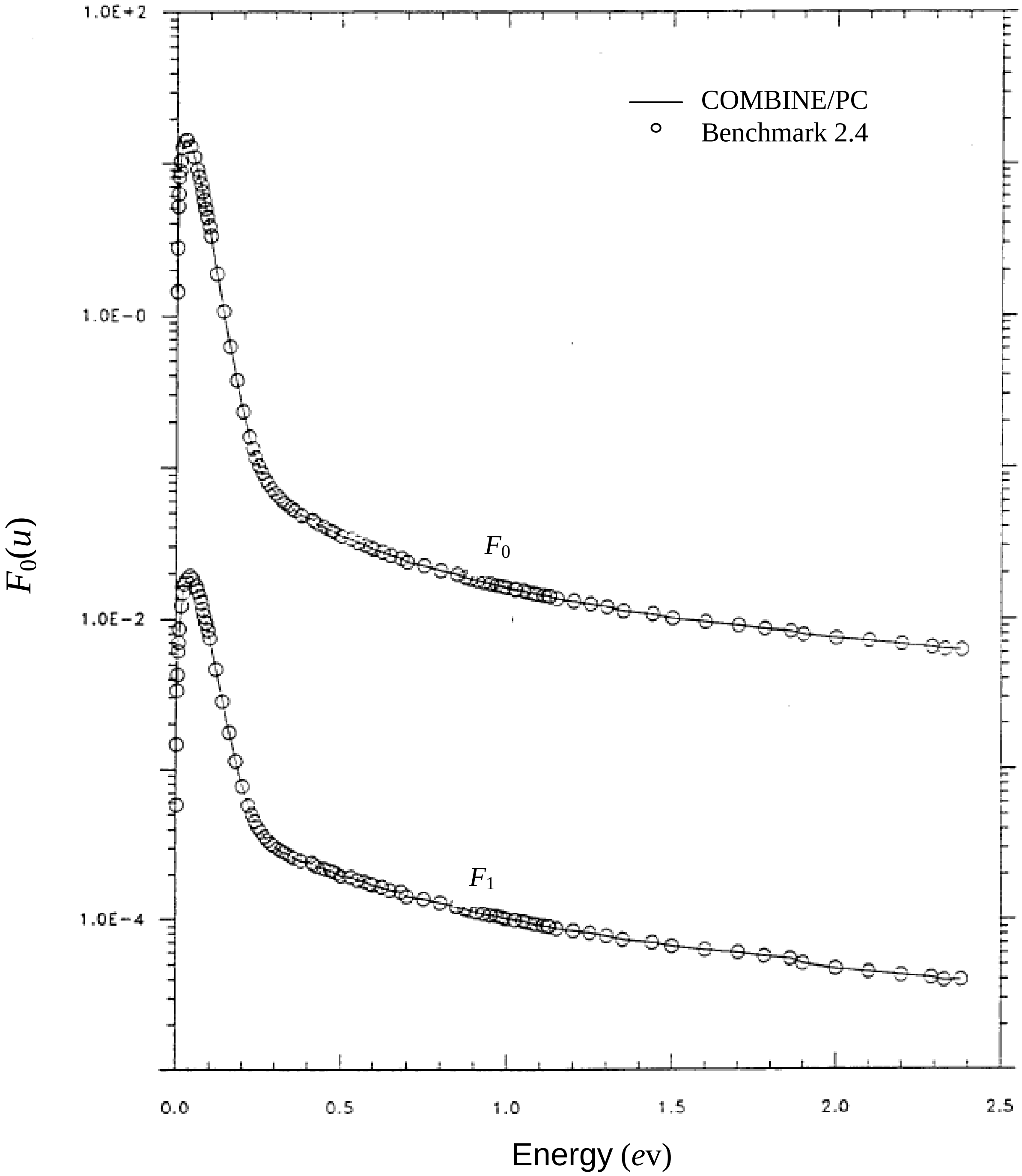

Chapter 3

ONE-GROUP NEUTRON TRANSPORT IN ONE-DIMENSION

By any stretch of the imagination, a nuclear reactor is certainly not an infinite medium. Because of the finite dimension of a reactor core, neutrons are able to escape through boundaries while slowing down or when thermalized. Thus, spatial extent must be a part of any realistic reactor analysis using either neutron transport or diffusion theory. The focus of this chapter is just that − spatial extent. Unfortunately, the analytical solution of the transport equation with both space and energy variation is formidable to say the least. To enable spatially dependent analytical solutions therefore, we consider the transport equation limited to spatial variation only. We will analyze neutrons diffusing from one position to another in the one-group approximation as derived in §1.3.1. Transport solutions for the one-group approximation are valuable for the physical and mathematical insight they provide. Further simplification is required however, since a full 3-D characterization has yet to admit, and indeed may never admit, a meaningful analytical solution. Here, only 1-D neutron transport in plane, spherical or cylindrical geometries is considered. We treat 2-D and 3-D geometries in Chapter 5.

At first, a 1-D, one-group investigation may seem unnecessarily restrictive. However, when considering realistic transport scenarios, the inner/outer iteration strategy [1] formulates multigroup solutions as a series of one-group problems. In addition, as shown in Benchmark 5.1, we solve a 2-D cylindrical transport equation with a 1-D (pseudo transport) solution. Most importantly, the essential mathematical aspects of the transport operator emerge when treating the one-group case, even for 1-D spatial variation. With regard to benchmarking, we again emphasize that a numerical algorithm developed for the most sophisticated of transport scenarios must also adequately resolve the simplest. We present 1-D, one-group benchmarks for precisely this reason.

We consider four one-group benchmarks in this chapter. The first treats the classic plane source in an infinite medium, solved in nearly every neutron transport text. We can solve this case through Fourier transforms, singular eigenfunctions, Legendre series expansion as well as other mathematical techniques. Here, we solve the fully anisotropic scattering case by the straightforward Fourier transform. The novelty of the solution is in performing the numerical inversion to obtain highly accurate spatial flux distributions. The second benchmark is for a half-space with an impinging source. This case represents the simplest meaningful transport problem with a surface. Chandrasekhar's method of invariant imbedding, originally for radiative transfer in participating media, is the solution method of choice. The third benchmark is for neutron transport in a slab and, arguably, is the first transport problem with practical application. The slab problem features the *Fn* solution, which is a novel solution of the singular integral equation form of the transport equation. For this benchmark, we present an entirely new derivation of the singular integral equations for the exiting and interior fluxes. Finally, Benchmark 3.4, patterned after the previous benchmark, considers transport in radial cylindrical geometry. Using the pseudo flux form of the transport equation, we consider critical and fixed source problems with isotropic scattering.

The one-group transport equation, Eq. (1.VI) of Chapter 1:

$$\left[\boldsymbol{\Omega}\bullet\nabla+\Sigma(\boldsymbol{r})\right]\phi(\boldsymbol{r},\boldsymbol{\Omega})= \tag{VI}$$

$$=\int_{4\pi} d\boldsymbol{\Omega}'\Sigma_s(\boldsymbol{r},\boldsymbol{\Omega}'\bullet\boldsymbol{\Omega})\phi(\boldsymbol{r},\boldsymbol{\Omega}')+$$

$$+\frac{1}{4\pi}\nu\Sigma_f(\boldsymbol{r})\int_{4\pi} d\boldsymbol{\Omega}'\phi(\boldsymbol{r},\boldsymbol{\Omega}')+Q(\boldsymbol{r},\boldsymbol{\Omega})$$

in 1-D plane and cylindrical geometries will be our focus. In plane geometry, this equation becomes Eq. (1.VIII.2)

$$\left[\mu\frac{\partial}{\partial x}+\Sigma(x)\right]\phi(x,\mu)= \tag{VIII.2}$$

$$=\frac{1}{2}\sum_{l=0}^{\infty}(2l+1)\Sigma_{sl}(x)P_l(\mu)\phi_l(x)+\frac{1}{2}\nu\Sigma_f(x)\phi_0(x)+Q(x,\mu)$$

In the following sections, these two equations are adapted to the problem of interest and solved by a variety of mathematical methods.

REFERENCES

[1] Lewis, E.E., W.F. Miller, *Computational Methods of Neutron Transport*, ANS La Grange Park, IL (1993).

Benchmark 3.1: Monoenergetic transport in an infinite medium/the Fourier transform solution

(a) Brief description

Neutron transport without energy loss in an anisotropically scattering infinite medium including space dependence.

(b) Classification

NT/I:P,SP,CY/LE(3)/OG/I,B/L,D/X(C),A(C)/NFTI

(c) Physical description

Neutrons, emitted at the center of a homogeneous infinite medium, are restricted to move in one linear dimension defined by a direction (cosine) as shown in Figure 3.1.1. Nuclei of sufficiently high mass scatter neutrons without energy loss and anisotropically. The solution defines the infinite medium Green's function.

(d) Analytical representation

(i)The one-group transport equation

Equation (1.VIII.2) for one-group of neutrons in a homogeneous plane medium is:

$$\left[\mu\frac{\partial}{\partial x}+\Sigma\right]\phi(x,\mu)= \qquad (1a)$$

$$=\frac{1}{2}\sum_{l=0}^{\infty}(2l+1)\Sigma_{sl}P_l(\mu)\phi_l(x)+\frac{1}{2}\nu\Sigma_f\phi_0(x)+Q(x,\mu)$$

with Legendre moments:

$$\phi_l(x)\equiv\int_{-1}^{1}d\mu P_l(\mu)\phi(x,\mu) \qquad (1b)$$

By measuring the spatial variable in units of mean free path, i.e. $x\rightarrow\Sigma x$, Eq. (1a) becomes:

$$\left[\mu\frac{\partial}{\partial x}+1\right]\phi(x,\mu)= \qquad (2)$$

$$=\frac{1}{2}c_s\sum_{l=0}^{\infty}(2l+1)f_{sl}P_l(\mu)\phi_l(x)+\frac{1}{2}c_f\phi_0(x)+Q(x,\mu)$$

where we have applied particle conservation in phase space ($dx\rightarrow\Sigma dx$) and have defined:

$$f_{s0}\equiv1,\ \Sigma_{sl}\equiv\Sigma_s f_{sl},\ c_s=\Sigma_s/\Sigma,\ c_f=\nu\Sigma_f/\Sigma$$

For a subcritical infinite medium, the number of secondaries, $c = c_s + c_f$, is less than unity.

For convenience, we replace f_{sl} by:

$$f_{s0} \equiv 1$$
$$f_{sl} \rightarrow \frac{c_s}{c} f_{sl}, \quad l = 1, 2, \ldots$$

to give the proper one-group transport equation in an infinite medium combining scattering and fission:

$$\left[\mu \frac{\partial}{\partial x} + 1\right] \phi(x,\mu) = \\ = \frac{1}{2} c \sum_{l=0}^{\infty} (2l+1) f_{sl} P_l(\mu) \phi_l(x) + Q(x,\mu) \tag{3a}$$

subject to the condition:

$$\lim_{|x|\to\infty} \phi(x,\mu) < \infty \tag{3b}$$

(ii) The Fourier transform solution

Application of the Fourier transformation to Eq. (3a):

$$\Psi(k,\mu) \equiv \int_{-\infty}^{\infty} dx e^{-ikx} \phi(x,\mu)$$

gives:

$$[1 + ik\mu] \Psi(k,\mu) = \frac{c}{2} \sum_{l=0}^{\infty} (2l+1) f_l P_l(\mu) \Psi_l(k) + Q(\mu) S(k) \tag{4}$$

where we assume the source is of the separable form:

$$Q(\mu, x) \equiv Q(\mu) S(x)$$

Fourier inversion to direct space is therefore:

$$\phi(x,\mu) \equiv \frac{1}{2\pi} \int_{-\infty}^{\infty} dk e^{ikx} \Psi(k,\mu)$$

Note the similarity thus far to the B_L approximation in Benchmark 2.2, but now we seek the inversion of $\Psi(k,\mu)$ to configuration space. In Eq. (4):

$$S(k) \equiv \int_{-\infty}^{\infty} dx e^{-ikx} S(x)$$

and we consider the following angular source distributions:

$$Q(\mu) \equiv \begin{cases} 1/2, & \text{Isotropic} \\ \delta(\mu - \mu_0), & \text{Beam} \end{cases}$$

In the following, any function of the variable *k* is a Fourier transform.

Projecting Eq. (4) over the Legendre polynomials $P_m(\mu)$ gives for $m = 0, 1, \ldots$:

$$\Psi_m(k) = c\sum_{l=0}^{\infty}(2l+1) f_l T_{ml}(k)\Psi_l(k) + Q_m(k)S(k) \tag{5}$$

where the transformed moments are:

$$\Psi_m(k) \equiv \int_{-1}^{1} d\mu P_m(\mu)\Psi(\mu,k)$$

We repeat the definition of $T_{ml}(k)$, originally given in Eq. (2.2.11b), here in terms of *k*:

$$T_{ml}(k) \equiv \frac{1}{2}\int_{-1}^{1} d\mu \frac{P_m(\mu)P_l(\mu)}{1+ik\mu} \tag{6a}$$

and:

$$Q_m(k) \equiv \frac{1}{2}\int_{-1}^{1} d\mu \frac{P_m(\mu)}{1+ik\mu} Q(\mu) \tag{6b}$$

in Eq. (5). For a finite scattering order *L*, the resulting set of equations becomes:

$$\sum_{l=0}^{L}\left[\delta_{ml} - (2l+1)cf_l A_{ml}(k)\right] F_l(k) = S(k)R_m(k) \tag{7}$$

with the change of dependent variable:

$$\Psi_m(k) = i^m F_m(k)$$

and:

$$R_m(k) \equiv i^{-m} Q_m(k)$$

Recall that $A_{ml}(k)$ is real valued and is [from Eq. (2.2.12b)]:

$$A_{ml}(k) \equiv i^{l-m} T_{ml}(k)$$

We can more easily visualize Eq. (7) in the following vector form:

$$\Lambda(k)\xi(k) = \boldsymbol{R}(k) \tag{8}$$

where the elements of $\Lambda(k)$ and $\xi(k)$, respectively, are:

$$\Lambda_{ml}(k) \equiv \delta_{ml} - (2l+1)cf_l A_{ml}(k), \quad m,l = 0,1,2,...,L$$

and:

$$\xi_m(k) = \frac{F_m(k)}{S(k)}$$

Note that $\Lambda(k)$ is a real valued matrix. In essence, $\xi_m(k)$ gives the m^{th} Legendre moment in k-space; and the desired scalar flux, from the inversion:

$$\Psi_0(x) = \frac{1}{2\pi} \int_{-\infty}^{\infty} dk e^{ikx} \xi_0(k) S(k) \tag{9}$$

$\xi_0(k)$, the first component of the vector $\xi(k)$, comes directly from the matrix inversion of Eq. (8):

$$\xi(k) = \Lambda^{-1}(k) \boldsymbol{R}(k) \tag{10}$$

(e) Numerical implementation and demonstration for Benchmark 3.1

We evaluate the Fourier inversion integral using a procedure (described in Appendix B.2) similar to that for the numerical Laplace transform inversion (Appendix B.1). The inversion integral given by Eq. (9) takes the form:

$$\begin{aligned}\Psi_0(x) = \frac{1}{\pi}\int_0^{\infty} dk\left[S_R(k)\xi_{0R}(k) - S_I(k)\xi_{0I}(k)\right]\cos(kx) - \\ - \frac{\operatorname{sgn}(x)}{\pi}\int_0^{\infty} dk\left[S_R(k)\xi_{0I}(k) + S_I(k)\xi_{0R}(k)\right]\sin(kx)\end{aligned} \tag{11}$$

Thus, before evaluating the inversion, we must determine the real and imaginary parts of $\xi(k)$, $\xi_{0R}(k)$ and $\xi_{0I}(k)$, from Eq. (10). Recasting Eq. (10) in terms of real and imaginary components and then equating each component (since Λ is real) gives:

$$\begin{aligned}\xi_R(k) &= \Lambda^{-1}(k) \boldsymbol{R}_R(k) \\ \xi_I(k) &= \Lambda^{-1}(k) \boldsymbol{R}_I(k)\end{aligned}$$

At least one matrix inversion is required for the determination of the real and imaginary parts of the zeroth component, which is computationally costly since the image function evaluation at each point k in the Fourier inversion integral requires a matrix inversion. To partially offset this, we perform the matrix inversion using the computer algebra package REDUCE [1] (as in Benchmark 2.2). By so doing, we obtain explicit expressions for the Fourier transform of $\xi_0(k)$, thus eliminating the need for unused extraneous terms. Because of storage limitations, however, we can only accommodate $L \leq 4$.

There are three sources of error in the above numerical algorithm, including errors from numerical quadrature, series truncation and round off. We evaluate each integral of the infinite series in Eq.

(B.2.2b) by Romberg integration (Appendix A.3). Convergence occurs when the addition of three consecutive terms produces a relative error below a user specified amount. We also sense the round off error from the magnitudes of the two integrals defining the scalar flux of Eq. (11). If a significant number of digits is lost through subtraction, we re-evaluate the two components of Eq. (11) at a reduced relative error until significance is restored or the relative error called for in the Romberg integration falls below 10^{-12} for double precision arithmetic.

Figures 3.1.2(a) and 3.1.2(b) show the scalar flux profiles in an isotropically scattering ($L = 0$) infinite medium with variation of c according to $0.1 \leq c \leq 0.9$ for both normal beam and isotropic sources. As expected, the flux increases as c approaches one. For beam incidence, the discontinuity at $x = 0$ is a result of the monodirectional nature of the uncollided contribution. Also of note is the exponential variation of the flux at large distances indicating the onset of the asymptotic flux variation. Figure 3.1.3 shows neutron penetration with source inclination μ_0. The greater the beam inclination, the greater the penetration for $x > 0$ and the less the penetration for $x < 0$. Figure 3.1.4 displays the flux for an anisotropically scattering medium with $f_1 = \pm 1, \pm 0.75, \pm 0.25, 0$ for a normally incident beam. At first glance, the appearance of negative fluxes near $x = 0$ for some values of f_l is disturbing. Recall, however, that for linearly anisotropic scattering, the scattering kernel is:

$$f\left(\mu', \mu\right) = \frac{1}{2}\left[1 + 3 f_1 \mu' \mu\right]$$

Thus, when $\left|f_1\right| \geq 1/3$, the scattering kernel can become negative, giving rise to a negative scattering source and consequently negative fluxes.

Application of the following well known geometrical transformations [2] (see Benchmark 4.1 for the derivation):

$$\Phi_{sp}\left(r\right) = -\frac{1}{2\pi r}\frac{d\Psi_0\left(r\right)}{dr}$$

$$\Phi_{cy}\left(\rho\right) = 2\int_0^\infty dz \Phi_{sp}\left(\sqrt{\rho^2 + z^2}\right)$$

gives the scalar flux in spherical (point source) and cylindrical (infinite line source) geometries directly from the scalar flux in infinite plane geometry. We have numerically implemented these expressions as Fourier transform inversions similar to the plane case. Figures 3.1.5(a) and 3.1.5(b) provide a comparison of the scalar fluxes for a variation of c in spherical and cylindrical geometries for $L = 3$ ($f_l =$ 1.0, 0.5, 0.3, 0.2, $l = 0,...,3$) indicating intuitive trends.

The one-group demonstration concludes with the determination of the flux from a distributed source. Figure 3.1.6 shows the flux in plane geometry for an isotropic source in the positive half-space:

$$S\left(x\right) = \Theta\left(x\right)$$

which has the Fourier transform:

$$S\left(k\right) = \frac{1}{ik}$$

for variation of c. We can confirm to three decimal places that the flux approaches $1/(1 - c)$ for large positive x, as theoretically predicted.

To qualify Benchmark 3.1, Table 3.1.1 presents results for a normal beam source in an isotropically scattering medium of $c = 0.9$ for a relative error ε varying from 10^{-3} to 10^{-6}. We expect the last column to be correct to all digits posted and conclude that the numerical inversion indeed is a convergent algorithm.

Table 3.1.1. Qualification of Benchmark 3.1

Scalar flux for a normal beam (isotropic scattering, c = 0.9)

$x\backslash\varepsilon$	10^{-3}	10^{-4}	10^{-5}	10^{-6}
-5.00000E+00	1.02520E-01	1.02510E-01	1.02507E-01	1.02506E-01
-4.00000E+00	1.73592E-01	1.73592E-01	1.73596E-01	1.73596E-01
-3.00000E+00	2.94351E-01	2.94474E-01	2.94474E-01	2.94474E-01
-2.00000E+00	5.01505E-01	5.01679E-01	5.01677E-01	5.01677E-01
-1.00000E+00	8.66711E-01	8.66742E-01	8.66764E-01	8.66764E-01
-1.00000E-02	1.66724E+00	1.66724E+00	1.66724E+00	1.66724E+00
1.00000E-02	2.71018E+00	2.71018E+00	2.71018E+00	2.71018E+00
1.00000E+00	2.17739E+00	2.17750E+00	2.17754E+00	2.17754E+00
2.00000E+00	1.42305E+00	1.42338E+00	1.42338E+00	1.42338E+00
3.00000E+00	8.83953E-01	8.83952E-01	8.83953E-01	8.83953E-01
4.00000E+00	5.36688E-01	5.36683E-01	5.36683E-01	5.36683E-01
5.00000E+00	3.22107E-01	3.22110E-01	3.22109E-01	3.22109E-01

REFERENCES

[1] MacCallum, M.A.H., F.J. Wright, *Algebraic Computing with REDUCE*, in Lecture Notes from the First Brazilian School on Computer Algebra, M.J. Reboucas (Ed.), Oxford University Press, Oxford, UK (1991).

[2] Case, K.M., P.F. Zweifel, *Linear Transport Theory*, Addison-Wesley, MA (1967).

Figure 3.1.1. Direction cosine in *x* direction

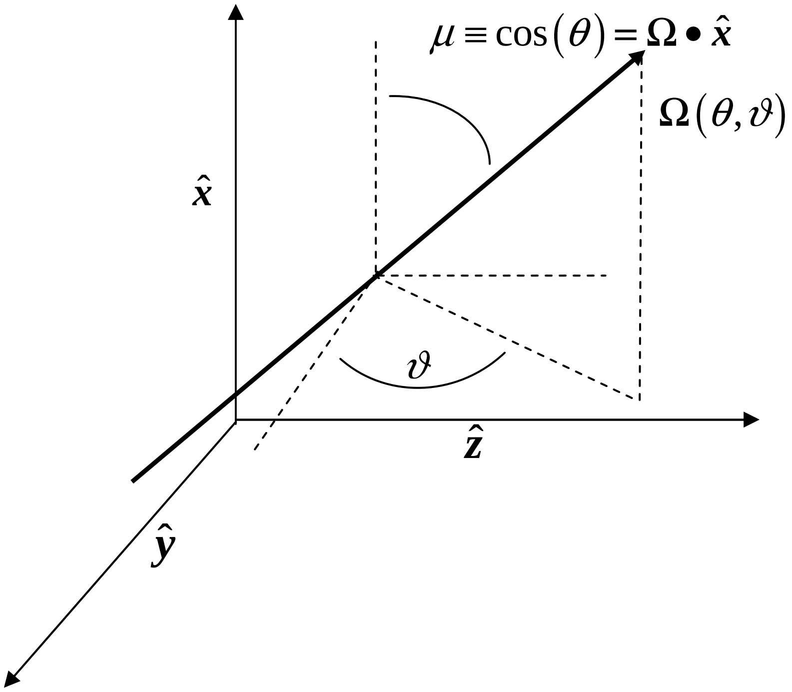

Figure 3.1.2. Monoenergetic 1-D neutron transport in an infinite medium (a) beam source: $\mu_0 = 1$ (b) isotropic source: variation of c

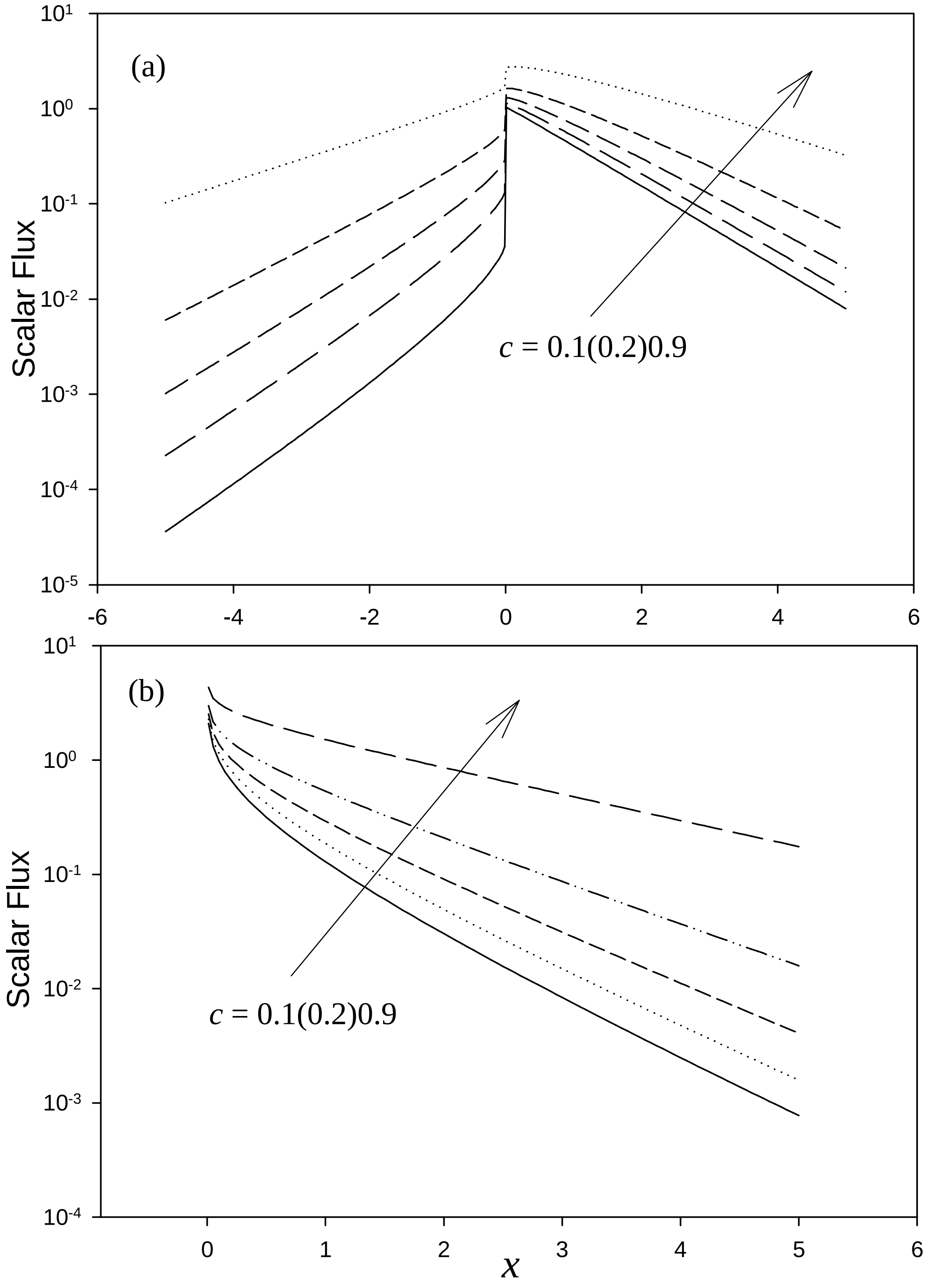

Figure 3.1.3. Monoenergetic neutron transport in an infinite medium with a beam source: variation of μ_0

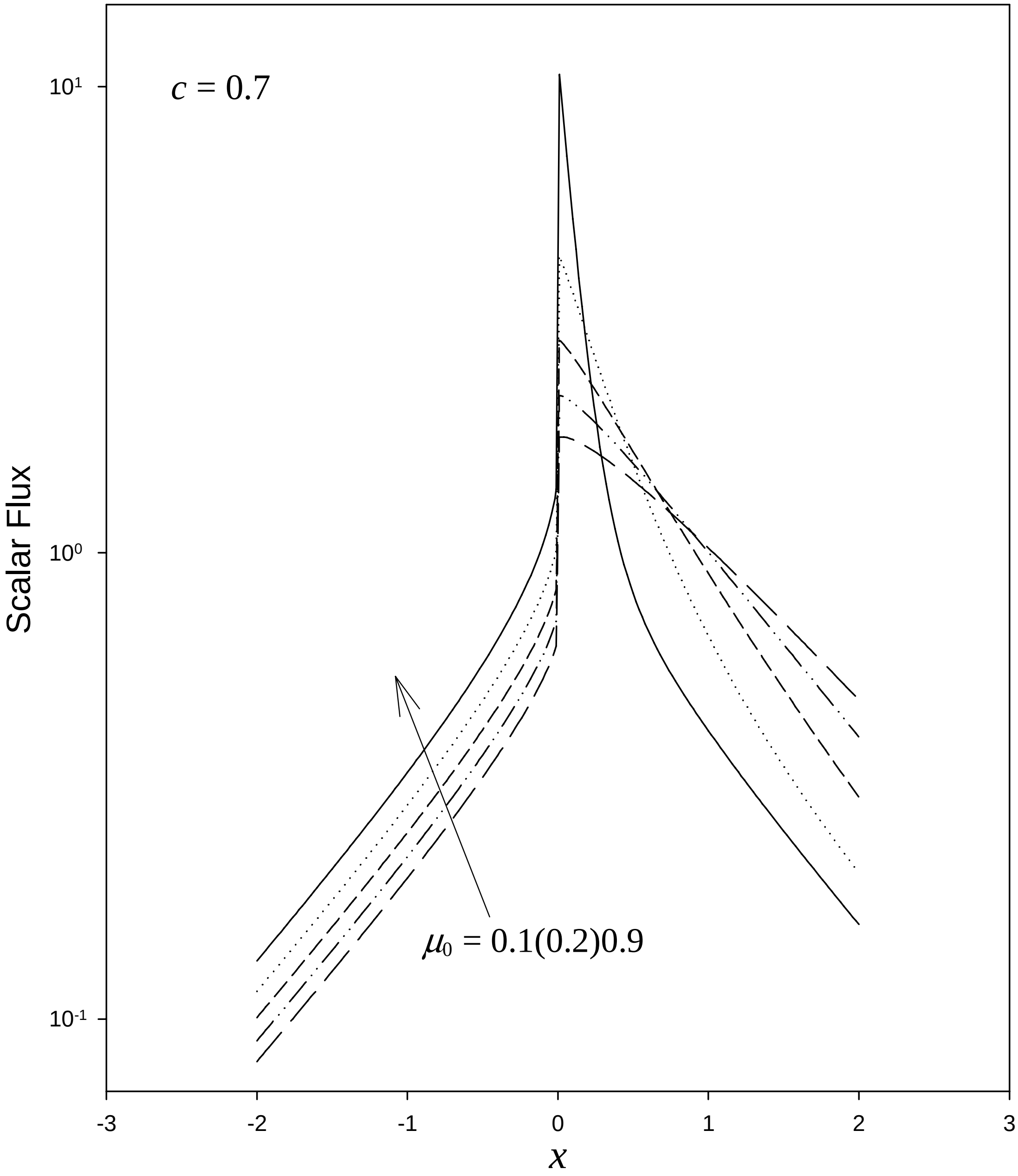

Figure 3.1.4. Monoenergetic 1-D neutron transport in an infinite medium: variation of f_1 for a beam source ($\mu_0 = 1$)

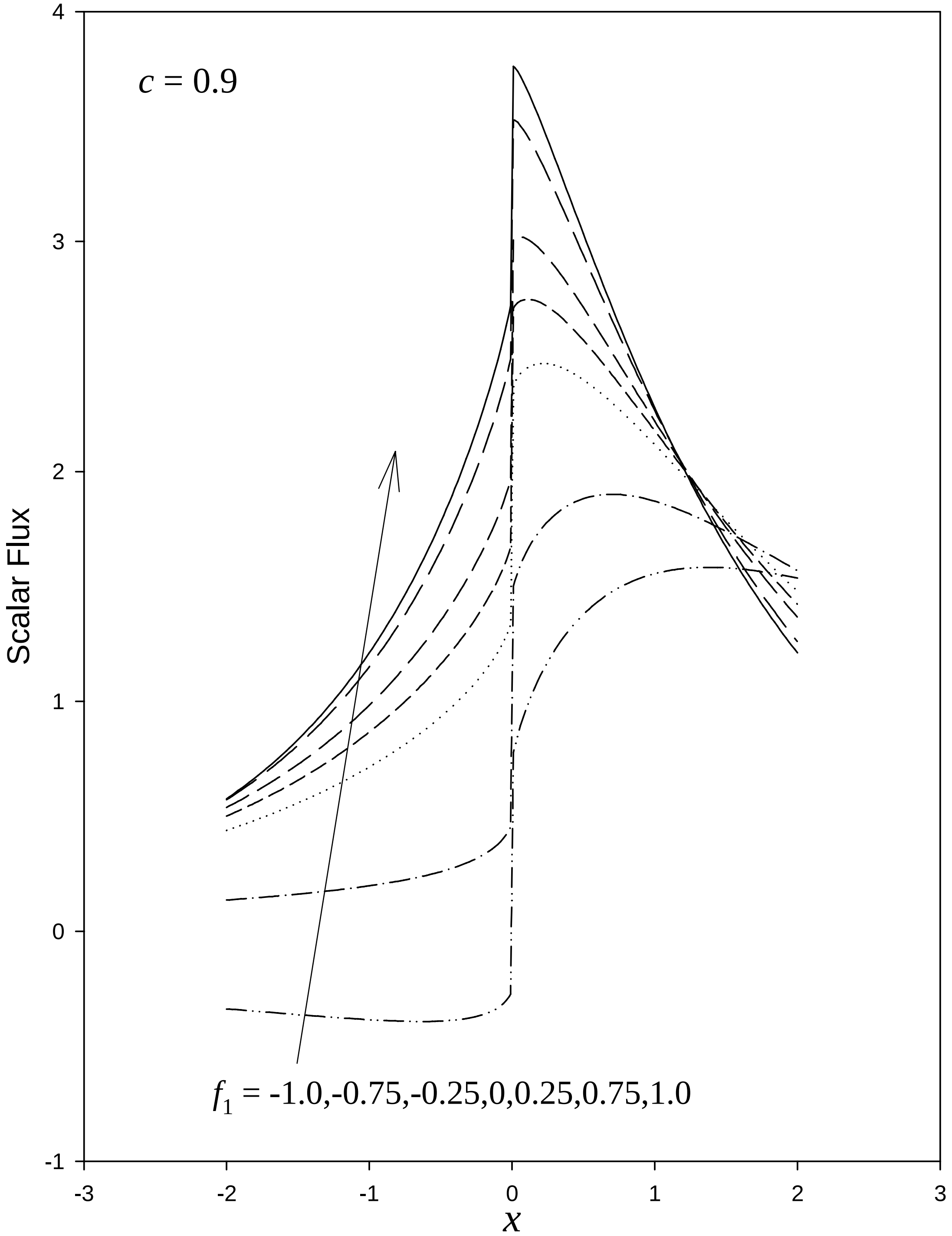

Figure 3.1.5. Monoenergetic 1-D neutron transport in an infinite medium

Variation of c in (a) spherical geometry (b) cylindrical geometry

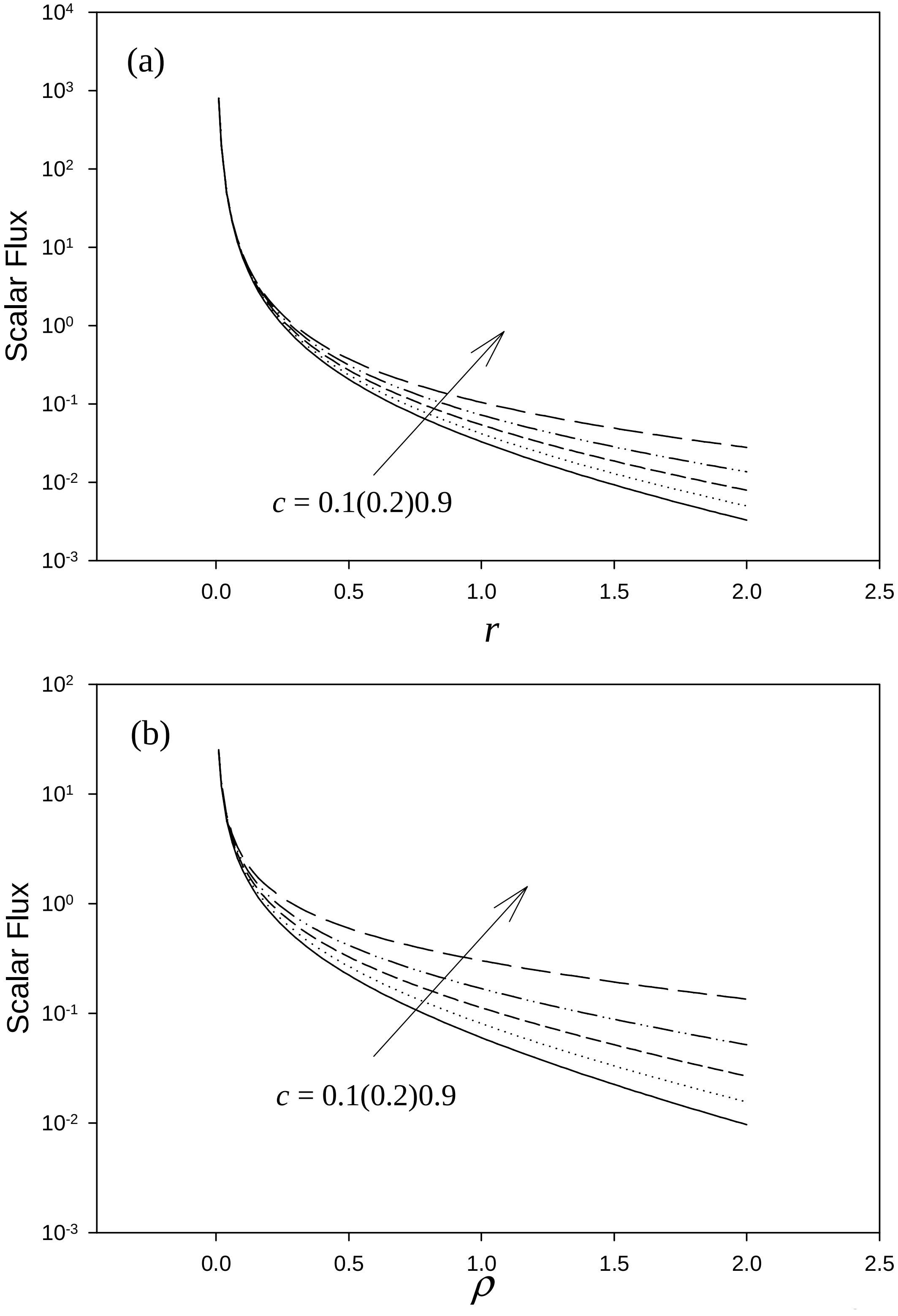

Figure 3.1.6. Monoenergetic 1-D neutron transport in an infinite medium for a uniformly distributed source in *x* > 0

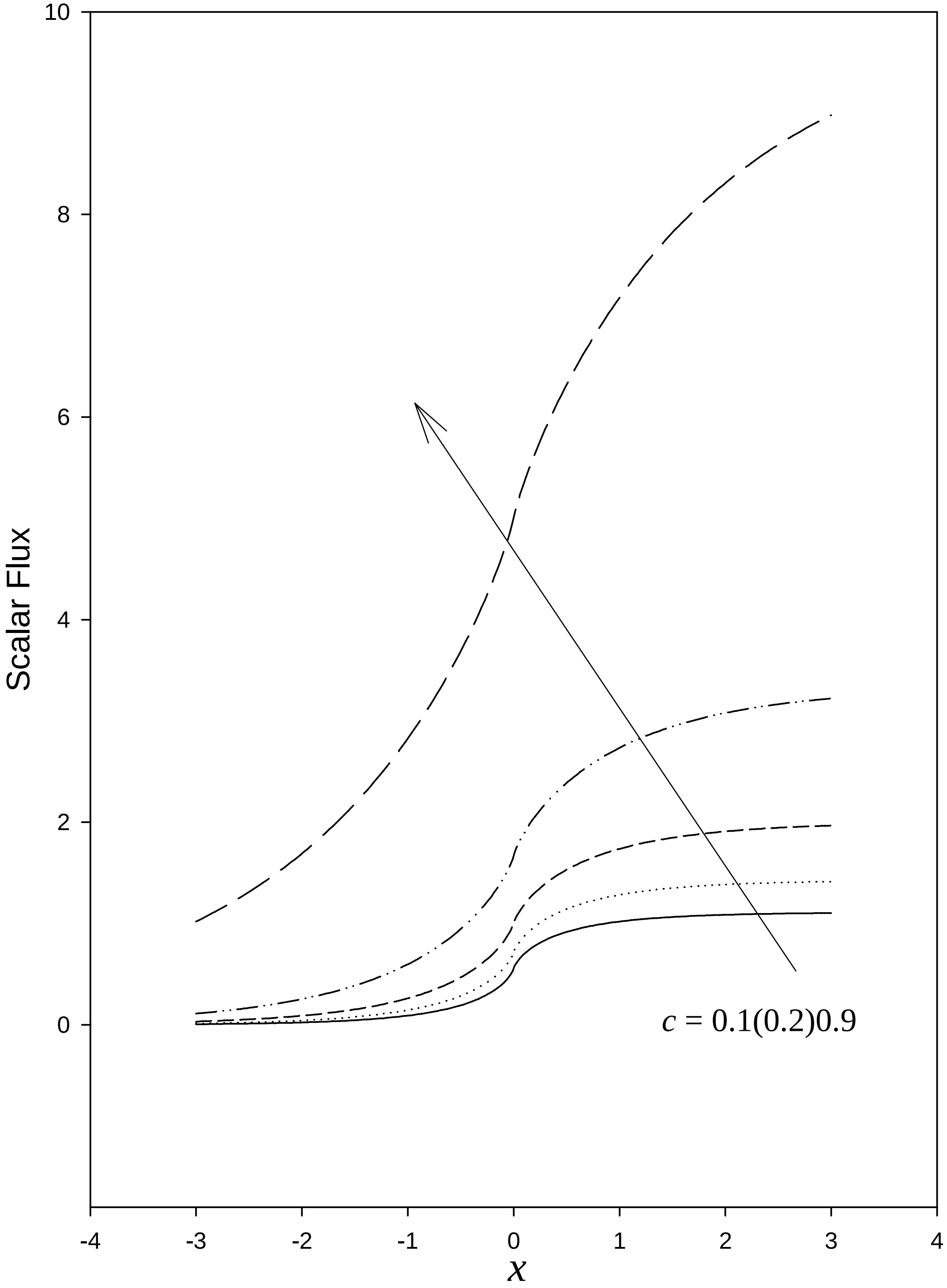

Benchmark 3.2: Monoenergetic transport in a semi-infinite medium/the Laplace transform solution

(a) Brief description

Monoenergetic neutron transport in a homogeneous half-space with isotropic scattering – the albedo problem.

(b) Classification

NT/H/I/OG/I,B/L/X(C),A(C)/NLTI

(c) Physical description

Neutrons, uniformly entering the free surface of a homogeneous semi-infinite medium, are restricted to move in one linear dimension defined by a direction (cosine) as shown in Figure 3.2.1. Nuclei of sufficiently high mass scatter neutrons without energy loss and isotropically. This is the most basic transport solution to include a boundary.

(d) Analytical representation

The transport equation, Eq. (1.VIII.2), assuming isotropic scattering (L = 0) for $x \geq 0$ without a distributed source and distance measure in mean free path is:

$$\left[\mu\frac{\partial}{\partial x}+1\right]\phi(x,\mu)=\frac{c}{2}\int_{-1}^{1}d\mu'\phi(x,\mu') \tag{1a}$$

A flux enters from a vacuum into the medium at the boundary x = 0 either as a beam or isotropically:

$$\phi(0,\mu)=Q(\mu)\equiv\begin{cases}\delta(\mu-\mu_0), & \text{Beam}\\ 1, & \text{Isotropic}\end{cases} \tag{1b}$$

for $\mu > 0$ with:

$$c=\frac{\Sigma_s+\nu\Sigma_f}{\Sigma}\leq 1$$

The flux infinitely far from the boundary obeys:

$$\lim_{x\to\infty}\phi(x,\mu)<\infty \tag{1c}$$

The solution of the integral transport equation determines a general expression for the angular flux. The identical procedure as presented in §1.2.1 applies to Eq. (1a) leading to an integral transport equation. Since the distance along the neutron trajectory between x and x', shown in Figure 3.2.1, is:

$$s = \frac{(x - x')}{\mu}$$

and since:

$$\frac{d}{ds} = \frac{\partial x'}{\partial s}\frac{\partial}{\partial x'} = -\mu\frac{\partial}{\partial x'}$$

Eq. (1a), evaluated at x' becomes:

$$\left[\frac{d}{ds} - 1\right]\phi(x',\mu) = -\frac{c}{2}\phi(x') \tag{2}$$

where the scalar flux is:

$$\phi(x) = \int_{-1}^{1} d\mu'\phi(x,\mu')$$

The formal solution to Eq. (2) is:

$$\phi(x,\mu) = e^{-(x-x')/\mu}\phi(x',\mu) + \frac{c}{2\mu}\int_{x'}^{x} dx'' e^{-(x-x'')/\mu}\phi(x'') \tag{3}$$

and if $\mu < 0$ and $x' \to \infty$, Eq. (3) becomes:

$$\phi(x,-|\mu|) = \frac{c}{2|\mu|}\int_{x}^{\infty} dx' e^{-(x-x')/|\mu|}\phi(x') \tag{4a}$$

In particular, at $x = 0$:

$$\phi(0,-|\mu|) = \frac{c}{2|\mu|}\int_{0}^{\infty} dx' e^{-x'/|\mu|}\phi(x') \tag{4b}$$

Note that, if we replace $|\mu|$ by $1/s$, the exiting angular flux is a Laplace transform and the scalar flux is formally the Laplace transform inversion:

$$\phi(x) = \frac{2}{c}\mathrm{L}_x^{-1}\left[\frac{\phi(0,-1/s)}{s}\right] \tag{5}$$

Thus, Eq. (5) determines the scalar flux either analytically or numerically if we know the analytic continuation of the exiting angular flux $\phi(0,-\mu)$. Fortunately, in the literature, these expressions do exist for the impinging flux distributions considered [Eq. (1b)]. With only modest modification, we derive the exiting distribution for the beam source in Benchmark 5.1; and therefore, do not repeat it here. In that derivation, with $a(\mu) = b(\mu) \equiv 1$ and ξ replaced by μ, the (Chandrasekhar) H-function emerges giving the following exiting distribution [1] for an entering beam:

$$\phi(0,-\mu;\mu_0)=\frac{c}{2\mu}\frac{\mu\mu_0}{\mu+\mu_0}H(\mu_0)H(\mu) \tag{6a}$$

Note that dependence on the source inclination μ_0 is now explicitly included.

Integration of Eq. (6a) over the inclination μ_0 on [0,1] gives the following exiting distribution for an isotropic source:

$$\phi(0,-\mu)=1-\sqrt{1-c}\,H(\mu) \tag{6b}$$

where the *H*-function satisfies [1]:

$$H(\mu)=1+\frac{c\mu}{2}H(\mu)\int_0^1 d\mu'\frac{H(\mu')}{\mu+\mu'} \tag{7}$$

Therefore, the final expressions for the interior scalar flux become:

$$\phi(x)=\frac{2}{c}\mathrm{L}_x^{-1}\left\{\begin{array}{l}\dfrac{c}{2}\dfrac{\mu_0}{1+s\mu_0}H(\mu_0)H(1/s),\ \text{Beam source}\\ \left[1-\sqrt{1-c}\,H(1/s)\right]/s,\ \text{Isotropic source}\end{array}\right\} \tag{8}$$

We can evaluate the inversions in Eq. (8) either by analytic continuation into the complex plane or numerically. Having developed a reliable numerical inversion in Appendix B.1, we will apply it here.

(e) Numerical implementation and demonstration for Benchmark 3.2

An iterative procedure gives the *H*-function. First, we discretize the angular variable μ according to the abscissa μ_m of a shifted Legendre Gauss quadrature of order *Lm*, and then follow a two-step iteration to solve Eq. (7) at each abscissa μ_m:

$$H_m^{k+1/2}=\left[1-\frac{c}{2}\mu_m\sum_{m'=1}^{Lm}\omega_{m'}\frac{H_{m'}^k}{\mu_m+\mu_{m'}}\right]^{-1} \tag{9a}$$

$$H_m^{k+1}=\frac{\alpha_0}{\alpha_0^{k+1/2}}H_m^{k+1/2}$$

where:

$$\alpha_0^{k+1/2}\equiv\sum_{m'=1}^{Lm}\omega_{m'}H_{m'}^{k+1/2} \tag{9b}$$

and [1]:

$$\alpha_0 \equiv \int_0^1 d\mu H(\mu) = \frac{2}{c}\left[1-\sqrt{1-c}\right] \tag{9c}$$

A shifted Gauss Legendre quadrature approximates the integral in Eq. (7) with the quadrature abscissa and weights obtained from the GAULEG subroutine of Ref. 2. This iterative scheme requires that the zeroth moment always be satisfied, which, fortunately, we obtain analytically from Eq. (9c). Interpolation gives *H*(1/*s*) in Eq. (8) from Eq. (7) as:

$$H(1/s) = \left[1 - \frac{c}{2}\sum_{m'=1}^{Lm} \omega_{m'} \frac{H_{m'}}{1+s\mu_{m'}}\right]^{-1} \tag{9}$$

The iterative procedure features increasing the order of the quadrature order, *Lm*, until convergence to give highly accurate results. Finally, the numerical Laplace transform inversion gives the flux from Eq. (8).

Figures 3.2.2(a) and 3.2.2(b) show the behavior of the flux in media with various scattering properties and impinging sources. For a beam source, note how the derivative of the flux at $x = 0^+$ changes sign as c passes through $c = 0.7$. This indicates the dominance of scattering over absorption and leakage, which allows more neutrons near the free surface as c increases. As c approaches one, the flux becomes more uniform, approaching an asymptotic value for c equal one at large x. For an isotopically entering flux, the derivative of the scalar flux at the free surface does not change sign. For c equal one, the uniform flux shown in Figure 3.2.2(c) comes about because the entering isotropic source simulates the same semi-infinite medium for $x < 0$ as for $x > 0$, thus together forming an infinite medium. Figure 3.2.3 shows how the neutrons penetrate deeper into the medium as the beam source inclination μ_0 tends toward normal incidence. Also, note the independence of the asymptotic flux decay away from the source with respect to μ_0. This is numerical confirmation that the eigenvalue of the transport equation depends on medium properties only.

Table 3.2.1 presents a qualification of Benchmark 3.2 for a normal beam on a half-space with $c = 0.99$. We expect all digits of the last column to be correct.

Table 3.2.1. Qualification of Benchmark 3.2

Scalar flux for normal beam (c = 0.99)

$x\backslash\varepsilon$	10^{-3}	10^{-4}	10^{-5}	10^{-6}
1.00000E-05	2.47287E+00	2.47287E+00	2.47287E+00	2.47287E+00
5.00000E-01	3.23071E+00	3.23075E+00	3.23075E+00	3.23075E+00
1.00000E+00	3.31079E+00	3.31086E+00	3.31086E+00	3.31086E+00
1.50000E+00	3.21258E+00	3.21262E+00	3.21262E+00	3.21262E+00
2.00000E+00	3.04184E+00	3.04188E+00	3.04188E+00	3.04188E+00
2.50000E+00	2.84329E+00	2.84333E+00	2.84333E+00	2.84333E+00
3.00000E+00	2.63831E+00	2.63836E+00	2.63836E+00	2.63836E+00
3.50000E+00	2.43752E+00	2.43757E+00	2.43757E+00	2.43757E+00
4.00000E+00	2.24608E+00	2.24612E+00	2.24612E+00	2.24612E+00
4.50000E+00	2.06629E+00	2.06633E+00	2.06633E+00	2.06633E+00
5.00000E+00	1.89895E+00	1.89899E+00	1.89899E+00	1.89899E+00

REFERENCES

[1] Chandrasekhar, S., *Radiative Transfer*, Dover, NY (1960).

[2] Press, W., *et al.*, *Numerical Recipes*, Cambridge University Press, NY (1986).

Figure 3.2.1. Neutron trajectory in a semi-infinite plane medium

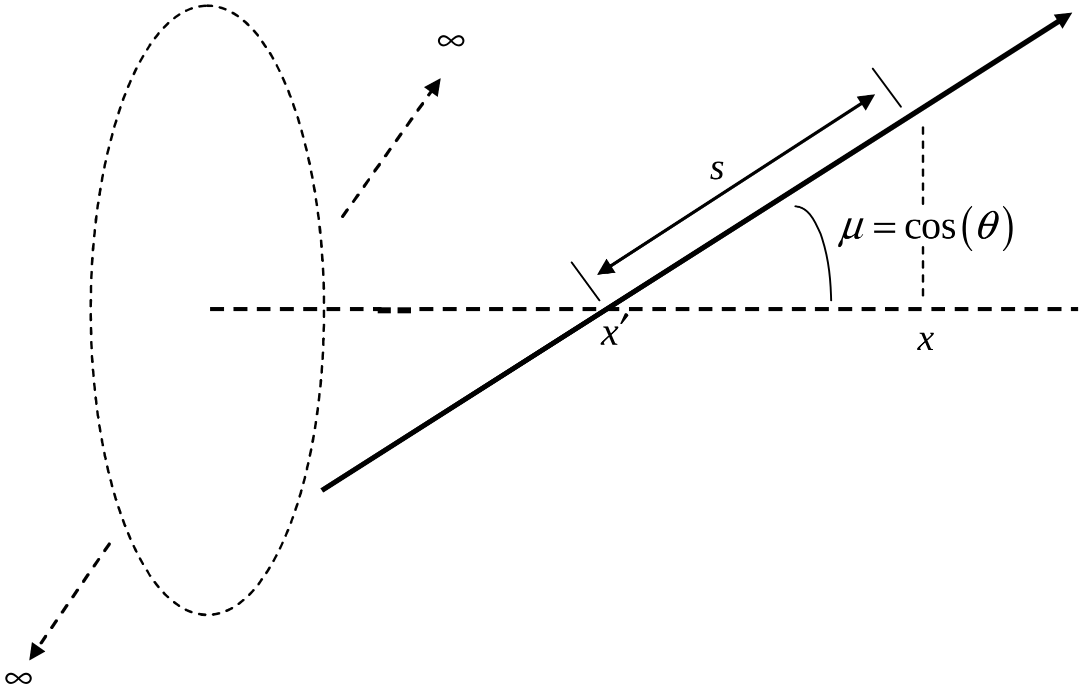

Figure 3.2.2(a). Monoenergetic 1-D neutron transport in a half-space

Variation of c for beam source ($\mu_0 = 1$)

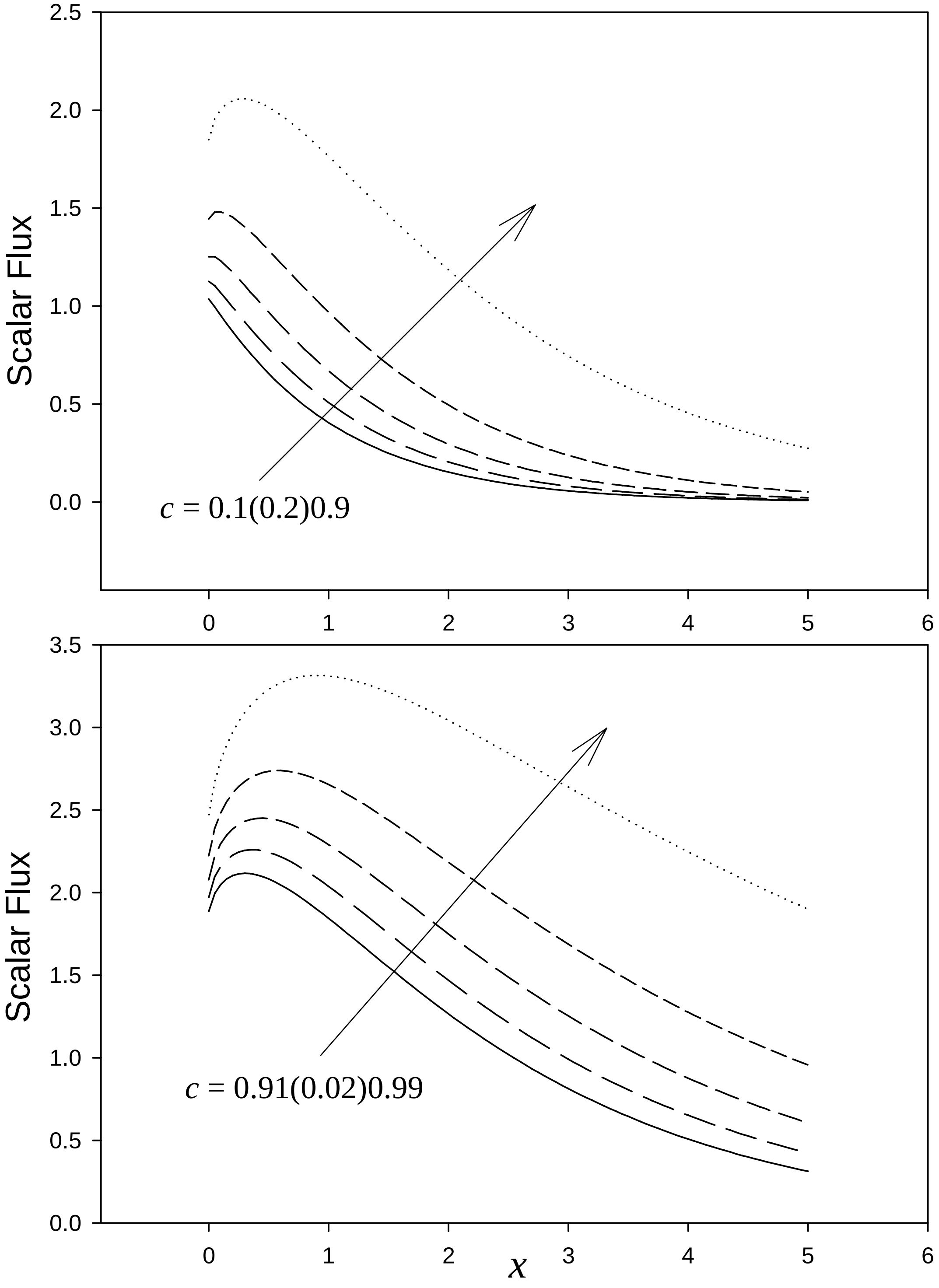

Figure 3.2.2(b). Monoenergetic 1-D neutron transport in a half-space

Variation of c for an isotropic source

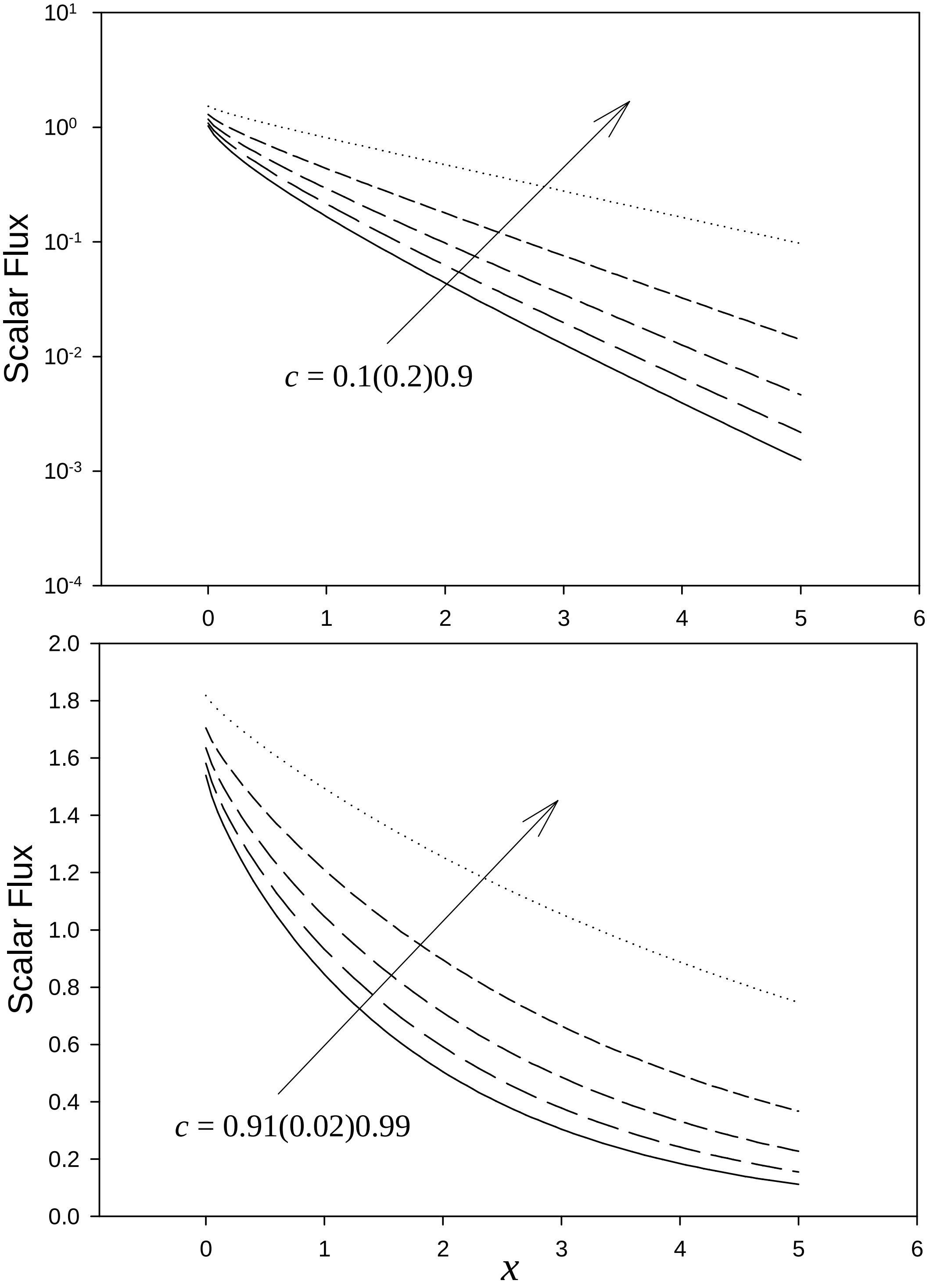

Figure 3.2.2(c). Flux variation near *c* = 1 for an isotropic source

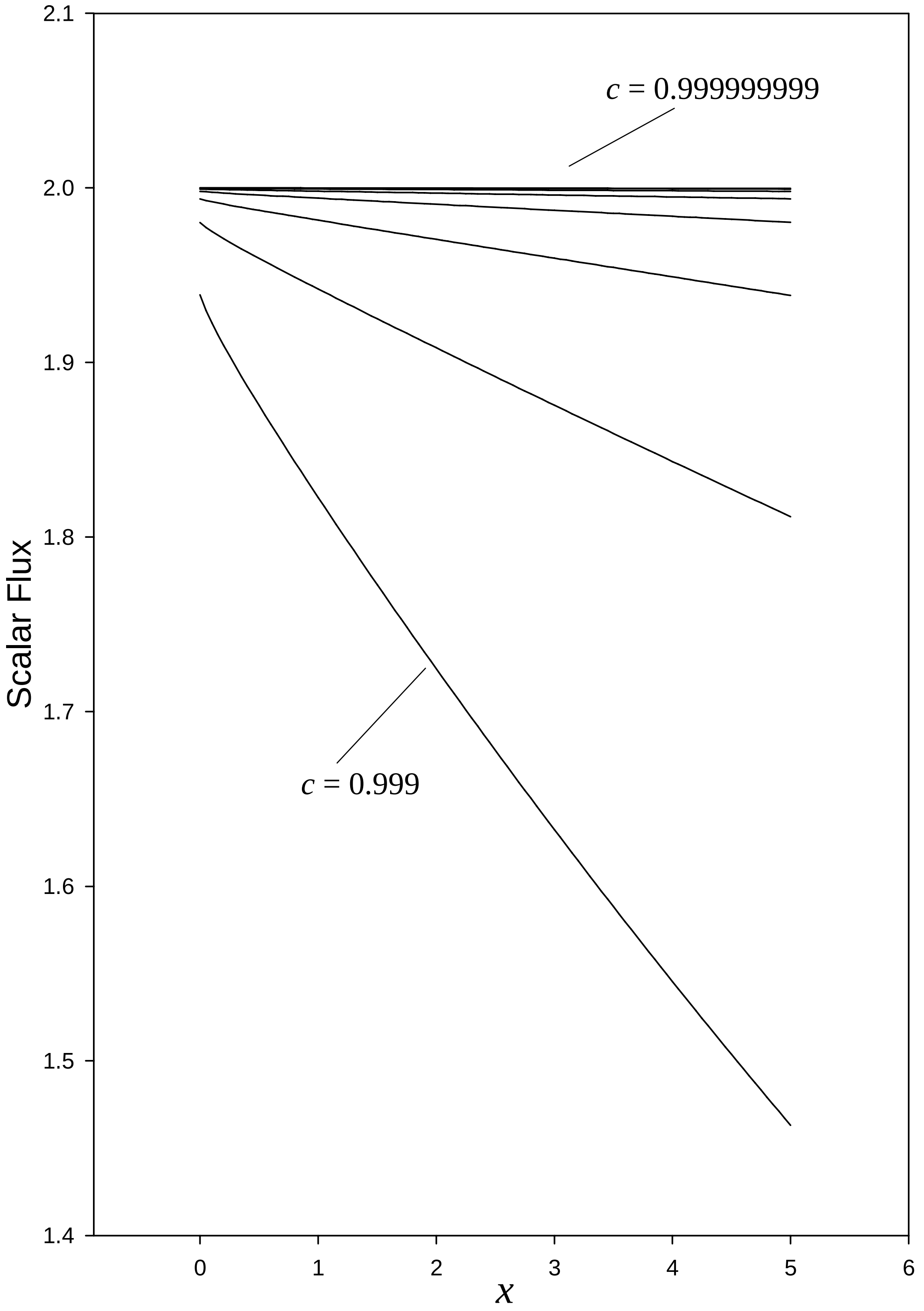

Figure 3.2.3. Monoenergetic neutron transport in a half-space

Variation of the beam angle on incidence

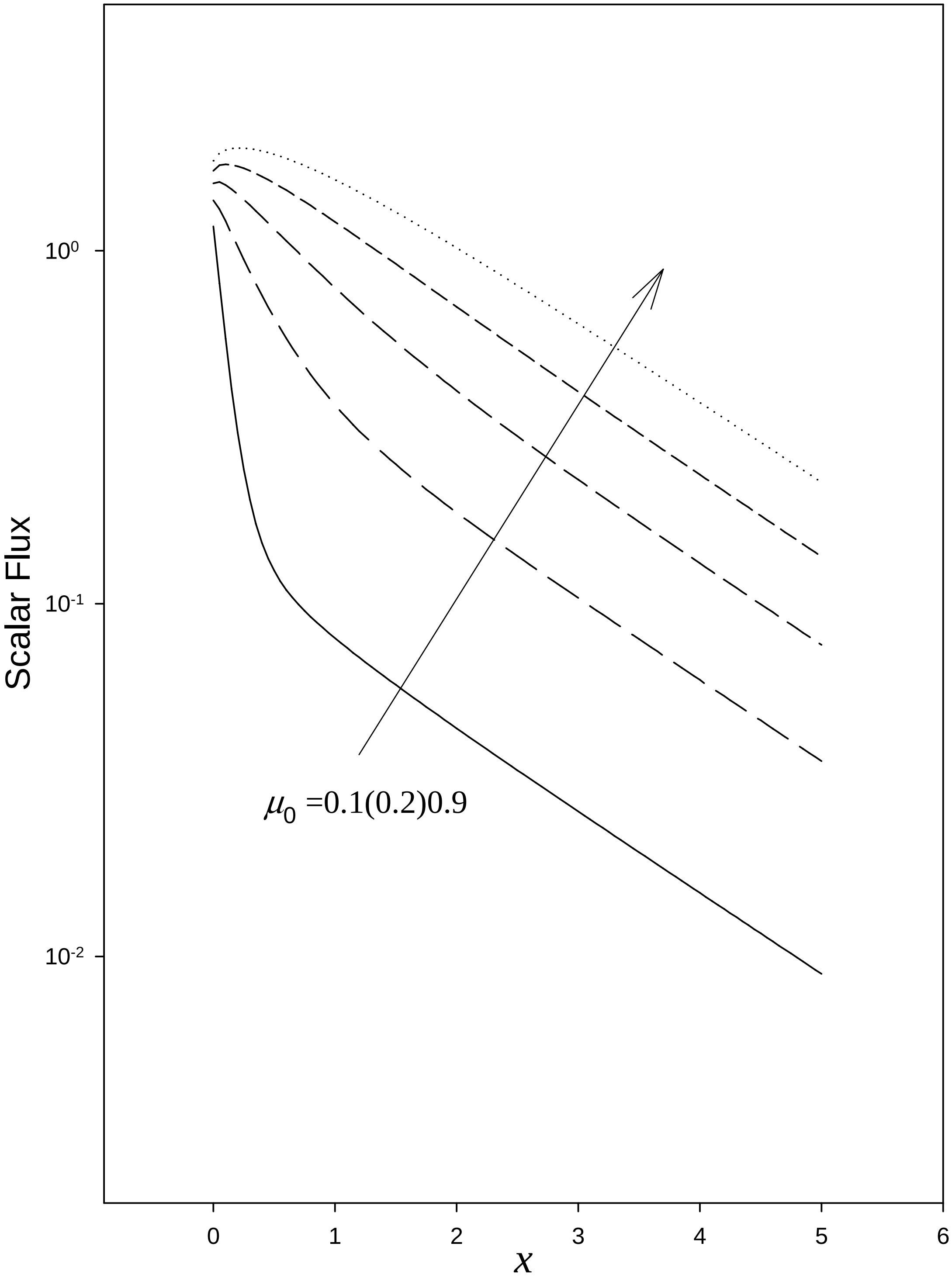

Benchmark 3.3: Monoenergetic transport in a 1-D slab/the *Fn* solution

(a) Brief description

Monoenergetic neutron transport in an isotropically scattering slab (two surfaces) with vacuum boundary conditions and an impinging flux on the left surface.

(b) Classification

NT/P:S/I/OG/B/L/X(C),A(D)/FN

(c) Physical description

Monodirectional neutrons enter the left surface of a slab and scatter isotopically without energy loss. The slab, embedded in a vacuum, is composed of a single homogeneous region.

(d) Analytical representation

Equation (1.VIII.2) gives the relevant 1-D, one-group neutron transport equation for a slab of width Δ:

$$\left[\mu\frac{\partial}{\partial x}+1\right]\phi(x,\mu)=\frac{c}{2}\int_{-1}^{1}d\mu'\phi(x,\mu') \tag{1a}$$

with the following boundary conditions for $\mu > 0$:

$$\phi(0,\mu)=F_L(\mu) \tag{1b}$$

$$\phi(\Delta,-\mu)=0 \tag{1c}$$

The number of secondaries *c*, including fission, is:

$$c=\frac{\Sigma_s+\nu\Sigma_f}{\Sigma}=c_s+c_f$$

The application of the *Fn* method, derived in detail by following an entirely new approach, yields the angular flux at the boundaries and the scalar flux in the interior.

(i) The integral transport equation and the pseudo flux

A new pseudo transport formulation will give the singular integral equations of the *Fn* method. The integral transport equation most conveniently gives the pseudo transport equation, as shown in §1.2.2. It is the pseudo equation, rather than the usual integro-differential equation, that will be the centerpiece of the following derivation.

For neutron travel between two points x' and x in plane geometry, the integral transport equation, as specified in the previous benchmark, is:

$$\phi(x,\mu) = e^{-(x-x')/\mu}\phi(x',\mu) + \frac{c}{2\mu}\int_{x'}^{x} dx'' e^{-(x-x'')/\mu}\phi(x'') \tag{2}$$

If $x' = 0$ and $x' = \Delta$, there results for $\mu > 0$:

$$\phi(x,\mu) = e^{-x/\mu}F_L(\mu) + \frac{c}{2\mu}\int_{0}^{x} dx' e^{-(x-x')/\mu}\phi(x') \tag{3a}$$

$$\phi(x,-\mu) = \frac{c}{2\mu}\int_{x}^{\Delta} dx' e^{-(x'-x)/\mu}\phi(x') \tag{3b}$$

in positive and negative directions respectively after application of the boundary conditions. The scalar flux is therefore:

$$\phi(x) = \int_{-1}^{1} d\mu\phi(x,\mu) = \int_{0}^{1} d\mu\left[\phi(x,\mu) + \phi(x,-\mu)\right] = \int_{0}^{1} d\mu\psi(x,\mu) \tag{4a}$$

with the pseudo (angular) flux defined as:

$$\psi(x,\mu) \equiv \phi(x,\mu) + \phi(x,-\mu) \tag{4b}$$

for $0 < \mu \leq 1$, or explicitly from Eqs. (3):

$$\psi(x,\mu) = \frac{c}{2\mu}\left[\begin{array}{l} \int_{0}^{x} dx' e^{-(x-x')/\mu}\phi(x') + \\ + \int_{x}^{\Delta} dx' e^{-(x'-x)/\mu}\phi(x') \end{array}\right] + e^{-x/\mu}F_L(\mu) \tag{5}$$

In plane geometry, we can relate the pseudo "angular" flux directly to the actual angular flux. This is not true in any other geometry however. In particular, at the surfaces:

$$\begin{aligned} \psi(0,\mu) &= F_L(\mu) + \phi(0,-\mu) \\ \psi(\Delta,\mu) &= \phi(\Delta,\mu) \end{aligned} \tag{6}$$

The angular flux comes from manipulation of Eq. (5).

We also note that the pseudo flux is equivalent to the even/odd parity form of the transport equation. However, the solution, expressed through singular integral equations, is preferred here because of its novelty and its connection to cylindrical geometry considered next.

(ii) The transport equation for the pseudo flux

On differentiating $\psi(x,\mu)$ in Eq. (5) and applying Liebinz's formula for differentiating an integral [1], we find:

$$\frac{\partial\psi(x,\mu)}{\partial x}=\frac{c}{2\mu^2}\begin{bmatrix}-\int_0^x dx'e^{-(x-x')/\mu}\phi(x')+\\+\int_x^\Delta dx'e^{-(x'-x)/\mu}\phi(x')\end{bmatrix}-\frac{1}{\mu}e^{-x/\mu}F_L(\mu) \tag{7}$$

Differentiating again, using Eq. (5), gives the pseudo flux form of the transport equation in plane geometry for $\mu\in[0,1]$ as:

$$\left[\frac{\partial^2}{\partial x^2}-\frac{1}{\mu^2}\right]\psi(x,\mu)=-\frac{c}{\mu^2}\phi(x) \tag{8}$$

Since there are two derivatives, two conditions on $\psi(x,\mu)$ are required for the solution. Equation (7), evaluated at $x = 0$, gives for the first derivative:

$$\left.\frac{\partial\psi(x,\mu)}{\partial x}\right|_{x=0}=\frac{c}{2\mu^2}\int_0^\Delta dx'e^{-x'/\mu}\phi(x')-\frac{1}{\mu}F_L(\mu)$$

and since, from Eq. (5):

$$\frac{c}{2\mu}\int_0^\Delta dx'e^{-x'/\mu}\phi(x')=\psi(0,\mu)-F_L(\mu)$$

we have:

$$\left.\frac{\partial\psi(x,\mu)}{\partial x}\right|_{x=0}=\frac{1}{\mu}\left[\psi(0,\mu)-2F_L(\mu)\right] \tag{9a}$$

The second condition comes from evaluation of Eq. (7) at the surface $x = \Delta$:

$$\left.\frac{\partial\psi(x,\mu)}{\partial x}\right|_{x=\Delta}=-\frac{c}{2\mu^2}\int_0^\Delta dx'e^{-(\Delta-x')/\mu}\phi(x')-\frac{1}{\mu}e^{-\Delta/\mu}F_L(\mu)$$

and again from Eq. (5):

$$\frac{c}{2\mu}\int_0^\Delta dx'e^{-(\Delta-x')/\mu}\phi(x')=\psi(\Delta,\mu)-e^{-\Delta/\mu}F_L(\mu)$$

giving:

$$\left.\frac{\partial\psi(x,\mu)}{\partial x}\right|_{x=\Delta}=-\frac{1}{\mu}\psi(\Delta,\mu) \tag{9b}$$

Eqs. (8), and (9a,b) will be recast as two singular integral equations for the exiting pseudo angular flux in the next section.

(iii) The singular integral transport equations for exiting angular pseudo fluxes

When we multiply Eq. (8) by $e^{x/s}$, where s is a complex variable, integrate x over the interval $[0,x]$ for $0 \le x \le \Delta$ with boundary conditions included and finally integrate μ over $[0,1]$, there results:

$$\Lambda(s)\phi_c(x,s)=s^2\int_0^1 d\mu\mu^2\left[\frac{\chi(x,\mu,s)-\chi(0,\mu,s)}{\mu^2-s^2}\right] \tag{10a}$$

with:

$$\Lambda(s)\equiv 1-\frac{cs}{2}\ln\left[\frac{s+1}{s-1}\right] \tag{10b}$$

$$\phi_c(x,s)\equiv\int_0^1 d\mu\int_0^x dx' e^{x'/s}\psi(x',\mu) \tag{10c}$$

and:

$$\chi(x,\mu,s)\equiv\left[\frac{1}{s}\psi(x,\mu)-\frac{\partial\psi(x,\mu)}{\partial x}\right]e^{x/s} \tag{10d}$$

Note that the integral in Eq. (10a) requires special attention when s is in the interval $|\nu| \le 1$, which defines a cut in the s-plane. When s is in this interval and from the Plemelj formula [2]:

$$\lim_{\varepsilon\to 0}\left[\frac{1}{\mu-(\nu\pm i\varepsilon)}\right]\equiv \boldsymbol{P}\frac{1}{\mu-\nu}\pm i\pi\delta(\mu-\nu)$$

where $\boldsymbol{P}$ signifies Cauchy principal value integration, we can write:

$$\Lambda^{\pm}(\nu)\equiv 1-cL^{\pm}(\nu)=\lambda(\nu)\pm\frac{i\pi c\nu}{2}$$

where $L^{\pm}(\nu)$ are the boundary values of the function:

$$L(z)\equiv\frac{cz}{2}\ln\left[\frac{z+1}{z-1}\right]$$

and:

$$\lambda(\nu)\equiv 1-\frac{c\nu}{2}\ln\left[\frac{1+\nu}{1-\nu}\right]$$

On the cut therefore, Eq. (10a) has the following boundary values:

$$\Lambda^{\pm}(\nu)\phi_c(x,\nu)=\nu^2\boldsymbol{P}\int_0^1 d\mu\mu^2\left[\frac{\chi(x,\mu,\nu)-\chi(0,\mu,\nu)}{(\mu+\nu)(\mu-\nu)}\right]\pm$$
$$\pm\frac{i\pi}{2}\nu^3\left[\chi(x,\nu,\nu)-\chi(0,\nu,\nu)\right]$$

If we add and subtract these, then:

$$\lambda(\nu)\phi_c(x,\nu)=\nu^2\boldsymbol{P}\int_0^1 d\mu\mu^2\left[\frac{\chi(x,\mu,\nu)-\chi(0,\mu,\nu)}{(\mu+\nu)(\mu-\nu)}\right] \tag{11a}$$

and

$$\phi_c(x,\nu)=\frac{\nu^2}{c}\left[\chi(x,\nu,\nu)-\chi(0,\nu,\nu)\right] \tag{11b}$$

where:

$$\lambda(\nu)\equiv\frac{1}{2}\left[\Lambda^{+}(\nu)+\Lambda^{-}(\nu)\right]$$

Introducing Eq. (11b) into Eq. (11a), results in the following singular integral equation for $\chi(x,\mu,\nu)$:

$$\lambda(\nu)\left[\chi(x,\nu,\nu)-\chi(0,\nu,\nu)\right]=c\boldsymbol{P}\int_0^1 d\mu\frac{\mu^2}{\mu^2-\nu^2}\left[\chi(x,\mu,\nu)-\chi(0,\mu,\nu)\right] \tag{12a}$$

Equation (12a), evaluated at $x = \Delta$, therefore becomes:

$$\lambda(\nu)\left[\chi(\Delta,\nu,\nu)-\chi(0,\nu,\nu)\right]=c\boldsymbol{P}\int_0^1 d\mu\frac{\mu^2}{\mu^2-\nu^2}\left[\chi(\Delta,\mu,\nu)-\chi(0,\mu,\nu)\right] \tag{13}$$

Using the relations:

$$\chi(0,\mu,\nu)=\frac{1}{\mu}\left[\frac{\mu-\nu}{\nu}\psi(0,\mu)+2F_L(\mu)\right]$$

$$\chi(0,\nu,\nu)=\frac{2}{\nu}F_L(\nu)$$

$$\chi(\Delta,\mu,\nu)=\frac{\mu+\nu}{\mu\nu}\psi(\Delta,\mu)e^{\Delta/\nu}$$

$$\chi(\Delta,\nu,\nu)=\frac{2}{\nu}\psi(\Delta,\mu)e^{\Delta/\nu}$$

and Eqs. (6) in the last equation gives the first of two singular integral equations relating the angular fluxes exiting the surfaces:

$$\lambda(\nu)\phi(\Delta,\nu)-\frac{c}{2}\boldsymbol{P}\int_0^1 d\mu\frac{\mu}{\mu-\nu}\phi(\Delta,\mu)+ \\ +e^{-\Delta/\nu}\frac{c}{2}\int_0^1 d\mu\frac{\mu}{\mu+\nu}\phi(0,-\mu)=e^{-\Delta/\nu}\chi_-(\nu) \tag{14a}$$

with:

$$\chi_-(\nu)\equiv\lambda(\nu)F_L(\nu)-\frac{c}{2}\boldsymbol{P}\int_0^1 d\mu\frac{\mu}{\mu-\nu}F_L(\mu)$$

Following the identical procedure when s replaced by $-s$ in Eq. (10a) yields:

$$\Lambda(s)\phi_c(x,-s)=s^2\int_{-1}^1 d\mu\mu^2\left[\frac{\chi(x,\mu,-s)-\chi(0,\mu,-s)}{\mu^2-s^2}\right]$$

with:

$$\chi(x,\mu,-s)\equiv-\left[\frac{1}{s}\psi(x,\mu)+\frac{\partial\psi(x,\mu)}{\partial x}\right]e^{-x/s}$$

and continuing gives:

$$\lambda(\nu)\left[\chi(x,\nu,-\nu)-\chi(0,\nu,-\nu)\right]=c\boldsymbol{P}\int_0^1 d\mu\frac{\mu^2}{\mu^2-\nu^2}\left[\chi(x,\mu,-\nu)-\chi(0,\mu,-\nu)\right]$$

If $x = \Delta$, we find:

$$\lambda(\nu)\left[\chi(\Delta,\nu,-\nu)-\chi(0,\nu,-\nu)\right]=c\boldsymbol{P}\int_0^1 d\mu\frac{\mu^2}{\mu^2-\nu^2}\left[\chi(\Delta,\mu,-\nu)-\chi(0,\mu,-\nu)\right] \tag{12b}$$

On substitution of:

$$\chi(0,\mu,-\nu)=-\frac{1}{\mu}\left[\frac{\mu+\nu}{\nu}\psi(0,\mu)-2F_L(\mu)\right]$$

$$\chi(0,\nu,-\nu)=-\frac{2}{\nu}\left[\psi(0,\nu)-F_L(\nu)\right]$$

$$\chi(\Delta,\mu,-\nu)=-\frac{\mu-\nu}{\mu\nu}\psi(\Delta,\mu)e^{-\Delta/\nu}$$

$$\chi(\Delta,\nu,-\nu)=0$$

and with Eqs. (6), the second singular integral equation emerges:

$$\begin{aligned}\lambda(\nu)\phi(0,-\nu)-\frac{c}{2}\boldsymbol{P}\int_0^1 d\mu\frac{\mu}{\mu-\nu}\phi(0,-\mu)+&\\ +e^{-\Delta/\nu}\frac{c}{2}\int_0^1 d\mu\frac{\mu}{\mu+\nu}\phi(\Delta,\mu)=\chi_+(\nu)&\end{aligned}\tag{14b}$$

with:

$$\chi_+(\nu)=\frac{c}{2}\int_0^1 d\mu\frac{\mu}{\mu+\nu}F_L(\mu)$$

The coupled singular integral equations, Eqs. (14a,b), are to be solved numerically subject to the constraint found from Eq. (10a) when $\Lambda(s) = 0$ at $s = \pm\nu_0$. We require only the positive root of the constraint to give:

$$-e^{-\Delta/\nu_0}\frac{c}{2}\int_0^1 d\mu\frac{\mu}{\mu+\nu_0}\phi(0,-\mu)+\frac{c}{2}\int_0^1 d\mu\frac{\mu}{\mu-\nu_0}\phi(\Delta,\mu)=e^{-\Delta/\nu_0}\chi_+(-\nu_0)\tag{14c}$$

(iv) The singular integral transport equations for the interior pseudo flux

The equation corresponding to Eq. (12a) for the interior point x is:

$$\lambda(\nu)\left[\chi(x,\nu,\nu)-\frac{2}{\nu}F_L(\nu)\right]=c\boldsymbol{P}\int_0^1 d\mu\left\{\begin{array}{l}\dfrac{\mu^2}{\mu^2-\nu^2}\chi(x,\mu,\nu)-\\ -\dfrac{\mu}{\nu}\left[\dfrac{\phi(0,-\mu)}{\mu+\nu}+\dfrac{F_L(\mu)}{\mu-\nu}\right]\end{array}\right\}\tag{15a}$$

and similarly from Eq. (12b):

$$\lambda(\nu)\left[\chi(x,\nu,-\nu)+\frac{2}{\nu}\phi(0,-\nu)\right]=c\boldsymbol{P}\int_0^1 d\mu\left\{\begin{array}{l}\dfrac{\mu^2}{\mu^2-\nu^2}\chi(x,\mu,-\nu)+\\ +\dfrac{\mu}{\nu}\left[\dfrac{\phi(0,-\mu)}{\mu-\nu}+\dfrac{F_L(\mu)}{\mu+\nu}\right]\end{array}\right\}\tag{15b}$$

Since, from Eq. (10d), the interior pseudo flux is:

$$\chi(x,\mu,s)e^{-x/s}-\chi(x,\mu,-s)e^{x/s}=\frac{2}{s}\psi\left(x,\mu\right)$$

by multiplying Eq. (15a) by $e^{-x/s}$ and Eq. (15b) by $e^{x/s}$, letting μ and s be ν and subtracting, we find:

$$\lambda(\nu)\begin{bmatrix}\psi(x,\nu)-F_L(\nu)e^{-x/\nu}- \\ -\phi(0,-\nu)e^{x/\nu}\end{bmatrix}= \\ =c\boldsymbol{P}\int_0^1 d\mu\begin{Bmatrix}\dfrac{\mu^2}{\mu^2-\nu^2}\psi(x,\mu)-\dfrac{\mu}{2}\left[\dfrac{e^{-x/\nu}}{\mu+\nu}+\dfrac{e^{x/\nu}}{\mu-\nu}\right]\phi(0,-\mu)- \\ -\dfrac{\mu}{2}\left[\dfrac{e^{-x/\nu}}{\mu-\nu}+\dfrac{e^{x/\nu}}{\mu+\nu}\right]F_L(\mu)\end{Bmatrix}$$

Then, from the substitution:

$$\psi(x,\mu)=F_L(\mu)e^{-x/\mu}+\theta(x,\mu)$$

we have:

$$\lambda(\nu)\theta(x,\nu)-c\boldsymbol{P}\int_0^1 d\mu\frac{\mu^2}{\mu^2-\nu^2}\theta(x,\mu)= \\ =e^{x/\nu}\left[\lambda(\nu)\phi(0,-\nu)-\frac{c}{2}\boldsymbol{P}\int_0^1 d\mu\frac{\mu}{\mu-\nu}\phi(0,-\mu)\right]-e^{-x/\nu}\frac{c}{2}\int_0^1 d\mu\frac{\mu}{\mu+\nu}\phi(0,-\mu)+ \\ +\frac{c}{2}\int_0^1 d\mu\frac{\mu}{\mu-\nu}\left[e^{-x/\mu}-e^{-x/\nu}\right]F_L(\mu)+\frac{c}{2}\int_0^1 d\mu\frac{\mu}{\mu+\nu}\left[e^{-x/\mu}-e^{x/\nu}\right]F_L(\mu) \tag{16}$$

which is a singular integral equation for $\theta(x,\mu)$. Equation (16), expressed in a more numerically favorable form using Eq. (14b), becomes:

$$\lambda(\nu)\theta(x,\nu)-\frac{c}{2}\boldsymbol{P}\int_0^1 d\mu\frac{\mu}{\mu-\nu}\theta(x,\mu)-\frac{c}{2}\int_0^1 d\mu\frac{\mu}{\mu+\nu}\theta(x,\mu)= \\ =-\frac{c}{2}e^{-(\Delta-x)/\nu}\int_0^1 d\mu\frac{\mu}{\mu+\nu}\phi(\Delta,\mu)-e^{-x/\nu}\frac{c}{2}\int_0^1 d\mu\frac{\mu}{\mu+\nu}\phi(0,-\mu)+ \\ +e^{x/\nu}\chi_+(\nu)+\frac{c}{2}\int_0^1 d\mu\mu C(\Delta,\mu,\nu)F_L(\mu) \tag{17}$$

with:

$$C(\Delta,\mu,\nu)\equiv\frac{e^{-\Delta/\mu}-e^{-\Delta/\nu}}{\mu-\nu}$$

In the next section, we apply the *Fn* approximation to the evaluation of Eqs. (14) and (17).

(v) The Fn approximation

In the *Fn* approximation, the following expansions in basis functions $\phi_\alpha(\mu)$ for the unknown reflected and transmitted fluxes apply:

$$\phi(0,-\mu)=\frac{c}{2}\sum_{\alpha=0}^{N-1}a_\alpha\phi_\alpha(\mu) \tag{18a}$$

$$\phi(\Delta,\mu)=F_L(\mu)e^{-\Delta/\mu}+\frac{c}{2}\sum_{\alpha=0}^{N-1}b_\alpha\phi_\alpha(\mu) \tag{18b}$$

where the first term in Eq. (18b) is the uncollided contribution. We determine the unknown coefficients a_α and b_α for a given N by substitution of Eqs. (18) into Eqs. (14) to give:

$$\sum_{\alpha=0}^{N-1}\left[B_\alpha(\nu)a_\alpha+\frac{c}{2}e^{-\Delta/\nu}A_\alpha(\nu)b_\alpha\right]=R_1(\nu) \tag{19a}$$

$$\sum_{\alpha=0}^{N-1}\left[\frac{c}{2}e^{-\Delta/\nu}A_\alpha(\nu)a_\alpha+B_\alpha(\nu)b_\alpha\right]=R_2(\nu) \tag{19b}$$

where:

$$R_1(\nu)\equiv\int_0^1 d\mu\mu S(\Delta,\mu,\nu)F_L(\mu),\ R_2(\nu)\equiv\int_0^1 d\mu\mu C(\Delta,\mu,\nu)F_L(\mu)$$

and:

$$S(\Delta,\mu,\nu)\equiv\frac{1-e^{-\Delta(1/\mu+1/\nu)}}{\mu+\nu}$$

The matrix elements in Eqs. (19) are:

$$A_\alpha(\nu)\equiv\int_0^1 d\mu\frac{\mu}{\mu+\nu}\phi_\alpha(\mu) \tag{20a}$$

$$B_\alpha(\nu)\equiv\lambda(\nu)\phi_\alpha(\nu)-\frac{c}{2}\int_0^1 d\mu\frac{\mu}{\mu-\nu}\phi_\alpha(\mu) \tag{20b}$$

Equations (19) become a set of linear equations via collocation by forcing equality at ν_β, β = 0,1,…,$N-1$. Therefore:

$$\sum_{\alpha=0}^{N-1}\left[B_\alpha(\nu_\beta)a_\alpha+\frac{c}{2}e^{-\Delta/\nu_\beta}A_\alpha(\nu_\beta)b_\alpha\right]=R_1(\nu_\beta) \tag{21a}$$

$$\sum_{\alpha=0}^{N-1}\left[\frac{c}{2}e^{-\Delta/\nu_\beta}A_\alpha(\nu_\beta)a_\alpha+B_\alpha(\nu_\beta)b_\alpha\right]=R_2(\nu_\beta) \tag{21b}$$

We can now solve Eqs. (21) by matrix inversion for the coefficients a_α and b_α once the collocation points have been specified.

Then, since we know a_α and b_α, we find the fluxes at the boundaries from Eqs. (18). Experience, however, has shown that an additional post-processing step provides the most accurate numerical values. Noting that when we introduce Eq. (20b) into Eqs. (21), there results (after some algebra):

$$\phi(0,-\mu)=\frac{c}{2\lambda^{+}(\nu)}\left\{R_1(\mu)+\sum_{\alpha=0}^{N-1}\left[B_\alpha^{*}(\mu)a_\alpha-A_\alpha^{*}(\mu)b_\alpha\right]\right\} \tag{22a}$$

$$\phi(\Delta,\mu)=F_L(\mu)e^{-\Delta/\mu}+\frac{c}{2\lambda^{+}(\nu)}\left\{R_2(\mu)+\sum_{\alpha=0}^{N-1}\left[B_\alpha^{*}(\mu)b_\alpha-A_\alpha^{*}(\mu)a_\alpha\right]\right\} \tag{22b}$$

where:

$$A_\alpha^{*}(\mu)\equiv\frac{c}{2}e^{-\Delta/\mu}A_\alpha(\mu)$$

$$B_\alpha^{*}(\mu)\equiv\lambda^{+}(\nu)\phi_\alpha(\mu)+\frac{c}{2}\int_0^1 d\mu'\left[\frac{\mu'\phi_\alpha(\mu')-\mu\phi_\alpha(\mu)}{\mu'-\mu}\right]$$

$$\lambda^{+}(\nu)\equiv 1-\frac{c\nu}{2}\ln\left[\frac{1+\nu}{\nu}\right]$$

Equations (22) are the post-processed expressions we eventually will evaluate.

From Eqs. (18), we can find the slab reflectance and transmittance R_f, T_n through angular integration:

$$R_f\equiv\int_0^1 d\mu\mu\phi(0,-\mu)=\frac{c}{2}\sum_{\alpha=0}^{N-1}a_\alpha\int_0^1 d\mu\mu\phi_\alpha(\mu) \tag{23a}$$

$$T_n\equiv\int_0^1 d\mu\mu\phi(\Delta,\mu)=\int_0^1 d\mu\mu F_L(\mu)e^{-\Delta/\mu}+\frac{c}{2}\sum_{\alpha=0}^{N-1}b_\alpha\int_0^1 d\mu\mu\phi_\alpha(\mu) \tag{23b}$$

which along with the exiting angular fluxes will be the desired results.

For the interior, when we introduce the expansion:

$$\theta(x,\mu)=\frac{c}{2}\sum_{\alpha=0}^{N-1}c_\alpha(x)\phi_\alpha(\mu) \tag{24}$$

into Eq. (17), we have the following matrix equations for $c_\alpha(x)$ where x is just a parameter:

$$\sum_{\alpha=0}^{N-1}\left[B_\alpha(\nu_\beta)-\frac{c}{2}A_\alpha(\nu_\beta)\right]c_\alpha(x)=\bar{R}_1(x,\nu_\beta) \tag{25}$$

with:

$$\bar{R}_1(x,\nu) \equiv -\frac{c}{2}\sum_{\alpha=0}^{N-1}\left[b_\alpha + e^{-x/\nu}a_\alpha\right]A_\alpha(\nu) + \chi_+(\nu) + \\ + \frac{c}{2}\int_0^1 d\mu\mu C(\Delta,\mu,\nu)F_L(\mu)$$

Since a_α and b_α are known, we solve Eq. (25) by matrix inversion at each x. With $c_\alpha(x)$, the scalar flux is from Eq. (4a):

$$\phi(x) = \int_0^1 d\mu F_L(\mu)e^{-x/\mu} + \sum_{\alpha=0}^{N-1} c_\alpha(x)\int_0^1 d\mu\phi_\alpha(\mu) \tag{26}$$

(vi) Extension to heterogeneous media

Specifying a source on the right boundary extends the theory to heterogeneous media composed of a series of slabs. The source for each slab results from transmission and reflection from adjacent slabs. An additional iteration through the slabs is therefore required to determine the boundary sources in the presence of more than one slab [3]. We will implement this algorithm as part of a future effort.

(e) Numerical implementation and demonstration for Benchmark 3.3

The implementation of the *Fn* method hinges several numerical decisions. These are the choice of:

- basis functions $\phi_\alpha(\mu)$;
- a numerical quadrature scheme;
- the zero search algorithm for $\nu_{0;}$
- how ν_β, $\beta = 0,1,\ldots,N-1$, are to be determined;
- the matrix inversion scheme.

There are many possibilities for the choice of basis functions, including shifted Legendre polynomials, monomials and shifted monomials. For our study, we use the following shifted monomials exclusively:

$$\phi_\alpha(\mu) = \left(2\mu^\gamma - 1\right)^\alpha$$

with $\gamma = 0.75$. Through experimentation, this choice seems to provide adequate accuracy at reasonable computational expense.

For the evaluation of the integrals over μ, we use shifted Gauss quadrature of order *Lm*. Typically, for $Lm = 15$, we obtain three- or four- place accuracy. A simple binary search yields accurate values for ν_0 from $\Lambda(\nu_0) = 0$. For the N collocation points ν_β, we specify N–1 as the zeros of shifted the Legendre polynomial $P_{N-1}(\mu)$ plus ν_0. The matrix inversion is simply a Gauss elimination scheme with pivoting [4].

For demonstration, we consider a homogeneous slab with $c = 0.9$ and an incident normal ($\mu_0 = 1$) beam of unit strength impinging on the left surface. Figures 3.3.1(a) and 3.3.1(b) show the exiting angular fluxes for slabs of thicknesses $\Delta = 1(1)10$. As Δ increases, the reflected distribution saturates becoming independent of Δ with the reflectance approaching that of the half-space. Figures 3.3.2(a) and 3.3.2(b) show the variation of the reflected and transmitted fluxes with c for a slab of thickness 1 *mfp*. The transmitted flux experiences a maximum with increasing c tending toward μ equal one with increasing slab thickness.

To qualify Benchmark 3.3 as a true benchmark, Table 3.3.1 presents the exiting fluxes for decreasing error indicating five-place accuracy. These results required an *Fn* order of $N = 46$ and are in complete agreement with those of Ref. 5. Note, however, that the normalization in Ref. 5 is 0.5.

Table 3.3.1. Qualification of Benchmark 3.3

$\phi(0,-|\mu|)$ $(\Delta = 1,\ c = 0.9)$

$\mu\backslash\varepsilon$	10^{-3}	10^{-4}	10^{-5}
1.00000E+00	4.20001E-01	4.20001E-01	4.20002E-01
9.00000E-01	4.47770E-01	4.47770E-01	4.47770E-01
8.00000E-01	4.78944E-01	4.78944E-01	4.78944E-01
7.00000E-01	5.13947E-01	5.13947E-01	5.13947E-01
6.00000E-01	5.53090E-01	5.53090E-01	5.53090E-01
5.00000E-01	5.96302E-01	5.96302E-01	5.96303E-01
4.00000E-01	6.42534E-01	6.42534E-01	6.42534E-01
3.00000E-01	6.88484E-01	6.88484E-01	6.88481E-01
2.00000E-01	7.26603E-01	7.26603E-01	7.26613E-01
1.00000E-01	7.45359E-01	7.45359E-01	7.45339E-01
1.00000E-10	7.18741E-01	7.18741E-01	7.18743E-01

$\phi(\Delta,\mu)$

1.00000E+00	3.80527E-01	3.80527E-01	3.80529E-01
9.00000E-01	4.01408E-01	4.01408E-01	4.01409E-01
8.00000E-01	4.23767E-01	4.23767E-01	4.23766E-01
7.00000E-01	4.47266E-01	4.47266E-01	4.47267E-01
6.00000E-01	4.71075E-01	4.71075E-01	4.71072E-01
5.00000E-01	4.93355E-01	4.93355E-01	4.93358E-01
4.00000E-01	5.10405E-01	5.10405E-01	5.10404E-01
3.00000E-01	5.15171E-01	5.15171E-01	5.15163E-01
2.00000E-01	4.96633E-01	4.96633E-01	4.96655E-01
1.00000E-01	4.48109E-01	4.48109E-01	4.48066E-01
1.00000E-10	3.72273E-01	3.72273E-01	3.72276E-01

REFERENCES

[1] Greenberg, M.D., *Advanced Engineering Mathematics*, Prentice Hall, New Jersey (1998).

[2] Roos, B.W., *Analytic Functions and Distributions in Physics and Engineering*, John Wiley & Sons, NY (1969).

[3] Ganapol, B., K. Parsons, “A Heterogeneous Medium Analytical Benchmark”, *M&C Topical Meeting*, Madrid Spain (1999).

[4] Press, W., *et al*., *Numerical Recipes*, Cambridge University Press, NY (1986).

[5] Chin, R.C.Y., G.W. Hedstrom, C.E. Siewert, “On the Use of the *Fn* Method with Splines for Radiative Transfer Problems”, *JQSRT*, **39**, 205-217 (1988).

Figure 3.3.1. Variation of the (a) reflected and (b) transmitted flux with slab thickness for *c* = 0.9

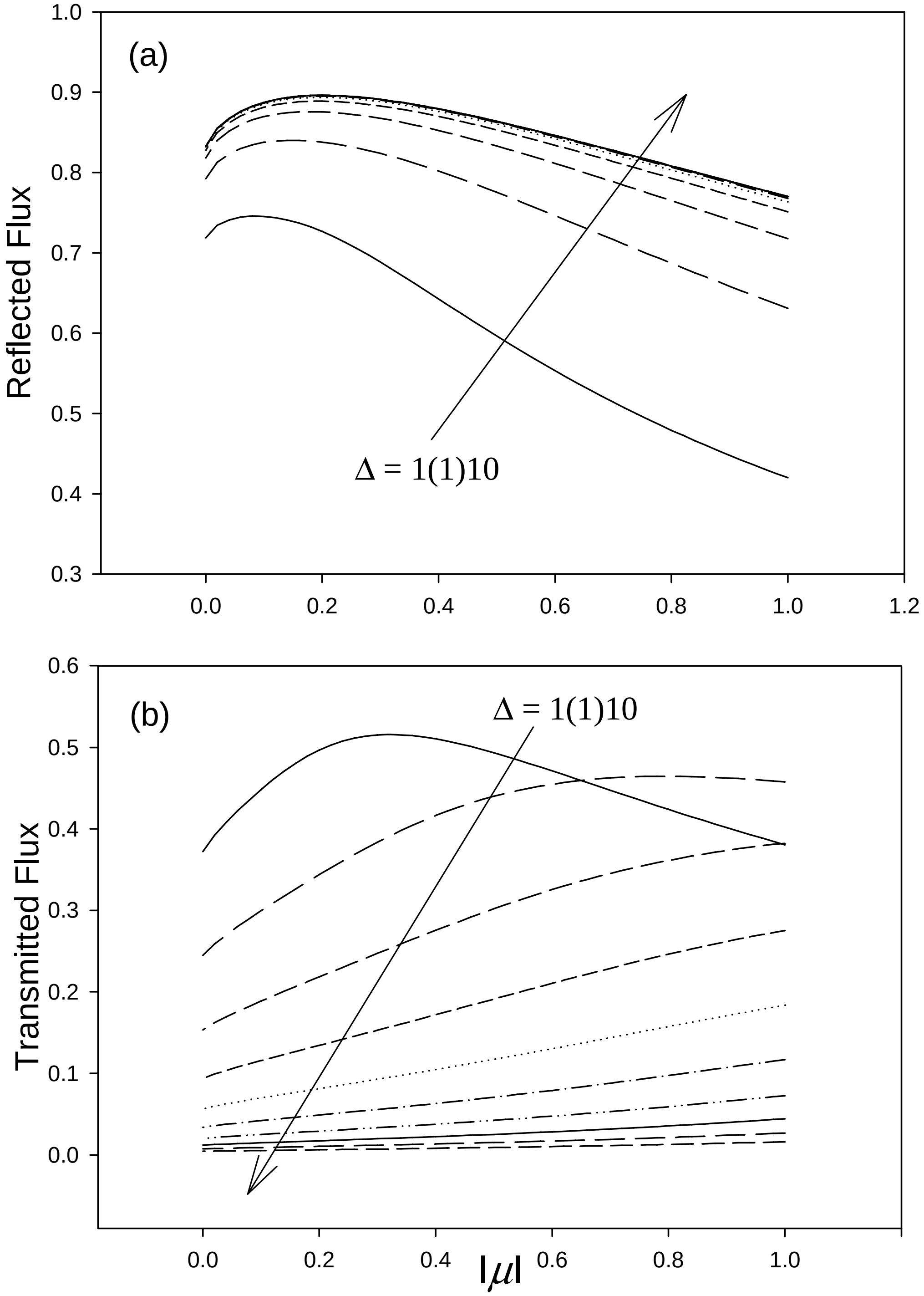

Figure 3.3.2. Variation of the (a) reflection and (b) transmitted flux with *c* for $\Delta = 1$

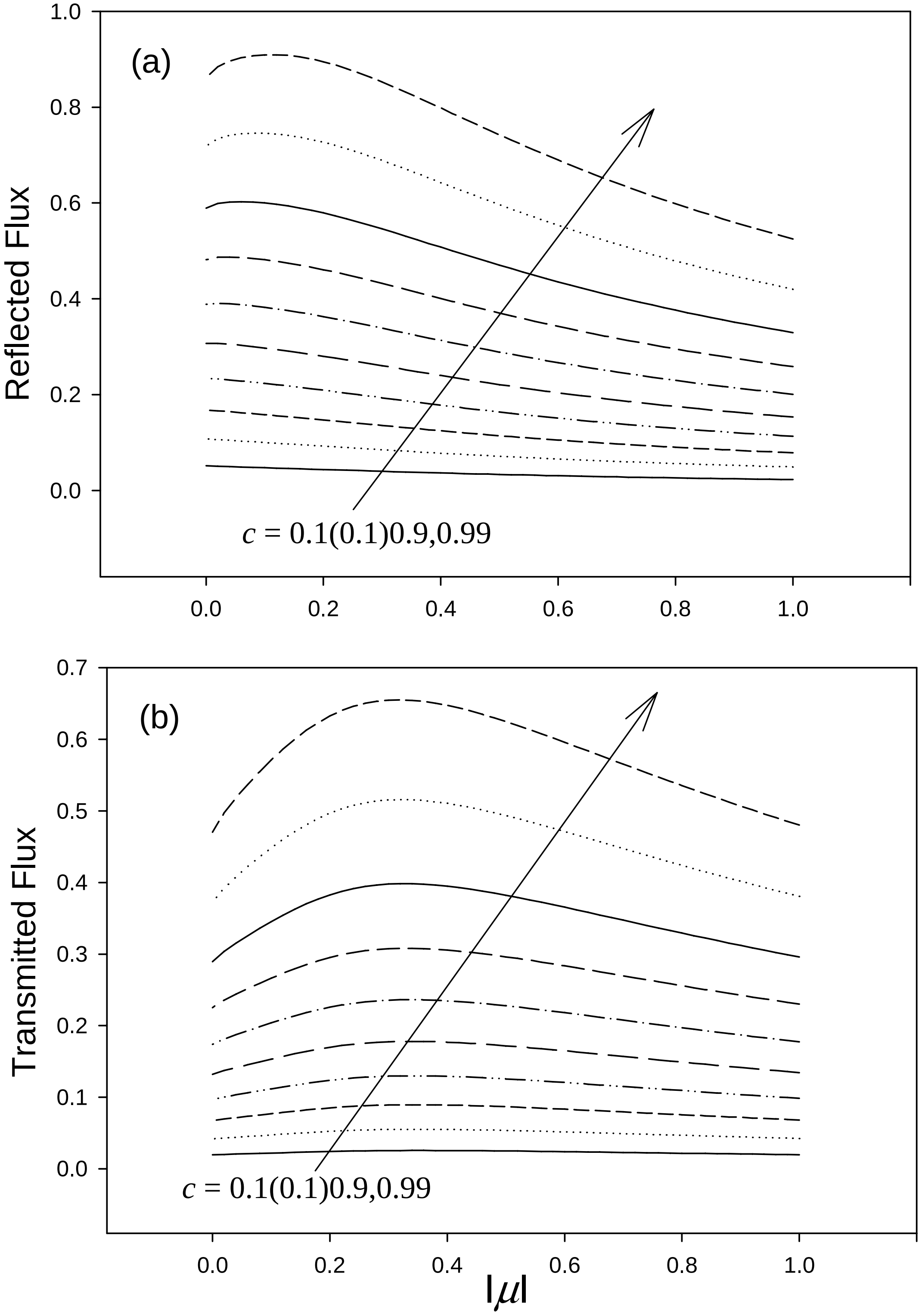

Benchmark 3.4: Monoenergetic transport in a 1-D cylinder/the *Fn* solution

(a) Brief description

Monoenergetic neutron transport in an isotropically scattering infinite cylinder (one surface) with vacuum boundary conditions.

(b) Classification

NT/CY/I/OG/I/L/X(C)/FN

(c) Physical description

Monodirectional neutrons enter the surface of a cylinder of infinite longitudinal length and scatter isotopically and monoenergetically. The 1-D infinite cylinder is composed of a single homogeneous region.

(d) Analytical representation

The pseudo formulation gives the desired solution to the transport equation with cylindrical symmetry. The formulation presented here is new and represents an extension of the *Fn* theory of Benchmark 3.3.

(i) The transport equation for 1-D cylindrical symmetry

To take advantage or the pseudo problem formulation, we now consider Eq. (1.VI) for isotropic scattering, without a volume source and for uniform nuclear properties:

$$\left[\mathbf{\Omega}\bullet\nabla+\Sigma(E)\right]\phi(\boldsymbol{r},\mathbf{\Omega},E)=\frac{1}{4\pi}\int_0^\infty dE'\Sigma(E'\to E)\phi(\boldsymbol{r},E') \tag{1a}$$

where:

$$\Sigma(E'\to E)\equiv\Sigma_s(E')f_s(E'\to E)+\nu(E')\Sigma_f(E')\chi(E)$$

An isotropic angular flux:

$$\phi(\boldsymbol{r}_s,\mathbf{\Omega},E)=\frac{1}{4\pi}F_0(E)h(z),\ \ \hat{\boldsymbol{n}}_s\bullet\mathbf{\Omega}\le 0 \tag{1b}$$

normalized to:

$$\int_{-\infty}^{\infty}dzh(z)\equiv 1,\ \int_0^\infty dEF_0(E)\equiv F$$

enters the free surface at $\rho = R$ of a longitudinally infinite (in the z-direction) cylinder. If we introduce the replacement:

$$\phi(\boldsymbol{r},\boldsymbol{\Omega},E) \to \phi(\boldsymbol{r},\boldsymbol{\Omega},E) + \frac{1}{4\pi} F_0(E) h(z)$$

into Eq(1a), there results after longitudinal integration and noting a zero current on the surfaces in the z-coordinate as $z \to \pm\infty$:

$$\begin{aligned} &\left[\boldsymbol{\Omega} \bullet \nabla_\rho + \Sigma(E)\right]\phi(\rho,\boldsymbol{\Omega},E) = \\ &= \frac{1}{4\pi}\int_0^\infty dE' \Sigma(E' \to E)\phi(\rho,E') + \frac{1}{4\pi} Q(E) \end{aligned} \tag{2a}$$

where $\boldsymbol{\rho}$ is a vector in the radial transverse plane and:

$$\phi(\rho,\boldsymbol{\Omega},E) \equiv \int_{-\infty}^{\infty} dz \phi(\boldsymbol{r}(\rho,z),\boldsymbol{\Omega},E)$$

In addition, the original boundary condition is now included in the external source:

$$Q(E) \equiv -\left[\Sigma(E)F_0(E) - \int_0^\infty dE' \Sigma(E' \to E) F_0(E')\right] \tag{2b}$$

The new radial boundary condition becomes:

$$\phi(R,\boldsymbol{\Omega},E) = 0, \quad \hat{\boldsymbol{n}}_s \bullet \boldsymbol{\Omega} \le 0 \tag{2c}$$

Since Eq. (2a) leads to Eq. (1.III) from which the pseudo problem, Eq. (1.IV):

$$\begin{aligned} &\left[\nabla_\rho^2 - \frac{1}{\nu^2}\right]\phi(\rho,\nu,E) = \\ &= -\int_0^\infty dE' \Sigma(E' \to E) \int_0^{1/\Sigma(E')} \frac{d\nu'}{\nu'^2}\phi(\rho,\nu',E') - Q(E) \end{aligned} \tag{3a}$$

follows, we can immediately write the scalar flux as Eq. (1.9b):

$$\phi(\rho,E) \equiv \int_0^{1/\Sigma(E)} \frac{d\nu}{\nu^2}\phi(\rho,\nu,E) \tag{3b}$$

Here, the angular pseudo flux has no physical meaning other than when integrated.

To obtain the monoenergetic version, we assume the nuclear properties to be independent of energy. If:

$$\nu = \frac{\mu}{\Sigma}, \ \nu' = \frac{\mu'}{\Sigma}$$

then, for $0 \le \mu,\mu' \le 1$:

$$\begin{aligned}&\left[\nabla_\rho^2 - \frac{\Sigma^2}{\mu^2}\right]\phi(\rho,\mu/\Sigma,E) = \\ &= -\Sigma\int_0^\infty dE'\Sigma(E'\to E)\int_0^1 \frac{d\mu'}{\mu'^2}\phi(\rho,\mu'/\Sigma,E') - Q(E)\end{aligned} \tag{4}$$

where:

$$\Sigma(E) \equiv \Sigma,\ \ \Sigma_s(E) = \Sigma_s,\ \ \nu(E)\Sigma_f(E) \equiv \nu\Sigma_f$$

Since:

$$\int_0^\infty dE\chi(E) \equiv 1, \qquad \int_0^\infty dE\Sigma(E'\to E) \equiv \Sigma_s + \nu\Sigma_f$$

and:

$$Q \equiv \int_0^\infty dEQ_0(E) \equiv -\left[\Sigma - \left(\Sigma_s + \nu\Sigma_f\right)\right]F$$

on integration of Eq. (4) over all energy:

$$\begin{aligned}&\left[\nabla_\rho^2 - \frac{\Sigma^2}{\mu^2}\right]\phi(\rho,\mu/\Sigma) = \\ &= -\Sigma\left[\Sigma_s + \nu\Sigma_f\right]\int_0^1 \frac{d\mu'}{\mu'^2}\phi(\rho,\mu'/\Sigma) - Q,\end{aligned} \tag{5a}$$

with the pseudo and scalar fluxes given by:

$$\phi(\rho,\mu/\Sigma) \equiv \int_0^\infty dE\phi(\rho,\mu/\Sigma) \tag{5b}$$

$$\phi(\rho) \equiv \Sigma\int_0^1 \frac{d\mu}{\mu^2}\phi(\rho,\mu/\Sigma) \tag{5c}$$

By dividing Eq. (5a) by Σ^2 and measuring the radial position in units of mean free path, we have:

$$\left[\nabla_\rho^2 - \frac{1}{\mu^2}\right]\phi(\rho,\mu) = -c\int_0^1 \frac{d\mu'}{\mu'^2}\phi(\rho,\mu') - Q \tag{6a}$$

with $\rho \to \Sigma\rho$, $\phi(\rho,\mu/\Sigma) \to \phi(\rho,\mu)$ and:

$$c \equiv \frac{\Sigma_s + \nu\Sigma_f}{\Sigma}$$

Now Q and the scalar flux are:

$$Q \equiv -(1-c)F \tag{6b}$$

$$\phi(\rho) \equiv \int_0^1 \frac{d\mu}{\mu^2}\phi(\rho,\mu)$$

Since:

$$\nabla_\rho^2 \equiv \frac{1}{\rho}\frac{\partial}{\partial\rho}\rho\frac{\partial}{\partial\rho} + \frac{1}{\rho^2}\frac{\partial^2}{\partial\theta^2}$$

Eqs. (6), integrated over azimuth, gives the following 1-D cylindrically symmetric pseudo transport equation:

$$\left[\frac{1}{r}\frac{\partial}{\partial r}r\frac{\partial}{\partial r} - \frac{1}{\mu^2}\right]\phi(r,\mu) = -c\int_0^1 \frac{d\mu'}{\mu'^2}\phi(r,\mu') - Q \tag{7a}$$

with ρ replaced by r. Now:

$$\phi(r,\mu) \equiv \frac{1}{2\pi}\int_0^{2\pi} d\theta\phi(r,\mu)$$

and the scalar flux is:

$$\phi(r) \equiv \int_0^1 \frac{d\mu}{\mu^2}\phi(r,\mu) \tag{7b}$$

Since Eq. (7a) is second order, we require two boundary conditions. One condition comes from finiteness of the pseudo flux at the cylinder center (assuming a solid center) and the second from the pseudo flux at the surface.

(ii)The integral equation and boundary condition at R

The most straightforward approach to obtain a boundary condition at R is through the integral equation formulation. Since Eq. (7a) is an inhomogeneous Helmholtz equation, modified Bessel functions of the first and second kinds:

$$I_0(r/\mu),\ K_0(r/\mu)$$

are appropriate complementary solutions. From the method of variation of parameters therefore, the general solution is:

$$\begin{aligned}\phi(r,\mu) &= A(\mu)I_0(r/\mu) + B(\mu)K_0(r/\mu) + \\ &+ \int_a^r dr'\frac{q(r')}{W(r')}I_0(r/\mu)K_0(r'/\mu) - \int_b^r dr'\frac{q(r')}{W(r')}I_0(r'/\mu)K_0(r/\mu)\end{aligned} \tag{8}$$

where $q(r)$ and the Wronskian $W(r)$ are:

$$q(r) \equiv c\int_0^1 \frac{d\mu'}{\mu'^2}\phi(r,\mu') + Q$$

$$W(r) \equiv I_0(r/\mu)\frac{dK_0(r/\mu)}{dr} - \frac{dI_0(r/\mu)}{dr}K_0(r/\mu)$$

Since:

$$\frac{dI_0(r/\mu)}{dr} = \frac{1}{\mu}I_1(r/\mu)$$

$$\frac{dK_0(r/\mu)}{dr} = -\frac{1}{\mu}K_1(r/\mu)$$

we have:

$$W(r) \equiv -\frac{1}{\mu}\left[I_0(r/\mu)K_1(r/\mu) + I_1(r/\mu)K_0(r/\mu)\right] = -\frac{1}{r} \tag{9}$$

and Eq. (8), for arbitrary *a* and *b*, reduces to:

$$\begin{aligned}\phi(r,\mu) = &\left[A(\mu) - \int_a^r dr'r'q(r')K_0(r'/\mu)\right]I_0(r/\mu) + \\ &+\left[B(\mu) + \int_b^r dr'r'q(r')I_0(r'/\mu)\right]K_0(r/\mu)\end{aligned} \tag{10}$$

Based on existence arguments supporting the vanishing of the coefficients in Eq. (10), *A* and *B* follow. The pseudo flux must be finite at the center of a homogeneous cylinder. Since as $r \to 0$:

$$I_0(r/\mu) \to 1, \quad K_0(r/\mu) \to \ln(r)$$

there results:

$$B(\mu) = \int_0^b dr'r'q(r')I_0(r'/\mu)$$

At $r = R$, Eq. (10) becomes:

$$\begin{aligned}\phi(R,\mu) = &\left[A(\mu) - \int_a^R dr'r'q(r')K_0(r'/\mu)\right]I_0(R/\mu) + \\ &+\int_0^R dr'r'q(r')I_0(r'/\mu)K_0(R/\mu)\end{aligned} \tag{11}$$

Since:

$$I_0\left(R/\mu\right)\to e^{R/\mu},\quad K_0\left(R/\mu\right)\to e^{-R/\mu}$$

and for any amount of absorption ($c < 1$), the flux must vanish as $R\to\infty$ requiring the coefficient of $I_0(R/\mu)$ to vanish identically for Eq. (11) to remain finite, or:

$$A(\mu)\equiv\int_a^R dr'r'q(r')K_0\left(r'/\mu\right)$$

The result is the integral equation:

$$\begin{aligned}\phi(r,\mu)&=I_0\left(r/\mu\right)\int_r^R dr'r'q(r')K_0\left(r'/\mu\right)+\\&+K_0\left(r/\mu\right)\int_0^r dr'r'q(r')I_0\left(r'/\mu\right)\end{aligned}\tag{12a}$$

which is in agreement with the literature [1-4].

A consistent boundary condition at $r = R$ comes about by differentiating Eq. (12a):

$$\frac{\partial\phi(r,\mu)}{\partial r}=\frac{1}{\mu}\left[\begin{aligned}&I_1\left(r/\mu\right)\int_r^R dr'r'q(r')K_0\left(r'/\mu\right)+\\&-K_1\left(r/\mu\right)\int_0^r dr'r'q(r')I_0\left(r'/\mu\right)\end{aligned}\right]$$

giving for $r = R$:

$$\left.\frac{\partial\phi(r,\mu)}{\partial r}\right|_R=-\frac{1}{\mu}K_1\left(R/\mu\right)\int_0^R dr'r'q(r')I_0\left(r'/\mu\right)$$

Since:

$$\phi(R,\mu)=K_0\left(R/\mu\right)\int_0^R dr'r'q(r')I_0\left(r'/\mu\right)$$

the boundary condition is:

$$\mu K_0\left(R/\mu\right)\left.\frac{\partial\phi(r,\mu)}{\partial r}\right|_R+K_1\left(R/\mu\right)\phi(R,\mu)=0\tag{12b}$$

This condition and the finiteness of the pseudo flux are sufficient for the solution of Eq. (7a).

Our approach will be to reformulate Eq. (7a) as a singular integral equation for the pseudo flux at *R*, and apply the *Fn* method as in the previous benchmark.

(iii) The theory of the Fn approximation for the surface scalar flux

(iii.1) The singular integral equation for the pseudo flux $\phi(R,\mu)$

By projecting Eq. (7a) over $rI_0(r/s)$ on $[0,R]$, we have:

$$\int_0^R drrI_0\left(r/s\right)\left\{\left[\frac{1}{r}\frac{\partial}{\partial r}\left(r\frac{\partial}{\partial r}\right)-\frac{1}{\mu^2}\right]\phi\left(r,\mu\right)\right\}=$$
$$=-\int_0^R drrI_0\left(r/s\right)\left[c\int_0^1\frac{d\mu'}{\mu'^2}\phi\left(r,\mu'\right)+Q\right]$$

At this point, s is a complex variable. Integrating the first term by parts yields:

$$\frac{\mu^2-s^2}{\mu^2s^2}\int_0^R drrI_{0s}^r\phi\left(r,\mu\right)= \tag{13}$$
$$= R\begin{bmatrix} I_{0s}^R\left.\dfrac{\partial\phi\left(r,\mu\right)}{\partial r}\right|_R - \\ -\dfrac{1}{s}I_{1s}^R\phi\left(R,\mu\right)\end{bmatrix}-c\phi_0\left(s\right)-QRsI_{1s}^R$$

since, as noted above:

$$\frac{dI_0\left(r/s\right)}{dr}=\frac{1}{s}I_1\left(r/s\right)$$

and in addition:

$$\int_0^R drrI_0\left(r/s\right)=RsI_1\left(R/s\right)$$

For notational convenience, we let:

$$I_{ns}^r\equiv I_n\left(r/s\right)$$
$$K_{ns}^r\equiv K_n\left(r/s\right)$$

and:

$$\phi_0\left(s\right)\equiv\int_0^1\frac{d\mu}{\mu^2}\int_0^R drrI_{0s}^r\phi\left(r,\mu\right)$$

We motivate this projection by noting that I_{0s}^{R} corresponds to the exponential kernel of the *Fn* formulation in the plane case (see Benchmark 3.3).

On substitution of:

$$\left.\frac{\partial\phi(r,\mu)}{\partial r}\right|_{R} = -\frac{K_{1\mu}^{R}}{\mu K_{0\mu}^{R}}\phi(R,\mu)$$

from the boundary condition Eq. (12b), dividing by $(\mu^2 - s^2)/s^2$ and integrating Eq. (13) over μ on [0,1], there results:

$$\phi_0(s) = s^2 R\int_0^1 \frac{d\mu}{\mu^2 - s^2}\left[\frac{I_{1s}^{R}}{s} + \frac{K_{1\mu}^{R}}{\mu K_{0\mu}^{R}} I_{0s}^{R}\right]\phi(R,\mu) + \\ + cL(s)\phi_0(s) + QRsL(s)I_{1s}^{R}$$

with:

$$L(s) \equiv s^2\int_0^1 \frac{d\mu}{\mu^2 - s^2} = \frac{s}{2}\ln\left[\frac{s+1}{s-1}\right]$$

Rearranging:

$$\left[1 - cL(s)\right]\phi_0(s) = \\ = sR\int_0^1 \frac{d\mu}{\mu^2 - s^2}\left[I_{1s}^{R} + \frac{s}{\mu}\frac{K_{1\mu}^{R}}{K_{0\mu}^{R}} I_{0s}^{R}\right]\phi(R,\mu) + QRsL(s)I_{1s}^{R} \tag{14}$$

and allowing s to approach the cut [0,1] by taking the limit of $s = \nu \pm i\varepsilon$ gives:

$$\left[1 - cL^{\pm}(\nu)\right]\phi_0(\nu) = \\ = \nu R\int_0^1 d\mu \begin{bmatrix} I_{1\nu}^{R} + \\ + \dfrac{\nu}{\mu}\dfrac{K_{1\mu}^{R}}{K_{0\mu}^{R}} I_{0\nu}^{R} \end{bmatrix}\left[\boldsymbol{P}\frac{1}{\mu - \nu} \pm i\pi\delta(\mu - \nu)\right]\frac{\phi(R,\mu)}{\mu + \nu} + \\ + QR\nu L^{\pm}(\nu)I_{1\nu}^{R} \tag{15}$$

Using the Plemelj formula [5], the boundary values of $L(s)$ on [0,1] are:

$$L^{\pm}(\nu) \equiv -\frac{\nu}{2}\left[\ln\left[\frac{1-\nu}{1+\nu}\right] \pm i\pi\right]$$

and by subtracting the boundary values of Eq. (15), it is apparent that:

$$\phi_0(\nu) = -\frac{1}{c}\left[\frac{i\pi\nu}{\left[L^+(\nu) - L^-(\nu)\right]}\frac{\phi(R,\nu)}{K_{0\nu}^R} + QR\nu I_{1\nu}^R\right]$$

Since:

$$L^+(\nu) - L^-(\nu) = -i\pi\nu$$

we can write:

$$\phi_0(\nu) = \frac{1}{c}\left[\frac{\phi(R,\nu)}{K_{0\nu}^R} - QR\nu I_{1\nu}^R\right] \tag{16a}$$

Alternatively, adding, the boundary values of Eq. (15) gives:

$$\begin{aligned}\left[1 - cL(\nu)\right]\phi_0(\nu) &= QR\nu L(\nu) I_{1\nu}^R + \\ &+ \nu \boldsymbol{P}\int_0^1 \frac{d\mu}{\mu^2 - \nu^2}\left\{R\left[I_{1\nu}^R + \frac{\nu}{\mu}\xi_\mu I_{0\nu}^R\right]\right\}\phi(R,\mu);\end{aligned} \tag{16b}$$

where:

$$L(\nu) \equiv \frac{\nu}{2}\ln\left[\frac{1+\nu}{1-\nu}\right] \quad \text{and} \quad \xi_\mu \equiv \frac{K_{1\mu}^R}{K_{0\mu}^R}$$

Then, substituting Eq. (16a) into Eq. (16b) results in the following singular integral equation for the boundary pseudo flux:

$$\begin{aligned}\left[1 - cL(\nu)\right]\phi(R,\nu) &= QR\nu K_{0\nu}^R I_{1\nu}^R + \\ &+ \nu cR\int_0^1 \frac{d\mu}{\mu - \nu}\left\{\frac{1}{\mu+\nu}\left[K_{0\nu}^R I_{1\nu}^R + \frac{\nu}{\mu}\xi_\mu K_{0\nu}^R I_{0\nu}^R\right]\right\}\phi(R,\mu)\end{aligned}$$

or in a more numerically convenient representation:

$$\begin{aligned}&\left[1 - cL(\nu)\right]\phi(R,\nu) = \\ &= QR\nu K_{0\nu}^R I_{1\nu}^R + c\nu^2 \boldsymbol{P}\int_0^1 d\mu \frac{\phi(R,\mu)}{\mu^2 - \nu^2} + \\ &+ \nu cRI_{0\nu}^R\int_0^1 d\mu \frac{1}{\mu+\nu}\left\{\frac{1}{\mu-\nu}\left[\frac{\nu}{\mu}\xi_\mu K_{0\nu}^R - K_{1\nu}^R\right]\right\}\phi(R,\mu)\end{aligned} \tag{17}$$

Substitution of the Wronskian [Eq. (9)] into the last integral in Eq. (17) removes the singularity at $\mu = \nu$.

(iii.2) The *Fn* approximation for the pseudo flux $\phi(R,\mu)$

We approximate the solution for $\phi(R,\mu)$ in the *Fn* spectral representation:

$$\phi(R,\mu) = \mu^2 \sum_{n=1}^{N} a_n(R) P_n^*(\mu) \tag{18}$$

where the shifted Legendre polynomials of degree n are:

$$P_n^*(\mu) \equiv P_n(2\mu - 1)$$

On substitution of Eq. (18) into Eq. (17), we have:

$$\sum_{n=1}^{N} a_n(R) A_n(\nu) = h(R,\nu) \tag{19a}$$

with:

$$A_n(\nu) \equiv \nu^2 \left[1 - cL(\nu)\right] P_n^*(\nu) - T_n(\nu) - V_n(\nu) \tag{19b}$$

and:

$$V_n(\nu) \equiv \nu c R I_{0\nu}^R \int_0^1 d\mu \frac{1}{\mu+\nu} \left\{ \frac{\mu^2}{\mu-\nu} \left[\frac{\nu}{\mu} \xi_\mu K_{0\nu}^R - K_{1\nu}^R \right] \right\} P_n^*(\mu) \tag{19c}$$

$$\begin{aligned} T_n(\nu) &\equiv c\nu^2 \int_0^1 d\mu \frac{\mu^2}{\mu-\nu} P_n^*(\mu) \\ &= c\nu^2 \left\{ \delta_{n,0} - \nu \left[Q_n(2\nu-1) + (-1)^n Q_n(2\nu+1) \right] \right\} \end{aligned} \tag{19d}$$

Q_n is the Legendre function of the second kind of order n and:

$$h(R,\nu) \equiv K_{0\nu}^R \bar{Q}_0(\nu)$$

$$\bar{Q}_0(\nu) \equiv QR\nu I_{1\nu}^R$$

One should note that the integrand of Eq. (19c) requires special consideration at the point of the (removable) singularity where it becomes:

$$\begin{aligned} &\frac{1}{2\nu} \lim_{\mu\to\nu} \left\{ \frac{1}{\mu-\nu} \left[\frac{\nu}{\mu} \xi_\mu K_{0\nu}^R - K_{1\nu}^R \right] \right\} = \\ &\qquad = \frac{1}{2\nu} \left(\frac{R}{\nu^2} \right) \left[1 - \left(\frac{K_{1\nu}^R}{K_{0\nu}^R} \right)^2 \right] K_{0\nu}^R \end{aligned}$$

Enforcing Eq. (19a) at the following N collocation points ν_j:

$$P^*_{N-1}(\nu) = P_{N-1}(2\nu - 1) = 0 \Rightarrow \nu_j,\ j = 1,\ldots,N-1$$

$$1 - cL(\bar{\nu}) = 0 \Rightarrow \nu_N = \bar{\nu}$$

gives the following set of equations:

$$\sum_{n=1}^{N} A_{jn} a_n(R) = K^R_{0\nu_j} \bar{Q}_{0j},\quad j = 1,\ldots,N \tag{20a}$$

with:

$$A_{jn} \equiv \nu_j^2 \left[1 - cL(\nu_j)\right] P^*_n(\nu_j) - T_n(\nu_j) - V_n(\nu_j) \tag{20b}$$

$$\bar{Q}_{0j} \equiv QR\nu_j I^R_{1\nu_j} \tag{20c}$$

to be solved for $a_n(R)$. The scalar flux at the outer surface, obtained by integration of Eq. (18), is conveniently:

$$\phi(R) \equiv \int_0^1 d\mu \sum_{n=1}^{N} a_n(R) P^*_n(\mu) = a_1(R) \tag{21}$$

As will now be shown, knowledge of the pseudo flux at the surface gives the interior flux in addition.

(iv) The theory of the Fn approximation for the interior scalar flux

(iv.1) The singular integral equation for the pseudo flux $\phi(r,\mu)$

To obtain the interior flux, additional projections are required. Projecting Eq. (7a) over rI^r_{0s} on $[0,r]$ gives:

$$\left[1 - cL(s)\right]\phi_{0+}(r,s) = s^2 \int_0^1 d\mu \frac{\chi(r,\mu,\nu)}{\mu^2 - s^2} + rQsL(s) I^r_{1s} \tag{22}$$

with:

$$\phi_{0+}(r,s) \equiv \int_0^1 \frac{d\mu}{\mu^2} \int_0^r dr' r' I^{r'}_{0s} \phi(r',\mu)$$

and:

$$\chi(r,\mu,s) \equiv r\left[\frac{1}{s} I_{1s}^{r} \phi(r,\mu) - I_{0s}^{r} \frac{\partial \phi(r,\mu)}{\partial r}\right]$$

resulting from integration by parts. Letting $s = \nu \pm i\varepsilon$ in Eq. (22) and taking the limit to the cut gives:

$$\begin{aligned} &\left[1 - cL^{\pm}(\nu)\right]\phi_{0+}(r,\nu) = \\ &= \nu^{2}\int_{0}^{1} d\mu \frac{\chi(r,\mu,\nu)}{\mu+\nu}\left[\boldsymbol{P}\frac{1}{\mu-\nu} \pm i\pi\delta(\mu-\nu)\right] + \\ &\qquad + rQ\nu L^{\pm}(\nu) I_{1\nu}^{r} \end{aligned} \tag{23}$$

By adding and subtracting the boundary values therefore:

$$\phi_{0+}(r,\nu) = \frac{1}{c}\left[\chi(r,\mu,\nu) - rQ\nu I_{1\nu}^{r}\right] \tag{24a}$$

$$\left[1 - cL(\nu)\right]\phi_{0+}(r,\nu) = \nu^{2}\boldsymbol{P}\int_{0}^{1}\frac{d\mu}{\mu^{2}-\nu^{2}}\chi(r,\mu,\nu) + rQ\nu L(\nu) I_{1\nu}^{r}, \tag{24b}$$

and from the substitution of Eq. (24a) into Eq. (24b), we find:

$$\begin{aligned} &\left[1 - cL(\nu)\right]\chi(r,\nu,\nu) = \\ &= c\nu^{2}\boldsymbol{P}\int_{0}^{1}\frac{d\mu}{\mu^{2}-\nu^{2}}\chi(r,\mu,\nu) + rQ\nu L(\nu) I_{1\nu}^{r} \end{aligned} \tag{25a}$$

Following a similar procedure by projection of Eq. (7a) over rK_{0s}^{r} on [*r*,*R*] gives:

$$\begin{aligned} \left[1 - cL(\nu)\right]\Upsilon(r,\nu,\nu) &= c\nu^{2}\boldsymbol{P}\int_{0}^{1}\frac{d\mu}{\mu^{2}-\nu^{2}}\Upsilon(r,\mu,\nu) \\ &- c\nu^{2}\boldsymbol{P}\int_{0}^{1}\frac{d\mu}{\mu^{2}-\nu^{2}}\Upsilon(R,\mu,\nu) + Q\nu\left[RK_{1\nu}^{R} - rK_{1\nu}^{r}\right] \end{aligned} \tag{25b}$$

where:

$$\Upsilon(r,\mu,\nu) \equiv -r\left[\frac{1}{\nu} K_{1\nu}^{r} \phi(r,\mu) + K_{0\nu}^{r} \frac{\partial \phi(r,\mu)}{\partial r}\right]$$

We combine Eqs. (25a) and (25b) by noting that:

$$\frac{\phi(r,\mu)}{I_{0\nu}^{r}K_{0\nu}^{r}}=\frac{\chi(r,\mu,\nu)}{I_{0\nu}^{r}}-\frac{\Upsilon(r,\mu,\nu)}{K_{0\nu}^{r}} \tag{26}$$

Thus subtracting Eq. (25b) divided by $K_{0\nu}^{r}$ from Eq. (25a) divided by $I_{0\nu}^{r}$ results in:

$$\begin{aligned}\left[1-cL(\nu)\right]\frac{\phi(r,\nu)}{I_{0\nu}^{r}K_{0\nu}^{r}}=c\nu^{2}\boldsymbol{P}\int_{0}^{1}\frac{d\mu}{\mu^{2}-\nu^{2}}\frac{\phi(r,\mu)}{I_{0\nu}^{r}K_{0\nu}^{r}}+&\\ +c\nu^{2}\boldsymbol{P}\int_{0}^{1}\frac{d\mu}{\mu^{2}-\nu^{2}}\frac{\Upsilon(R,\mu,\nu)}{K_{0\nu}^{r}}+\int_{0}^{r}dr'r'\frac{I_{0\nu}^{r'}}{I_{0\nu}^{r}}Q(r')-&\\ -Q\nu\left[R\frac{K_{1\nu}^{R}}{K_{0\nu}^{r}}-r\frac{K_{1\nu}^{r}}{K_{0\nu}^{r}}\right].&\end{aligned} \tag{27}$$

Since at the boundary:

$$\Upsilon(R,\mu,\nu)=R\left[\frac{K_{1\mu}^{R}K_{0\nu}^{R}}{\mu K_{0\mu}^{R}}-\frac{K_{1\mu}^{R}}{\nu}\right]\phi(R,\mu)$$

and from Eq. (26):

$$\frac{\Upsilon(R,\mu,\nu)}{K_{0\nu}^{R}}=\frac{\chi(R,\mu,\nu)}{I_{0\nu}^{R}}-\frac{\phi(R,\mu)}{I_{0\nu}^{R}K_{0\nu}^{R}}$$

we find for Eq. (27):

$$\begin{aligned}&\left[1-cL(\nu)\right]\phi(r,\nu)-c\nu^{2}\boldsymbol{P}\int_{0}^{1}\frac{d\mu}{\mu^{2}-\nu^{2}}\phi(r,\mu)=\\ &=\left\{\left[1-cL(\nu)\right]\phi(R,\nu)-c\nu^{2}\boldsymbol{P}\int_{0}^{1}\frac{d\mu}{\mu^{2}-\nu^{2}}\phi(R,\mu)\right\}\frac{I_{0\nu}^{r}}{I_{0\nu}^{R}}+h(r,\nu)\end{aligned} \tag{28}$$

where:

$$h(r,\nu)\equiv Q\left[\begin{aligned}K_{0\nu}^{r}\int_{0}^{r}dr'r'I_{0\nu}^{r'}+I_{0\nu}^{r}\int_{r}^{R}dr'r'K_{0\nu}^{r'}-&\\ -\left[\frac{I_{0\nu}^{r}K_{0\nu}^{R}}{I_{0\nu}^{R}}\right]\int_{0}^{R}dr'r'I_{0\nu}^{r'}&\end{aligned}\right]$$

or from known integrals and the Wronskian:

$$h\left(r,\nu\right)=\nu^{2}\bar{Q}_{0}\left[1-\frac{I_{0\nu}^{r}}{I_{0\nu}^{R}}\right]$$

Equation (28) is a singular integral equation for the interior pseudo flux based on the pseudo boundary flux.

(iv.2) The *Fn* approximation for the pseudo flux $\phi(r,\mu)$

The *Fn* approximation for the interior flux will be:

$$\phi\left(r,\mu\right)=\mu^{2}\sum_{n=1}^{N}a_{n}\left(r\right)P_{n}^{*}\left(\mu\right) \tag{29}$$

which when introduced into Eq. (28) yields:

$$\sum_{n=1}^{N}a_{n}\left(r\right)\bar{A}_{n}\left(\nu\right)=\frac{I_{0\nu}^{r}}{I_{0\nu}^{R}}\sum_{n=1}^{N}a_{n}\left(R\right)\bar{A}_{n}\left(\nu\right)+h\left(r,\nu\right) \tag{30a}$$

with:

$$\bar{A}_{n}\left(\nu\right)\equiv\nu^{2}\left[1-cL\left(\nu\right)\right]P_{n}^{*}\left(\nu\right)-T_{n}\left(\nu\right) \tag{30b}$$

At the *N* collocation points ν_j, Eq. (30a) becomes the following set of algebraic equations for $a_n(r)$:

$$\sum_{n=1}^{N}\bar{A}_{jn}a_{n}\left(r\right)=\frac{I_{0\nu_j}^{r}}{I_{0\nu_j}^{R}}\sum_{n=1}^{N}\bar{A}_{jn}a_{n}\left(R\right)+h_{j}\left(r\right) \tag{31}$$

with:

$$\bar{A}_{jn}\equiv\nu_{j}^{2}\left[1-cL\left(\nu_{j}\right)\right]P_{n}^{*}\left(\nu_{j}\right)-T_{n}\left(\nu_{j}\right)$$

$$h_{j}\left(r\right)\equiv Q\left[\begin{array}{r}K_{0\nu_j}^{r}\int_{0}^{r}dr'r'I_{0\nu_j}^{r'}+I_{0\nu_j}^{r}\int_{r}^{R}dr'r'K_{0\nu_j}^{r'}Q-\\ -\left[\frac{I_{0\nu_j}^{r}K_{0\nu_j}^{R}}{I_{0\nu_j}^{R}}\right]\int_{0}^{R}dr'r'I_{0\nu_j}^{r'}\end{array}\right]$$

or:

$$h_{j}\left(r\right)=\nu_{j}^{2}\bar{Q}_{0}\left[1-\frac{I_{0\nu_j}^{r}}{I_{0\nu_j}^{R}}\right]$$

Thus, the desired scalar flux at position *r*, obtained from orthogonality, is:

$$\phi(r) \equiv \int_0^1 d\mu \sum_{n=1}^{N} a_n(r) P_n^*(\mu) = a_1(r) \tag{32}$$

(e) Numerical implementation and demonstration for Benchmark 3.4

The entire *Fn* algorithm, rests on the evaluation of the matrix elements $A_n(\nu)$ and $\overline{A}_n(\nu)$ from Eqs. (19b) and (30b) respectively. The evaluation requires Legendre functions of the second kind as well as modified Bessel functions as found in Ref. 6. We use a Gauss-Legendre quadrature of order *Lm* to evaluate the integrals. The same procedure gives the integrals when ν is $\bar{\nu}$ (for $\bar{\nu}$ real or imaginary in the case of criticality), found by bisection for $0.1 \le c \le 1.1$. Otherwise, series representations [7] for $c(\nu)$ provide the necessary accuracy. We apply LU decomposition [8] for the matrix inversions of Eqs. (20a) and (31) leading to the desired scalar flux distributions of Eqs. (21) and (32).

Since the following results are to be true semi-analytical benchmarks, we must consider the approximations contained in the *Fn* solution. In particular, the two approximations are the quadrature evaluation and the order of the *Fn* approximation itself. Since discretization in the function space of solutions is necessary, a single solution corresponding to discretizations *Lm* and *N* carries no information concerning the accuracy of the solution. For this reason, convergence acceleration can provide a measure of accuracy. In this procedure, a solution is a sequence of solutions along a path in the discretized *Lm*/*N* space. Assumed to possess a limit, we then rearrange the sequence to converge more quickly to that limit through a convergence acceleration procedure. For our purpose, the Wynn-epsilon convergence accelerator (Appendix A.2) seems best. The path chosen is on the "diagonal" of the discretization space where the sequence is created for approximation orders (*Lm*0+*j*, *N*0+*j*) with *j* incremented until convergence to a desired relative error for the quantity of interest. Convergence acceleration, applied in this manner, represents the latest innovation in semi-analytical benchmarks, and will eventually be an integral part of all future analytical benchmarking efforts.

We present numerical results for two classes of problems. The first is for the flux distribution from a uniformly distributed isotropic fixed source and the second for a critical cylinder.

(i) Flux comparisons

To conform to the results in Ref. 4, we report the surrogate flux:

$$F(r) \equiv 1 - \frac{\phi(r)}{Q}$$

in Tables 3.4.1(a) and 3.4.1(b) where we provide a head-to-head comparison with a Siewert benchmark [4] for cylinders of radii 1 and 10. The discrepant digits are highlighted. As we observe, only three values are in disagreement (all by a single digit), which is within the quoted accuracy of the published benchmark. For completeness, Tables 3.4.2(a) and 3.4.2(b) are included for *c* = 0.1(0.5)0.25. We expect the values to be correct to one unit in the last digit. Again for completeness, Figure 3.4.1 shows the spatial flux distribution for *R* = 10 and *c* = 0.3(0.2)0.9.

(ii) Criticality

(ii.1) Critical radii

For a critical system, the source vanishes and the eigenvalue $\bar{\nu}$ becomes imaginary, $\bar{\nu} = i\bar{z}$. The matrix element [Eq. (19b)] for *j* = *N* is therefore:

$$A_{Nn} = \int_0^1 d\mu \frac{\mu^2}{\mu^2 + \bar{z}^2} \left[J_{1\bar{z}}^R + \frac{\tilde{z}}{\mu} \xi_\mu J_{0\bar{z}}^R \right] P_n^*(\mu)$$

where $J_{n\bar{z}}^R$ is the Bessel function of the first kind of order *n*. From Eq. (19a) (without a source), the critical equation becomes:

$$\sum_{n=1}^{N} A_{jn} a_n(R) = 0, \quad j = 1, \ldots, N \tag{33a}$$

for which a nontrivial solution exists if and only if:

$$Det\left[\boldsymbol{A}\right] = 0 \tag{33b}$$

where:

$$\boldsymbol{A} \equiv \left\{ A_{jn}(c, R);\ j, n = 1, \ldots, N \right\}$$

Note that we include the explicit dependence of the matrix element on *c* and *R*. Given a value of *c*, we resolve this determinental equation for the critical radius *R* using bisection.

Table 3.4.3(a) gives the critical radii for the indicated values of *c* considered in the literature [2,3]. The highlighted digits are in disagreement with Siewert's benchmark of Ref. 3. In addition, we find nearly complete agreement with Sanchez's results [10]. We include Table 3.4.3(b) to provide a more complete set of critical radii and expect the values to be accurate to within ± one digit in the last place.

(ii.2) Critical flux distribution

The critical flux distribution becomes particularly straightforward to compute from the critical equation, Eq. (33a), with the fundamental eigenvector normalized to:

$$a_1(R) \equiv 1 \tag{34a}$$

Thus, $a_n(R)$, $n = 2,\ldots,N$ are determined from:

$$\sum_{n=2}^{N} A_{jn} a_n(R) = -A_{j1} \tag{34b}$$

For criticality and $j = 1,\ldots,N-1$, Eq. (31) becomes:

$$\sum_{n=1}^{N} \bar{A}_{jn} a_n(r) = \frac{I_{0\nu_j}^{r}}{I_{0\nu_j}^{R}} \sum_{n=1}^{N} \bar{A}_{jn} a_n(R) \tag{35a}$$

and for $j = N$:

$$\sum_{n=1}^{N} \bar{A}_{Nn} a_n(r) = \frac{J_{0\nu_N}^{r}}{J_{0\nu_N}^{R}} \sum_{n=1}^{N} \bar{A}_{Nn} a_n(R) \tag{35b}$$

which gives $a_n(r)$, $n = 1,\ldots,N$. Finally, the normalized critical flux distribution is:

$$\frac{\phi(r)}{\phi(0)} = \frac{a_1(r)}{a_1(0)}$$

Table 3.4.4 gives the normalized critical fluxes for several values of c. The highlighted digits are discrepant with respect to the Siewert Benchmark [3]. The distributions are again within the quoted accuracy however.

For completeness, Figure 3.4.2 gives the critical flux distributions for c = 1.05(0.05)2.00.

Table 3.4.1(a). Surrogate flux: *R* = 1

r**c	**0.3**	**0.5**	**0.7**	**0.9**
0.00000E+00	3.64405E-01	4.57065E-01	5.96607E-01	8.24677E-01
1.00000E-01	3.66325E-01	4.58897E-01	5.98138E-01	8.25431E-01
2.00000E-01	3.72157E-01	4.64449E-01	6.02766E-01	8.27704E-01
3.00000E-01	3.82121E-01	4.73895E-01	6.10603E-01	8.31533E-01
4.00000E-01	3.96622E-01	4.87552E-01	6.21852E-01	8.36986E-01
5.00000E-01	4.16309E-01	5.05927E-01	6.36839E-01	8.44173E-01
6.00000E-01	4.42206E-01	5.29816E-01	6.56077E-01	8.53271E-01
7.00000E-01	4.75976E-01	5.60510E-01	6.80397E-01	8.64571E-01
8.00000E-01	5.20597E-01	6.00306E-01	7.11290E-01	8.78607E-01
9.00000E-01	5.82596E-01	6.54245E-01	7.52048E-01	8.96589E-01
1.00000E+00	6.94369E-01	7.47538E-01	8.19470E-01	9.24929E-01

Table 3.4.1(b). Surrogate flux: *R* = 10

*r**c*	0.3	0.5	0.7	0.9
0.00000E+00	4.60882E-05	1.38859E-04	8.01829E-04	2.01898E-02
1.00000E+00	5.95324E-05	1.73680E-04	9.46293E-04	2.16079E-02
2.00000E+00	1.12121E-04	3.05085E-04	1.45897E-03	2.61624E-02
3.00000E+00	2.53579E-04	6.37744E-04	2.62685E-03	3.48252E-02
4.00000E+00	6.25301E-04	1.44881E-03	5.12494E-03	4.94721E-02
5.00000E+00	1.62250E-03	3.44884E-03	1.04520E-02	7.33358E-02
6.00000E+00	4.37880E-03	8.48704E-03	2.19360E-02	1.11811E-01
7.00000E+00	1.22887E-02	2.15284E-02	4.71009E-02	1.73872E-01
8.00000E+00	3.62559E-02	5.66444E-02	1.03616E-01	2.74762E-01
9.00000E+00	1.16748E-01	1.58763E-01	2.37138E-01	4.42664E-01
1.00000E+01	5.58360E-01	6.00996E-01	6.63330E-01	7.81243E-01

Table 3.4.2(a). Surrogate flux: *R* = 1

*r**c*	0.1	0.15	0.2	0.25
0.00000E+00	2.99256E-01	3.13617E-01	3.29165E-01	3.46040E-01
1.00000E-01	3.01163E-01	3.15533E-01	3.31087E-01	3.47964E-01
2.00000E-01	3.06966E-01	3.21362E-01	3.36930E-01	3.53809E-01
3.00000E-01	3.16920E-01	3.31351E-01	3.46935E-01	3.63807E-01
4.00000E-01	3.31495E-01	3.45954E-01	3.61539E-01	3.78379E-01
5.00000E-01	3.51447E-01	3.65905E-01	3.81450E-01	3.98205E-01
6.00000E-01	3.77974E-01	3.92362E-01	4.07785E-01	4.24356E-01
7.00000E-01	4.13044E-01	4.27224E-01	4.42369E-01	4.58580E-01
8.00000E-01	4.60197E-01	4.73899E-01	4.88471E-01	5.04003E-01
9.00000E-01	5.27241E-01	5.39894E-01	5.53285E-01	5.67491E-01
1.00000E+00	6.52895E-01	6.62411E-01	6.72459E-01	6.83091E-01

Table 3.4.2(b). Surrogate flux: *R* = 10

*r**c*	0.1	0.15	0.2	0.25
0.00000E+00	2.18198E-05	2.56864E-05	3.06790E-05	3.72505E-05
1.00000E+00	2.86832E-05	3.36496E-05	4.00294E-05	4.83781E-05
2.00000E+00	5.60906E-05	6.53170E-05	7.70364E-05	9.21787E-05
3.00000E+00	1.32442E-04	1.52913E-04	1.78578E-04	2.11254E-04
4.00000E+00	3.42077E-04	3.91281E-04	4.52101E-04	5.28318E-04
5.00000E+00	9.33715E-04	1.05700E-03	1.20704E-03	1.39184E-03
6.00000E+00	2.66667E-03	2.98339E-03	3.36212E-03	3.81968E-03
7.00000E+00	7.98668E-03	8.81266E-03	9.78051E-03	1.09243E-02
8.00000E+00	2.54732E-02	2.76356E-02	3.01085E-02	3.29550E-02
9.00000E+00	9.07754E-02	9.62760E-02	1.02371E-01	1.09156E-01
1.00000E+01	5.26092E-01	5.33447E-01	5.41241E-01	5.49525E-01

Table 3.4.3(a). Critical radii comparisons

c	*R* (Ref. 3)	*R* (Ref. 10)
1.01E+00	1.312551649E+01	1.312551647E+01
1.02E+00	9.04325485E+00	------------
1.05E+00	5.41128829E+00	------------
1.10E+00	3.57739130E+00	3.57739129E+00
1.20E+00	2.28720926E+00	------------
1.30E+00	1.72500292E+00	1.72500292E+00
1.40E+00	1.39697859E+00	------------
1.50E+00	1.17834085E+00	1.17834085E+00
1.60E+00	1.02083901E+00	------------
1.80E+00	8.07426618E-01	------------
2.00E+00	6.68612867E-01	6.6861287E-01

Table 3.4.3(b). Additional critical radii

c	*R*	*c*	*R*
1.01E+00	1.3125516E+01	1.48E+00	1.2161455E+00
1.02E+00	9.0432549E+00	1.50E+00	1.1783408E+00
1.03E+00	7.2314062E+00	1.52E+00	1.1429117E+00
1.04E+00	6.1499466E+00	1.54E+00	1.1096324E+00
1.05E+00	5.4112883E+00	1.56E+00	1.0783058E+00
1.06E+00	4.8657524E+00	1.58E+00	1.0487589E+00
1.07E+00	4.4416675E+00	1.60E+00	1.0208390E+00
1.08E+00	4.0998327E+00	1.62E+00	9.9441094E-01
1.09E+00	3.8167572E+00	1.64E+00	9.6935444E-01
1.10E+00	3.5773913E+00	1.66E+00	9.4556217E-01
1.12E+00	3.1922162E+00	1.68E+00	9.2293801E-01
1.14E+00	2.8934088E+00	1.70E+00	9.0139555E-01
1.16E+00	2.6531096E+00	1.72E+00	8.8085691E-01
1.18E+00	2.4546128E+00	1.74E+00	8.6125168E-01
1.20E+00	2.2872093E+00	1.76E+00	8.4251603E-01
1.22E+00	2.1436738E+00	1.78E+00	8.2459196E-01
1.24E+00	2.0189307E+00	1.80E+00	8.0742662E-01
1.36E+00	1.5108142E+00	1.82E+00	7.9097174E-01
1.28E+00	1.8120184E+00	1.84E+00	7.7518314E-01
1.30E+00	1.7250029E+00	1.86E+00	7.6002032E-01
1.32E+00	1.6466161E+00	1.88E+00	7.4544605E-01
1.34E+00	1.5755658E+00	1.90E+00	7.3142605E-01
1.36E+00	1.5108142E+00	1.92E+00	7.1792869E-01
1.38E+00	1.4515168E+00	1.94E+00	7.0492476E-01
1.40E+00	1.3969786E+00	1.96E+00	6.9238723E-01
1.42E+00	1.3466215E+00	1.98E+00	6.8029102E-01
1.44E+00	1.2999606E+00	2.00E+00	6.6861287E-01
1.46E+00	1.2565852E+00		

Table 3.4.4. Critical flux distributions

r/R:c	**1.05**	**1.1**	**1.6**	**2.0**
0.00E+00	1.00000E+00	1.00000E+00	1.00000E+00	1.00000E+00
0.25E-01	9.29851E-01	9.36052E-01	9.54996E-01	9.59783E-01
0.50E-01	7.33990E-01	7.56084E-01	8.24845E-01	8.42634E-01
0.75E-01	4.52168E-01	4.92189E-01	6.21823E-01	6.56963E-01
0.85E-01	3.26662E-01	3.71791E-01	5.22344E-01	5.64397E-01
0.91E-01	2.49166E-01	2.96040E-01	4.56627E-01	5.02561E-01
0.95E-01	1.95805E-01	2.43013E-01	4.08837E-01	4.57218E-01
0.98E-01	1.53086E-01	1.99922E-01	3.68806E-01	4.18990E-01
1.00E-00	1.17908E-01	1.64122E-01	3.35065E-01	3.86650E-01

REFERENCES

[1] Mitsis, G.J., *Transport Solutions to the Monoenergetic Critical Problems*, ANL, ANL-6787, (1963).

[2] Westfall, R.M., "Singular Eigenfunction Solution of the Monoenergetic Neutron Transport Equation for Finite Radially Reflected Critical Cylinders", *Nucl. Sci. & Eng.*, **52**, 1 (1973).

[3] Siewert, C.E., "The Critical Problem for an Infinite Cylinder", *Nucl. Sci. & Eng.*, **84**, 79 (1983).

[4] Siewert, C.E., "Neutron Transport in Cylindrical Geometry", *Nucl. Sci. & Eng.*, **87**, 107 (1984).

[5] Roos, B.W., *Analytic Functions and Distributions in Physics and Engineering*, John Wiley & Sons, NY (1969).

[6] Zhang, S., J. Jin, *Computation of Special Functions*, John Wiley & Sons, NY (1996).

[7] Case, K.M., F. De Hoffman, G. Placzek, *Introduction to the Theory of Neutron Diffusion*, Los Alamos Scientific Laboratory, Los Alamos, NM (1953).

[8] Press, W., *et al.*, *Numerical Recipes*, Cambridge University Press, NY (1986).

[9] Baker, G., P. Graves-Morris, *Pade' Approximants*, Cambridge University, NY (1996).

[10] Sanchez, R., *Generalization of Asaoka's Method to Linearly Anisotropic Scattering: Benchmark Data in Cylindrical Geometry*, CEA-N-1831, CEN de Saclay, Gif-sur-Yvette, France (1975).

Figure 3.4.1. Surrogate flux variation with *c* in a cylinder of radius *R* = 10

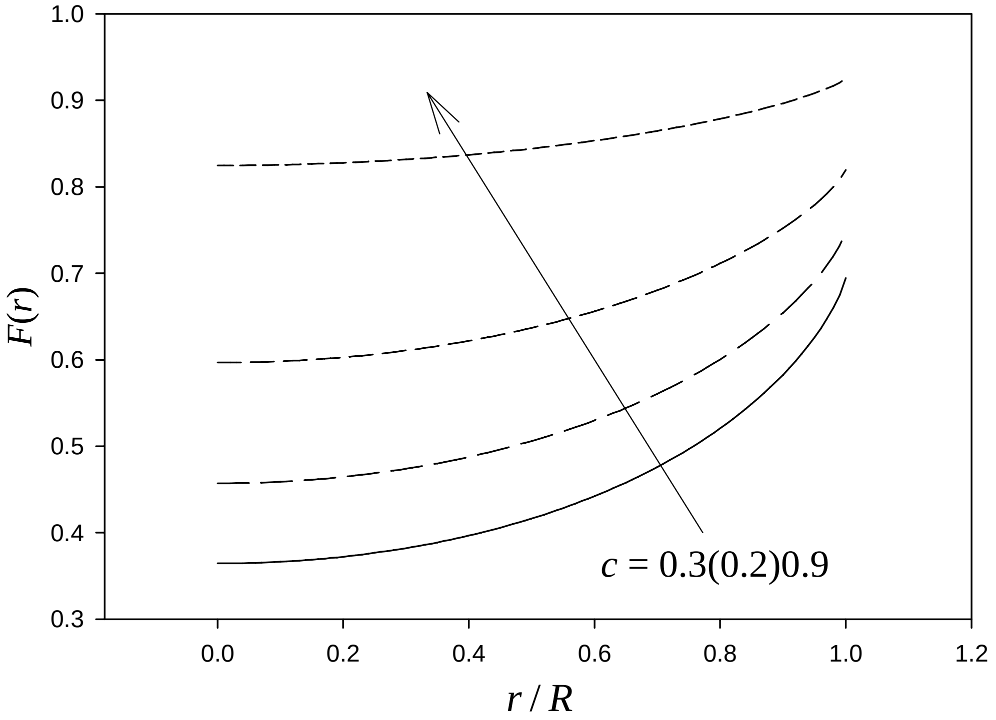

Figure 3.4.2. Variation of critical flux distributions with *c*

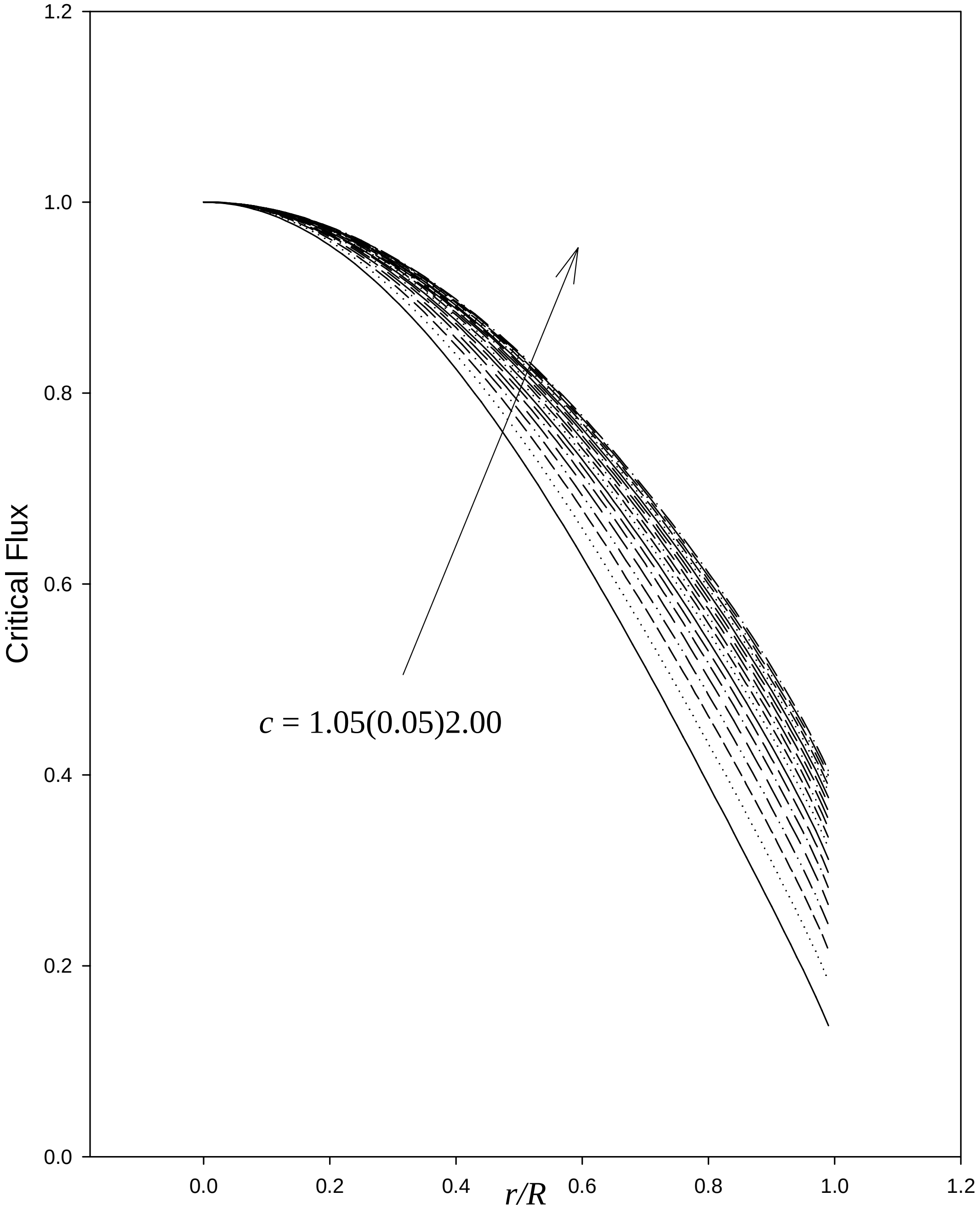

Chapter 4

ONE-DIMENSIONAL MULTIGROUP NEUTRON TRANSPORT

Having considered slowing down and spatial diffusion separately in the previous two chapters, it is now appropriate to consider these transport process simultaneously. This, of course, is much easier said than done. Again, the challenge is mathematical tractability since the two physical phenomena together bring new mathematics. Complexity, therefore, dictates we begin with the simplest possible case, which still has the transport features we would like to test through benchmarking. For this reason, we start with slowing down in a homogeneous infinite medium from a plane source. The avoidance of boundaries allows simplification by virtue of a Fourier transform and its numerical inversion. As has been already demonstrated, we can conveniently treat slowing down in the multigroup approximation. Thus, having tested both the numerical Fourier transform inversion and the multigroup solution, we can apply these two numerical procedures to this more difficult, but more meaningful, case with some confidence in achieving a benchmark result. The second benchmark in this chapter will be for slowing down in a slab – a more important though difficult undertaking.

The first benchmark is concerned with neutron slowing down from a localized plane source in an anisotropic scattering medium. In particular, neutrons, emitted at the center of an infinite medium, diffuse outwardly while simultaneously losing energy. The solution is through a Fourier transform and essentially is just an extension of one-group theory. In addition, we consider point source emission but only for isotropic scattering, fission and for up- and down- scattering. The approach is substantially different from the previous cases because upscattering requires matrix inversion in the transform space.

In the second benchmark, we assume the multigroup approximation in a slab. The solution is through the Green's function method (GFM/MG), which first requires the determination of the Green's function and then the exiting angular flux distributions from Placzek's lemma.

Both of these benchmarks begin with the multigroup form of the transport equation [Eq. (1.VIII.2)] in plane 1-D geometry:

$$\begin{aligned}\left[\mu\frac{\partial}{\partial x}+\Sigma_g\left(x\right)\right]\phi_g\left(x,\mu\right) &= \\ &=\frac{1}{2}\sum_{l=0}^{\infty}\left(2l+1\right)\sum_{g'=1}^{G}\Sigma_{slgg'}\left(x\right)P_l\left(\mu\right)\phi_{lg'}\left(x\right)+ \\ &\quad+\frac{1}{2}\chi_g\sum_{g'=1}^{G}\nu_{g'}\Sigma_{fg'}\left(x\right)\phi_{0g'}\left(x\right)+Q_g\left(x,\mu\right)\end{aligned} \tag{VIII.2}$$

This is the main equation of deterministic transport theory serving as the basis of modern-day reactor analysis whether for two-groups, few-groups, multigroups or 70,000 ultra-fine groups.

Benchmark 4.1: Multigroup transport in infinite media/the Fourier transform solution

(a) Brief description

Neutrons slowing down in an infinite medium with spatial dependence in the multigroup approximation.

(b) Classification

NT/I:P,SP,CY/I/MG/I,B/L,D/X(C),A(C),E(D)/NFTI

(c) Physical description

Neutrons, emitted at one energy at the center of an infinite medium, slow down upon collision with stationary nuclei (no upscattering). One spatial dimension and one angle describe the neutron motion after emission. We solve the neutron transport equation in the multigroup approximation in plane and spherical geometries. Upscattering and fission are included for isotropic point source emission in the last example.

(d) Analytical representation

(i) The plane source

From Eq. (1.VIII.2), the 1-D slab transport equation for anisotropic scattering in the multigroup approximation without fission and uniform cross sections in a homogeneous medium with down scattering only is:

$$\left[\mu\frac{\partial}{\partial x}+\Sigma_g\right]\phi_g(x,\mu)= \tag{1a}$$
$$=\frac{1}{2}\sum_{l=0}^{L}(2l+1)\sum_{g'=1}^{g}\Sigma_{slgg'}P_l(\mu)\phi_{lg'}(x)+Q_g(x,\mu)$$

subject to:

$$\lim_{|x|\to\infty}\phi_g(x,\mu)<\infty \tag{1b}$$

Note that we have truncated the scattering kernel at L for practical purposes. Taking a spatial Fourier transform:

$$\psi_g(k,\mu)\equiv\int_{-\infty}^{\infty}dxe^{-ikx}\phi_g(x,\mu)$$

gives:

$$\left[\Sigma_g+ik\mu\right]\psi_g(k,\mu)=\sum_{g'=1}^{g}\sum_{l=0}^{L}\frac{2l+1}{2}\Sigma_{lgg'}P_l(\mu)\psi_{g'l}(k)+Q_g(k,\mu) \tag{2}$$

with:

$$Q_g(k,\mu) \equiv \int_{-\infty}^{\infty} dx e^{-ikx} Q_g(x,\mu)$$

and the transformed Legendre moments are:

$$\psi_{gl}(k) \equiv \int_{-1}^{1} d\mu P_l(\mu)\psi_g(k,\mu)$$

We assume a source having an angular distribution $Q_g(\mu)$ in group g at the center plane (x = 0):

$$Q_g(x,\mu) \equiv Q_g(\mu)\delta(x)$$

Now rearranging Eq. (2) gives the following one-group form:

$$\begin{aligned}\left[\Sigma_g + ik\mu\right]\psi_g(k,\mu) = \sum_{l=0}^{L} \frac{2l+1}{2}\Sigma_{lgg} P_l(\mu)\psi_{gl}(k) + \\ + \Lambda_g(k,\mu) + Q_g(\mu)\end{aligned} \tag{3a}$$

where the (known) in-scattering source coming from higher energy groups is:

$$\Lambda_g(k,\mu) \equiv \sum_{g'=1}^{g-1}\sum_{l=0}^{L} \frac{2l+1}{2}\Sigma_{lgg'} P_l(\mu)\psi_{g'l}(k) \tag{3b}$$

We solve for the moments by projecting Eq. (3a) over $P_m(\mu)$ to give the following set of algebraic equations:

$$\sum_{l=0}^{L}\left[\delta_{ml} - (2l+1)\Sigma_{lgg}T_{gml}(k)\right]\psi_{gl}(k) = \bar{\Lambda}_{gm}(k) + Q_{gm}(\mu) \tag{4}$$

In this set:

$$\bar{\Lambda}_{gm}(k) \equiv T_{gml}(k)\sum_{g'=1}^{g-1}\sum_{l=0}^{L}(2l+1)\Sigma_{lgg'}\psi_{g'l}(k)$$

with:

$$T_{gml}(k) \equiv \frac{1}{2}\int_{-1}^{1} d\mu \frac{P_m(\mu)P_l(\mu)}{\Sigma_g + ik\mu}$$

$$Q_{gm}(k) \equiv \int_{-1}^{1} d\mu \frac{P_m(\mu)}{\Sigma_g + ik\mu} Q_g(\mu)$$

The expression for $T_{gml}(k)$ has appeared in several of the previous benchmarks. Only the transformed scalar flux, ψ_{g0}, from the solution of Eqs. (4) and its subsequent inversion will be of interest. Note that we can solve Eq. (4) for the group moments by matrix inversion and reconstruct the group source recursively.

For the special case of isotropic scattering ($L = 0$) (which we consider in the remainder of this section), there results:

$$\psi_{g0}(k) = \left[\bar{\Lambda}_{g0}(k) + Q_{g0}(\mu)\right]\left[1 - \Sigma_{0gg} T_{g00}(k)\right]^{-1} \tag{5}$$

with:

$$\bar{\Lambda}_{g0}(k) \equiv T_{g00}(k) \sum_{g'=1}^{g-1} \Sigma_{0gg'} \psi_{g'0}(k)$$

$$Q_{g0}(k) \equiv \int_{-1}^{1} d\mu \frac{Q_g(\mu)}{\Sigma_g + ik\mu}$$

Once we know ψ_{g0}, the inversion for the scalar flux is:

$$\phi_{g0}(x) \equiv \frac{1}{2\pi} \int_{-\infty}^{\infty} dx e^{ikx} \psi_{g0}(k)$$

which we evaluate by the same numerical Fourier transform inversion (Appendix B.2) as presented previously (see Benchmark 3.1).

For a source in the highest energy group only:

$$Q_g(\mu) \equiv Q(\mu)\delta_{g1}$$

Eq. (5) becomes:

$$\psi_{g0}(k) = \left[\bar{\Lambda}_{g0}(k) + Q(\mu)\delta_{g1}\right]\left[1 - \Sigma_{0gg} T_{g00}(k)\right]^{-1} \tag{6}$$

As noted above, for anisotropic scattering, we would employ the same inversion procedure for all L moments from the matrix inversion of Eqs. (4). Here, we seek only the zeroth moment however.

In general, we consider the two common angular source distributions:

$$Q(\mu) \equiv \begin{cases} 1/2, & \text{isotropic} \\ \delta(\mu - \mu_0), & \text{beam} \end{cases}$$

in presenting benchmark results. In addition, however, the flux in plane geometry for an isotropic source leads to the determination of the flux from a point source as will now be demonstrated.

(ii) The point source

The plane/point transformation will give the flux from a point source in an spherically symmetric infinite medium, which we now consider.

(ii.1) Multigroup transport in plane geometry

The multigroup transport equation in a homogeneous plane infinite medium with isotropic up- and down- scattering, including fission and an isotropic source of strength Q_g at its center, is [Eq. (1.VIII.2)]:

$$\begin{aligned}&\left[\mu\frac{\partial}{\partial x}+\Sigma_g\right]\phi_g(x,\mu)=\\&=\frac{1}{2}\sum_{g'=1}^{G}\Sigma_{s0gg'}\phi_{0g'}(x)+\frac{1}{2}\chi_g\sum_{g'=1}^{G}\nu_{g'}\Sigma_{fg'}\phi_{0g'}(x)+\frac{1}{2}Q_g\delta(x)\end{aligned} \tag{7}$$

More appropriately, in compact vector form, Eq. (7) becomes:

$$\left[\mu\boldsymbol{I}\frac{\partial}{\partial x}+\Sigma\right]\boldsymbol{\phi}(x,\mu)=\frac{1}{2}\left[\Sigma_s+\chi\left(\boldsymbol{\nu}\Sigma_f\right)^T\right]\boldsymbol{\phi}(x)+\frac{1}{2}\boldsymbol{Q}\delta(x) \tag{8a}$$

where the angular flux and source are the group vectors:

$$\begin{aligned}&\boldsymbol{\phi}(x,\mu)\equiv\left\{\phi_g(x,\mu)\right\}\\&\boldsymbol{Q}\equiv\left\{Q_g\right\}\end{aligned} \tag{8b}$$

The group scalar flux is:

$$\boldsymbol{\phi}(x)\equiv\int_{-1}^{1}d\mu\boldsymbol{\phi}(x,\mu)$$

and the group parameters are:

$$\begin{aligned}&\Sigma\equiv diag\left\{\Sigma_g;g=1,\ldots,G\right\}\\&\Sigma_s\equiv\left\{\Sigma_{s0gg'};g,g'=1,\ldots,G\right\}\\&\chi\left(\boldsymbol{\nu}\Sigma_f\right)^T\equiv\left\{\chi_g\nu_{g'}\Sigma_{fg'};g,g'=1,\ldots,G\right\}\end{aligned}$$

Following the same procedure as in the one-group case (Benchmark 3.1), the Fourier transform:

$$\boldsymbol{\Psi}(k,\mu)\equiv\int_{-\infty}^{\infty}dxe^{-ikx}\boldsymbol{\phi}(x,\mu)$$

gives:

$$\boldsymbol{D}(k,\mu)\boldsymbol{\Psi}(k,\mu)=\frac{1}{2}\left[\Sigma_s+\chi\left(\boldsymbol{\nu}\Sigma_f\right)^T\right]\boldsymbol{\Psi}(k)+\frac{1}{2}\boldsymbol{Q} \tag{9}$$

with:

$$\boldsymbol{D}(k,\mu) \equiv [\Sigma + ik\mu \boldsymbol{I}] = diag\left\{\Sigma_g + ik\mu\right\}$$

We obtain the transformed angular flux directly from matrix inversion of Eq. (9) as:

$$\Psi(k,\mu) = \frac{1}{2}\boldsymbol{D}^{-1}(k,\mu)\left[\Sigma_s + \chi\left(\nu\Sigma_f\right)^T\right]\Psi(k) + \frac{1}{2}\boldsymbol{D}^{-1}(k,\mu)\boldsymbol{Q}$$

with:

$$\boldsymbol{D}(k,\mu)^{-1} = diag\left\{\frac{1}{\Sigma_g + ik\mu}\right\}$$

Then, by integration over μ and the solution of the resulting algebraic equation, we determine the zeroth moment to be:

$$\boldsymbol{\Psi}(k) = \left\{\Sigma - \boldsymbol{L}(k)\left[\Sigma_s + \chi\left(\nu\Sigma_f\right)^T\right]\right\}^{-1}\boldsymbol{L}(k)\boldsymbol{Q} \tag{10}$$

where:

$$\boldsymbol{L}(k) \equiv diag\left\{T_g(k)\right\},\ \ T_g(k) = \frac{tan^{-1}\left(k/\Sigma_g\right)}{k/\Sigma_g}$$

The explicit Fourier transform inversion:

$$\boldsymbol{\phi}(x) \equiv \frac{1}{2\pi}\int_{-\infty}^{\infty} dk e^{ikx}\boldsymbol{\Psi}(k)$$

is therefore:

$$\boldsymbol{\phi}(x) = \frac{1}{2\pi}\int_{-\infty}^{\infty} dk e^{ikx}\left\{\Sigma - \boldsymbol{L}(k)\left[\Sigma_s + \chi\left(\nu\Sigma_f\right)^T\right]\right\}^{-1}\boldsymbol{L}(k)\boldsymbol{Q} \tag{11}$$

which is identical in format to the one-group case.

(ii.2) Plane/point transformation

We obtain the plane/point transformation by considering the flux at a distance x from the plane isotropically emitting source shown in Figure 4.1.1. The flux at x is an accumulation of the fluxes from all the infinitesimal point sources comprising the plane source. The collective effect at x from the point source from all elements $\rho d\rho d\vartheta$ of the plane source is therefore:

$$\int_0^{2\pi} d\vartheta \int_0^{\infty} d\rho \rho \phi_{pt}(r) = \phi(x) \tag{12}$$

Since:

$$r^2 = \rho^2 + x^2$$

Eq. (12) becomes:

$$2\pi \int_x^\infty drr\phi_{pt}(r) = \phi(x)$$

and differentiating gives the plane/point transformation:

$$\phi_{pt}(r) = -\frac{1}{2\pi r}\frac{d\phi(r)}{dr} \tag{13}$$

Hence, from Eqs. (11) and (13), the Fourier transform inversion for the group flux vector from a point source at the origin of a spherical infinite medium is:

$$\boldsymbol{\phi}_{pt}(r) = \frac{1}{2\pi i}\frac{1}{2\pi r}\int_{-\infty}^{\infty} dkke^{ikr}\left\{\Sigma - \boldsymbol{L}(k)\left[\Sigma_s + \boldsymbol{\chi}\left(\boldsymbol{\nu}\Sigma_f\right)^T\right]\right\}^{-1}\boldsymbol{L}(k)\boldsymbol{Q} \tag{14}$$

which we can numerically evaluate.

(e) Numerical implementation and demonstration for Benchmark 4.1

Here, we demonstrate multigroup neutron transport in both the infinite plane and spherically symmetric infinite media.

(i) The plane source

The numerical inversion for the multigroup benchmark is essentially identical to that of the infinite medium one-group benchmark. The reader should consult Benchmark 3.1 for further details.

To verify that the multigroup determination is indeed operational, we present a comparison to a one-group calculation. The comparison is for slowing down in carbon from energy E_0 (zero lethargy) for a constant total cross section with $c = 0.5$. We generate the multigroup cross sections by the procedure outlined in Benchmark 2.3. Since the total cross section is assumed constant ($\Sigma_g \equiv 1$) and the transfer cross sections are normalized to the total scattering cross section,

$$\sum_{g=1}^{G} \Sigma_{0gg'} \equiv c = 0.5$$

on summation of the flux over all groups, we have:

$$\phi(x) = \sum_{g=1}^{G} \phi_g(x)$$

where $\phi(x)$ is the one-group flux. Table 4.1.1 gives the comparison of the group sum with the one-group flux profile for a beam source ($\mu_0 = 1$) in the lethargy range $0 \le u \le 12$ for $G = 6$, 15 and 30. We observe excellent agreement with increasing total groups – even for the fewest number of groups. Thus, the one-group self-consistency check is satisfied.

Figure 4.1.2(a) shows the energy spectrum at six positions in the spatial interval [–3,3] for a 70%/30% carbon/iron mixture with $G = 78$ and normal beam incidence. Note the appearance of the characteristic Placzek transients for both elements at points near the source ($x \approx 0$). For points further away, the Placzek transients diminish and eventually disappear because of the relatively large amount of scattering. Figures 4.1.2(b) and (c) gives the spatial distribution for selected groups for beam and isotropic sources. The presence of the source is lost as the neutrons gain (lose) lethargy (energy).

Figures 4.1.3(a) and 4.1.3(b) provide a study of the convergence of the lethargy spectrum for a 70%/30% carbon/iron mixture for a beam source and indicates convergence with total number of groups G. Figure 4.1.3(a) shows overall convergence with total number of groups near the source and Figure 4.1.3(b) shows global spatial/lethargy convergence. The Placzek discontinuities are clearly visible.

Table 4.1.2 provides fluxes for qualification of this benchmark. The last group in $G = 49$ calculation for a 70%/30% carbon/iron mixture is given at 12 positions for decreasing error. We observe that the inversion remains accurate with the last column expected to be correct to all digits shown.

(ii) The point source

Since the flux, for a point source, is singular directly on the source, we anticipate numerical difficulties at the origin. For this reason, we treat the uncollided contribution, containing the singularity, separately. The uncollided scalar flux emerges by setting scattering and fission cross sections to zero in Eq. (14):

$$\boldsymbol{\phi}_{pt0}(r) = \frac{1}{2\pi i}\frac{1}{2\pi r}\Sigma^{-1}\int_{-\infty}^{\infty} dk k e^{ikr}\boldsymbol{L}(k)\boldsymbol{Q}$$

giving the analytical inversion:

$$\boldsymbol{\phi}_{pt0}(r) = \frac{1}{2\pi r^2}\left\{Q_g e^{-\Sigma_g r}\right\} \tag{15}$$

Thus, the final inversion is:

$$\begin{aligned}\boldsymbol{\phi}_{pt}(r) &= \boldsymbol{\phi}_{pt0}(r) + \\ &+ \frac{1}{2\pi i}\frac{1}{2\pi r}\int_{-\infty}^{\infty} dk k e^{ikr}\left[\left\{\Sigma - \boldsymbol{L}(k)\left[\Sigma_s + \chi\left(\nu\Sigma_f\right)^T\right]\right\}^{-1} - \Sigma^{-1}\right]\boldsymbol{L}(k)\boldsymbol{Q}\end{aligned} \tag{16}$$

We demonstrate the numerical evaluation of Eq. (16) for the 18-group fast reactor example introduced in Benchmark 2.3 including both elastic and inelastic isotropic scattering. Since $k_\infty = 1.2$ for this case, the ^{239}Pu volume fraction was reduced from 0.104 to 0.0728 to give a k_∞ of 0.99619 which is now an appropriate subcritical infinite medium.

Figure 4.1.4(a) shows the spatial variation of the flux from a point source of unit strength in the first group. The flux of neutrons reaching lower groups is noticeably less in comparison to the groups where the fission neutrons appear. Figure 4.1.4(b) more clearly illustrates this in the spectral variation. An informative variation is to consider the source in the last group as shown in Figures 4.1.5. The energy variation reverses with the highest flux now in the source group. Since neutrons do not upscatter, they are transported to the higher groups through fission only, which is an example of how neutrons are "pumped" to higher energies through fission.

Table 4.1.1. One-group and multigroup flux comparison

x**G	***One-group***	**6**	**15**	**30**
-5.0000E+00	1.0158E-03	1.0147E-03	1.0156E-03	1.0157E-03
-4.0000E+00	2.7653E-03	2.7634E-03	2.7653E-03	2.7653E-03
-3.0000E+00	7.6563E-03	7.6527E-03	7.6565E-03	7.6564E-03
-2.0000E+00	2.1842E-02	2.1835E-02	2.1842E-02	2.1842E-02
-1.0000E+00	6.6635E-02	6.6623E-02	6.6635E-02	6.6634E-02
-1.0000E+00	2.8728E-01	2.8727E-01	2.8729E-01	2.8729E-01
1.0000E-02	1.3017E+00	1.3017E+00	1.3017E+00	1.3017E+00
1.0000E+00	6.7845E-01	6.7843E-01	6.7846E-01	6.7846E-01
2.0000E+00	2.9816E-01	2.9815E-01	2.9816E-01	2.9816E-01
3.0000E+00	1.2570E-02	1.2569E-01	1.2570E-01	1.2570E-01
4.0000E+00	5.1866E-02	5.1860E-02	5.1857E-02	5.1866E-02
5.0000E+00	2.1113E-02	2.1109E-02	2.1113E-02	2.1113E-02

Table 4.1.2. Qualification of Benchmark 4.1

Group flux at g = 49 for a beam source

$x\backslash\varepsilon$	10^{-3}	10^{-4}	10^{-5}	10^{-6}
-3.0000E+00	1.19288E-01	1.19345E-01	1.19345E-01	1.19345E-01
-2.4000E+00	1.58462E-01	1.58496E-01	1.58496E-01	1.58496E-01
-1.8000E+00	2.04306E-01	2.04325E-01	2.04324E-01	2.04325E-01
-1.2000E+00	2.54111E-01	2.54110E-01	2.54115E-01	2.54115E-01
-6.0000E-01	3.02510E-01	3.02510E-01	3.02510E-01	3.02510E-01
-1.0000E-02	3.40891E-01	3.40932E-01	3.40932E-01	3.40932E-01
1.0000E-02	3.41928E-01	3.41969E-01	3.41970E-01	3.41970E-01
6.0000E-01	3.62125E-01	3.62125E-01	3.62125E-01	3.62125E-01
1.2000E+00	3.59979E-01	3.59979E-01	3.59983E-01	3.59984E-01
1.8000E+00	3.37144E-01	3.37169E-01	3.37170E-01	3.37170E-01
2.4000E+00	2.99838E-01	2.99896E-01	2.99896E-01	2.99896E-01
3.0000E+00	2.55209E-01	2.55279E-01	2.55278E-01	2.55279E-01

Figure 4.1.1. Plane source contribution to flux at *x*

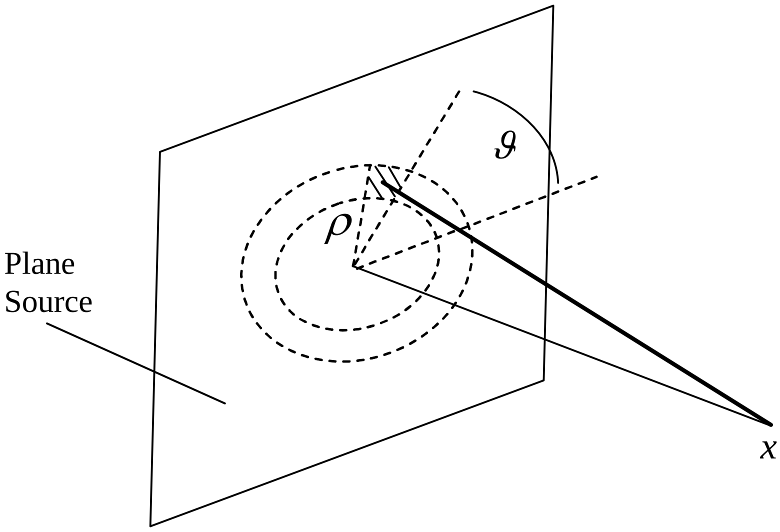

Figure 4.1.2(a). Flux for slowing down in a C/Fe (70%/30%) mixture with *G* = 78

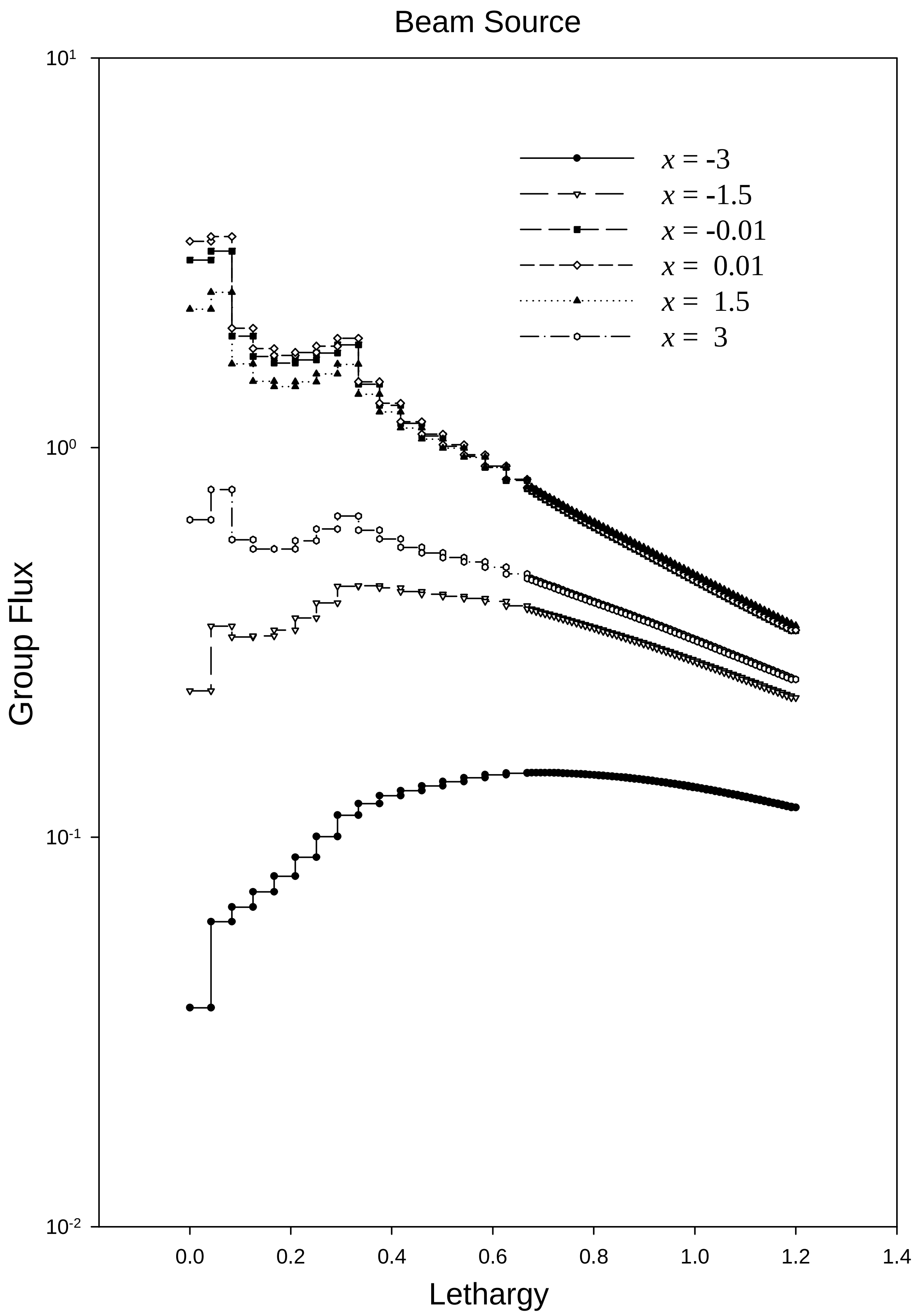

Figure 4.1.2(b). Multigroup neutron transport in an infinite medium of C/Fe (70%/30%) mixture: spatial variation of group flux

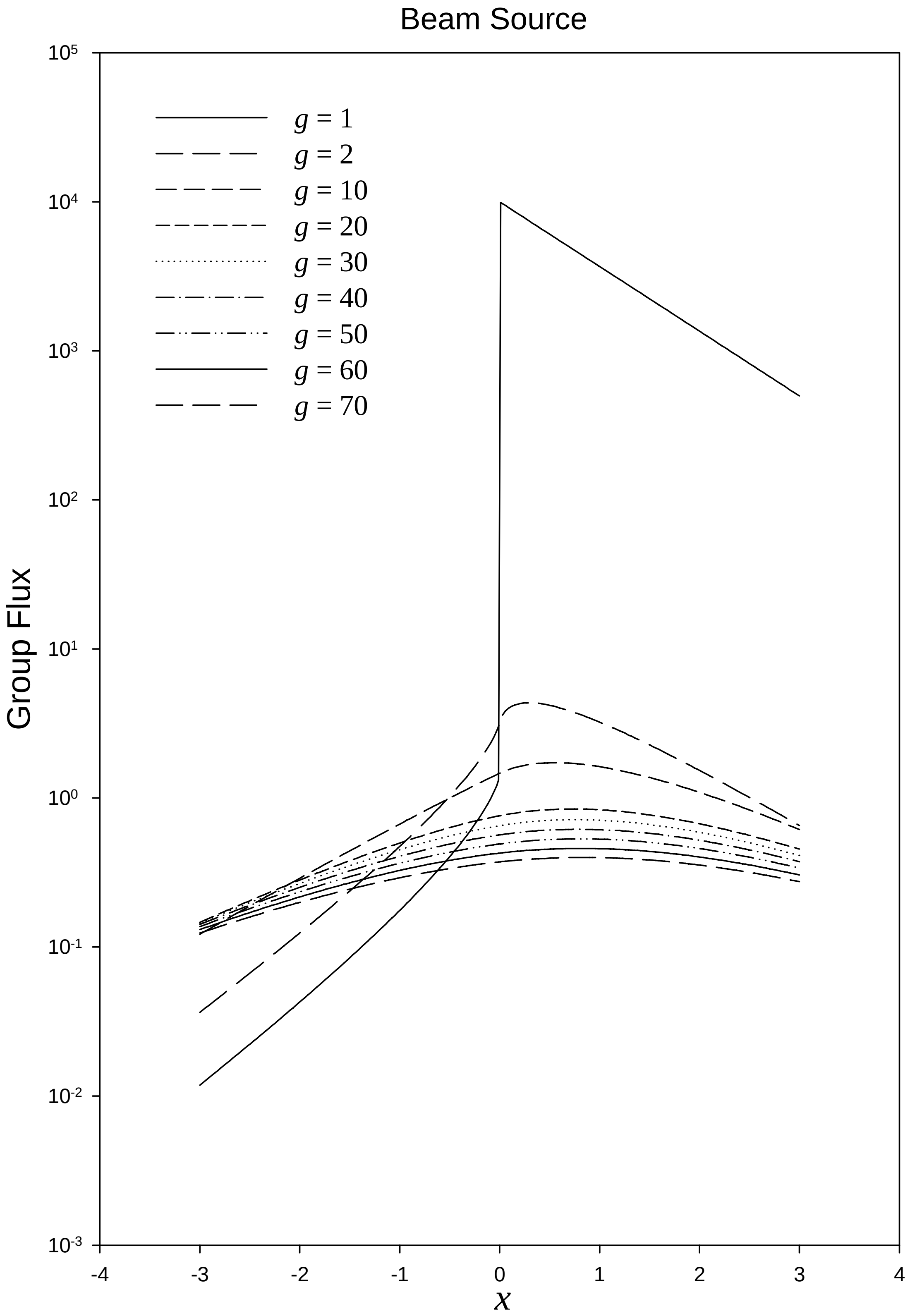

Figure 4.1.2(c). Multigroup neutron transport in an infinite medium of C/Fe (70%/30%) mixture: spatial variation of group flux

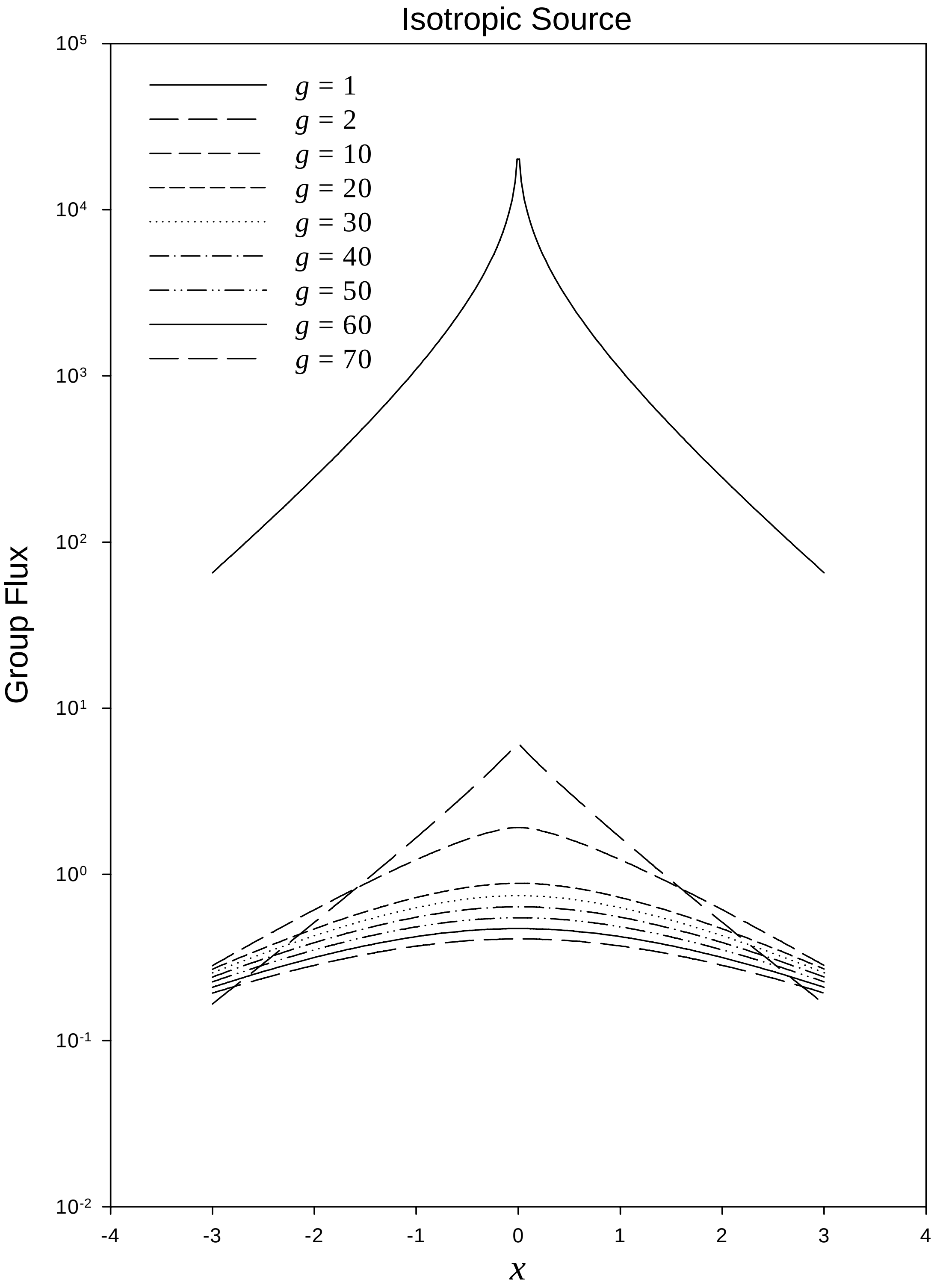

Figure 4.1.3(a). Multigroup slowing down near the source: convergence in *G*

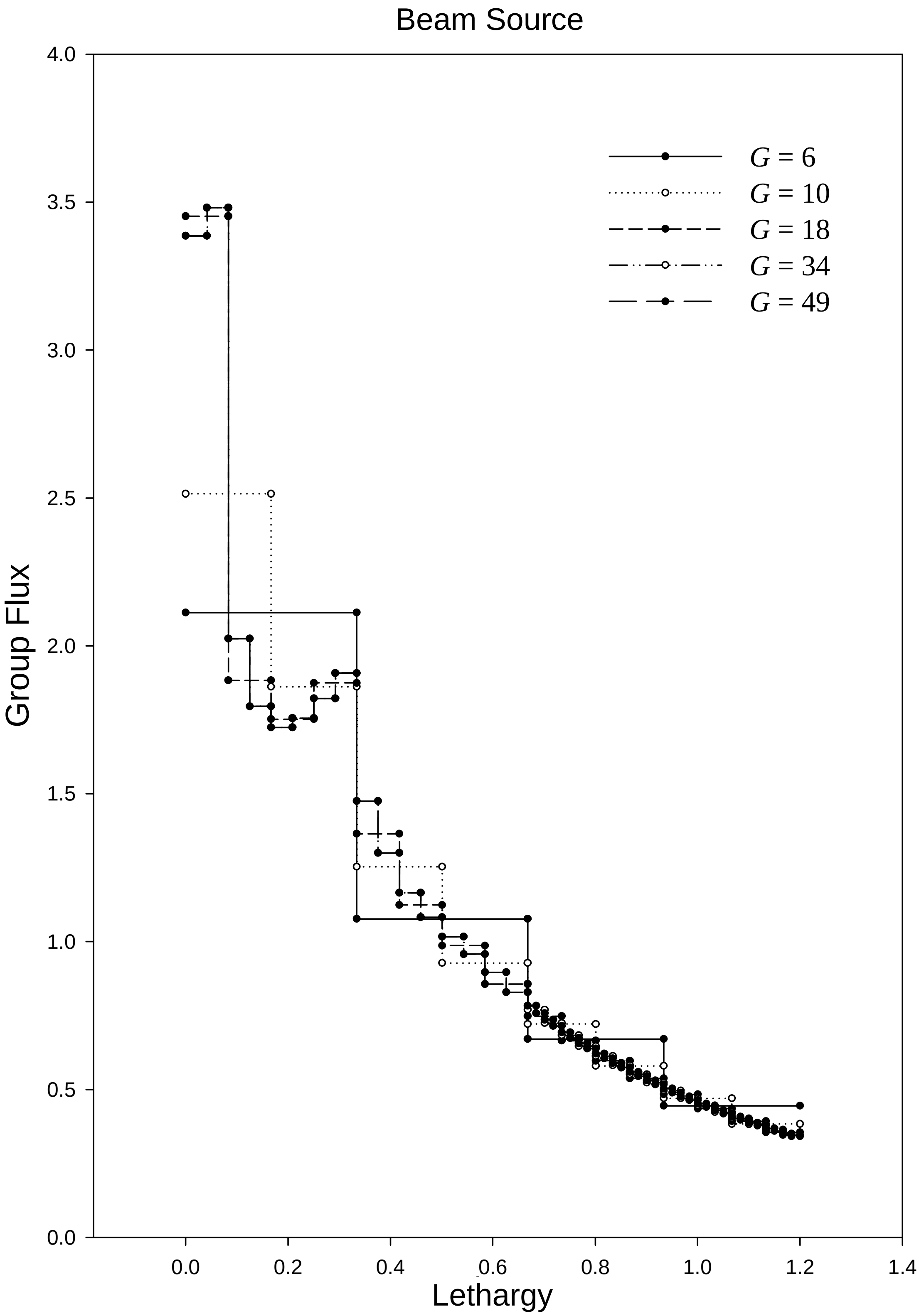

Figure 4.1.3(b). Graphical convergence in *G*

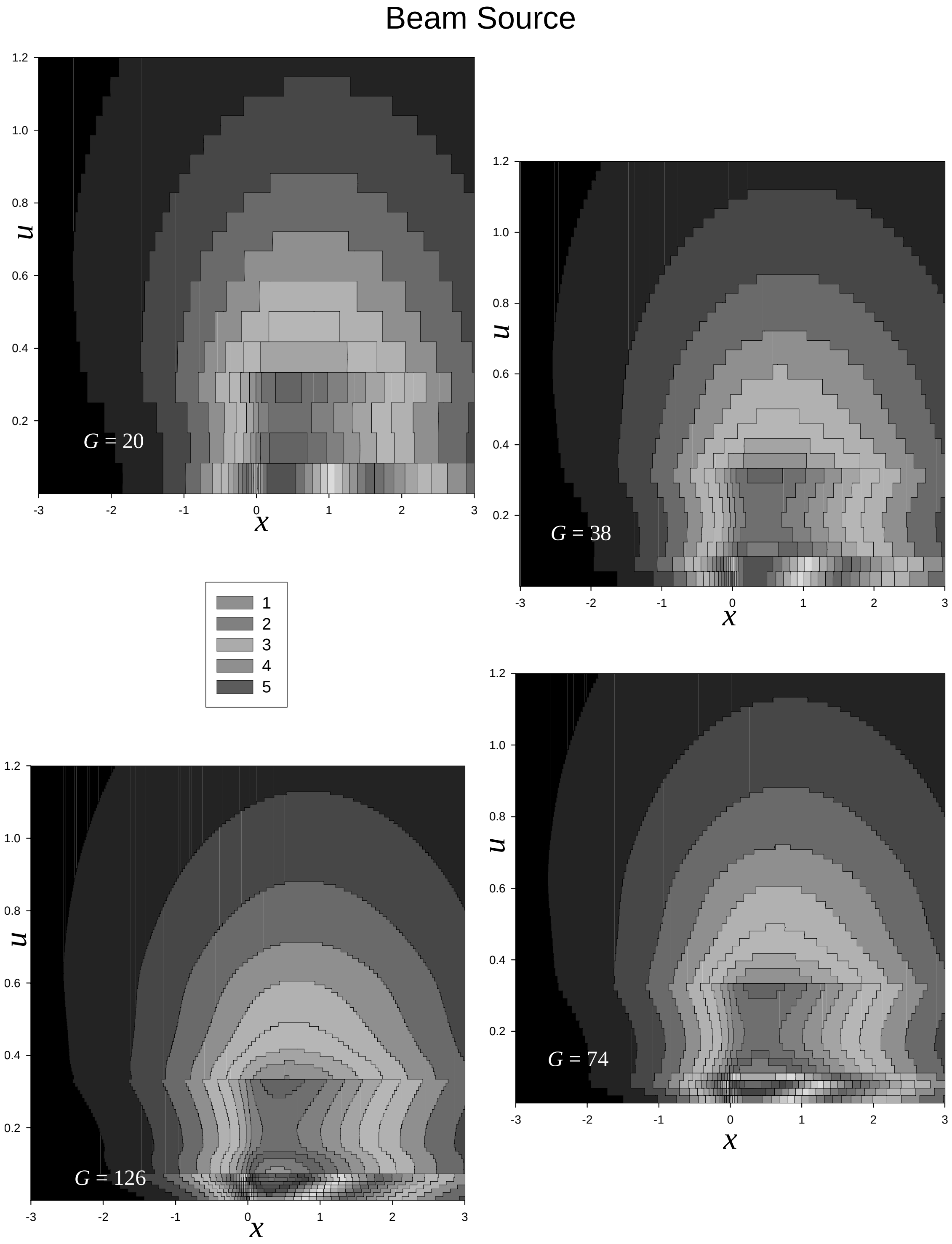

Figure 4.1.4(a). Spatial variation by group for point source in Group 1

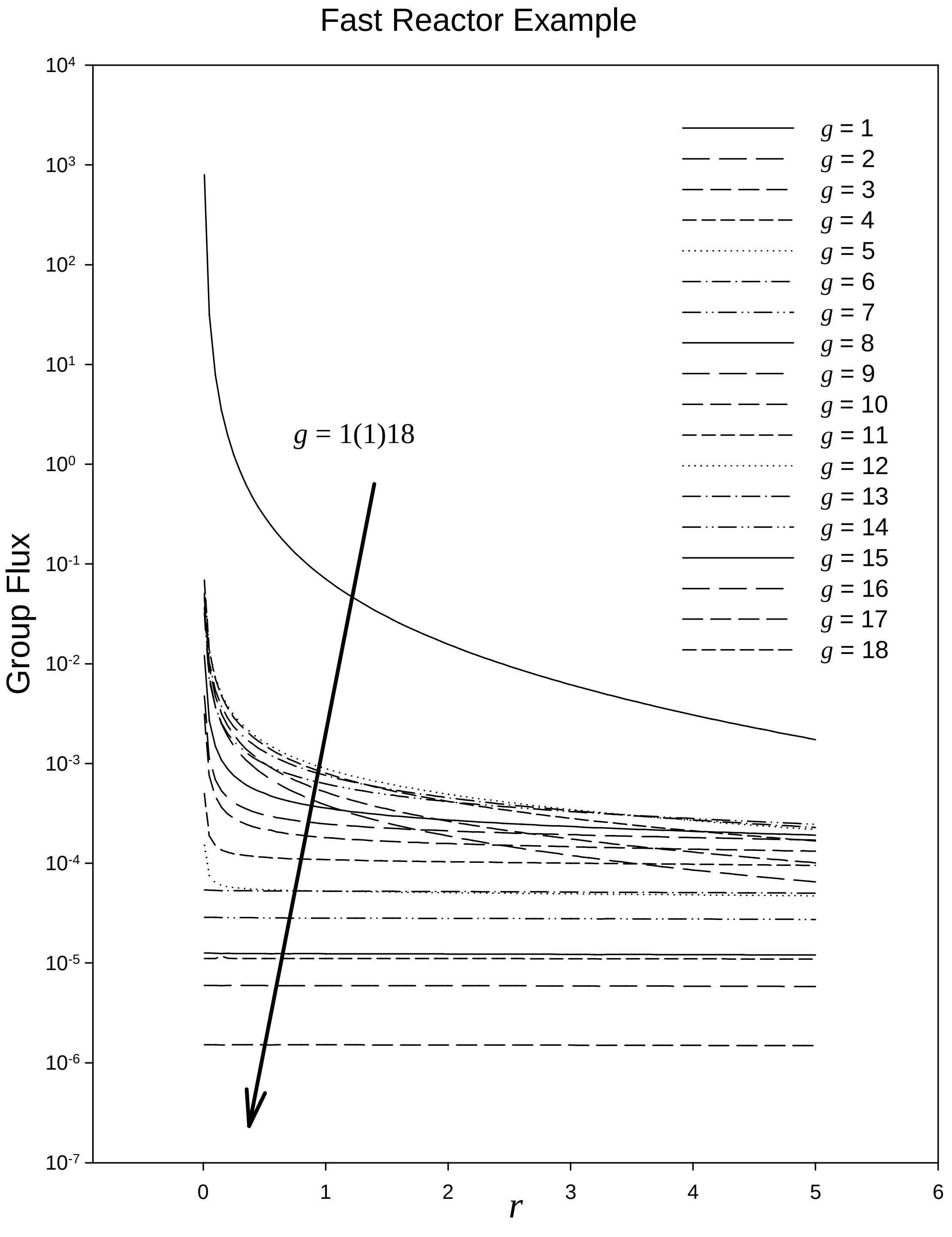

Figure 4.1.4(b). Spectral variation of group flux at selected positions

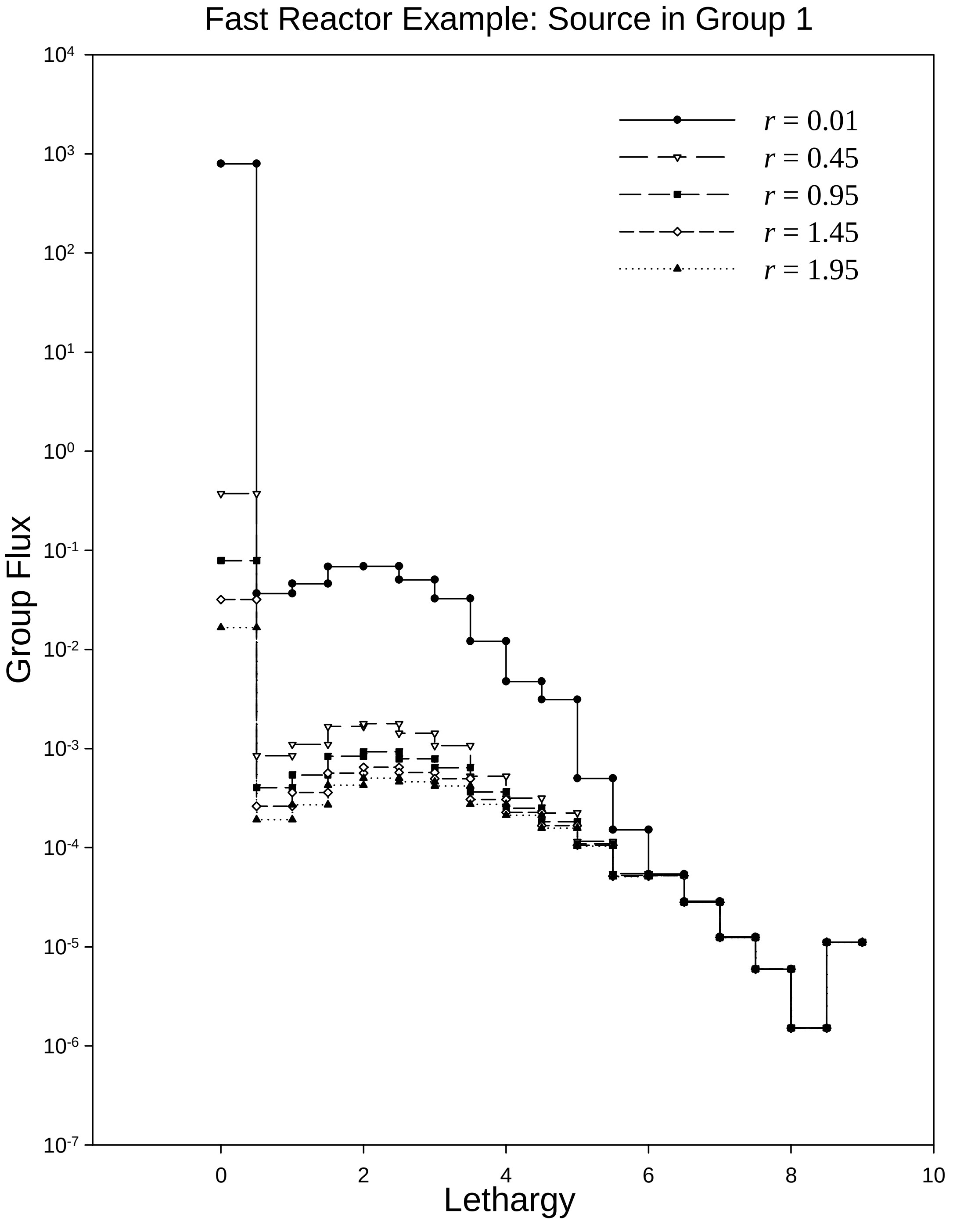

Figure 4.1.5. Spectral variation of group flux at selected positions

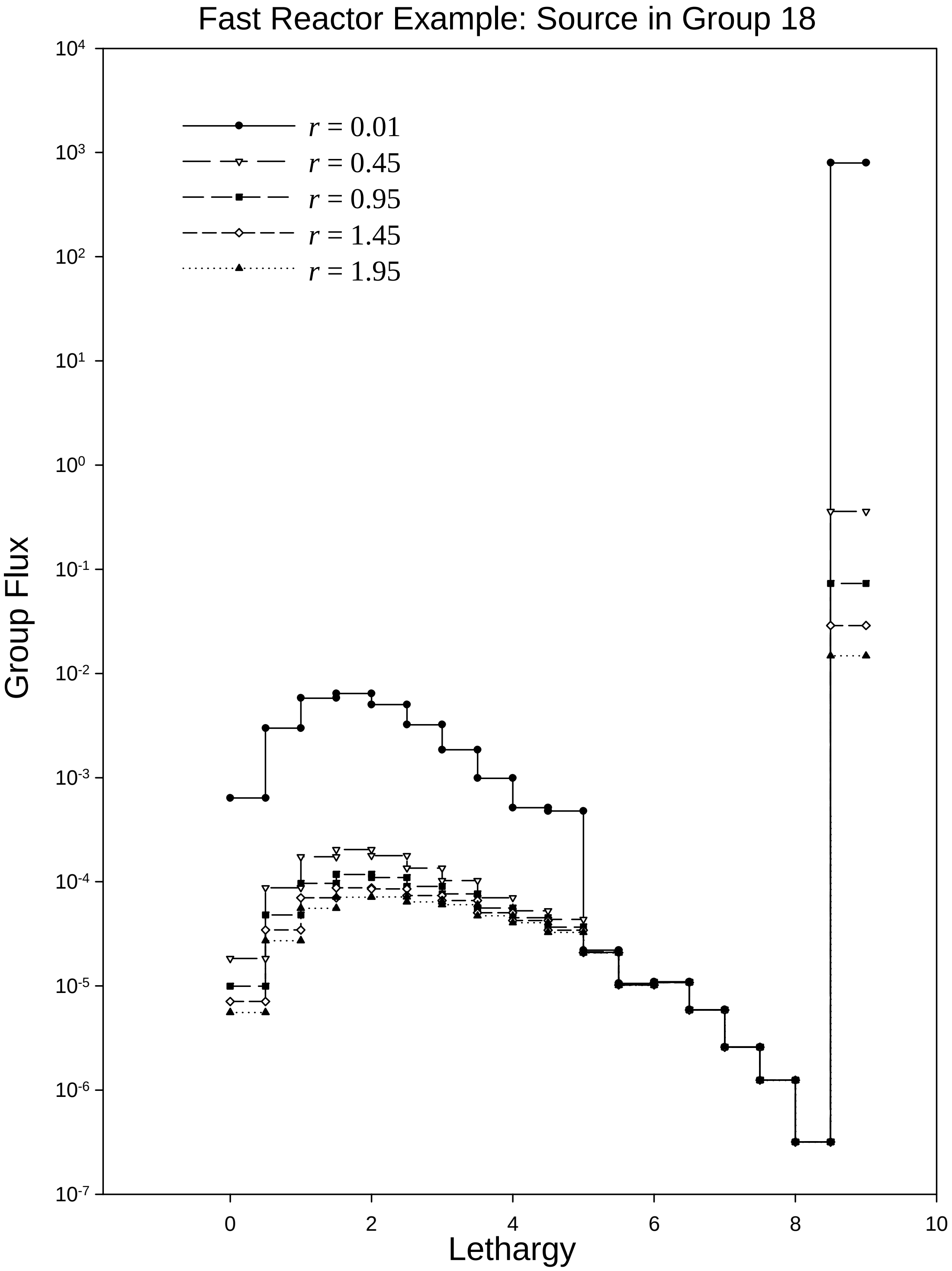

Benchmark 4.2: Multigroup slab transport/the Green's function method

(a) Brief description

Neutrons slowing down in a homogeneous slab medium with spatial dependence in the multigroup approximation.

(b) Classification

NT/S/I/MG/B/L,D/X(C),A(D),E(D)/GFM

(c) Physical description

Neutrons of one energy impinging on the surface of a homogeneous slab medium undergo energy loss and gain through scattering. One spatial dimension and one direction describe the neutron motion. We solve the transport equation in the multigroup approximation by the Green's function method (GFM/MG) also called the boundary source method.

(d) Analytical representation

For this benchmark, we establish an analytical solution of multigroup neutron transport in a slab through the Green's Function Method [1], denoted GFM/MG and also called the boundary source method [2,3]. The method features a form of the transport equation where the spatial variable enters only as a parameter [Eqs. (1.V.1,2,3)]. In the GFM/MG, Placzek's lemma [4] combines with the fundamental multigroup Green's function to give coupled integral equations for the exiting angular fluxes. The numerical Fourier transform inversion of the image function (as in Benchmark 3.1 and described in Appendix B.2), then gives the Green's function in the multigroup approximation. We solve the integral equations for the exiting angular flux numerically via iteration to facilitate matrix inversion.

(i) The multigroup Green's function form

The transport scenario to be considered is for the 1-D homogeneous slab of width a, $x \in [0,a]$, in the multigroup approximation. We cast the solution in terms of the Green's function formed by reducing Eq. (1.V.2) appropriately to the 1-D multigroup form.

The 1-D assumption is that the nuclear data varies in one spatial dimension only, in this case x:

$$\begin{aligned}
&\Sigma(\boldsymbol{r}) = \Sigma(x) \\
&\Sigma_s(\boldsymbol{r}) = \Sigma_s(x) \\
&\Sigma_s(\boldsymbol{r}, \Omega' \bullet \Omega, E' \to E) = \Sigma_s(x, \Omega' \bullet \Omega, E' \to E) \\
&\Sigma_f(\boldsymbol{r}) = \Sigma_f(x)
\end{aligned}$$

If we integrate Eq. (1.V.2) over the transverse *yz*-plane and apply the following definitions:

$$\phi\left(x,\Omega,E\right)\equiv\int_{-\infty}^{\infty}dy\int_{-\infty}^{\infty}dz\phi\left(\boldsymbol{r},\Omega,E\right)$$

$$Q\left(x,\Omega,E\right)\equiv\int_{-\infty}^{\infty}dy\int_{-\infty}^{\infty}dzQ\left(\boldsymbol{r},\Omega,E\right)$$

and similarly [for the Green's function of Eq. (1.V.1)] define:

$$\begin{aligned}&Q\left(x',\Omega',E'\right)G\left(x,\Omega,E;x',\Omega',E'\right)\equiv\\&\equiv\int_{-\infty}^{\infty}dy\int_{-\infty}^{\infty}dz\int_{-\infty}^{\infty}dy'\int_{-\infty}^{\infty}dz'Q\left(\boldsymbol{r}',\Omega',E'\right)G\left(\boldsymbol{r},\Omega,E;\boldsymbol{r}',\Omega',E'\right)\end{aligned}$$

which implies at boundaries:

$$\begin{aligned}&\phi\left(x_s,\Omega',E'\right)G\left(x,\Omega,E;x_s,\Omega',E'\right)\equiv\\&\equiv\int_{-\infty}^{\infty}dy\int_{-\infty}^{\infty}dz\int_{-\infty}^{\infty}dy_s\int_{-\infty}^{\infty}dz_s\phi\left(\boldsymbol{r}_s,\Omega',E'\right)G\left(\boldsymbol{r},\Omega,E;\boldsymbol{r}_s,\Omega',E'\right)\end{aligned}$$

the following two-angle form of Eq. (1.V.2) results:

$$\begin{aligned}\psi\left(x,\Omega,E\right)=&\int_{x_{s1}}^{x_{s2}}dx'\int_{0}^{\infty}dE'\int_{4\pi}d\Omega'Q\left(x',\Omega',E'\right)G\left(x,\Omega,E;x',\Omega',E'\right)-\\&-\sum_{j=1}^{2}\int_{0}^{\infty}dE'\int_{4\pi}d\Omega'\hat{\boldsymbol{n}}_{sj}\bullet\Omega'G\left(x,\Omega,E;x_{sj},\Omega',E'\right)\phi\left(x_{sj},\Omega',E'\right)\end{aligned}\tag{1}$$

The surfaces are located at $x_{s1}\equiv 0$ and $x_{s2}\equiv a$, and the 1-D Green's function satisfies:

$$\begin{aligned}&\left[\mu\frac{\partial}{\partial x}+\Sigma\left(x,E\right)\right]G\left(x,\Omega,E;x',\Omega',E'\right)=\\&=\int_{0}^{\infty}dE''\int_{4\pi}d\Omega''\Sigma_s\left(x,\Omega''\bullet\Omega,E''\rightarrow E\right)G\left(x,\Omega'',E'';x',\Omega',E'\right)+\\&+\frac{\chi\left(E\right)}{4\pi}\int_{0}^{\infty}dE''\int_{4\pi}d\Omega''\nu\left(E''\right)\Sigma_f\left(x,E''\right)G\left(x,\Omega'',E'';x',\Omega',E'\right)+\\&+\delta\left(x-x'\right)\delta\left(\Omega-\Omega'\right)\delta\left(E-E'\right)\end{aligned}\tag{2}$$

where the direction cosine for a single spatial dimension is:

$$\mu\equiv\hat{\boldsymbol{x}}\bullet\Omega$$

We obtain the one-angle form by azimuthal integration of Eq. (1):

$$\begin{aligned}\psi(x,\mu,E) &= \int_0^a dx' \int_0^\infty dE' \int_{-1}^1 d\mu' Q(x',\mu',E') G(x,\mu,E;x',\mu',E') + \\ &+ \int_0^\infty dE' \int_{-1}^1 d\mu' \mu' G(x,\mu,E;0,\mu',E') \phi(0,\mu',E') - \\ &- \int_0^\infty dE' \int_{-1}^1 d\mu' \mu' G(x,\mu,E;a,\mu',E') \phi(a,\mu',E')\end{aligned} \tag{3}$$

with the usual definitions of azimuthal averages:

$$\begin{aligned}\phi(x,\mu,E) &\equiv \frac{1}{2\pi} \int_0^{2\pi} d\vartheta \phi(x,\Omega,E) \\ \psi(x,\mu,E) &\equiv \frac{1}{2\pi} \int_0^{2\pi} d\vartheta \psi(x,\Omega,E) \\ Q(x,\mu,E) &\equiv \frac{1}{2\pi} \int_0^{2\pi} d\vartheta Q(x,\Omega,E)\end{aligned}$$

$$\begin{aligned}G(x,\mu,E;x',\mu',E') &\equiv \int_0^{2\pi} d\vartheta G(x,\Omega,E;x',\Omega',E') \\ &= \int_0^{2\pi} d\vartheta G(x,\mu,E;x',\mu',E';\vartheta-\vartheta')\end{aligned}$$

Note that on the free surfaces:

$$\begin{aligned}\hat{\boldsymbol{n}}_{s1} \bullet \Omega' &= -\mu' \\ \hat{\boldsymbol{n}}_{s2} \bullet \Omega' &= \mu'\end{aligned}$$

The Green's function is now the solution of:

$$\begin{aligned}&\left[\mu \frac{\partial}{\partial x} + \Sigma(x,E)\right] G(x,\mu,E;x',\mu',E') = \\ &= \int_0^\infty dE'' \int_{-1}^1 d\mu'' \Sigma_s(x,\mu'',\mu,E'' \to E) G(x,\mu'',E'';x',\mu',E') + \\ &+ \frac{\chi(E)}{2} \int_0^\infty dE'' \int_{-1}^1 d\mu'' \nu(E'') \Sigma_f(x,E'') G(x,\mu'',E'';x',\mu',E') + \\ &\qquad + \delta(x-x') \delta(\mu-\mu') \delta(E-E')\end{aligned} \tag{4}$$

The multigroup form comes about by imposing the multigroup approximation, as in Benchmark 2.3:

$$\begin{aligned}\psi(x,\mu,E) &= f(E) \psi_g(x,\mu) \\ Q(x,\mu,E) &= g(E) Q_g(x,\mu)\end{aligned} \tag{5}$$

in each group (where the integrals of *f* and *g* are normalized groupwise to unity) giving:

$$\begin{aligned}\psi_g\left(x,\mu\right)= & \qquad (6)\\ =\int_0^a dx'\int_{-1}^1 d\mu'\sum_{g'=1}^G & \left[\int_{\Delta E_g} dE\int_{\Delta E_{g'}} dE' f\left(E'\right)G\left(x,\mu,E;x',\mu',E'\right)\right]Q_{g'}\left(x',\mu'\right)+\\ +\int_{-1}^1 d\mu'\mu'\sum_{g'=1}^G & \left[\int_{\Delta E_g} dE\int_{\Delta E_{g'}} dE' f\left(E'\right)G\left(x,\mu,E;0,\mu',E'\right)\right]\phi_{g'}\left(0,\mu'\right)-\\ -\int_{-1}^1 d\mu'\mu'\sum_{g'=1}^G & \left[\int_{\Delta E_g} dE\int_{\Delta E_{g'}} dE' f\left(E'\right)G\left(x,\mu,E;a,\mu',E'\right)\right]\phi_{g'}\left(a,\mu'\right)\end{aligned}$$

after integration over each group and partitioning the integrals over energy. If we assume *f*(*E*) ≡ *g*(*E*) and define:

$$G_{gg'}\left(x,\mu;x',\mu'\right)\equiv\int_{\Delta E_g} dE\int_{\Delta E_{g'}} dE' f\left(E'\right)G\left(x,\mu,E;x',\mu',E'\right)$$

then:

$$\begin{aligned}\psi_g\left(x,\mu\right)= & \int_0^a dx'\int_{-1}^1 d\mu'\sum_{g'=1}^G G_{gg'}\left(x,\mu;x',\mu'\right)Q_{g'}\left(x',\mu'\right)+ \qquad (7)\\ & +\int_{-1}^1 d\mu'\mu'\sum_{g'=1}^G G_{gg'}\left(x,\mu;0,\mu'\right)\phi_{g'}\left(0,\mu'\right)-\\ & -\int_{-1}^1 d\mu'\mu'\sum_{g'=1}^G G_{gg'}\left(x,\mu;a,\mu'\right)\phi_{g'}\left(a,\mu'\right)\end{aligned}$$

In addition:

$$\begin{aligned}\left[\mu\frac{\partial}{\partial x}+\Sigma_g\left(x\right)\right] & G_{gg'}\left(x,\mu;x',\mu'\right)= \qquad (8a)\\ =\sum_{g''=1}^G\int_{-1}^1 d\mu''\Sigma_{sgg''}\left(x,\mu'',\mu\right) & G_{g''g'}\left(x,\mu'';x',\mu'\right)+\\ +\frac{1}{2}\chi_g\sum_{g''=1}^G\nu_{g''}\Sigma_{fg''}\left(x\right) & G_{g''g'}\left(x;x',\mu'\right)+\delta_{gg'}\delta\left(x-x'\right)\delta\left(\mu-\mu'\right)\end{aligned}$$

To obtain Eq. (8a), we have assumed that the Green's function satisfies the multigroup approximation as well:

$$G\left(x,\mu,E;x',\mu',E'\right)=f\left(E\right)G\left(x,\mu;x',\mu',E'\right) \qquad (8b)$$

Finally, for a single homogeneous medium, Eq. (7) becomes:

$$\psi_g(x,\mu)=\int_0^a dx'\int_{-1}^1 d\mu'\sum_{g'=1}^{G} G_{gg'}(x-x',\mu;\mu')Q_{g'}(x',\mu')+ \quad (9)$$

$$+\int_{-1}^1 d\mu'\mu'\sum_{g'=1}^{G} G_{gg'}(x,\mu;\mu')\phi_{g'}(0,\mu')-$$

$$-\int_{-1}^1 d\mu'\mu'\sum_{g'=1}^{G} G_{gg'}(x-a,\mu;\mu')\phi_{g'}(a,\mu')$$

where $G_{gg'}(x,\mu,x';\mu')=G_{gg'}(x-x',\mu;\mu')$ satisfies Eq. (8a) when we assume uniform nuclear properties since the Green's function is translationally invariant. The angular flux therefore emerges from knowledge of the exiting angular flux and the Green's function as shown in Eq. (9).

Before finalizing the solution given by Eq. (9), it is important to remark that the representation of the angular group flux in this way is a most elegant solution indeed. In particular, it is valid for any order anisotropy in that the Green's function contains all the scattering information. Another notable feature is that x appears as a passive variable. Thus, knowledge of the exiting distributions from any numerical method or even from only an approximation, gives an interpolation from Eq. (9) for the scalar flux within a medium.

(ii) The solution via fundamental matrix Green's function

Assuming isotropic scattering, one obtains the solution representation by first expressing the matrix plane parallel Green's function of Eq. (8a) as the solution to the following fundamental matrix transport equation:

$$\left[\mu\boldsymbol{I}\frac{\partial}{\partial x}+\Sigma\right]\boldsymbol{G}(x,\mu;\mu')=\frac{1}{2}\Sigma_s\boldsymbol{G}(x;\mu')+ \quad (10a)$$

$$+\frac{1}{2}\chi(\nu\Sigma_f)^T\boldsymbol{G}(x;\mu')+\delta(x)\delta(\mu-\mu')\boldsymbol{I}$$

subject to the finiteness condition:

$$\lim_{|x|\to\infty}\boldsymbol{G}(x,\mu;\mu')<\infty \quad (10b)$$

where:

$$\boldsymbol{G}(x,\mu;\mu')=\left\{G_{gg'}(x,\mu;\mu');\ g,g'=1,\ldots,G\right\}$$

$$\Sigma\equiv diag\left\{\Sigma_g,g=1,\ldots,G\right\}$$

$$\Sigma_s\equiv\left\{\Sigma_{sgg'},g,g'=1,\ldots,G\right\}$$

$$\chi(\nu\Sigma_f)^T\equiv\left\{\chi_g\nu_{g'}\Sigma_{fg'},g,g'=1,\ldots,G\right\}$$

Equation (9) in vector form, for the angular group flux, becomes:

$$\begin{aligned}\psi(x,\mu) = \int_0^a dx' \int_{-1}^{1} d\mu' \boldsymbol{G}(x-x',\mu;\mu')\boldsymbol{Q}(x',\mu') + \\ + \int_{-1}^{1} d\mu'\mu'\boldsymbol{G}(x,\mu;\mu')\boldsymbol{\phi}(0,\mu') - \\ - \int_{-1}^{1} d\mu'\mu'\boldsymbol{G}(x-a,\mu;\mu')\boldsymbol{\phi}(a,\mu')\end{aligned} \tag{11}$$

where:

$$\begin{aligned}\psi(x,\mu) &\equiv \left\{\psi_g(x,\mu), g=1,\ldots,G\right\} \\ \boldsymbol{\phi}(x,\mu) &\equiv \left\{\phi_g(x,\mu), g=1,\ldots,G\right\} \\ \boldsymbol{Q} &\equiv \left\{Q_g, g=1,\ldots,G\right\}\end{aligned}$$

Without a volume source in the interval $0^+ \le x \le a^-$ and for an entering group angular flux vector $\boldsymbol{h}(\mu)$ at $x = 0$, Eq. (11) reduces to:

$$\begin{aligned}\boldsymbol{\phi}(x,\mu) = \int_0^1 d\mu'\mu'\boldsymbol{G}(x,\mu;\mu')\boldsymbol{h}(\mu') - \\ - \int_0^1 d\mu'\mu'\boldsymbol{G}(x,\mu;-\mu')\boldsymbol{\phi}(0^+,-\mu') - \\ - \int_0^1 d\mu'\mu'\boldsymbol{G}(x-a,\mu;\mu')\boldsymbol{\phi}(a^-,\mu')\end{aligned} \tag{12}$$

The fluxes exiting from just inside the medium, are denoted $\boldsymbol{\phi}(0^+,-\mu')$ and $\boldsymbol{\phi}(a^-,\mu')$. By integration of Eq. (12) over μ, the corresponding scalar flux emerges as:

$$\begin{aligned}\boldsymbol{\phi}(x) = \int_0^1 d\mu'\mu'\boldsymbol{G}(x;\mu')\boldsymbol{h}(\mu') - \\ - \int_0^1 d\mu'\mu'\boldsymbol{G}(x;-\mu')\boldsymbol{\phi}(0^+,-\mu') - \\ - \int_0^1 d\mu'\mu'\boldsymbol{G}(x-a;\mu')\boldsymbol{\phi}(a^-,\mu')\end{aligned} \tag{13}$$

where, from a corresponding integration, the fundamental matrix scalar Green's function is:

$$\boldsymbol{G}(x;\mu_0) \equiv \int_{-1}^{1} d\mu \boldsymbol{G}(x,\mu;\mu_0)$$

Note that we have yet to specify the unknown exiting flux vectors in Eqs. (12) and (13).

By alternatively setting x to 0^+ (with μ replaced by $-\mu$) and to a^- in Eq. (12), we see that the exiting angular fluxes satisfy the following coupled integral equations:

$$\begin{aligned}\boldsymbol{\phi}\left(0^{+},-\mu\right)= & \int_0^1 d\mu'\mu'\boldsymbol{G}\left(0^{+},-\mu;\mu'\right)\boldsymbol{h}(\mu')- \\ & -\int_0^1 d\mu'\mu'\boldsymbol{G}\left(0^{+},-\mu;-\mu'\right)\boldsymbol{\phi}\left(0^{+},-\mu'\right)- \\ & -\int_0^1 d\mu'\mu'\boldsymbol{G}\left(a^{-},\mu;-\mu'\right)\boldsymbol{\phi}\left(a^{-},\mu'\right)\end{aligned} \tag{14a}$$

$$\begin{aligned}\boldsymbol{\phi}\left(a^{-},\mu\right)= & \int_0^1 d\mu'\mu'\boldsymbol{G}\left(a^{-},\mu;\mu'\right)\boldsymbol{h}(\mu')- \\ & -\int_0^1 d\mu'\mu'\boldsymbol{G}\left(a^{-},\mu;-\mu'\right)\boldsymbol{\phi}\left(0^{+},-\mu'\right)- \\ & -\int_0^1 d\mu'\mu'\boldsymbol{G}\left(0^{-},\mu;\mu'\right)\boldsymbol{\phi}\left(a^{-},\mu'\right)\end{aligned} \tag{14b}$$

These equations will require further modification when the impinging flux $\boldsymbol{h}$ is a monodirectional beam (delta function in direction).

(iii) Representation of the fundamental matrix Green's function

The matrix Green's function is essential to the evaluation of the exiting angular flux and the interior scalar flux, which are of primary interest. We desire the solution to Eqs. (10) in the form:

$$\begin{aligned}&\left[\mu\boldsymbol{I}\frac{\partial}{\partial x}+\Sigma\right]\boldsymbol{G}\left(x,\mu;\mu'\right)= \\ &=\frac{1}{2}\left[\Sigma_s+\chi\left(\nu\Sigma_f\right)^T\right]\boldsymbol{G}\left(x;\mu'\right)+\delta(x)\delta\left(\mu-\mu'\right)\boldsymbol{I}\end{aligned} \tag{15}$$

The strategy is to perform the matrix Fourier transform:

$$\boldsymbol{G}\left(k,\mu;\mu'\right)\equiv\int_{-\infty}^{\infty}dxe^{-ikx}\boldsymbol{G}\left(x,\mu;\mu'\right) \tag{16a}$$

to obtain an explicit image function and then compute the inversion:

$$\boldsymbol{G}\left(x,\mu;\mu'\right)\equiv\frac{1}{2\pi}\int_{-\infty}^{\infty}dke^{ikx}\boldsymbol{G}\left(k,\mu;\mu'\right) \tag{16b}$$

numerically. In the following, functions with arguments of k or z are Fourier transforms.

Upon application of the Fourier transform, Eq. (15) becomes:

$$\left[\Sigma+ik\mu\boldsymbol{I}\right]\boldsymbol{G}\left(k,\mu;\mu'\right)=\frac{1}{2}\left[\Sigma_s+\chi\left(\nu\Sigma_f\right)^T\right]\boldsymbol{G}\left(k;\mu'\right)+\delta\left(\mu-\mu'\right)\boldsymbol{I} \tag{17}$$

The method of solution follows the standard analysis where one solves algebraically for the angular flux transform and then integrates over direction for the transformed scalar flux. When introduced into the angular flux transform, we can express the scalar Green's function matrix image function explicitly as:

$$\boldsymbol{G}(k;\mu') = \Sigma^{-1}\left[\boldsymbol{I} - \boldsymbol{L}(z\Sigma)\ \boldsymbol{C}\right]^{-1} z\Sigma\left[z\Sigma + \mu'\boldsymbol{I}\right]^{-1} \tag{18}$$

with the secondary scattering matrix given by:

$$\boldsymbol{C} \equiv \ \Sigma^{-1}\left[\Sigma_s + \chi\left(\nu\Sigma_f\right)^T\right]$$

Here, we assume that Σ_{gg} is never zero so, in general, Σ^{-1} will exist. In addition:

$$z \equiv \frac{1}{ik}$$

$$\boldsymbol{L}(z\Sigma) \equiv diag\left\{L\left(z\Sigma_g\right)\right\}$$

with:

$$L\left(z\Sigma_g\right) \equiv \frac{z\Sigma_g}{2}\ln\left[\frac{z\Sigma_g + 1}{z\Sigma_g - 1}\right]$$

The angular Green's function matrix is therefore:

$$\boldsymbol{G}(k,\mu;\mu') = \\ = \Sigma^{-1}\begin{Bmatrix} z\Sigma\left[z\Sigma + \mu\boldsymbol{I}\right]^{-1}\delta(\mu - \mu') + \\ +\frac{1}{2}z\Sigma\left[z\Sigma + \mu\boldsymbol{I}\right]^{-1}\left\{\ \boldsymbol{C}\left[\boldsymbol{I} - \boldsymbol{L}(z\Sigma)\ \boldsymbol{C}\right]^{-1}\ \right\} z\Sigma\left[z\Sigma + \mu'\boldsymbol{I}\right]^{-1} \end{Bmatrix} \tag{19}$$

Thus, the image function explicitly depends upon z with the first term representing the uncollided contribution. Note the symmetry in μ and μ', which is the expression of reciprocity.

(e) Numerical implementation and demonstration for Benchmark 4.2

(i) Numerical implementation

Numerical implementation of the solution to Eqs. (14) requires several numerical procedures – the first of which is the determination of the Fourier transform matrix Green's function followed by numerical Fourier inversion (Appendix B.2) according to the procedure previously outlined in Benchmarks 3.1 and 4.1. The second procedure requires the solution of the integral equations for the exiting angular flux. For this, a Gauss/Legendre quadrature (*GLQ*) (Appendix A.4) coupled with matrix inversion by iteration will generally yield high quality results. The final numerical evaluation will be for slab reflectance and transmittance.

(i.1) Determination of the exiting angular fluxes

Equations (14) are coupled integral equations for the exiting angular fluxes. They are solved numerically most conveniently via *GLQ* with subsequent iteration. First, however, we partition the Green's function into its uncollided and collided components:

$$\boldsymbol{G}\left(x,\mu;\mu'\right)=\boldsymbol{G}_0\left(x,\mu;\mu'\right)+\boldsymbol{G}_c\left(x,\mu;\mu'\right) \tag{20a}$$

where:

$$\boldsymbol{G}_0\left(x,\mu;\mu'\right)\equiv\frac{e^{-\Sigma x/\mu}}{\mu}\delta\left(\mu-\mu'\right)\Theta\left(x/\mu\right) \tag{20b}$$

Θ is the Heaviside step function, and $e^{-\Sigma x/\mu}$ is a diagonal exponential matrix.

When we introduce Eqs. (20) into Eqs.(14), the following modified coupled integral equations result:

$$\begin{aligned}\boldsymbol{\phi}\left(0^+,-\mu\right)=&\int_0^1 d\mu'\mu'\boldsymbol{G}_c\left(0^+,-\mu;\mu'\right)\boldsymbol{h}\left(\mu'\right)-\\&-\int_0^1 d\mu'\mu'\boldsymbol{G}_c\left(0^+,-\mu;-\mu'\right)\boldsymbol{\phi}\left(0^+,-\mu'\right)-\\&-\int_0^1 d\mu'\mu'\boldsymbol{G}_c\left(a^-,\mu;-\mu'\right)\boldsymbol{\phi}\left(a^-,\mu'\right)\end{aligned} \tag{21a}$$

$$\begin{aligned}\boldsymbol{\phi}\left(a^-,\mu\right)=&\,e^{-\Sigma a/\mu}\boldsymbol{h}\left(\mu\right)+\int_0^1 d\mu'\mu'\boldsymbol{G}_c\left(a^-,\mu;\mu'\right)\boldsymbol{h}\left(\mu'\right)-\\&-\int_0^1 d\mu'\mu'\boldsymbol{G}_c\left(a^-,\mu;-\mu'\right)\boldsymbol{\phi}\left(0^+,-\mu'\right)-\\&-\int_0^1 d\mu'\mu'\boldsymbol{G}_c\left(0^-,\mu;\mu'\right)\boldsymbol{\phi}\left(a^-,\mu'\right)\end{aligned} \tag{21b}$$

By adding and subtracting Eqs. (21a,b), we arrive at the following uncoupled set of integral equations:

$$\begin{aligned}\boldsymbol{r}^{\pm}\left(\mu\right)=&\pm e^{-\Sigma a/\mu}\boldsymbol{h}\left(\mu\right)+\int_0^1 d\mu'\mu'\mathrm{X}_2^{\pm}\left(\mu,\mu'\right)\boldsymbol{h}\left(\mu'\right)-\\&-\int_0^1 d\mu'\mu'\mathrm{X}_1^{\pm}\left(\mu,\mu'\right)\boldsymbol{r}^{\pm}\left(\mu'\right)\end{aligned} \tag{22}$$

with:

$$\begin{aligned}\boldsymbol{r}^{\pm}\left(\mu\right)&\equiv\boldsymbol{\phi}\left(0^+,-\mu\right)\pm\boldsymbol{\phi}\left(a^-,\mu\right)\\\mathrm{X}_1^{\pm}\left(\mu,\mu'\right)&\equiv\boldsymbol{G}_c\left(0^+,-\mu;-\mu'\right)\pm\boldsymbol{G}_c\left(a^-,\mu;-\mu'\right)\\\mathrm{X}_2^{\pm}\left(\mu,\mu'\right)&\equiv\boldsymbol{G}_c\left(0^+,-\mu;\mu'\right)\pm\boldsymbol{G}_c\left(a^-,\mu;\mu'\right)\end{aligned}$$

We can solve Eqs. (22) directly by matrix inversion after angular collocation at μ_k and application of *GLQ* of order *Lm* to the angular integral. Thus, for $k = 1,\ldots,Lm$:

$$\sum_{j=1}^{Lm}\left[\delta_{jk}\boldsymbol{I}+\omega_j\mu_j\mathrm{X}_{1jk}^{\pm}\right]\boldsymbol{r}_j^{\pm}=\pm e^{-\Sigma a/\mu_k}\boldsymbol{h}_k+\sum_{j=1}^{Lm}\mathrm{X}_{2jk}^{\pm}\boldsymbol{h}_j \tag{23}$$

with:

$$\begin{aligned}
&\boldsymbol{r}_k^{\pm} \equiv \boldsymbol{\phi}\left(0^+,-\mu_k\right) \pm \boldsymbol{\phi}\left(a^-,\mu_k\right) \\
&\mathrm{X}_{1jk}^{\pm} \equiv \boldsymbol{G}_c\left(0^+,-\mu_k;-\mu_j\right) \pm \boldsymbol{G}_c\left(a^-,\mu_k;-\mu_j\right) \\
&\mathrm{X}_{2jk}^{\pm} \equiv \boldsymbol{G}_c\left(0^+,-\mu_k;\mu_j\right) \pm \boldsymbol{G}_c\left(a^-,\mu_k;-\mu_j\right) \\
&\boldsymbol{h}_k \equiv \boldsymbol{h}\left(\mu_k\right)
\end{aligned}$$

However, here, we will perform the matrix inversion iteratively according to the procedure discussed below. We recover the exiting angular fluxes from:

$$\boldsymbol{\phi}\left(0^+,-\mu_k\right) = \frac{1}{2}\left[\boldsymbol{r}_k^+ + \boldsymbol{r}_k^-\right] \qquad \boldsymbol{\phi}\left(a^-,\mu_k\right) = \frac{1}{2}\left[\boldsymbol{r}_k^+ - \boldsymbol{r}_k^-\right] \tag{24}$$

(i.2) Determination of the interior angular and scalar fluxes

Once we know the exiting angular fluxes, the interior angular and scalar fluxes come from numerical quadrature applied to Eqs. (12) and (13) to give:

$$\begin{aligned}
\boldsymbol{\phi}\left(x,\mu\right) = e^{-\Sigma a/\mu}\boldsymbol{h}\left(\mu\right)\Theta\left(\mu\right) + \sum_{j=1}^{Lm}\omega_j\mu_j\boldsymbol{G}_c\left(x,\mu;\mu_j\right)\boldsymbol{h}_j - \\
-\sum_{j=1}^{Lm}\omega_j\mu_j\boldsymbol{G}_c\left(x,\mu;-\mu_j\right)\boldsymbol{\phi}\left(0^+,-\mu_j\right) - \\
-\sum_{j=1}^{Lm}\omega_j\mu_j\boldsymbol{G}_c\left(x-a,\mu;\mu_j\right)\boldsymbol{\phi}\left(a^-,\mu_j\right)
\end{aligned} \tag{25a}$$

$$\begin{aligned}
\boldsymbol{\phi}\left(x\right) = \sum_{j=1}^{Lm}\omega_j\mu_j\boldsymbol{G}\left(x;\mu_j\right)\boldsymbol{h}_j - \\
-\sum_{j=1}^{Lm}\omega_j\mu_j\boldsymbol{G}\left(x;-\mu_j\right)\boldsymbol{\phi}\left(0^+,-\mu_j\right) - \\
-\sum_{j=1}^{Lm}\omega_j\mu_j\boldsymbol{G}\left(x-a;\mu_j\right)\boldsymbol{\phi}\left(a^-,\mu_j\right)
\end{aligned} \tag{25b}$$

with:

$$\boldsymbol{G}\left(x;\mu_j\right) = \frac{e^{-\Sigma x/\mu_j}}{\mu_j}\Theta\left(x/\mu_j\right) + \boldsymbol{G}_c\left(x;\mu_j\right)$$

(i.3) Green's function inversion

As indicated, the numerical evaluation of the full Green's function is through the numerical Fourier inversion of Eq. (19) which we now verify. The first collided contribution provides a measure of the effectiveness of this evaluation. By expanding the matrix inverse formally in a power series in

LC and focusing on the second term (the first collided component), we find the following expression for the *j*,*l* element of first collided angular Green's function matrix:

$$\left[\boldsymbol{G}_1\left(k,\mu;\mu'\right)\right]_{jl}=\frac{\Sigma_{sjl}}{\left(\Sigma_j+ik\mu\right)\left(\Sigma_l+ik\mu'\right)}$$

where we have taken advantage of the diagonal nature of $[\Sigma + ik\mu\boldsymbol{I}]^{-1}$. The analytical inversion therefore becomes:

$$\begin{aligned}&\left[\boldsymbol{G}_1\left(x,\mu;\mu'\right)\right]_{jl}=\\&=\frac{1}{2}\left[\frac{\Sigma_{sjl}}{\mu'\Sigma_j-\mu\Sigma_l}\right]\begin{bmatrix}\operatorname{sgn}\left(\mu'\right)e^{-\Sigma_l x/\mu'}\Theta\left(x/\mu'\right)-\\-\operatorname{sgn}\left(\mu\right)e^{-\Sigma_l x/\mu}\Theta\left(x/\mu\right)\end{bmatrix}\end{aligned}\tag{26}$$

When the numerical inversion is compared to this analytical expression for the two-group cross sections found in Table 4.2.1 at $x = 10^{-12}$ *cm* (approximating zero) and $x = 2$ *cm*, exact agreement to the desired relative error is achieved – again indicating the proper implementation of the numerical inversion algorithm. Only for angles near 90° near the source does the inversion become problematic.

Since we know the first collided component analytically, the collided Green's function now becomes:

$$\boldsymbol{G}_c\left(x,\mu;\mu'\right)=\boldsymbol{G}_1\left(x,\mu;\mu'\right)+\boldsymbol{G}_{2c}\left(x,\mu;\mu'\right)\tag{27}$$

where the multiple collided contribution for two or more collisions is the inversion of:

$$\boldsymbol{G}_{2c}\left(k,\mu;\mu'\right)=\frac{1}{2}\left[\Sigma+ik\mu\boldsymbol{I}\right]^{-1}\left[\Sigma_s\left[\boldsymbol{I}-\boldsymbol{L}\Sigma_s\right]^{-1}\boldsymbol{L}\Sigma_s\right]\left[\Sigma+ik\mu\boldsymbol{I}\right]^{-1}$$

(ii) Demonstration

(ii.1) Iteration error for the exiting angular flux

The determination of the exiting angular group flux vector requires the solution of the integral equations given by Eqs. (22). Since this involves block coefficient matrices, we could reformulate Eqs. (22) as one large matrix inversion. However, rather than deal with the increased computational effort for large matrix inversion, we take a more straightforward iterative approach.

For an incident beam of strength $\boldsymbol{S}_0$ in direction μ_0 on the left boundary, Eqs. (22) become:

$$\begin{aligned}\boldsymbol{r}^{\pm}\left(\mu\right)=\pm e^{-\Sigma a/\mu_0}\delta\left(\mu-\mu_0\right)\boldsymbol{S}_0+\\+\mu_0\mathrm{X}_2^{\pm}\left(\mu,\mu_0\right)\boldsymbol{S}_0-\int_0^1 d\mu'\mu'\mathrm{X}_1^{\pm}\left(\mu,\mu'\right)\boldsymbol{r}^{\pm}\left(\mu'\right)\end{aligned}$$

With the substitution:

$$\boldsymbol{r}^{\pm}\left(\mu\right)=\pm e^{-\Sigma a/\mu_0}\delta\left(\mu-\mu_0\right)\boldsymbol{S}_0+\boldsymbol{r}_c^{\pm}\left(\mu\right)$$

we have:

$$\boldsymbol{r}_c^{\pm}(\mu) = \mu_0 \left[\mathbf{X}_2^{\pm}(\mu,\mu_0) - \pm \mathbf{X}_1^{\pm}(\mu,\mu_0) e^{-\Sigma a/\mu_0} \right] \boldsymbol{S}_0 - \\ - \int_0^1 d\mu' \mu' \mathbf{X}_1^{\pm}(\mu,\mu') \boldsymbol{r}_c^{\pm}(\mu') \tag{28}$$

When the integrals in Eq. (28) are approximated by Gauss quadrature, we then solve the resulting set of algebraic equations iteratively until convergence and anticipate the closer we are to criticality more iterations will be necessary. For the nominal two-group case [cross sections of Table 4.2.1] for a 2 *cm* thick slab, Table 4.2.2 shows the maximum error associated with the iterative solution of Eq. (28). As observed, we achieve machine accuracy after nine iterates with *Lm* equal to 20.

(ii.2) "Faux" angular interpolation

The concept of "faux" interpolation lends itself particularly well to the above angular iterative procedure. Specifically, faux interpolation uses the transport solution algorithm itself to interpolate between quadrature points rather than some external, approximate, interpolation scheme. In particular, if we include the angular edit points in the quadrature list with zero weight, we find the angular flux at these points as a natural consequence (interpolation) of the solution algorithm. The nominal two-group case of Table 4.2.1 was run for quadrature order *Lm* = 32 with 10 uniformly spaced angular edit grid points in the interval [0,1] entered with zero weight. Figure 4.2.1 shows the exiting angular fluxes from both surfaces for this case. We denote the edit points of the faux interpolation as symbols (INT). The interpolation gives nearly three-place accuracy.

(ii.3) Multigroup self-consistency

Under certain circumstances, we can check the self-consistency of a multigroup calculation by comparison to a one-group model. As shown in Benchmark 4.1, a one-group simulation results for a multigroup calculation when the total cross section is constant across all groups. Since the group transfer cross sections sum to:

$$\sum_{g=1}^{G} \Sigma_{gg'} = \Sigma_s \tag{29}$$

and if Σ_s is the one-group scattering cross section, then:

$$\phi(x,\mu) = \sum_{g=1}^{G} \phi_g(x,\mu) \tag{30}$$

where ϕ is the one-group flux. The angular flux results of Table 4.2.3 indicate the multigroup calculation is indeed self-consistent.

(ii.4) Fast reactor example

As a final demonstration, we consider the 18-group fast reactor example of Benchmark 2.3 for a slab of 20 *cm* with a beam entering normal to the left boundary. Figure 4.2.2 shows the reflection and transmission group vectors:

$$\boldsymbol{R}_f \equiv \int_0^1 d\mu\mu\phi\left(0^+,-\mu\right) \qquad \boldsymbol{T}_n \equiv \int_0^1 d\mu\mu\phi\left(a^-,\mu\right) \tag{31}$$

for sources in Groups 1 and 15 respectively and numerically evaluated through the *GLQ*. We clearly observe the reduction in the flux when transferred to the higher lethargies through fission, which is the case with the source in Group 15.

Finally, Table 4.2.4 gives the reflectance and transmittance for various desired errors and indicates that Benchmark 4.2 is indeed a true semi-analytical benchmark to four places.

Table 4.2.1. Two-group cross sections

g	1	2
Σ_g (cm^{-1})	0.3208	0.5360
Σ_{1g} (cm^{-1})	0.0792	0.0000
Σ_{2g} (cm^{-1})	0.0432	0.23616

Table 4.2.2. Maximum error in comparison with the analytical inversion

a = 2, Lm = 20

Itr#	*x* = 0	*x* = *a*
1	3.0078E+01	3.2885E+01
2	2.8092E-03	4.8380E-03
3	7.5694E-05	1.2545E-04
4	1.3346E-06	2.2431E-06
5	1.7985E-08	3.0065E-08
6	1.9147E-10	3.2080E-10
7	1.6078E-12	2.6906E-12
8	9.5558E-15	1.5999E-14
9	1.9265E-16	2.1395E-16
10	0.0000E+00	0.0000E 00

Table 4.2.3. Multigroup simulation of one-group flux

Reflected Angular Flux

$\mu \backslash G$	5	10	20	One-group
1.000000E+00	4.200016E-01	4.200016E-01	4.200017E-01	4.200016E-01
9.000000E-01	4.477700E-01	4.477700E-01	4.477701E-01	4.477700E-01
8.000000E-01	4.789436E-01	4.789436E-01	4.789437E-01	4.789437E-01
7.000000E-01	5.139471E-01	5.139471E-01	5.139471E-01	5.139471E-01
6.000000E-01	5.530898E-01	5.530898E-01	5.530898E-01	5.530898E-01
5.000000E-01	5.963025E-01	5.963025E-01	5.963026E-01	5.963026E-01
4.000000E-01	6.425338E-01	6.425338E-01	6.425339E-01	6.425338E-01
3.000000E-01	6.884812E-01	6.884812E-01	6.884813E-01	6.884812E-01
2.000000E-01	7.266127E-01	7.266127E-01	7.266127E-01	7.266127E-01
1.000000E-01	7.453386E-01	7.453386E-01	7.453387E-01	7.453387E-01
1.000000E-02	7.287179E-01	7.287179E-01	7.287183E-01	7.287183E-01

Transmitted Angular Flux

1.000000E+00	3.805293E-01	3.805293E-01	3.805293E-01	3.805293E-01
9.000000E-01	4.014085E-01	4.014085E-01	4.014085E-01	4.014085E-01
8.000000E-01	4.237664E-01	4.237664E-01	4.237667E-01	4.237666E-01
7.000000E-01	4.472668E-01	4.472668E-01	4.472669E-01	4.472668E-01
6.000000E-01	4.710723E-01	4.710723E-01	4.710724E-01	4.710724E-01
5.000000E-01	4.933579E-01	4.933579E-01	4.933580E-01	4.933580E-01
4.000000E-01	5.104043E-01	5.104043E-01	5.104044E-01	5.104044E-01
3.000000E-01	5.151634E-01	5.151634E-01	5.151633E-01	5.151633E-01
2.000000E-01	4.966552E-01	4.966552E-01	4.966551E-01	4.966550E-01
1.000000E-01	4.480660E-01	4.480660E-01	4.480663E-01	4.480663E-01
1.000000E-02	3.832960E-01	3.832960E-01	3.832960E-01	3.832960E-01

Table 4.2.4. Convergence for fast reactor example

Reflectance

$g\backslash\varepsilon$	10^{-3}	10^{-4}	10^{-5}	10^{-6}
1	1.2722E-01	1.2722E-01	1.2722E-01	1.2722E-01
2	3.6342E-02	3.6342E-02	3.6342E-02	3.6342E-02
3	5.4362E-02	5.4362E-02	5.4362E-02	5.4362E-02
4	9.2104E-02	9.2105E-02	9.2105E-02	9.2105E-02
5	1.2236E-01	1.2236E-01	1.2236E-01	1.2236E-01
6	1.2554E-01	1.2554E-01	1.2554E-01	1.2554E-01
7	1.2815E-01	1.2815E-01	1.2815E-01	1.2815E-01
8	8.8294E-02	8.8296E-02	8.8295E-02	8.8295E-02
9	6.6602E-02	6.6602E-02	6.6602E-02	6.6602E-02
10	4.2770E-02	4.2769E-02	4.2769E-02	4.2769E-02
11	2.4302E-02	2.4301E-02	2.4301E-02	2.4301E-02
12	9.4520E-03	9.4515E-03	9.4515E-03	9.4515E-03
13	8.6403E-03	8.6397E-03	8.6397E-03	8.6397E-03
14	3.7276E-03	3.7274E-03	3.7274E-03	3.7274E-03
15	1.2873E-03	1.2872E-03	1.2872E-03	1.2872E-03
16	4.8498E-04	4.8497E-04	4.8496E-04	4.8496E-04
17	7.3049E-05	7.3042E-05	7.3039E-05	7.3039E-05
18	7.5417E-04	7.5418E-04	7.5417E-04	7.5417E-04

Transmittance

1	9.1256E-02	9.1257E-02	9.1257E-02	9.1257E-02
2	1.3823E-02	1.3823E-02	1.3823E-02	1.3823E-02
3	2.3277E-02	2.3276E-02	2.3276E-02	2.3276E-02
4	4.2764E-02	4.2763E-02	4.2763E-02	4.2763E-02
5	6.3653E-02	6.3651E-02	6.3652E-02	6.3652E-02
6	6.9495E-02	6.9493E-02	6.9493E-02	6.9493E-02
7	7.8535E-02	7.8534E-02	7.8535E-02	7.8535E-02
8	5.7821E-02	5.7823E-02	5.7823E-02	5.7823E-02
9	4.7614E-02	4.7619E-02	4.7618E-02	4.7618E-02
10	2.9780E-02	2.9783E-02	2.9783E-02	2.9783E-02
11	1.7773E-02	1.7773E-02	1.7773E-02	1.7773E-02
12	6.1679E-03	6.1677E-03	6.1675E-03	6.1675E-03
13	6.4243E-03	6.4233E-03	6.4235E-03	6.4234E-03
14	2.5844E-03	2.5840E-03	2.5840E-03	2.5840E-03
15	7.8966E-04	7.8945E-04	7.8946E-04	7.8945E-04
16	2.9169E-04	2.9161E-04	2.9160E-04	2.9160E-04
17	4.0576E-05	4.0545E-05	4.0542E-05	4.0542E-05
18	4.6766E-04	4.6772E-04	4.6769E-04	4.6770E-04

REFERENCES

[1] Ganapol, B.D., “Multigroup 1-D Homogeneous Medium Benchmark Using the Green’s Function Method”, *ANS M&C Topical*, Avignon, France (2005).

[2] Benoist, P., A. Kavenoky, “A New Method of Approximation of the Boltzmann Equation”, *Nuc. Sci. & Eng.*, **32**, 225 (1968).

[3] Van de Eynde, G., *et al.*, “The Boundary Source Method with Arbitrary Order Anisotropic Scattering”, *ANS M&C Topical*, Avignon, France (2005).

[4] Case, K.M., F. De Hoffman, G. Placzek, *Introduction to the Theory of Neutron Diffusion,* Los Alamos Scientific Laboratory, Los Alamos, NM (1953).

Figure 4.2.1. Demonstration of "faux" angular interpolation (INT)

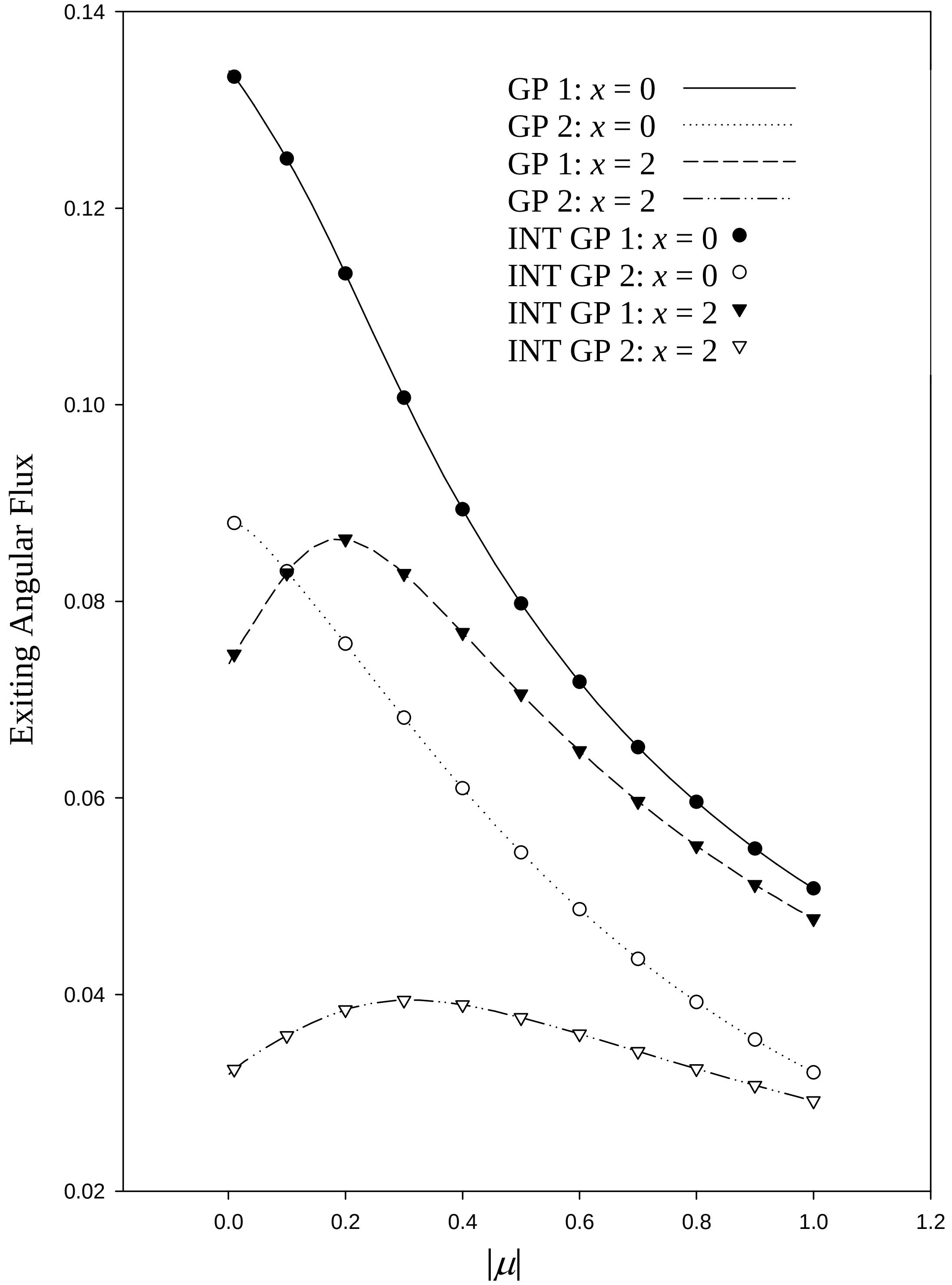

Figure 4.2.2. Reflectance and transmittance for fast reactor core of width 20 *cm*

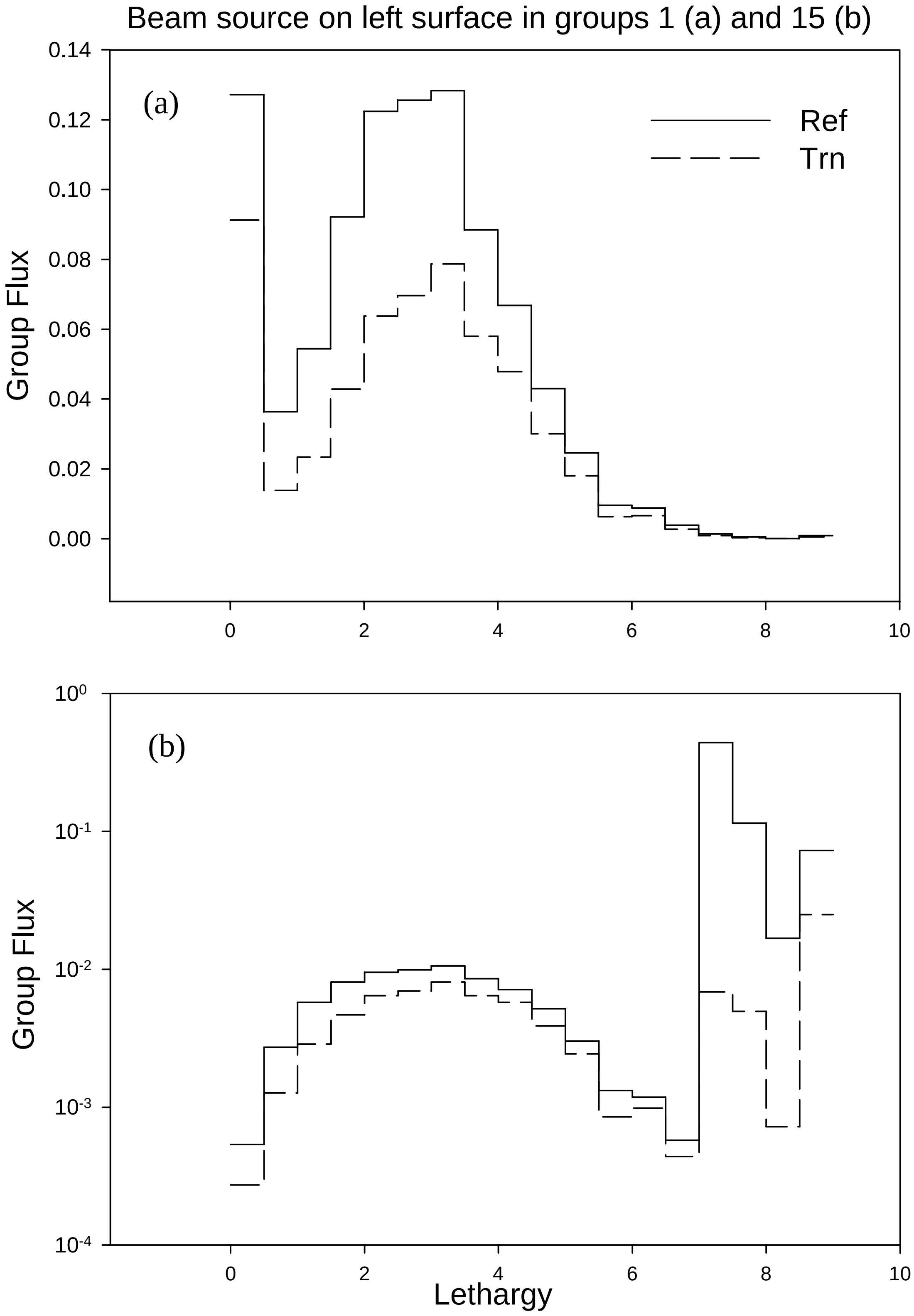

Chapter 5

MULTIDIMENSIONAL NEUTRON TRANSPORT IN SEMI-INFINITE AND INFINITE MEDIA

Neutron transport in a reactor is, in reality, a multidimensional phenomenon approximated by the 1-D transport equation we have thus far considered. Thus, a compilation of transport benchmarks would not be complete without multidimensional entries. However, the development of such benchmarks is problematic. Multidimensional semi-analytical benchmarks that provide highly accurate standards for assessment of particle transport algorithms are rare. The reason is obvious since a semi-analytical benchmark requires an analytical solution representation as its basis and multidimensional solutions are virtually non-existent. Because of the well-established one-dimensional theory for analytical solutions to the transport equation, it is sometimes possible to “bootstrap” a one-dimensional solution to generate a more comprehensive solution representation. The monoenergetic searchlight problem (SLP) is one such case since a 1-D transport solution lies at its heart. Therefore, it is possible to consider the SLP as a potential multidimensional benchmark. The SLP, however, is certainly non-trivial, as an accurate numerical evaluation requires the solution of many “inner” 1-D transport problems integrated to form the “outer” multidimensional solution. Thus, even the 2-D, one-group SLP presents a significant benchmarking challenge.

The first benchmark we consider in this chapter is the standard searchlight problem where a neutron beam illuminates a point on a smooth plane surface of a half-space in the monoenergetic approximation. We give numerical results for normal incidence only, since the canted beam is a 3-D problem requiring an additional integration, which stretches the computational effort beyond today’s reality. In addition, we consider several additional source configurations including the flashlight, which is now a relatively simple matter since the point beam source serves as the partial angular Green’s function.

The second benchmark is for localized emission from a wire source in a plane of an infinite medium in the multigroup approximation. The 3-D nature of the flux derives from that of the source itself, which we will apply to a mixed oxide fuel. Given the equation of a wire source in a plane emitting neutrons isotropically into an isotropically scattering medium, we establish a 3-D multigroup benchmark through integration of the point source kernel over the source. The numerical algorithm takes advantage of the efficient evaluation of the multigroup flux from a point source, enabling true 3-D benchmarks for the first time. This benchmark leads the way to the development of additional, more comprehensive benchmarks and represents just the beginning of a new and exciting benchmarking era.

Benchmark 5.1: Monoenergetic transport in a two-dimensional semi-infinite medium/the searchlight problem (SLP)

(a) Brief description

Two-dimensional neutron transport in an isotropically scattering medium with no energy loss upon collision commonly called the searchlight problem, referring to a beam of neutrons illuminating a point on the surface of a semi-infinite medium.

(b) Classification

NT/H/I/OG/I,B/L,D/X(C),A(C)/NFTI,NLTI

(c) Physical description

Neutrons, tracked in the longitude (*z*) and the plane radial (ρ) dimensions, impinge at a point on the surface of a semi-infinite homogeneous medium. We assume the nuclei scattering centers to be of sufficiently high mass to scatter neutrons without energy loss. All scattering directions after collision are equally probable (isotropic scattering).

(d) Analytical representation

(i) The 3-D transport equation

From Eq. (1.VI), the appropriate monoenergetic neutron transport equation in 3-D cylindrical geometry assuming isotropic scattering in the absence of fission is:

$$\left[\mu\frac{\partial}{\partial z}+\boldsymbol{\omega}\bullet\frac{\partial}{\partial\boldsymbol{\rho}}+1\right]\phi(z,\boldsymbol{\rho},\boldsymbol{\Omega})=\frac{c}{4\pi}\int_{4\pi}d\boldsymbol{\Omega}'\phi(z,\boldsymbol{\rho},\boldsymbol{\Omega}') \tag{1a}$$

where Figure 5.1.1 shows the coordinates assumed in Eq. (1a). Note that the gradient is partitioned into the longitudinal (*z*) and transverse ($\boldsymbol{\rho}$) operators. In addition, the total cross section has been taken as one and $c \equiv \Sigma_s/\Sigma$. For a slab of width *a*, a beam enters the surface at $z = 0$:

$$\phi(0,\boldsymbol{\rho},\boldsymbol{\Omega})=\frac{S(\rho)}{2\pi}\delta(\mu-\mu_0)\delta\left(\vartheta-\vartheta_0\right);\ \mu_0,\mu>0,\ \vartheta,\vartheta_0\in\left[0,2\pi\right] \tag{1b}$$

with a no return condition at the free surface $z = a$:

$$\phi(a,\boldsymbol{\rho},\boldsymbol{\Omega})=0;\ \mu<0,\quad \vartheta\in\left[0,2\pi\right] \tag{1c}$$

Note that the radial distribution of the entering flux depends on the magnitude of $\boldsymbol{\rho}$ only with normalization:

$$\int_0^\infty d\boldsymbol{\rho}\int_{4\pi}d\boldsymbol{\Omega}\,\phi(0,\boldsymbol{\rho},\boldsymbol{\Omega})=1$$

implying:

$$\int_0^\infty d\rho \rho S(\rho) = 1 \tag{2}$$

We desire only the scalar flux:

$$\phi(z,\rho) \equiv \int_{4\pi} d\boldsymbol{\Omega}\, \phi(z,\boldsymbol{\rho},\boldsymbol{\Omega}) \tag{3}$$

The incident beam, canted in the direction (μ_0, ϑ_0), is a three-dimensional problem, where the flux depends on the two spatial coordinates z, ρ and the azimuthal angle α in the radial plane:

$$\boldsymbol{\rho} = \boldsymbol{\rho}(\rho,\alpha), \quad \rho = |\boldsymbol{\rho}|$$

However, if the incident beam is normal to the surface (μ_0 = 1) and the source is independent of azimuth, the flux is also independent of α, since symmetry reduces the problem to two dimensions. In the following derivation of the expression for $\phi(z,\rho)$, we initially consider the full 3-D slab with the incident beam restricted to normal incidence at the conclusion. In addition, we let $a \to \infty$ to simulate a semi-infinite medium for which numerical results are obtained.

(ii) The Fourier transformed equation

When we apply the 2-D cylindrical Fourier transform operator:

$$\int d\boldsymbol{\rho} e^{i\boldsymbol{k}\bullet\boldsymbol{\rho}}(\bullet)$$

to Eqs. (1), the following transformed transport equation results:

$$\left[\mu\frac{\partial}{\partial z} + u(\mu,\vartheta,k)\right]\psi(z,\mu,\vartheta;\boldsymbol{k}) = \frac{c}{4\pi}\int_1^1 d\mu' \int_0^{2\pi} d\vartheta' \psi(z,\mu',\vartheta';\boldsymbol{k}) \tag{4a}$$

subject to:

$$\psi(0,\mu,\vartheta;\boldsymbol{k}) = \overline{S}(k)\delta(\mu-\mu_0)\delta\left(\vartheta-\vartheta_0\right), \quad \mu > 0 \tag{4b}$$

$$\psi(a,\mu,\vartheta;\boldsymbol{k}) = 0, \quad \mu < 0 \tag{4c}$$

with:

$$u(\mu,\vartheta,k) \equiv 1 - ik(1-\mu^2)^{1/2}\cos(\vartheta - \psi) \tag{5a}$$

$$\psi(z,\mu,\vartheta;\boldsymbol{k}) \equiv \int d\boldsymbol{\rho} e^{i\boldsymbol{k}\bullet\boldsymbol{\rho}}\, \phi(z,\boldsymbol{\rho},\boldsymbol{\Omega}) \tag{5b}$$

$$\overline{S}(k) \equiv \int_0^\infty d\rho \rho S(\rho) J_0(k\rho) \tag{5c}$$

$J_0(k\rho)$ is the zeroth-order Bessel function of the first kind. If the transformed scalar flux is:

$$\psi(z;\boldsymbol{k}) \equiv \int d\boldsymbol{\Omega}\, \psi(z,\mu,\vartheta;\boldsymbol{k}) \tag{6}$$

then:

$$\psi(z;\boldsymbol{k}) = \int d\boldsymbol{\rho} e^{i\boldsymbol{k}\boldsymbol{\cdot}\boldsymbol{\rho}}\ \phi(z,\boldsymbol{\rho}) \tag{7}$$

From the Fourier inversion integral, the desired scalar flux is therefore:

$$\phi(z,\boldsymbol{\rho}) = \frac{1}{(2\pi)^2} \int d\boldsymbol{k} e^{-i\boldsymbol{k}\boldsymbol{\cdot}\boldsymbol{\rho}}\, \psi(z;\boldsymbol{k}) \tag{8}$$

(iii)The integral equation for $\psi(z;\boldsymbol{k})$

Following integral transport theory by integrating Eq. (4a) along the particle trajectory gives (see §1.2.1):

$$\psi(z,\mu,\vartheta;\boldsymbol{k}) = e^{-u(z-z')/\mu}\, \psi(z',\mu,\vartheta;\boldsymbol{k}) + \frac{c}{4\pi\mu} \int_{z'}^{z} dz'' e^{-u(z-z'')/\mu}\, \psi(z'';\boldsymbol{k}) \tag{9}$$

Thus, making use of the boundary conditions at $z = 0$ and a, we have for $\mu > 0$:

$$\psi(z,\mu,\vartheta;\boldsymbol{k}) = e^{-z/U_0(k)} \overline{S}(k) \delta(\mu-\mu_0) \delta(\vartheta-\vartheta_0) + \frac{c}{4\pi\mu} \int_0^z dz' e^{-(z-z')/U} \psi(z';\boldsymbol{k}) \tag{10a}$$

and:

$$\psi(z,-\mu,\vartheta;\boldsymbol{k}) = \frac{c}{4\pi\mu} \int_z^a dz' e^{-(z-z')/U}\, \psi(z';\boldsymbol{k}) \tag{10b}$$

where:

$$U(\mu,\vartheta,k) \equiv \frac{\mu}{u(\mu,\vartheta,k)},\ \ U_0(k) \equiv U(\mu_0,\vartheta_0,k) \tag{11}$$

Integrating Eqs. (10) to form the scalar flux transform generates the following integral equation:

$$\psi(z;\boldsymbol{k}) = e^{-z/U_0(k)} \overline{S}\,(k) + \frac{c}{2} \int_0^a dz' K(|z-z'|;k) \psi(z';\boldsymbol{k}) \tag{12a}$$

with:

$$K(z,k) \equiv \int_0^1 d\mu\, \frac{e^{-z/\mu}}{\mu} J_0\left(\frac{kz}{\mu} \sqrt{1-\mu^2} \right) \tag{12b}$$

from which one can show that [1]:

$$K\left(z;k\right)=\int_0^1\frac{d\mu}{\mu}\frac{e^{-z\left(1+k^2\mu^2\right)^{1/2}/\mu}}{\left(1+k^2\mu^2\right)^{1/2}} \tag{13}$$

We obtain the last expression by first noting that [2]:

$$\int_1^\infty dte^{-st}J_0\left(\eta\sqrt{t^2-1}\right)=\frac{e^{-\sqrt{s^2+\eta^2}}}{\sqrt{s^2+\eta^2}}$$

With this integral, re-written as:

$$\int_0^1 d\mu\frac{e^{-s/\mu}}{\mu^2}J_0\left(\frac{\eta}{\mu}\sqrt{1-\mu^2}\right)$$

we find Eq. (13) from Eq. (12b) by integration over s on $[z,\infty)$ and the substitutions $s = z$, $\eta = kz$.

With this form of the kernel, we can define an equivalent 1-D pseudo problem allowing direct determination of ψ by applying one-dimensional transport methods. We emphasize that the 1-D pseudo problem enables the solution to the 3-D SLP.

(iv) The 1-D pseudo problem

Consider the following generalized transport equation:

$$\left[\mu a(\mu)\frac{\partial}{\partial z}+b(\mu)\right]\phi(z,\mu;\mu^*)=\frac{c}{2}\int_{-1}^{1}d\mu'\phi(z,\mu';\mu^*) \tag{14a}$$

$$\phi(0,\mu;\mu^*)=\delta(\mu-\mu^*)\quad \mu^*,\mu>0 \tag{14b}$$

$$\phi(a,\mu;\mu^*)=0\qquad \mu<0 \tag{14c}$$

where a and b are even functions of μ. Again, by integrating along a neutron trajectory, Eqs. (14) give for $\mu > 0$:

$$\phi(z,\mu;\mu^*)=\delta(\mu-\mu^*)e^{-z/\xi^*}+\frac{c}{2\mu a(\mu)}\int_0^z dz' e^{-(z-z')/\xi}\,\phi(z';\ \mu^*) \tag{15a}$$

and:

$$\phi(z,-\mu;\mu^*)=\frac{c}{2\mu a(\mu)}\int_z^a dz'\,e^{-(z'-z)/\xi}\,\phi(z';\mu^*) \tag{15b}$$

where:

$$\xi\equiv\mu\frac{a(\mu)}{b(\mu)} \tag{16}$$

Integrating Eqs. (15) over μ therefore gives the following integral equation for $\phi(z;\mu^*)$:

$$\phi(z;\mu^*) = e^{-z/\xi^*} + \frac{c}{2}\int_0^a dz' K^*(|z-z'|)\phi(z';\mu^*) \tag{17a}$$

with:

$$K^*(z) \equiv \int_0^1 \frac{d\mu}{\mu}\frac{e^{-z/\xi(\mu)}}{a(\mu)} \tag{17b}$$

We find the relation between Eq. (12a) and Eq. (17a) by letting:

$$\xi^* \equiv \mu\frac{a(\mu)}{b(\mu)}$$

$$a(\mu) = [1+(k\mu)^2]^{1/2} \tag{18a}$$

$$b(\mu) = 1+(k\mu)^2 \tag{18b}$$

where $a(\mu)$ and $\beta(\mu)$ are our choice. On multiplying Eq. (17a) by $\bar{S}(k)$, the following equivalence must hold:

$$\psi(z;\boldsymbol{k}) = \bar{S}(k)\phi\left(z;\mu^*(U_0(k))\right) \tag{19}$$

Therefore, knowing $\phi(z;\mu^*)$, yields $\psi(z;\boldsymbol{k})$ and the Fourier transform inversion gives the radial distribution.

We will now apply the above theory to the half-space SLP.

(v) The solution for $\phi(z;\mu^*)$ via invariant embedding: beam incidence

For the half-space, let $a\to\infty$. Here, we follow the approach of Busbridge [3] which we now summarize for the SLP and also apply to Benchmark 3.2.

Step 1: We begin by defining the operator:

$$L_z \equiv \frac{c}{2}\int_0^\infty dz' K^*(|z-z'|)(\bullet) \tag{20}$$

giving for Eq. (17a):

$$\left(1-L_z\right)\phi(z;\mu^*) = e^{-z/\xi^*} \tag{21}$$

where μ^*, at this point, is a real variable.

Step 2: A derivative of Eq. (21) with respect to z yields:

$$(1-L_z)\left[\frac{\partial}{\partial z}+\frac{1}{\xi^*}\right]\phi(z;\mu^*)=\frac{c}{2}K^*(z)\phi(0;\mu^*) \tag{22}$$

Step 3: Noting the structure of K^* from Eq. (17b), we can show from Eq. (21) that:

$$K^*(z)=(1-L_z)\int_0^1 d\mu'\frac{\phi(z;\mu')}{\mu' a(\mu')}$$

and Eq. (22) becomes:

$$(1-L_z)\left[\left(\frac{\partial}{\partial z}+\frac{1}{\xi^*}\right)\phi(z;\mu^*)-\frac{c}{2}\phi(0;\mu^*)\int_0^1 d\mu'\frac{\phi(z;\mu')}{\mu' a(\mu')}\right]=0 \tag{23}$$

The term in square brackets is in the null space of the operator (1 – L_z) and is therefore zero. Thus, we have the following equation to solve:

$$\left[\frac{\partial}{\partial z}+\frac{1}{\xi^*}\right]\phi(z;\mu^*)=\frac{c}{2}\phi(0;\mu^*)\int_0^1 d\mu'\frac{\phi(z;\mu')}{\mu' a(\mu')} \tag{24}$$

Step 4: We establish reciprocity by noting L_z is a self-adjoint operator. Thus, if:

$$(1-L_z)\,\phi(z;\mu)=e^{-z/\xi} \tag{25a}$$

$$(1-L_z)\;\phi(z;\mu^*)=e^{-z/\xi^*} \tag{25b}$$

multiplying Eq. (25a) by $\phi(z;\mu^*)$ and Eq. (25b) by $\phi(z;\mu)$, integrating and subtracting after applying the self-adjoint property:

$$\langle u, L_z \mathrm{v}\rangle=\langle \mathrm{v}, L_z u\rangle$$

where $\langle\ \ \rangle$ indicates inner product, gives:

$$\frac{c}{2}\int_0^\infty dz' e^{-z'/\xi}\phi(z';\mu^*)=\frac{c}{2}\int_0^\infty dz' e^{-z'/\xi^*}\phi(z';\mu) \tag{26}$$

or from Eq. (15b) with $z = 0$:

$$\mu a(\mu)\phi(0,-\mu;\mu^*)=\frac{c}{2}\int_0^\infty dz' e^{-z'/\xi}\phi(z';\mu^*) \tag{27}$$

Equation (26) is the following reciprocity (equivalence on interchange of source and detector):

$$\mu a(\mu)\phi(0,-\mu;\mu^*)=\mu^* a(\mu^*)\phi(0,-\mu^*;\mu) \tag{28}$$

Step 5: When we multiply Eq. (24) by $e^{-z/\xi}$ and integrate over z on $[0,\infty)$ with liberal use made of Eq. (27), there results (after some algebra):

$$\phi(0,-\mu;\mu^*)=\frac{c}{2}\frac{1}{\mu a(\mu)}\frac{\xi\,\xi^*}{\xi^*+\xi}\,\phi(0;\mu^*)\phi(0;\mu) \tag{29}$$

Substituting this expression into the representation of the scalar flux at $z = 0$ and assuming an incident beam:

$$\phi(0;\mu^*)=1+\int_0^1 d\mu'\phi(0,-\mu';\mu^*) \tag{30}$$

gives for Eq. (29):

$$\phi(0,-\mu;\mu^*)=\frac{c}{2}\frac{1}{\mu a(\mu,k)}\frac{\xi^*\xi}{\xi^*+\xi}H(\xi^*;k)H(\xi;k) \tag{31}$$

where the H-function satisfies the following non-linear integral equation from Eq. (30):

$$H(\xi;k)=1+\frac{c}{2}\,\xi H(\xi;k)\int_0^1\frac{d\mu'}{b(\mu')}\frac{H(\xi';k)}{\xi+\xi'} \tag{32}$$

In addition, ξ depends on k. When k is zero, we find the H-function referred to in Benchmark 3.2.

Step 6: The exiting scalar flux comes about by integrating Eq. (31) over μ and using Eq. (32) to give:

$$\phi(0;\mu^*)=H(\xi^*;k) \tag{33}$$

Step 7: The interior scalar flux comes from Eq. (27) by letting $\xi \equiv 1/s$:

$$\frac{2}{c}\,\mu(s)a(\mu(s))\phi(0,-\mu\,(s);\mu^*)=\mathrm{L}_s\Big[\phi(z';\mu^*)\Big]$$

where L_s represents the Laplace transform operator leading to the inversion:

$$\phi(z;\mu^*\left(\xi^*\right))=\ \xi^*H(\xi^*;k)\ \mathrm{L}_z^{-1}\left[\frac{H(1/\,s;k)}{1+s\xi^*}\right] \tag{34}$$

It is this last expression we will numerically evaluate for the interior distribution.

(vi) *The Fourier transform inversion for the scalar flux*: *normal beam incidence*

First considering $z = 0$, there results from Eqs. (19) and (33):

$$\psi(0;\boldsymbol{k})=\overline{S}(k)H(U_0(k);k) \tag{35}$$

and from the Fourier inversion given by Eq. (8) evaluated at $z = 0$:

$$\phi(0,\rho) = \frac{1}{(2\pi)^2}\int_0^{2\pi} d\,\psi \int_0^{\infty} dkke^{-ik\rho\cos(\alpha-\psi)}\overline{S}(k)H(U_0(k);k) \tag{36}$$

Recalling that:

$$U_0(k) = \frac{\mu_0}{\left[1 - ik\left(1-\mu_0^2\right)^{1/2}\cos(\vartheta_0-\psi)\right]}$$

for a normally incident beam ($\mu_0 = 1$), we therefore have:

$$\phi(0,\rho) = \frac{1}{2\pi}\int_0^{\infty} dkk\overline{S}(k)H(1;k)J_0(\rho k). \tag{37}$$

by using the integral definition of the Bessel function [2]. Note that $\phi(0,\rho)$ is independent of α as required for normal incidence. Numerical experience has shown that accounting for the uncollided contribution separately leads to a numerically better-behaved integration:

$$\phi(0,\rho) = \frac{1}{2\pi}S(\rho) + \frac{1}{2\pi}\int_0^{\infty} dkk\overline{S}(k)[H(1;k)-1]J_0(\rho k) \tag{38}$$

For the interior flux ($z > 0$), since:

$$\psi(z;k) = \phi\left(z;\mu^*(U_0(k))\right) \tag{39}$$

the Fourier transform inversion from Eq. (34) is, in general:

$$\begin{aligned}\phi(z,\rho) &= \\ &= \frac{1}{(2\pi)^2}\int_0^{2\pi} d\psi \int_0^{\infty} dkk\overline{S}(k)e^{-ik\rho\cos(\alpha-\psi)}U_0(k)H(U_0(k);k)\mathcal{L}_z^{-1}\left[\frac{H(1/s;k)}{1+sU_0(k)}\right];\end{aligned} \tag{40}$$

and for the normal beam reduces to:

$$\phi(z,\rho) = \frac{1}{2\pi}\int_0^{\infty} dkk\overline{S}(k)H(1;k)\mathcal{L}_z^{-1}\left[\frac{H(1/s;k)}{1+s}\right]J_0(k\rho) \tag{41}$$

Again, $\phi(z,\rho)$ is independent of α as it must be. Accounting for the uncollided contribution separately then gives:

$$\phi(z,\rho) = \frac{e^{-z}}{2\pi}S(\rho) + \frac{1}{2\pi}\int_0^{\infty} dkk\overline{S}(k)\left\{H(1;k)\mathcal{L}_z^{-1}\left[\frac{H(1/s;k)}{1+s}\right] - e^{-z}\right\}J_0(k\rho) \tag{42}$$

(vii) The solution for an isotopic source

We now consider the scalar flux for an isotopically illuminating flux of particles at a point on the free surface. For this case, the boundary condition is:

$$\hat{\phi}(0,\rho,\mathbf{\Omega}) = \frac{1}{4\pi^2} S(\rho), \quad \mu > 0 \tag{43}$$

implying:

$$\hat{\phi}(0,\rho,\mathbf{\Omega}) = \frac{1}{2\pi} \int_{2\pi} d\mathbf{\Omega}_0 \phi(0,\rho,\mathbf{\Omega};\mathbf{\Omega}_0) \tag{44}$$

where $\phi(0,\rho,\mathbf{\Omega};\mathbf{\Omega}_0)$ is the flux for an incident beam in direction $\mathbf{\Omega}_0$. Thus, the integral equation for the transformed scalar flux from integrating Eq. (12a) over $\mathbf{\Omega}_0$ after dividing by 2π is:

$$\hat{\psi}(z;k) = \bar{S}(k)\int_0^1 d\mu_0\, e^{-z/\mu_0} J_0\left(kz\frac{\sqrt{1-\mu_0^2}}{\mu_0}\right) + \frac{c}{2}\int_0^\infty dz' K(|z-z'|;k)\hat{\psi}(z';k) \tag{45}$$

where the leading integral is also:

$$\int_0^1 d\mu\, e^{-z\left(1+k^2\mu^2\right)^{1/2}/\mu}$$

When we integrate μ^* in Eq. (17a) over [0,1], there results by uniqueness:

$$\hat{\psi}(z;k) = \int_0^1 d\mu^* \phi(z;\mu^*) \tag{46}$$

Therefore, for $z = 0$ in Eq. (45) and from Eq. (35):

$$\hat{\psi}(0;k) = \bar{S}(k)\left[\int_0^1 d\mu^* H(\xi^*;k)\right] \tag{47a}$$

and for the interior, from Eqs. (45) and (34):

$$\hat{\psi}(z;k) = \bar{S}(k)\, \mathrm{L}_z^{-1}\left[H(1/s;k)\int_0^1 d\mu^* \frac{\xi^* H(\xi^*;k)}{1+s\,\xi^*}\right] \tag{47b}$$

The final inversion is therefore:

$$\hat{\phi}(z,\rho) = \frac{1}{2\pi}\int_0^\infty dk k \bar{S}(k) q_0(z;k) J_0(k\rho) \tag{48}$$

where q_0 is the term in square brackets in Eqs. (47b). Again from numerical experience a more numerically appropriate form for Eq. (48) for $z > 0$ is:

$$\tilde{\phi}(z,\rho) = \phi_0(z,\rho) + \frac{1}{2\pi}\int_0^\infty dkk\bar{S}(k) \bullet \tag{49}$$
$$\bullet \int_0^1 dk^* \frac{\xi^*}{1+s\xi^*}\left[H(1/s;k)\, H(\xi^*;k) - 1 \right] J_0(k\rho)$$

(viii) Various distributed sources

The above derivation is valid for any radially distributed source that possesses a Fourier transform. We now consider some special cases with the normalization given by Eq. (2). Some particular sources of interest are:

1. Point source: $$S(\rho) = \frac{\delta(\rho)}{\rho},\ \bar{S}(k) = 1 \tag{50a}$$

2. Ring source at ρ_0: $$S(\rho) = \frac{\delta(\rho-\rho_0)}{\rho_0},\ \bar{S}(k) = J_0(k\rho_0) \tag{50b}$$

3. Gaussian source: $$S(\rho) = 2a^2 e^{-a^2\rho^2},\ \bar{S}(k) = e^{-k^2/4a^2} \tag{50c}$$

4. Disk source of radius ρ_0: $$S(\rho) = \frac{2}{\rho_0^2}\theta(\rho_0 - \rho)\ ,\ \bar{S}(k) = 2\,\frac{J_1(k\rho_0)}{k\rho_0} \tag{50d}$$

(e) Numerical implementation and demonstration for Benchmark 5.1

The evaluation of the scalar flux at $z = 0$ and in the interior presents a significant numerical challenge. In particular, a Hankel transform inversion is required for a complicated integrand which itself contains additional integrations and possibly a Laplace transform inversion. We therefore require the evaluation of the *H*-function, the numerical Hankel transform inversion and the numerical Laplace transform inversion (see Appendix B.1).

(i) Numerical procedures

(i.1) Evaluation of the *H*-function

The evaluation of the *H*-function is central to the numerical determination of the scalar flux. The integral equation to solve is [Eq. (32)]:

$$H(\xi) = 1 + \frac{c}{2}\xi H(\xi)\int_0^1 \frac{d\mu'}{b(\mu')}\frac{H(\xi')}{\xi+\xi'}$$

where we have suppressed the dependence on k for brevity. With a change of variable and rearrangement, Eq. (32) becomes:

$$H(\xi) = \left[1 - \frac{c}{2}\xi \int_0^{\frac{1}{\sqrt{1+k^2}}} \frac{d\xi'}{\sqrt{1-(k\xi')^2}}\frac{H(\xi')}{\xi+\xi'} \right]^{-1} \tag{51a}$$

In addition, the H-function has the explicit zeroth moment obtained from the integration of Eq. (32):

$$\alpha_0 \equiv \int_0^1 d\mu \frac{H(\xi)}{b(\mu)} \;=\; \frac{2}{c}\left[1-\sqrt{1-c\,\frac{\tan^{-1}k}{k}}\,\right] \tag{51b}$$

We anticipate numerical difficulty in the evaluation of Eq. (51a) in that for k large the integrand becomes almost (weakly) singular (at $\xi \approx 1/k$) which is certain to have an adverse effect on the behavior of any standard numerical integration scheme. To overcome this difficulty, we impose the change of variable:

$$\xi' = \frac{1}{k}\sin\theta'$$

to give:

$$H(\xi) = \left[1 - \frac{c}{2}\,\xi \int_0^a d\theta' \frac{H\left(\dfrac{\sin\theta'}{k}\right)}{k\,\xi + \sin\theta'}\right]^{-1} \tag{52a}$$

where:

$$a \equiv \sin^{-1}\left(\frac{k}{\sqrt{1+k^2}}\right) \tag{52b}$$

Further, if:

$$\theta'' = \theta'/a$$

then:

$$H(\xi) = \left[1 - \frac{c}{2}\,\xi\,\frac{a}{k}\int_0^1 d\theta'' \frac{H\left(\dfrac{\sin(a\theta'')}{k}\right)}{\xi + \dfrac{\sin\,(a\theta'')}{k}}\right]^{-1} \tag{53}$$

In effect, we have eliminated the almost singular part of the integrand, enabling a standard shifted Gauss-Legendre quadrature (*GLQ*). With these substitutions, the zeroth moment becomes:

$$\alpha_0 = \frac{a}{k}\int_0^1 d\theta' H\left(\frac{\sin(a\theta')}{k}\right) \tag{54}$$

The algorithm for the evaluation of the H-function is first to let:

$$\xi = \frac{\sin(a\theta)}{k}$$

and then to evaluate the integral in Eq. (53) through a shifted Gauss-Legendre quadrature of order *Lm* to give the two-step iterative scheme:

$$H_m^0 = \alpha_0 \tag{55a}$$

$$H_m^{j+1/2} = \left[1 - \frac{c}{2}\frac{a}{k}\frac{\sin(a\theta_m)}{k}\sum_{m'=1}^{Lm}\omega_{m'}\frac{H_{m'}^{j}}{\dfrac{\sin(a\theta_m)}{k} + \dfrac{\sin(a\theta_{m'})}{k}} \right]^{-1} \tag{55b}$$

$$H_m^{j+1} = \left(\frac{\alpha_0}{\alpha_0^{j+1/2}} \right) H_m^{j+1/2} \tag{55c}$$

$$\alpha_0^{j+1/2} = \frac{a}{k}\sum_{m'=1}^{Lm}\omega_{m'}H_{m'}^{j+1/2} \tag{55d}$$

For any ξ, even complex, we can view Eq. (32) as the interpolation formula:

$$H(\xi) = \left[1 - \frac{c}{2}\xi\frac{a}{k}\sum_{m'=1}^{Lm}\omega_{m'}\frac{H_{m'}^{c}}{\xi + \dfrac{\sin(a\theta_{m'})}{k}} \right]^{-1} \tag{56}$$

once we know H_m^c, the converged *H*-function at μ_m,. When, $k = 0$, the above algorithm reduces to the usual Chandrasekhar *H*-function [3] implemented in Benchmark 3.2 since:

$$\lim_{k \to 0}\left[\frac{a}{k}\right] = 1$$

$$\lim_{k \to 0}\left[\frac{\sin(a\theta)}{k}\right] = \theta$$

$$\lim_{k \to 0}\left[\frac{\tan k}{k}\right] = 1$$

(i.2) Hankel inversion

The second numerical procedure involves the numerical Hankel inversion [2]:

$$I \equiv \int_0^\infty du\, u f(u) J_0(u) \tag{57}$$

The most straightforward evaluation of *I* is to reformulate the integration over the intervals between the zeros of J_0 giving the infinite series:

$$I = \sum_{j=0}^{\infty}\int_{a_j}^{a_{j+1}} du\, u f(u) J_0(u)$$

where a_j is the j^{th} zero of J_0. We evaluate the integrals by an iterated Gauss-Legendre quadrature (Appendix A.4) and iterate on quadrature order. The Euler-Knopp transformation (Appendix A.1) applied to the partial sums accelerates series convergence. We then filter the accelerated sequence through a Wynn-epsilon convergence accelerator (Appendix A.2) for additional acceleration.

(ii) Benchmark demonstration

In this section, the SLP benchmark described above will be qualified, i.e. shown to be a true semi-analytical benchmark. We also present some results of a general nature, and a comparison to several standard codes.

Table 5.1.1 shows the convergence of the scalar flux in the radial coordinate with expected error for $z = 2$ *mfp* and $c = 0.99$. We expect the last column to be correct to all digits quoted. Compared to the last column, the number of digits requested is always satisfied for the requested error.

Figure 5.1.2 shows the longitudinal scalar flux variation at $r = 1.75$ *mfp* for a point source and variation of c. As c approaches unity, the flux becomes spatially uniform since scattering dominates.

We now consider a disk (flashlight) source of 3 *mfp* radius shining on the surface of the highly reflective medium of $c = 0.99$. Figures 5.1.3(a) and 5.1.3(b) show the longitudinal and radial variations respectively. For this highly scattering case, the source penetrates (~10 *mfp*) deeply into the medium. The outline of the source is evident in the radial profile and remains at 9.25 *mfp* from the surface.

With regard to practical benchmarking, Figure 5.1.4 shows the flux at $z = 0$ and for selected values of z in the interior of a $c = 0.99$ scattering medium [5] in comparison to the MCNP [6] and DORT [7] transport codes. The agreement is excellent for all cases.

Table 5.1.1. Qualification of Benchmark 5.1

Radial scalar flux (*z = 2 mfp, c = 0.99*)

$r\backslash\varepsilon$	10^{-3}	10^{-4}	10^{-5}	10^{-6}
2.0000E-01	3.0108E-01	3.0112E-01	3.0112E-01	3.0111E-01
1.1800E+00	8.0201E-02	8.0206E-02	8.0206E-02	8.0206E-02
2.1600E+00	3.7865E-02	3.7865E-02	3.7865E-02	3.7865E-02
3.1400E+00	1.9928E-02	1.9927E-02	1.9927E-02	1.9927E-02
4.1200E+00	1.1240E-02	1.1239E-02	1.1239E-02	1.1239E-02
5.1000E+00	6.6789E-03	6.6778E-03	6.6778E-03	6.6777E-03
6.0800E+00	4.1351E-03	4.1346E-03	4.1345E-03	4.1345E-03
7.0600E+00	2.6471E-03	2.6471E-03	2.6470E-03	2.6470E-03
8.0400E+00	1.7422E-03	1.7424E-03	1.7424E-03	1.7423E-03
9.0200E+00	1.1735E-03	1.1739E-03	1.1738E-03	1.1738E-03
1.0000E+01	8.0635E-04	8.0654E-04	8.0654E-04	8.0654E-04

REFERENCES

[1] Siewert, C.E., “The Searchlight Problem in Radiative Transfer”, *JQSRT*, **41**, 467 (1989).

[2] Magnus, W., F. Oberhettinger, *Functions of Mathematical Physics*, Springer-Verlag OHG, Berlin (1947).

[3] Busbridge, I., *The Mathematics of Radiative Transfer*, Cambridge University Press, London (1960).

[4] Press, W., *et al*., *Numerical Recipes*, Cambridge University Press, NY (1986).

[5] Ganapol, B.D., *et al*., “The Searchlight Problem for Neutrons in a Semi-infinite Medium”, *Nucl. Sci. & Engr*., **118**, 38 (1994).

[6] *MCNP, Version 3A*, LANL, LA-7396-M, Rev. 2, J.F. Briemeister (Ed.) (1986).

[7] Rhoades, W.A., R.L. Childs, *DORT*, CCC-543, ORNL (1991).

Figure 5.1.1. Cylindrical geometry coordinates in direct and transform space

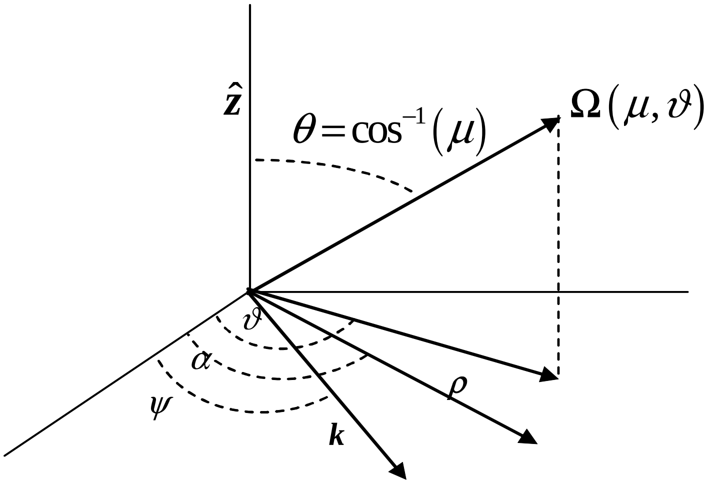

Figure 5.1.2. Variation of the scalar flux from a point source with *c* at ρ = 1.75 *mfp*

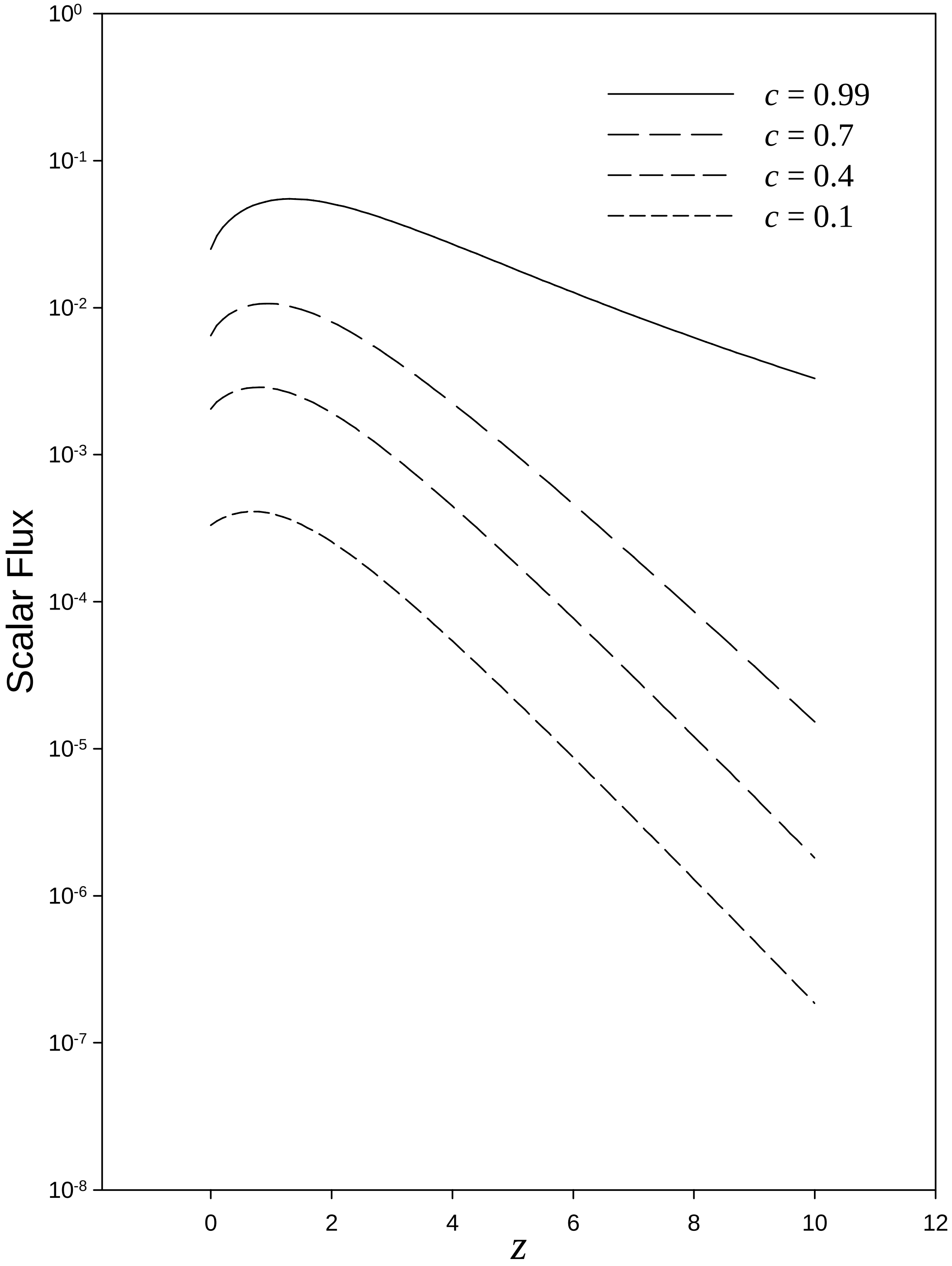

Figure 5.1.3. Flux variation from a disk source of radius 3 *mfp* for $c = 0.99$ (a) longitudinal and (b) radial

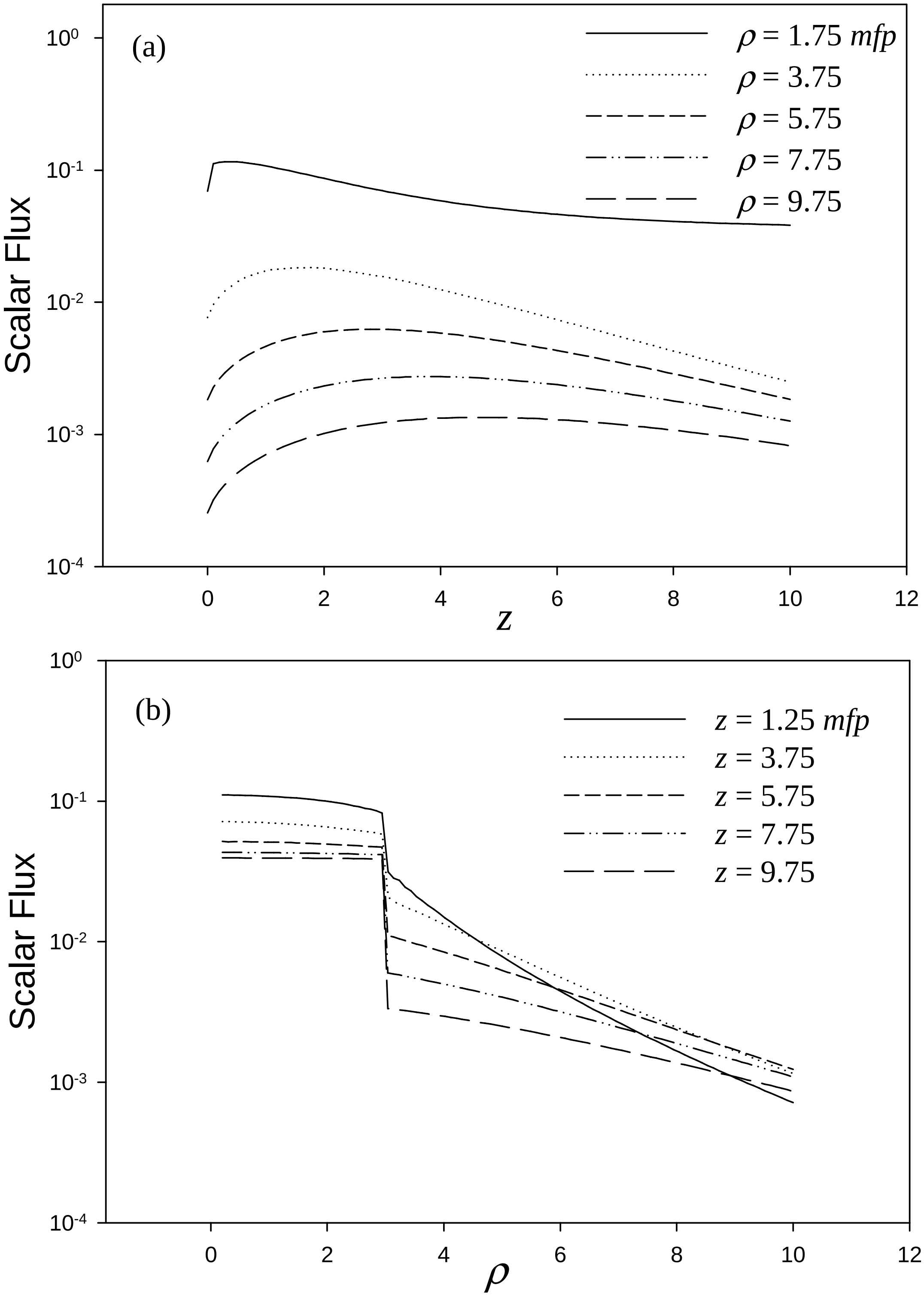

Figure 5.1.4. Comparison with DORT and MCNP codes (c = 0.99) (a) z-axis and (b) ρ-axis

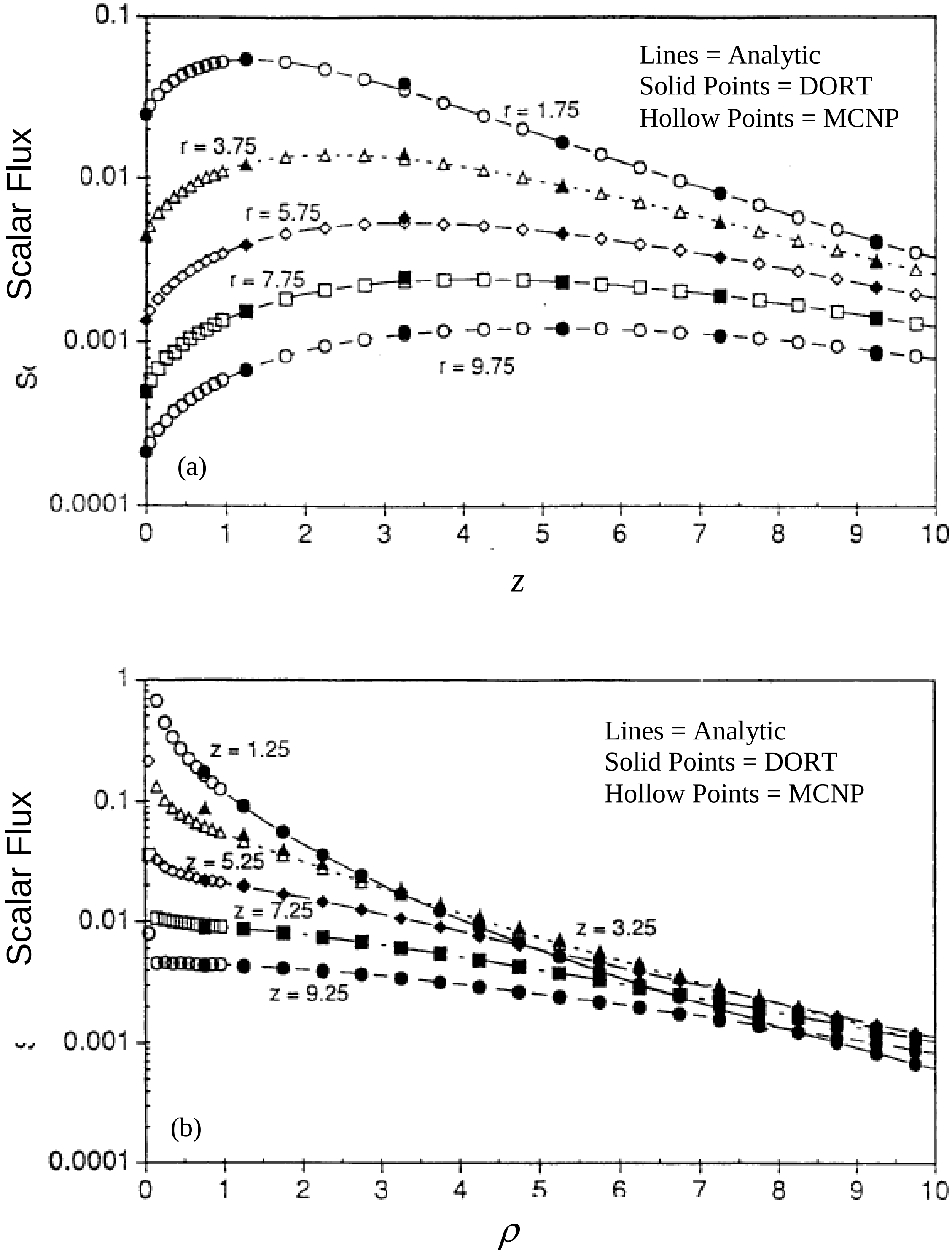

Benchmark 5.2: Multigroup transport in a three-dimensional infinite medium/the point kernel method

(a) Brief description

Multigroup, multidimensional neutron transport in an isotropically scattering/fissioning infinite medium from an isotropically emitting wire source configured in a plane.

(b) Classification

NT/H/I/MG/I/L,D/X(C)/NFTI,PKM

(c) Physical description

Neutrons diffuse from a wire source into an isotropically scattering/fissioning infinite medium. Neutrons, emitted isotropically, gain or lose energy through scattering and appear through fission. We assume the multigroup approximation.

(d) Analytical representation

(i) The point kernel

Consider an isotropically and uniformly emitting finite wire source located in the (x,y) plane in an infinite medium shown in Figure 5.2.1. Integrating the group flux $\phi_{pt}(r)$, called the point kernel, from a point source, over the line source gives the following scalar group flux at position $\boldsymbol{r}(\rho,\theta,z)$:

$$\phi(\rho,\theta,z)=\frac{Q_0}{l}\int_{\theta_0}^{\theta_l} d\theta'\left[\rho_s(\theta')^2+\left(\frac{d\rho_s(\theta')}{d\theta'}\right)^2\right]^{1/2}\phi_{pt}\left(\left|\boldsymbol{r}-\boldsymbol{r}'\right|\right) \tag{1}$$

where ρ_s is the equation of the line defining the source configuration in the plane. l is the length of the wire and Q_0 is the (uniform) source strength. The distance between the edit point (also called a detector) and a point on the source is:

$$\left|\boldsymbol{r}\text{ - }\boldsymbol{r}'\right|=\left[\rho_s(\theta')^2+\rho^2-2\rho_s(\theta')\rho\cos(\theta-\theta')+z^2\right]^{1/2}$$

As was shown in Benchmark 4.1, the scalar group flux a distance r from a point source is:

$$\phi_{pt}(r)=\frac{1}{2\pi i}\frac{1}{2\pi r}\int_{-\infty}^{\infty} dkke^{ikr}\left\{\boldsymbol{\Sigma}-\boldsymbol{L}(k)\left[\boldsymbol{\Sigma}_s+\boldsymbol{\chi}\left(\nu\boldsymbol{\Sigma}_f\right)^T\right]\right\}^{-1}\boldsymbol{L}(k)\boldsymbol{Q} \tag{4.1.14}$$

where $\boldsymbol{Q}$ is the group source vector.

Equation (1) represents a true 3-D neutron transport multigroup scalar flux solution in an anisotropically scattering infinite medium since all scattering information is contained in the point kernel. For this benchmark, however, we shall only consider isotropic scattering.

(ii) The analytical solution and some properties

While not particularly useful, nevertheless interesting, we can express Eq. (1) in an analytically explicit representation. From the relation [1]:

$$\frac{e^{ikR}}{R} = \tag{2}$$

$$= \sum_{m=0}^{\infty} \varepsilon_m \cos\left(m\left(\theta-\theta'\right)\right) \int_0^{\infty} d\omega \frac{\omega}{\sqrt{\omega^2-k^2}} e^{-|z|\sqrt{\omega^2-k^2}} J_m\left(\omega\rho_s\right) J_m\left(\omega\rho\right)$$

where:

$$R \equiv \left|\boldsymbol{r}-\boldsymbol{r}'\right| \equiv \sqrt{\rho_s{}^2+\rho^2-2\rho_s\left(\theta'\right)\rho\cos\left(\theta-\theta'\right)+z^2}, \quad \varepsilon_m \equiv 2-\delta_{m0}$$

substituted into Eq. (4.1.14) and the result into Eq. (1), we obtain the explicit representation:

$$\phi\left(\rho,\theta,z\right) = \tag{3}$$

$$= \frac{Q_0}{4\pi^2 il} \sum_{m=0}^{\infty} \varepsilon_m \int_{-\infty}^{\infty} dkk \left[\begin{array}{l} \displaystyle\int_0^{\infty} d\omega \frac{\omega}{\sqrt{\omega^2-k^2}} e^{-|z|\sqrt{\omega^2-k^2}} J_m\left(\omega\rho\right) \bullet \\ \bullet \displaystyle\int_{\theta_0}^{\theta_1} d\theta' \left\{ \begin{array}{l} \left[\rho_s\left(\theta'\right)^2 + \left(\dfrac{d\rho_s\left(\theta'\right)}{d\theta'} \right)^2 \right]^{1/2} \bullet \\ \bullet J_m\left(\omega\rho_s\left(\theta'\right)\right) \cos\left(m\left(\theta-\theta'\right)\right) \end{array} \right\} \end{array} \right] \bullet$$

$$\bullet \left\{ \boldsymbol{\Sigma} - \boldsymbol{L}\left(k\right) \left[\boldsymbol{\Sigma}_s + \boldsymbol{\chi}\left(\boldsymbol{\nu\Sigma}_f\right)^T \right] \right\}^{-1} \boldsymbol{L}\left(k\right)\boldsymbol{Q}$$

which is actually the Fourier series representation of the solution.

For a closed circular (ring) source of radius R, $\rho_s(\theta) = R$, Eq. (3) simplifies to:

$$\phi\left(\rho,\theta,z\right) = \frac{Q_0}{\left(2\pi\right)^2 i} \int_{-\infty}^{\infty} dkk I\left(k,\rho,z\right) \left\{ \boldsymbol{\Sigma} - \boldsymbol{L}\left(k\right) \left[\boldsymbol{\Sigma}_s + \boldsymbol{\chi}\left(\boldsymbol{\nu\Sigma}_f\right)^T \right] \right\}^{-1} \boldsymbol{L}\left(k\right)\boldsymbol{Q} \tag{4a}$$

where:

$$I\left(k,\rho,z\right) \equiv \int_0^{\infty} d\omega \frac{\omega}{\sqrt{\omega^2-k^2}} e^{-|z|\sqrt{\omega^2-k^2}} J_0\left(\omega R\right) J_0\left(\omega\rho\right) \tag{4b}$$

To see that Eqs. (4) are consistent, we can shrink the ring source to a point by letting $R \to 0$ to obtain [using Eq. (2)]:

$$I\left(k,\rho,z\right) \to \frac{e^{ikr}}{r}, \;\; r \equiv \sqrt{\rho^2 + z^2}$$

Equation (4a) therefore becomes the point kernel, Eq. (4.1.14).

By reformulation of Eq. (3) as a contour integral and analytically continuing into the complex plane, one can obtain additional information concerning the asymptotic behavior of the solution. In particular, the following asymptotic form emerges from the poles of the Fourier transform:

$$\phi\left(\rho,\theta,z\right) \cong \frac{Q_0}{2\pi l} \sum_{j=1}^{J} \frac{adj\boldsymbol{W}\left(k_j\right)}{\frac{d}{dk}\left|\boldsymbol{W}\left(k\right)\right|_{k_j}} \boldsymbol{L}\left(k_j\right) \int_{\theta_0}^{\theta_l} d\theta' \left[\rho_s\left(\theta'\right)^2 + \left(\frac{d\rho_s\left(\theta'\right)}{d\theta'}\right)^2\right]^{1/2} \frac{e^{-\left|\boldsymbol{r}-\boldsymbol{r}'\right|/\nu_j}}{\left|\boldsymbol{r}-\boldsymbol{r}'\right|} \boldsymbol{Q} \tag{5}$$

where:

$$\boldsymbol{W}\left(k\right) \equiv \boldsymbol{\Sigma} - \boldsymbol{L}\left(k\right)\left[\boldsymbol{\Sigma}_s + \boldsymbol{\chi}\left(\boldsymbol{\nu\Sigma}_f\right)^T\right]$$

with:

$$\left|\boldsymbol{W}\left(k_j\right)\right| \equiv \det\left[\boldsymbol{W}\left(k_j\right)\right] = 0$$

$$k_j \equiv \frac{i}{\nu_j}$$

and *adj* signifies adjugate. Unfortunately, we cannot pursue the numerical implementation of this analytical representation here, though rich with possibility.

(e) Numerical implementation for Benchmark 5.2

We could numerically evaluate the analytical expression given by Eq. (5); however, this would be a Herculean effort that would indeed stretch today's computational resources. Instead, we use conventional quadrature to evaluate Eq. (1).

The evaluation of the integral in Eq. (1) requires two numerical procedures. The first is the evaluation of the point kernel for which the numerical Fourier transform inversion is most appropriate (see Benchmark 4.1). The second is the evaluation of the integral in Eq. (1) itself. For this, we choose a Gauss-Legendre quadrature scheme of order *Lm*:

$$\phi\left(\rho,\theta,z\right) \cong \frac{Q_0}{l} \sum_{m=1}^{Lm} \omega_m \left[\rho_s\left(\theta_m\right)^2 + \left(\frac{d\rho_s\left(\theta_m\right)}{d\theta_m}\right)^2\right]^{1/2} \phi_{pt}\left(\left|\boldsymbol{r}-\boldsymbol{r}'\left(\theta_m\right)\right|\right) \tag{6}$$

In general, this evaluation requires many point kernel evaluations to arrive at benchmark accuracy and therefore considerable CPU time. An iterative interpolation scheme, as will now be described, greatly reduces the computational effort. The initial step is to determine the maximum and minimum distances, $R_{max} \equiv max|\boldsymbol{r}-\boldsymbol{r}'_m|$ and $R_{min} \equiv min|\boldsymbol{r}-\boldsymbol{r}'_m|$, from any point on the source to any detector (edit point) at (ρ,θ,z). We do this for all detectors in a plane a distance z above the source plane where the flux edit points of interest are, as shown in Figure 5.2.2,. Next, we numerically evaluate the point kernel, given by Eq. (4.1.14), at N_{int} nodes (distances) in the interval $[R_{min}, R_{max}]$. A rational interpolation [2] then gives the point kernel at any required quadrature point $|\boldsymbol{r}-\boldsymbol{r}'_m|$. In this way, we avoid recalculating the point kernel for all quadrature points at each edit. Finally, with N_{int} set to $N_{int}+2$, we recalculate the desired fluxes as the last step in the iteration. On comparison of successive interpolation iterates, convergence occurs when all fluxes at the edit points change less than a prescribed amount. We refer to this procedure as “iterative interpolation”.

(i) Calibration: a circular source

The initial numerical example is for a circular source of radius R for which Eq. (1) becomes simply:

$$\phi(\rho,\theta,z) = R\int_0^{2\pi} d\theta'\phi_{pt}\left(\left|\boldsymbol{r}-\boldsymbol{r}'\right|\right) \tag{7}$$

with normalization:

$$\frac{Q_0}{2\pi R} \equiv 1$$

For the following demonstrations, we assume a homogenized seven-group 7% MOX cross sections reproduced in Table 5.2.1. The data represents a homogenized fuel pin of partial weapons-grade plutonium and is part of the MOX Fuel Assembly 3-D Extension benchmark [3] published by the OECD/NEA. The fission cross section was divided by k_{eff} = 1.14308 (multiplication factor for the assembly) to ensure that the system is subcritical, since a wire source is a fixed source in an infinite medium which necessarily must be subcritical.

Since we now are dealing with neutron transport in multidimensions, the number of choices for our numerical algorithm is considerable including:

- Gauss-Legendre quadrature order for the point kernel group flux;
- number of the interpolation nodes and their distribution;
- Gauss-Legendre quadrature order for the integration over the point flux;
- detector grid (edit) point distribution;
- distance of the detector plane from the source plane;
- wire source configuration;
- number of energy groups G.

Thus, establishing a true multidimensional benchmark becomes a considerably more difficult proposition than thus far encountered.

We place the detector plane at 0.1 *cm* above the source plane, which is sufficient to give four- or five-place accuracy for all edits considered. This requirement comes from the unavoidable poor convergence of the point kernel integration when the quadrature points are too close to the point source singularity at $|\boldsymbol{r}-\boldsymbol{r}'| = 0$.

Next, we calibrate the numerical computation for a circular source of radius 0.5 *cm* on a detector plane composed of a 25 by 25 detector array. The Gauss-Legendre quadrature order for the point kernel evaluation is 45, giving better than 10^{-7} relative error accuracy. Since we need the point kernel only at $N_{int} \times G$ nodes, its evaluation is a relatively insignificant part of the overall calculation. Thus, by requesting such high accuracy for the point kernel, we add little to the computational time. The integration over the point kernel uses a quadrature order of 36, which gives graphical accuracy. For all numerical results in this section, the source is in group 1.

Table 5.2.2 gives the variation of the maximum $L2$ error over all groups with increasing number of interpolation nodes N_{int}. We choose the nodes to be either uniformly spaced or Legendre (quadrature) abscissa shifted to the interval $[R_{min}, R_{max}]$. The Legendre nodes seem to give the best accuracy and therefore are used in all subsequent numerical evaluations. We shall use a quadrature order of 30 for the integration over the point kernel. To see the effect of the variation of quadrature order on accuracy, we successively increased the order by increments of six, from 30 to 48. As observed in the last entries of Table 5.2.2, the initial accuracy is only 10^{-4}, but decreases to a satisfying 6×10^{-6}.

Thus, the results of this sensitivity exercise confirm that iterative interpolation with quadrature refinement can indeed give benchmark quality. For completeness, Figure 5.2.3 displays the group fluxes (20 nodes/36 order quadrature) in groups 1 and 7 showing the dispersive effect of scattering to lower energies as the circular source fades away.

(ii) Demonstration: two sources

In this section, we consider two true 3-D benchmarks – the broken elliptical and spiral wire sources.

The equation of an ellipse in the (x,y) plane is:

$$\left(\frac{x}{a}\right)^2 + \left(\frac{y}{b}\right)^2 = 1$$

where a and b are the elliptical axes and $x = a\cos(\theta)$, $y = b\sin(\theta)$. The equation defining the source configuration in the plane is therefore:

$$\rho_s(\theta) = \sqrt{b^2 + \left(a^2 - b^2\right)\cos^2(\theta)}$$

giving for Eq. (1):

$$\phi(\rho,\theta,z) = \int_{\theta_0}^{\theta_1} d\theta' \rho_s(\theta') \left[1 + \left(\frac{ae\sin(\theta')\rho_s(\theta')^2}{b^2}\right)^2\right]^{1/2} \phi_{pt}\left(\left|\boldsymbol{r}-\boldsymbol{r}'\right|\right) \tag{8}$$

where e is the eccentricity $\sqrt{a^2 - b^2}/a$ for $a > b$, and the normalization is:

$$\frac{Q_0}{2\pi l} \equiv 1$$

The broken elliptical source is located in the region:

$$0 \leq \theta \leq 140^{\circ},\ 180^{\circ} \leq \theta \leq 360^{\circ}$$

which includes a 40° gap. We again use the cross sections for the 7% MOX fuel assembly.

Figure 5.2.4(a) shows the flux in all seven groups for the broken elliptical source with major and minor axes 0.5 *cm* and 0.3 *cm* respectively. The gap is clearly visible in the top groups, but vanishes by group 4 from scattering to the lower groups. Since this is an entirely analytical calculation, we can zoom in on the flux in the gap as shown for groups 1 and 4 in Figure 5.2.4(b). This is a novel feature of an analytical representation since we can view any segment of the detector plane without determining the flux distribution over the entire plane.

The final display is for a spiral line source in a plane whose equation is simply:

$$\rho_s(\theta) = R\theta$$

giving for Eq. (1) with normalization:

$$\phi(\rho,\theta,z) = R\int_{\theta_0}^{\theta_1} d\theta' \sqrt{1+\theta'^2}\,\phi_{pt}\left(\left|\mathbf{r}-\mathbf{r}'\right|\right) \tag{9}$$

Figure 5.2.5 shows the flux from a spiral source with R = 0.25 *cm* in the first three groups of the MOX infinite lattice. We doubled the quadrature order to 72 and increased the number of edit points to 50 by 50 in the detector plane to have adequate graphical coverage. The spiral source calculation presented here represents one of the most sophisticated and accurate evaluations of a 3-D solution to the transport equation to date. The results are graphically accurate, but can be made more so if desired as indicated in the next section.

(iii) Qualification

We now qualify the 3-D elliptical broken source benchmark. Table 5.2.3 gives the fluxes in groups 1 and 7 at a selected number of detectors in a plane a distance 0.1 *cm* above the source plane. Through experimentation, the values are accurate to all places quoted with N_{int} = 20 and for quadrature order 36 for the integration over the point kernel. It is both surprising and indeed satisfying that the interative interpolation scheme is so effective.

Table 5.2.1. MOX cross sections

7% MOX homogenized macroscopic cross sections

g	Σ	Σ_a	Σ_c	Σ_f	ν	χ
1	1.81323E-01	9.06570E-03	8.11240E-04	8.25446E-03	2.88498E+00	5.87910E-01
2	3.34368E-01	4.29670E-03	2.97105E-03	1.32565E-03	2.91079E+00	4.11760E-01
3	4.93785E-01	3.28810E-02	2.44594E-02	8.42156E-03	2.86574E+00	3.39060E-04
4	5.91216E-01	1.22030E-01	8.91570E-02	3.28730E-02	2.87063E+00	1.17610E-07
5	4.74198E-01	1.82980E-01	1.67016E-01	1.59636E-02	2.86714E+00	0.00000E+00
6	8.33601E-01	5.68460E-01	2.44666E-01	3.23794E-01	2.86658E+00	0.00000E+00
7	8.53603E-01	5.85210E-01	2.22407E-01	3.62803E-01	2.87539E+00	0.00000E+00

Scattering transfer cross sections $\Sigma_{gg'}$

g'/g	1	2	3	4	5	6	7
1	1.30457E-01	4.17920E-02	8.51050E-06	5.13290E-09	0.00000E+00	0.00000E+00	0.00000E+00
2	0.00000E+00	3.28428E-01	1.64360E-03	2.20170E-09	0.00000E+00	0.00000E+00	0.00000E+00
3	0.00000E+00	0.00000E+00	4.58371E-01	2.53310E-03	0.00000E+00	0.00000E+00	0.00000E+00
4	0.00000E+00	0.00000E+00	0.00000E+00	4.63709E-01	5.47660E-03	0.00000E+00	0.00000E+00
5	0.00000E+00	0.00000E+00	0.00000E+00	1.76190E-04	2.82313E-01	8.72890E-03	9.00160E-09
6	0.00000E+00	0.00000E+00	0.00000E+00	0.00000E+00	2.27600E-03	2.49751E-01	1.31140E-02
7	0.00000E+00	0.00000E+00	0.00000E+00	0.00000E+00	0.00000E+00	8.86450E-03	2.59529E-01

Table 5.2.2. Convergence of flux with number of interpolation nodes

Lmt	N_{int}	*L2* (*leg*)	*L2* (*uniform*)
30	10	–	–
30	15	1.6e-05	2.3e-06
30	20	1.6e-05	2.2e-06
30	25	2.3e-06	3.2e-07
30	30	9.4e-06	3.7e-07
30	35	9.4e-06	5.0e-05
30	40	3.5e-06	5.0e-05
30	45	3.4e-06	4.0e-06
30	50	1.7e-06	4.0e-06
36	50	1.2e-04	
42	50	2.8e-05	
48	50	6.2e-06	

Table 5.2.3. Qualification of broken elliptical source

x	*y*	*g* = 1	*g* = 7
-6.0000E-01	-6.0000E-01	2.9683E-01	1.6601E-05
-6.0000E-01	-2.0000E-01	1.0413E+00	3.0567E-05
-6.0000E-01	2.0000E-01	4.9178E-01	2.2450E-05
-6.0000E-01	6.0000E-01	2.2745E-01	1.4310E-05
-2.0000E-01	-6.0000E-01	5.7765E-01	2.5123E-05
-2.0000E-01	-2.0000E-01	2.1538E+00	5.0513E-05
-2.0000E-01	2.0000E-01	1.8298E+00	4.4944E-05
-2.0000E-01	6.0000E-01	5.0932E-01	2.2886E-05
2.0000E-01	-6.0000E-01	5.9223E-01	2.5816E-05
2.0000E-01	-2.0000E-01	2.2423E+00	5.3270E-05
2.0000E-01	2.0000E-01	2.2271E+00	5.2696E-05
2.0000E-01	6.0000E-01	5.7540E-01	2.5037E-05
6.0000E-01	-6.0000E-01	3.2467E-01	1.8009E-05
6.0000E-01	-2.0000E-01	1.2223E+00	3.5837E-05
6.0000E-01	2.0000E-01	1.2199E+00	3.5701E-05
6.0000E-01	6.0000E-01	3.2025E-01	1.7737E-05

REFERENCES

[1] Magnus, W., F. Oberhettinger, *Functions of Mathematical Physics*, Springer-Verlag OHG, Berlin (1947).

[2] Press, W., *et al.*, *Numerical Recipes*, Cambridge University Press, NY (1986).

[3] *Benchmark on Deterministic Transport Calculations Without Spatial Homogenisation*, OECD/NEA, No. 5420 (2005).

Figure 5.2.1. Finite wire source configuration in a plane

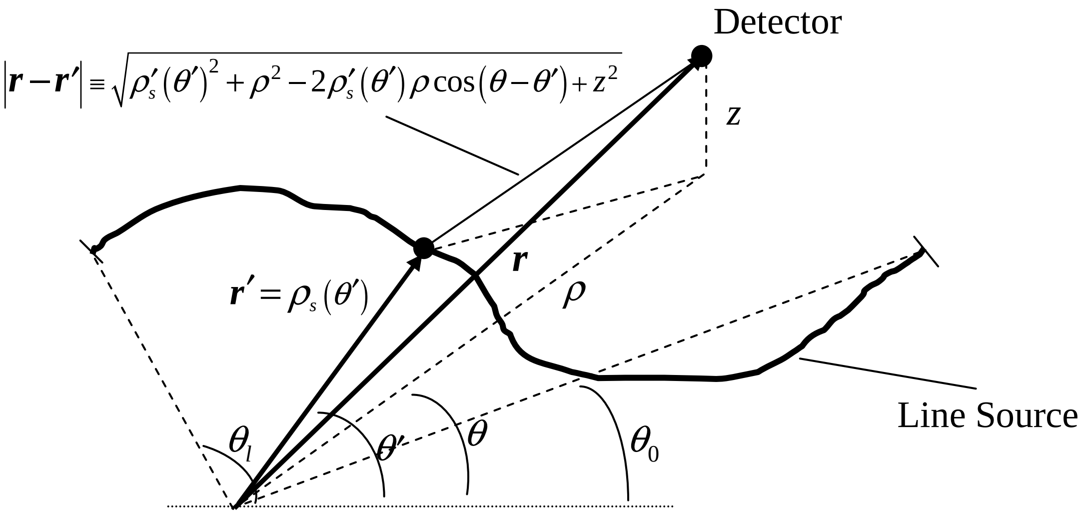

Figure 5.2.2. Source/detector plane

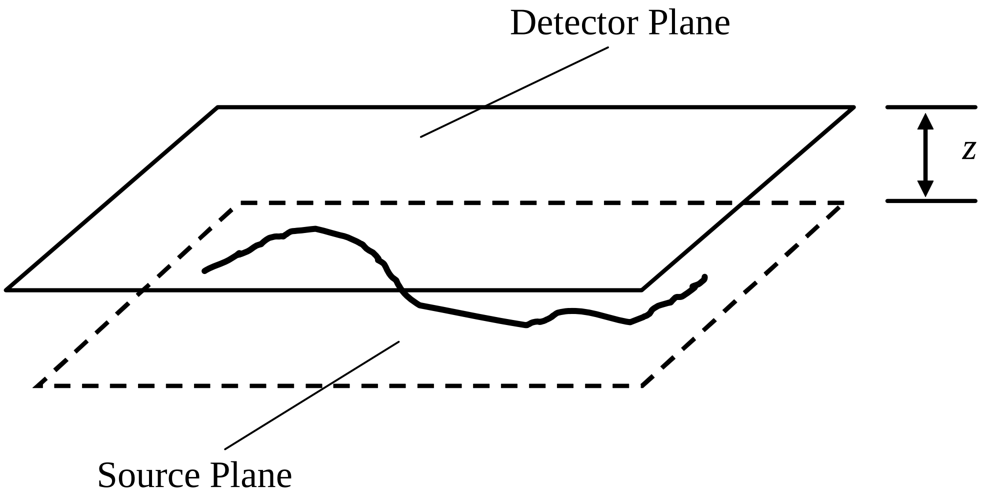

Figure 5.2.3. Fluxes in groups 1 and 7 from a circular source

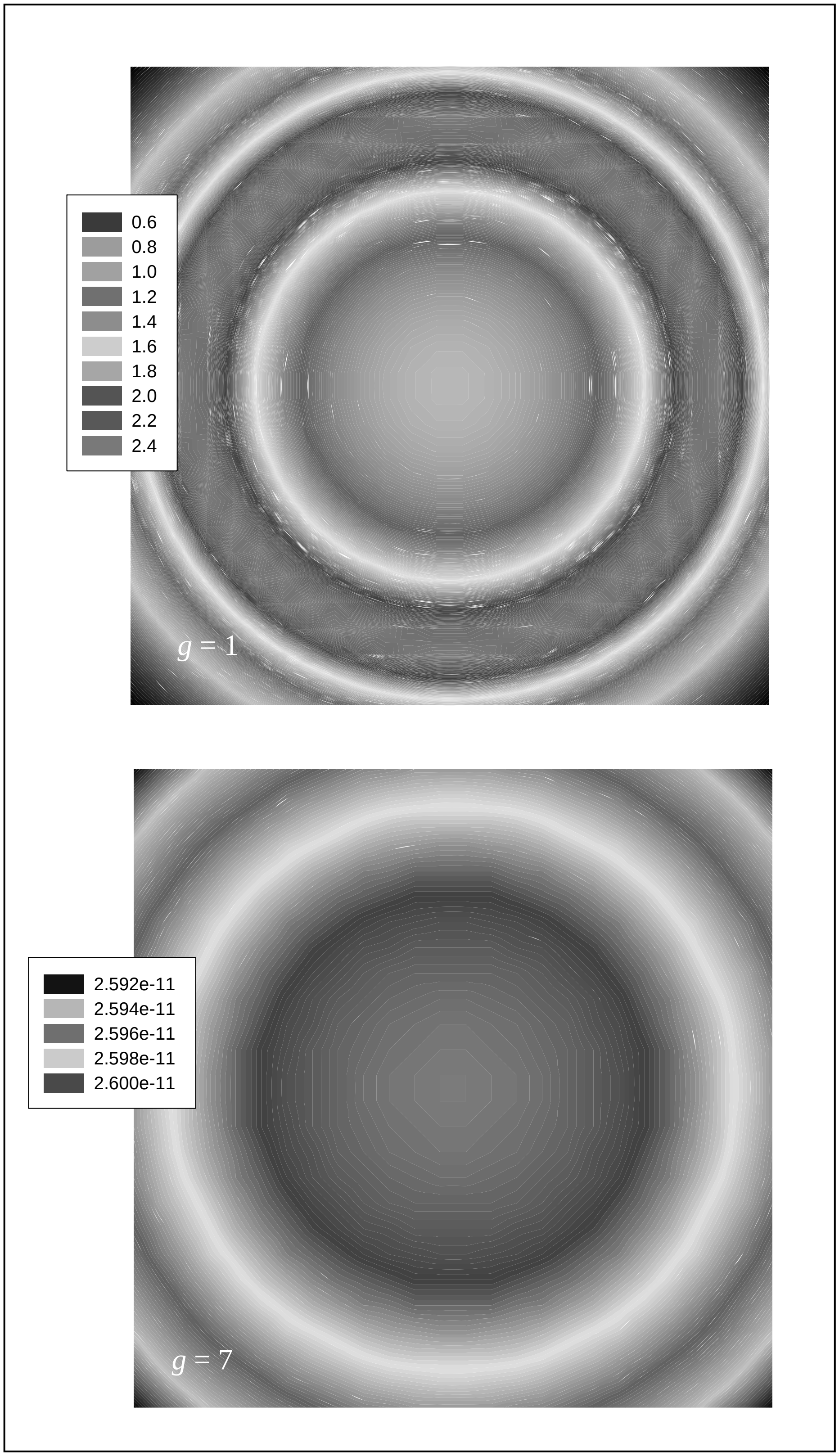

Figure 5.2.4(a). Group flux for a broken elliptical source

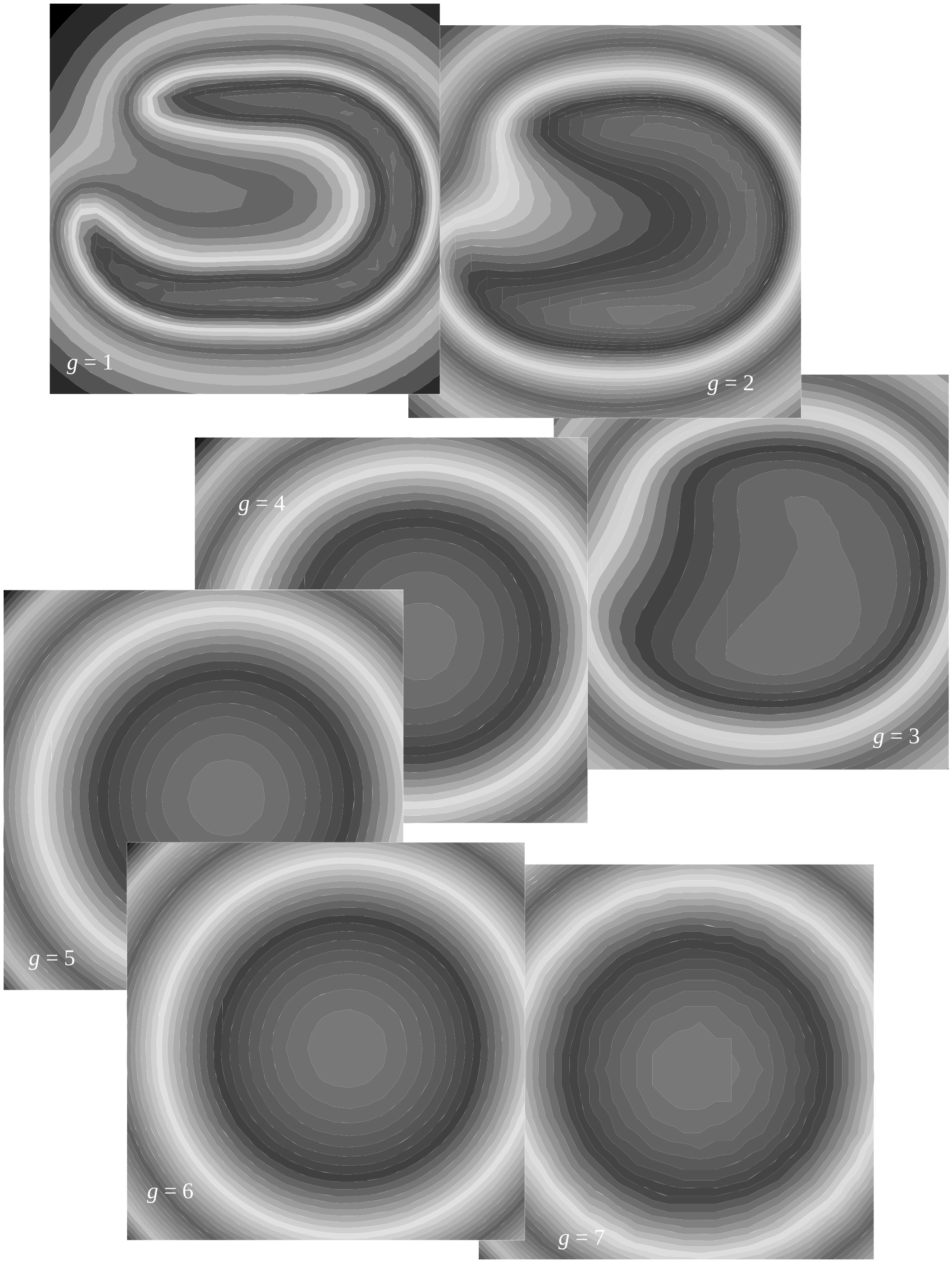

Figure 5.2.4(b). In the gap of a broken elliptical source for groups *g* = 1 and 4

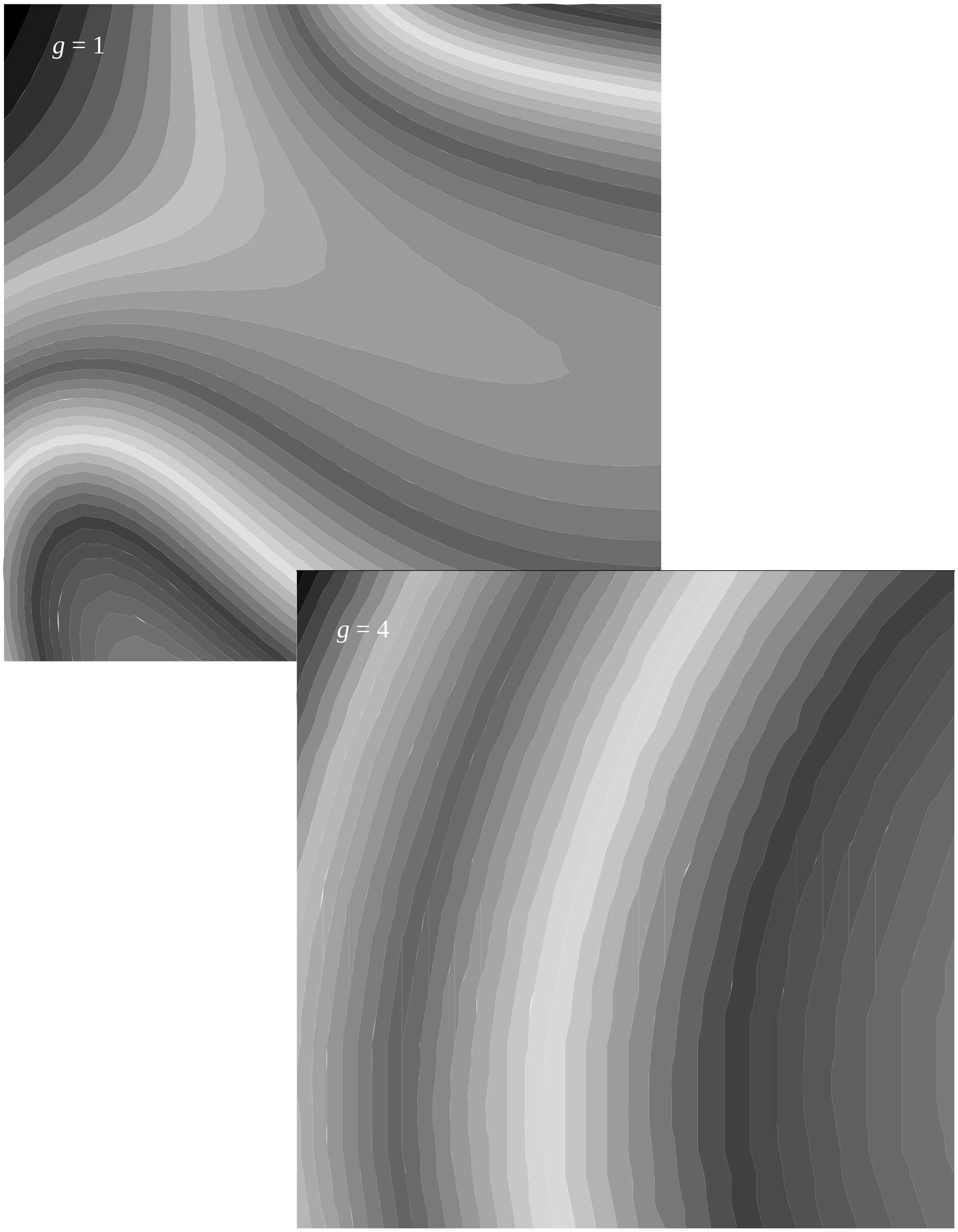

Figure 5.2.5. Flux in groups 1, 2 and 3 for a spiral wire source

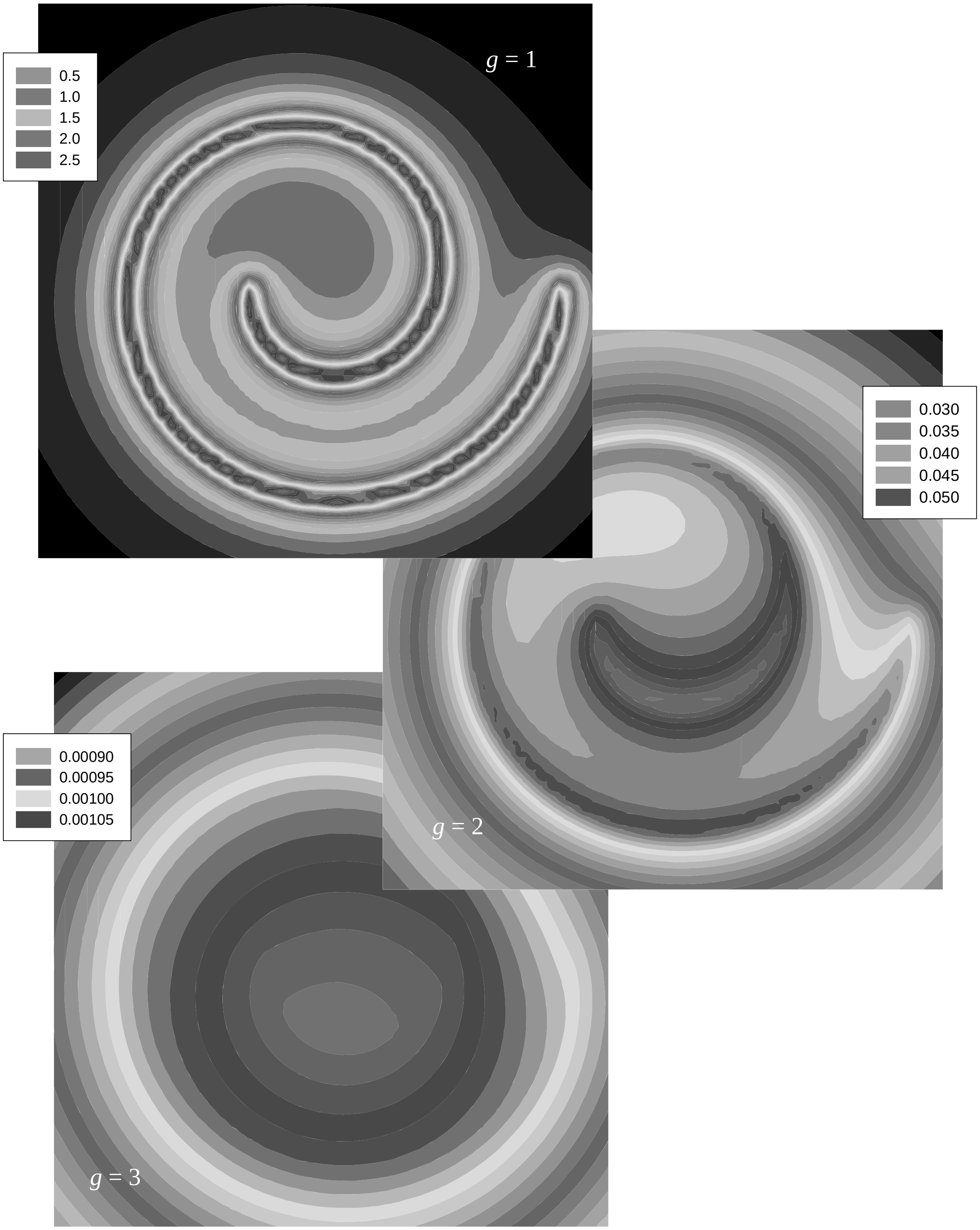

EPILOGUE

While completing this anthology on analytical benchmarks in neutron transport theory, I could not help but see how I could improve each and every one. For a start, the computer programs could be re-written in FORTRAN 90, C++ or even MATLAB^{TM}, and would represent an enormous improvement of the numerical presentation. Formatting the benchmark book in a GUI would also be very helpful and aid in the classroom presentation and its use as a reference. The next task would be to update all numerical methods to the more efficient ones we use today. For example, the current numerical Fourier transform inversion uses Talbot's algorithm [1], which immeasurably streamlines infinite media and SLP evaluations. A new Laplace transform is under development employing this method and should provide more efficient slowing down evaluations as well. Convergence acceleration has proven to be an effective way to "mine" for higher accuracy from less accurate solutions and should be included as part of any discretization scheme. Indeed, it is now possible to benchmark "in place" where the discretization itself gives benchmark quality [2]. Finally, I have found new analytical expressions, such as mentioned in the last benchmark and by solving the pseudo transport equation, which could generate even more comprehensive benchmarks.

While this case study is only a beginning, it nonetheless represents what one can accomplish with a little analytical perseverance. If someone had told me twenty years ago that I would be doing 3-D multigroup benchmarks (simple as they are), I would not have believed them. The strides we have made in today's analytical benchmarking indicate what we can do in the future. I have laid the groundwork and it is now up to the young, more energetic transport theorists to carry on to the next level. They must address such issues as:

- How far can we push the methods presented here and how can we improve them?
- How does parallel computing figure into extending analytical benchmarking?
- How do we intimately integrate analytical benchmarks into transport methods development to promote a "benchmarking culture"?

I see the last two questions as the future of analytical benchmarking – and I hope to live long enough to see them addressed.

REFERENCES

[1] Talbot, A., "The Accurate Numerical Inversion of Laplace Transforms", *J. Inst. Math. Appl.*, 23, 97-120 (1979).

[2] Ganapol, B.D., "Mining the Multigroup Discrete Ordinates Algorithm for High Quality Solution", *ANS M&C Topical*, Avignon, France (1999).

Appendix A

NUMERICAL METHODS

We briefly describe some of the numerical methods used to evaluate the benchmarks in this appendix.

A.1 Euler-Knopp (*EK*) acceleration

The Euler-Knopp acceleration, also known as the Euler transformation, is an accelerator to convergence of alternating series of the form:

$$S=\sum_{k=0}^{\infty}\left(-1\right)^{k}a_{k} \tag{A.1.1}$$

To derive an alternative form for an alternating series, which is usually more quickly convergent, we note the definition of the shift operator *E*:

$$Ea_{k-1}\equiv a_{k} \tag{A.1.2}$$

which implies:

$$a_{k}=E^{k}a_{0} \tag{A.1.3}$$

By introducing Eq. (A.1.3) into Eq. (A.1.1), we formally obtain:

$$S=\sum_{k=0}^{\infty}\left(-1\right)^{k}E^{k}a_{0}=\frac{1}{1+E}a_{0} \tag{A.1.4}$$

One adds and subtracts the acceleration parameter p_e in the denominator:

$$S=\frac{1}{1+p_{e}-\left(p_{e}-E\right)}a_{0}=\frac{1}{1+p_{e}-\frac{p_{e}-E}{1+p_{e}}}a_{0} \tag{A.1.5}$$

which when redeployed as an infinite series becomes the following alternative expression for Eq. (A.1.1):

$$S=\frac{1}{1+p_{e}}\sum_{k=0}^{\infty}\left(-1\right)^{k}\frac{1}{\left(1+p_{e}\right)^{k}}\sum_{j=0}^{k}\left(-1\right)^{j}\frac{k!\,p_{e}^{j}}{j!\left(k-j\right)!}a_{k-j} \tag{A.1.6}$$

This series is likely to converge more quickly than the original depending on the value of p_e.

A.2 Wynn-epsilon (*We*) acceleration

The *We* acceleration is a strongly non-linear sequence accelerator that can exhibit spectacular acceleration for some sequences and has been described as the most elegant of all convergence acceleration methods [1].

Consider the power series:

$$f(z) = \sum_{i=0}^{\infty} c_i z^i \tag{A.2.1}$$

The Pádé approximant for this series is [2]:

$$f(z) = \sum_{i=0}^{\infty} c_i z^i = [L/M]_f(z) + O\left(z^{L+M+1}\right) \tag{A.2.2a}$$

with the notation:

$$[L/M]_f(z) \equiv \frac{\sum_{i=0}^{L} a_i z^i}{\sum_{i=0}^{M} b_i z^i} \tag{A.2.2b}$$

From Eq. (A.2.2a), we formally have in the limit:

$$f(z) = \lim_{L\to\infty} [L/M]_f(z) \tag{A.2.3}$$

Now consider the sequence:

$$S_0, S_1, \ldots, S_i, \ldots. \tag{A.2.4a}$$

with the limit:

$$S \equiv \lim_{i\to\infty}\left(S_i\right) \tag{A.2.4b}$$

If:

$$\begin{aligned} c_0 &\equiv S_0 \\ c_{i+1} &\equiv \Delta S_i = S_{i+1} - S_i \end{aligned}$$

then:

$$S = \lim_{L\to\infty} [L/M]_f(1) \tag{A.2.5}$$

We construct the *We* algorithm from:

$$\begin{aligned}
&\varepsilon_{-1}^{(j)} \equiv 0 \\
&\varepsilon_{0}^{(j)} \equiv S_j \\
&\varepsilon_{k+1}^{(j)} = \varepsilon_{k-1}^{(j+1)} + \left[\varepsilon_{k}^{(j+1)} - \varepsilon_{k}^{(j)}\right]^{-1}
\end{aligned} \tag{A.2.6}$$

The elements $\varepsilon_k^{(j)}$ form a tableau, where the even *k*-columns approximate the sequence limit. One can show that:

$$\varepsilon_{2k}^{(j)} \equiv \left[(k+j)/k\right]_f (1) \tag{A.2.7}$$

therefore for all *j*:

$$S = \lim_{k\to\infty}\left[(k+j)/k\right]_f (1) = \lim_{k\to\infty}\left(\varepsilon_{2k}^{(j)}\right) = \lim_{k\to\infty}\left(\varepsilon_{2k}^{(0)}\right) \tag{A.2.8}$$

Thus, only the even columns are relevant to the acceleration. Interrogation of the tableau for convergence is along the diagonal $\varepsilon_{2k}^{(2k-i)},\ i = 0, 2, ..., 2k$.

A.3 Romberg integration

We now turn to the numerical evaluation of the integral:

$$I \equiv \int_{x_i}^{x_{i+1}} dx f\left(x\right) \tag{A.3.1}$$

on the interval:

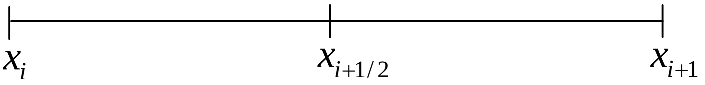

where:

$$h \equiv x_{i+1} - x_i \tag{A.3.2}$$

If one forms the Taylor series for an infinitely differentiable function about the interval center $x_{i+1/2}$:

$$f\left(x\right) = \sum_{n=0}^{\infty} \frac{f_{i+1/2}^{(n)}}{n!}\left(x - x_{i+1/2}\right)^n \tag{A.3.3}$$

the integral, on substitution into Eq. (A.3.1), is:

$$I = hf_{i+1/2} + \sum_{k=1}^{\infty} \frac{f_{i+1/2}^{(2k)}}{2^{2k}\left(2k+1\right)!} h^{2k} \tag{A.3.4}$$

Since:

$$f_i = \sum_{n=0}^{\infty} \frac{\left(-1\right)^n f_{i+1/2}^{(n)}}{2^n n!} h^n$$

$$f_{i+1} = \sum_{n=0}^{\infty} \frac{f_{i+1/2}^{(n)}}{2^n n!} h^n$$

we obtain:

$$hf_{i+1/2} = \frac{h}{2}\left[f_i + f_{i+1}\right] - \sum_{k=1}^{\infty} \frac{f_{i+1/2}^{(2k)}}{2^{2k}\left(2k\right)!} h^{2k+1} \tag{A.3.5}$$

When we introduced this expression into Eq. (A.3.4), there results:

$$I = \frac{h}{2}\left[f_i + f_{i+1}\right] + \sum_{k=1}^{\infty} \alpha_{1k} h^{2k+1} \tag{A.3.6}$$

where the first term in Eq. (A.3.6) is the single panel trapezoidal rule approximation:

$$T_1\left(h\right) \equiv \frac{h}{2}\left[f_i + f_{i+1}\right] \tag{A.3.7}$$

Halving the interval gives for Eq. (A.3.6):

$$I = T_1(h/2) + \frac{\alpha_{11}}{2^3} h^3 + \sum_{k=2}^{\infty} \alpha_{1k} \frac{h^{2k+1}}{2^{2k+1}} \tag{A.3.8}$$

which, when combined with Eq. (A.3.6) to eliminate α_{11}, gives a new quadrature rule $T_2(h)$ and its error:

$$I = T_2(h) + \sum_{k=2}^{\infty} \alpha_{2k} h^{2k+1} \tag{A.3.9a}$$

where:

$$T_2(h) \equiv \frac{2^3 T_1(h/2) - T_1(h)}{2^3 - 1} \tag{A.3.9b}$$

By continually halving the integral, one can show that:

$$I = T_{j+1}(h) + \frac{\alpha_{j+1,1}}{2^{2j+3}} h^{2j+3} + \sum_{k=j+2}^{\infty} \alpha_{j+1,k} \frac{h^{2k+1}}{2^{2k+1}} \tag{A.3.10a}$$

and we define Romberg algorithm as:

$$T_{j+1}(h) \equiv \frac{2^{2j+1} T_j(h/2) - T_j(h)}{2^{2j+1} - 1} \tag{A.3.10b}$$

The Romberg integration rule is of order $2j+1$ and exactly integrates polynomials of degree $2j-1$.

A.4 Gauss-Legendre quadrature (*GLQ*)

The *GLQ* is the workhorse of the benchmark evaluations. For a given effort, it is one of the most efficient quadratures with respect to accuracy.

Let us investigate the following integral [3]:

$$I_c \equiv \frac{1}{2\pi i}\int_C d\omega \frac{P_n(x)}{P_n(\omega)(\omega - x)} f(\omega) \tag{A.4.1}$$

where $P_n(x)$ is the n^{th}-order Legendre polynomial. On analytical continuation into the complex plane, we find:

$$\begin{aligned} f(x) &= \\ &= \sum_{k=1}^{n} f(x_k)\left[\frac{P_n(x)}{P_n'(x_k)(x - x_k)}\right] + \frac{1}{2\pi i}\int_C d\omega \frac{P_n(x)}{P_n(\omega)(\omega - x)} f(\omega) \end{aligned} \tag{A.4.2}$$

where x_k is found from $P_n(x_k) = 0$, $k=1,2,\ldots,n$. Now integrating to form:

$$I = \int_{-1}^{1} dx f(x) \tag{A.4.3}$$

gives:

$$I = \sum_{k=1}^{n} \omega_k f_k + E_n(f) \tag{A.4.4a}$$

with:

$$\omega_k \equiv -2\frac{Q_n(x_k)}{P_n'(x_k)} = \frac{2}{(1 - x_k^2)\left[P_n'(x_k)\right]^2} \tag{A.4.4b}$$

and error term:

$$E_n(f) \equiv -\frac{1}{i\pi}\int_C d\omega \frac{Q_n(\omega)}{P_n(\omega)} f(\omega) \tag{A.4.4c}$$

We render the error term in its familiar form by assuming f has K+1 derivatives in the following Taylor series representation:

$$f(\omega) = \sum_{k=0}^{K} \frac{f^{(k)}(0)}{k!}\omega^k + \frac{\omega^{K+1}}{(K+1)!} f^{(K+1)}(\xi) \tag{A.4.5}$$

with $|\xi| \le 1$. Since [3]:

$$\frac{Q_n(\omega)}{P_n(\omega)} = -\frac{c_n}{2\omega^{2n+1}}\left[1+O\left(\omega^{-2}\right)\right],\ c_n \equiv \frac{2^{2n+1}(n!)^4}{(2n+1)\left[(2n)!\right]^2}$$

on the circular contour of radius *R*, where $\omega = Re^{i\theta}$, we find for Eq. (A.4.4c):

$$E_n(f) = \frac{c_n}{\pi}\sum_{k=0}^{K}\frac{f^{(k)}(0)}{k!}R^{k-2n}\int_0^{2\pi} d\theta e^{i(k-2n)\theta}\left[1+O\left(R^{-2}e^{-2i\theta}\right)\right] + + \frac{c_n}{\pi}\frac{R^{K+1-2n}f^{(K+1)}(\xi)}{(K+1)!}\int_0^{2\pi} d\theta e^{i(K+1-2n)\theta} \tag{A.4.6}$$

If $R\to\infty$, then for $K = 2n–1$:

$$E_n(f) = \frac{2c_n}{(2n)!}f^{(2n)}(\xi) \tag{A.4.7}$$

which is the common form for the error associated with Gauss quadrature.

Finally, the integral over the interval $[a,b]$:

$$I(a,b) = \int_a^b dyf(y)$$

transformed to the interval $[-1,1]$ is obtained with transformation:

$$x = \frac{2y-a-b}{b-a}$$

to give:

$$I(a,b) = \frac{b-a}{2}\int_{-1}^{1} dxf(y(x))$$

REFERENCES

[1] Borneman, F., A. Laurie, S. Wagen, J. Waldvogel, *The SIAM 100-digit Challenge*, SIAM, Philadelphia, PA (2004).

[2] Baker, G., P. Graves-Morris, *Padé Approximants*, Cambridge University Press, NY (1996).

[3] Davis, P.J., P. Rabinowitz, *Methods of Numerical Integration*, Academic Press, MA (1984).

Appendix B

NUMERICAL TRANSFORM INVERSIONS

B.1 The numerical Laplace transform inversion

From a casual scan of the applied mathematics literature [1,2], one finds various methods for numerical inversion of Laplace and Fourier transforms. Inversion algorithms, based on a wide variety of numerical algorithms include:

- limit of an equivalence class of functions;
- expansion in terms of exponentials;
- Gauss quadrature;
- expansion in orthogonal polynomials;
- Fourier series representations;
- Pádé approximants.

The primary reason for so many approaches is that any purely numerical inversion is ill-conditioned in the sense that a small numerical error in the transform amplifies the error in the inverse. Each of the methods referred to has a particular way (choice of a parameter) to address this difficulty. In addition, each method is usually best suited to a class of functions relating to a specific application. With the increased efficiency of today's computational platforms, it is now possible to introduce numerical procedures into inversion schemes that were too costly just a few years ago.

The numerical procedure used in the evaluation of Laplace transform solutions to the transport equation begins with the Fourier cosine integral representation of the inversion integral [1,2]:

$$f\left(u\right)=\frac{2e^{\gamma u}}{\pi u}\int_0^\infty du\,\mathrm{Re}\,\overline{f}\left(\gamma+i\omega/u\right)\cos\left(\omega\right) \tag{B.1.1}$$

with:

$$\overline{f}\left(p\right)=\int_0^\infty due^{-pu}f\left(u\right)$$

where γ is the coordinate on the real axis of the Bromwich contour chosen to be greater than the largest real part of any singularity (γ_s) of the image function $\overline{f}\left(p\right)$. We can reformulate the above representation as an infinite series by decomposing the integral over the half periods of the cosine:

$$f\left(u\right)=\frac{2e^{\gamma u}}{\pi u}\left[\begin{array}{l}\int\limits_{0}^{\pi/2}du\,\mathrm{Re}\,\overline{f}\left(\gamma+i\omega/u\right)\cos\left(\omega\right)+\\+\sum\limits_{k=1}^{\infty}\left(-1\right)^{k}\int\limits_{-\pi/2}^{\pi/2}du\,\mathrm{Re}\,\overline{f}\left(\gamma+i\left(\omega+k\pi\right)/u\right)\cos\left(\omega\right)\end{array}\right] \tag{B.1.2}$$

Hurwitz and Zweifel [3] seem to have been the first to suggest the numerical evaluation of the inversion integral via series and their subsequent acceleration toward convergence. Thus, for the evaluation of the series in Eq. (B.1.2), we can introduce an acceleration procedure to reduce the number of terms required in the summation. A modified Euler-Knopp (*EK*) acceleration scheme (see Appendix A.1) is effective in this regard. The *EK* transformation replaces the convergent series:

$$S=\sum_{k=0}^{\infty}\left(-1\right)^{k}a_{k} \tag{B.1.3a}$$

by the equivalent series:

$$S=\frac{1}{1+p_{e}}\sum_{k=0}^{\infty}\left(-1\right)^{k}\frac{1}{\left(1+p_{e}\right)^{k}}\sum_{j=0}^{k}\left(-1\right)^{j}\frac{k!\,p_{e}^{j}}{j!\left(k-j\right)!}a_{k-j} \tag{B.1.3b}$$

where the user chooses the acceleration parameter p_e. Note that for $p_e = 0$, we recover the original series; while, for $p_e = 1$, we find the classical Euler-Knopp transformation. The van Wijngaarden modification [4] enhances the *EK* transformation by choosing between adding the original term of the series or an accelerated term depending on which gives the least error. Accelerations of series convergence are an essential part of the numerical inversion procedure and are considered an enabling feature.

As with any method of numerical inversion, the proper choice of the Bromwich contour defined by γ is crucial for an efficient inversion. To help guide this choice, let us estimate the theoretical dependence of the error associated with truncation of the series representation for $f(u)$ [Eq. (B.1.2)]. Thus, for truncation at K_0, we have:

$$f\left(u\right)=\frac{2e^{\gamma u}}{\pi u}\left[\begin{array}{l}\int\limits_{0}^{\pi/2}du\,\mathrm{Re}\,\overline{f}\left(\gamma+i\omega/u\right)\cos\left(\omega\right)+\\+\sum\limits_{k=1}^{K_0}\int\limits_{-\left(2k-1\right)\pi/2}^{\left(2k+1\right)\pi/2}du\,\mathrm{Re}\,\overline{f}\left(\gamma+i\omega/u\right)\cos\left(\omega\right)+E_{L}\left(u\right)\end{array}\right] \tag{B.1.4a}$$

where the truncation error is:

$$E_{L}\left(u\right)\equiv\int\limits_{T_L}^{\infty}du\,\mathrm{Re}\,\overline{f}\left(\gamma+i\omega/u\right)\cos\left(\omega\right) \tag{B.1.4b}$$

with:

$$T_L \equiv \left(2K_0 + 1\right)\frac{\pi}{2}$$

For a smooth function, $f(u)$, where $u^{-\alpha+1}$ $f(u)$ is analytic for $\alpha > 0$, the asymptotic form for the image function $\bar{f}(p)$ is:

$$\bar{f}(p) \approx \frac{1}{p^{\alpha}}\sum_{n=0}^{N}\frac{\beta_n}{p^n} \tag{B.1.5}$$

Then, substituting Eq. (B.1.5) into the error term given by Eq. (B.1.4b) yields:

$$E_L = \sum_{n=0}^{N}\beta_n u^{(n+\alpha)} I_n(\gamma u) \tag{B.1.6a}$$

where:

$$I_n(\gamma u) \equiv \frac{1}{(\gamma u)^{n+\alpha+1}}\int_{T_L/\gamma u}^{\infty} du' \frac{\cos\left(\left[n+\alpha\right]\tan^{-1}(u')\right)}{\left(1-u'^{-2}\right)^{(n+\alpha)/2}}\cos(\gamma u u') \tag{B.1.6b}$$

From this expression, we conclude that the error depends on the product of γ and u. E_L, in general, should decrease with increasing T_L. With this result taken as a guide, we choose the appropriate contour γ such that:

$$\gamma = \bar{\gamma} + a/u \tag{B.1.7}$$

where a and $\bar{\gamma}$ are specified by the user with $\bar{\gamma}$ greater than γ_s for $T_L/\gamma u$ sufficiently large. The specification of a u^{-1} variation for γ is reasonable when one considers that from the Tauberian theorems [5] for u small, $f(u)$ comes primarily from large $|p|$ (large γ) and, for u large, from small $|p|$ (small γ).

There is one particular feature of the proposed inversion algorithm that distinguishes it from all others. Theoretically, the actual Bromwich contour is immaterial as long as $\gamma \geq \gamma_s$. Numerically, however, from experience, the choice of the contour can be the determining factor in an evaluation. For this reason, we incorporate a contour iteration. One obtains the inverse for the following N successive contours approaching γ_s:

$$\begin{aligned} &\gamma_0 = \gamma,\ \gamma \geq \gamma_s \\ &\gamma_j = \left(\gamma_s + \gamma_{j-1}\right)/2; \quad j = 1,\ldots,N \end{aligned} \tag{B.1.8}$$

At each contour, one samples the dimensionless derivative:

$$\left|\frac{f(u;\gamma_j) - f(u;\gamma_{j-1})}{f(u;\gamma_j)}\right| \left|\frac{\gamma_j - \gamma_{j-1}}{\gamma_j}\right| \tag{B.1.9}$$

in order to determine if it is less than a specified tolerance ε_γ. Theoretically, of course, the numerator of this expression should vanish. The denominator is included to guard against false convergence, i.e., when $f(u;\gamma_j)$ and $f(u;\gamma_{j-1})$ are within the specified tolerance by virtue of the proximity of γ_{j-1} and γ_j.

The primary reason for including the contour iteration is to provide confidence in the result, because, if we do not have (contour) convergence, then most probably the numerical inversion is inaccurate. If, however, the contour iteration converges without any other error indications, we can be relatively confident in the result. The addition of the contour iteration increases the required computational time but is well worth the expense to avoid inaccuracy.

We can perform an assessment of the above algorithm by comparison to several other algorithms representative of the various inversion methods referred to earlier [2]. In Table B.1.1, we compare the measure of accuracy:

$$L_x \equiv \left\{ \sum_{k=1}^{30} \left[f\left(k/2\right) - f_a\left(k/2\right) \right] / 30 \right\}^{1/2} \tag{B.1.10}$$

for various numerical inversions and image functions. f_a is the analytical inversion. The present algorithm certainly provides acceptable practical accuracies in comparison to the other methods. In general, it seems to do better for discontinuities while giving reasonable accuracy for all other functions tested.

Table B.1.1. Comparison to other Laplace transform inversion algorithms

$\bar{f}(p)$	$f_a(t)$	**Gauss quadrature**	**Expansion in Laguerre polynomials**	**Fourier series**	**Present algorithm**
$\dfrac{e^{1/p}}{\sqrt{p}}$	$\dfrac{\cos\left(2\sqrt{t}\right)}{\sqrt{\pi t}}$	2.1×10^{-6}	1.7×10^{-17}	4.3×10^{-10}	9.5×10^{-7}
$\dfrac{1}{p^2+1}$	$\sin t$	3.0×10^{-7}	9.4×10^{-16}	2.6×10^{-11}	2.4×10^{-7}
$p^{-1} \ln p$	$-\gamma^* - \ln t$	7.0×10^{-5}	9.9×10^{-3}	1.7×10^{-10}	3.6×10^{-6}
$\dfrac{e^{5p}}{p}$	$\Theta\left(t-5\right)$	8.4×10^{-1}	2.1	2.1	1.2×10^{-3}
$\dfrac{i}{2}\ln\left[\dfrac{p-1}{p+1}\right]$	$\dfrac{\sin t}{t}$	2.7×10^{-2}	3.3×10^{-11}	4.4×10^{-9}	1.8×10^{-8}
$e^{-4\sqrt{p}}$	$\dfrac{2e^{-4/t}}{\sqrt{\pi t^3}}$	2.7×10^{-7}	1.0×10^{-5}	1.8×10^{-11}	4.8×10^{-9}

[*] Euler's Constant $\gamma = 0.57721566\ldots$.

B.2 The numerical Fourier transform inversion

We treat the numerical Fourier transform inversion similarly to the Laplace transform inversion. The Fourier transform and its inversion are:

$$\begin{aligned}\phi(k) &\equiv \int_{-\infty}^{\infty} dx e^{-ikx} f(x) \\ f(x) &\equiv \frac{1}{2\pi}\int_{-\infty}^{\infty} dk e^{ikx}\phi(k)\end{aligned} \tag{B.2.1}$$

In some sense, the Fourier transform is a more straightforward evaluation than the Laplace transform since it is restricted to the real axis and therefore requires less numerical parameter choices. The inversion, when written as:

$$f(x) \equiv \frac{1}{\pi}\int_{0}^{\infty} dk \left\{\mathrm{Re}\left[\phi(k)\right]\cos(kx) - \mathrm{Im}\left[\phi(k)\right]\sin(kx)\right\} \tag{B.2.2a}$$

becomes on decomposition over the periods of sine and cosine:

$$f(x) \equiv \frac{1}{\pi x}\sum_{j=0}^{\infty}(-1)^j \int_{0}^{\pi} du \left\{\begin{array}{l}\mathrm{Re}\left[\phi\left(\dfrac{u+j\pi}{x}\right)\right]\cos(u) - \\ -\,\mathrm{Im}\left[\phi\left(\dfrac{u+j\pi}{x}\right)\right]\sin(u)\end{array}\right\} \tag{B.2.2b}$$

The task we now face is the efficient evaluation of an infinite series.

We evaluate the integral in each term in the series either through Romberg integration (Appendix A.3) or Gauss quadrature (Appendix A.4) schemes. The Romberg scheme is iterative in that the result comes from sequentially higher order integration schemes. The advantage of the Romberg integration scheme is that each order builds upon the last by using all the previous function evaluations. The disadvantage is that it requires a doubling of the number of function evaluations at each subsequent order. Benchmarks 3.1 and 4.1, use this scheme. The more recent benchmarks include an iterative Gauss-Legendre quadrature integration scheme rather than a Romberg scheme. This is simply a Gauss quadrature shifted to the interval $[0,\pi]$ with the order increased by one until convergence. We trade the advantage of utilizing previous function values for faster convergence.

We treat series convergence in several different ways. Benchmarks 3.1 and 4.1 use the previously described Euler-Knopp (*EK*) convergence acceleration described in Appendix A.1. Benchmarks 4.2 and 5.2 use the more sophisticated Wynn-epsilon (*We*) convergence acceleration described in Appendix A.2.

We now discuss several special implementations. When $x \leq 0.1$, we treat the first interval of the series in Eq. (2.2b) separately. In particular, the first integral in the series is:

$$I_0(x) \equiv \frac{1}{\pi}\int_{0}^{\pi/x} dk \left\{\mathrm{Re}\left[\phi(k)\right]\cos(kx) - \mathrm{Im}\left[\phi(k)\right]\sin(kx)\right\} \tag{B.2.3}$$

and is further partitioned and evaluated through an iterative Gauss quadrature to give the desired accuracy.

Finally, we consider the case $x = 0$ separately through the change of variable:

$$t = \frac{k-1}{k+1}$$

to give:

$$f(0) \equiv \frac{1}{\pi} \int_{-1}^{1} dt \frac{1}{(1-t)^2} \phi\left(\frac{1+t}{1-t}\right) \tag{B.2.4}$$

We evaluate this integral through a Gauss quadrature by ignoring the singularity.

The examples of Table B.2.1 demonstrate the effectiveness of the above inversion. Nine known integrals provide the test basis for the numerical inversion. The numerical inversions give at least nine digits of accuracy. Except for integral I_5, all inversions require a reasonable number of function evaluations. From the excellent agreement of the test cases with the analytical inversions, we are encouraged that the inversion is working properly and effective.

Table B.2.1. Numerical Fourier test inversions

n	**Test integral I_n**	**Fourier inversion integral**	**No. of function evaluations**
1	$\int_0^\infty dx \frac{x}{1+x^2} \sin(x)$	$-i\pi \int_{-\infty}^{\infty} dk e^{ikx} \frac{k}{1+k^2};\ x=1$	486
2	$\int_\pi^\infty dx \frac{\sin(x)}{x^2}$	$i\pi \int_{-\infty}^{\infty} dk e^{ikx} \frac{\mathrm{sgn}(k)}{(\lvert k\rvert+\pi)^2};\ x=1$	396
3	$\int_0^\infty dx \frac{\sin(x)}{x} e^{-x/2}$	$-i\pi \int_{-\infty}^{\infty} dk e^{ikx} \frac{e^{-\lvert k\rvert/2}}{k};x=1$	264
4	$\int_0^\infty dx \,\mathrm{sech}(2x)\cos(4x)$	$2\pi \int_{-\infty}^{\infty} dk e^{ikx} \frac{e^{-2\lvert k\rvert}}{1+e^{-4\lvert k\rvert}};\ x=4$	190
5	$\int_0^\infty dx \frac{\sin(x)}{x^{0.1}}$	$-i\pi \int_{-\infty}^{\infty} dk e^{ikx} \frac{\mathrm{sgn}(k)}{\lvert k\rvert^{0.1}};\ x=1$	5466
6	$\frac{1}{2}\int_0^\infty dx x^{1/2} \sin(100x)$	$-\frac{i\pi}{2x^{3/2}} \int_{-\infty}^{\infty} dk e^{ikx} \sqrt{\lvert k\rvert};\ x=1$	1520
7	$\int_0^\infty dx \frac{\cos(x)}{(x^2+4)}$	$\int_{-\infty}^{\infty} dk e^{ikx} \frac{\pi}{(k^2+4)};\ x=1$	524
8	$\int_{-\infty}^{\infty} dx \frac{2+x}{(2+2x+x^2)} \cos(x)$	$\pi \int_{-\infty}^{\infty} dk e^{ikx} \left[\frac{2+k}{(2+2k+k^2)} + \frac{2-k}{(2-2k+k^2)}\right];x = 1$	660
9	$\int_0^\infty dx e^{-(x+1/x)} \frac{\sin(10x)}{\sqrt{x}}$	$-i\pi \int_{-\infty}^{\infty} dx e^{ikx} \frac{e^{-(\lvert k\rvert+1/\lvert k\rvert)}}{\sqrt{\lvert k\rvert}} \mathrm{sgn}(k);\ x=10$	510

REFERENCES

[1] Davis, B., *Integral Transforms and Their Applications*, Springer-Verlag, NY (1984).

[2] Davis, B., B. Martin, “Numerical Inversion of the Laplace Transform; A Survey and Comparison of Methods”, *J. Comp. Phys.*, **1**, 33 (1979).

[3] Hurwitz, H., P. Zweifel, *M.A.T.C.*, **10**, 170 (1956).

[4] Press, W., *et al*., *Numerical Recipes*, Cambridge University Press, NY (1986).

[5] Borwein, D., “Tauberian Theorems Concerning Laplace Transforms and Dirichlet Series”, *Archiv der Mathematik*, **53**, # 4, 352-362 (1989).

Appendix C

DERIVATION OF A CLOSED FORM EXPRESSION FOR $\bar{Q}_{sl}\left(p\right)$

From the standard representation of the Legendre polynomial in terms of monomials, we have:

$$P_l\left(\mu_s\right) = \frac{1}{2^l}\sum_{m=0}^{[l/2]} C_{lm}\mu_s^{l-2m} \tag{C.1a}$$

where:

$$C_{lm} \equiv \left(-1\right)^m \binom{l}{m}\binom{2l-2m}{l} \tag{C.1b}$$

[*l*/2] indicates the greatest integer contained in *l*/2 and $\binom{}{}$ is the binomial coefficient. Then from Eq. (2.2.9b) and using the binomial theorem for a non-negative integer *r*:

$$\mu_s^r\left(\omega\right) = \left[\alpha_+ e^{-\omega/2} - \alpha_- e^{\omega/2}\right]^r = \sum_{m=0}^{r} b_{mr}\alpha_+^{r-m}\alpha_-^m e^{\left(m-r/2\right)\omega} \tag{C.2}$$

with:

$$\alpha_+ \equiv \frac{A+1}{2},\ \ \alpha_- \equiv \frac{A-1}{2}$$

$$b_{mr} \equiv \left(-1\right)^m \binom{r}{m}$$

When we introduce Eq. (C.2) into Eq. (C.1a) and subsequently Eq. (C.1a) into Eq. (2.2.13c), after integration over the exponentials, we obtain Eq. (2.2.13d) when summed over all scattering species.

Appendix D

PROGRAM INPUT DESCRIPTIONS

Benchmark 2.1: Infinite medium slowing down/the Laplace transform solution

Descriptive title

Neutron slowing down in an infinite medium without spatial dependence and with constant cross sections.

Physical description

Neutrons slow down through elastic scattering with nuclei to thermal energies in an infinite medium. We obtain an analytical representation for the collision density of the slowing down equation in an infinite medium including multiple species and assuming constant cross sections.

```
c sdim.dat
c input*********************************************************
c
c If input parameter is not used enter either 0 for fixed
c point or 0.0 for floating point entries unless line is
c not read.
c
c line 0  case identifier
c
c line 1  ic      number of isotopes (<=30)
c         ifs   1 include fission
c              -1 no fission
c         iplt  1 write plot file (file o3.dat:user to specify
c                 an appropiate format
c              -1 do not write plot file
c
c note:repeat line 2 for each scattering species (ic times)
c line 2  aa   scattering species atomic mass number
c         an   atom density (units of e-24)
c         sis  microscopic scattering cross section (barns)
c         sia  microscopic absorption cross section (barns)
c         vf   volume fraction
c
c note:enter line 3 if ifs .eq. 1
c line 3  anu  number of neutrons/fission
c         anf  atom density of fissionable isotope (units of e-24)
c         sif  microscopic fission cross section (barns)
c         vff  volume fraction of fissionable isotope
c note:if fission included, fission spectrum is a delta function
c         at u=0
```

```
c
c line 4  is   0 delta function source in lethargy (at u=0)
c              1 uniformly distributed source over the lethargy
c                range [0,s1] normalized to 1
c         s0   source strength
c         s1   extent of uniform source (for is=1)
c
c line 5  lj   maximum number of terms in inversion
c              series (150)
c         lg   number of bromwich contour iterations (5)
c         err  relative truncation error for inversion series
c              (err=1.0e-03 for 3-digit accuracy)
c         xp   density not calculated below 10**(-xp) (8)
c         ct   c.gt.ct use collective determination
c                      to find f(u)
c              c.le.ct use multiple collision formulation
c                      to find f(u) (0.1)
c
c line 6  gt  parameter to control inversion contour (1.0)
c         gs0 contour nearest singularity of f(p) (0.0)
c             (initial contour gs0+gt/u)
c
c line 7  ia    1 call for analytical solution (for ic=1,img=0)
c              -1 do not call for analytical solution
c         irel  1 edit collision density
c              -1 edit relative error (for ic=1,img=0)
c
c line 8  lq      number of lethargy intervals in smallest collision
c                 interval (lq+1 edit points for each of the nq
c                 intervals)
c         nq      number of collision intervals adjacent to u0
c                 where lq applies
c         lu      number of lethargy edit grid in [u0+nq*q,ul]
c         irdu  0 use input on this line for lethargy grid (but
c                 must enter ul on line 9)
c               1 read in lethargy grid endpoints (line 9)
c         img   0 pointwise density edit
c               1 numerical (exact) multigroup density edit
c               2 do both img=0,1
c note:lu+nq*lq must be less than 500 if irdu .eq. 0 or
c      lu must be less than 500 if irdu .eq. 1
c
c line 9  u0   initial lethargy (u0 .ge. 1.0e-03)
c         ul   last lethargy
c         du   lethargy interval
c
c line 10 nor  -1 normalize  collision density to integral
c                 over [0,ul]
c               1 do not normalize
c
c***************************************************************
c
c file assignments**********************************************
c     file 20  input               (file:sdim.dat)
c     file 21  output              (file:o1.dat)
c     file 22  diagnostic messages (file:o2.dat)
c     file 23  plot file           (file:o3.dat)
```

```
c*************************************************************
c
c diagnostic messages
c  error 1   Romberg integration did not converge for term j,
c            at lethargy u and contour ga. Estimated error also
c            given.
c  error 2   Inversion series did not converge at lethargy u and
c            contour ga. Estimated error also given.
c  error 3   Contour iteration did not converge at lethargy u.
c            estimated error also given.
c  error 4   Significance of multigroup density may be less than
c            desired.
c*************************************************************
```

Benchmark 2.2: Slowing down/the Laplace transform solution in the B_L approximation

Descriptive title

Stationary neutron slowing down in an infinite medium with non-zero buckling in the continuous lethargy B_L approximation with constant cross sections.

Physical description

Neutrons slow down through elastic scattering with nuclei to thermal energies in an infinite medium. We obtain an analytical representation for the moments of the collision density of the slowing down equation in the B_L approximation with constant cross sections and multiple species scattering.

```
c sdiml.dat
c input*******************************************************
c
c If input parameter is not used enter either 0 for fixed
c point or 0.0 for floating point entries unless line is
c not read
c
c line 0  case identifier
c
c line 1  ic      number of isotopes (<30)
c         ifs   1 include fission
c              -1 no fission
c         b       geometrical buclkling
c         lm      number of moments desired (lm <= 3)
c         iplt  1 write plot file (file 23:user to specify
c                 an appropiate format)
c              -1 do not write plot file
c
c note:repeat line 2 for each scattering species (ic times)
c line 2  aa   scattering species atomic mass number
c         an   atom density (units of e-24)
c         sis  microscopic scattering cross section (barns)
c         sia  microscopic absorption cross section (barns)
c         vf   volume fraction
c
```

```
c note:enter line 3 if ifs .eq. 1
c line 3  anu  number of neutrons/fission
c         anf  atom density of fissionable isotope (units of e-24)
c         sif  microscopic fission cross section (barns)
c         vff  volume fraction of fissionable isotope
c note:if fission included, fission spectrum is a delta function
c      at u=0
c
c line 4  is   0 delta function source in lethargy
c              1 uniformly distributed source over the lethargy
c                range [0,s1] normalized to 1
c         s0     source strength
c         s1     extent of uniform source (for is=1)
c
c line 5  lj   maximum number of terms in inversion
c              series (75)
c         lg   number of Bromwich contour iterations (5)
c         err  relative truncation error for inversion series
c              (err=1.0e-03 for 3-digit accuracy)
c
c line 6  gt   parameter to control inversion contour (1.0)
c         gs0  contour nearest singularity of f(p)
c              (initial contour gs0+gt/u)
c
c line 7  lq      number of lethargy intervals in smallest collision
c                 interval (lq+1 edit points for each of the nq
c                 intervals)
c         nq      number of collision intervals adjacent to u0
c                 where lq applies
c         lu      number of lethargy edit grid in [u0+nq*q,ul]
c         irdu  0 use input on this line for lethargy grid (but
c                 must enter ul on line 8)
c               1 read in lethargy grid endpoints (line 8)
c         img   0 pointwise density edit
c               1 numerical multigroup density edit
c               2 do both img=0,1
c note:lu+nq*lq must be less than 500 if irdu. eq. 0 or
c      lu must be less than 500 if irdu .eq. 1
c
c line 8  u0  initial lethargy (u0 .le. 1.0e-03)
c         ul  last lethargy
c         du  lethargy interval
c
c line 9 nor  -1 normalize  collision density to integral of f0
c                over [0,ul]
c              1 do not normalize
c
c*****************************************************************
c
c file assignments*************************************************
c     file 20  input              (file:sdim.dat)
c     file 21  output             (file:o1.out)
c     file 22  diagnostic messages (file:o2.out)
c     file 23  plot file          (file:o3.out)
c*****************************************************************
c
c diagnostic messages:
```

```
c  error 1   Romberg integration did not converge for term j,
c            at lethargy u and contour ga. estimated error also
c            given.
c  error 2   inversion series did not converge at lethargy u and
c            contour ga. estimated error also given.
c
c  error 3   contour iteration did not converge at lethargy u.
c            estimated error also given.
c
c  error 4   significance of multigroup density may be less than
c            desired
c
c  error 5   Taylor series for small u did not converge, therefore
c            numerical inversion used
c
c****************************************************************
```

Benchmark 2.3: Slowing down/the multigroup solution in the B_L approximation

Descriptive title

Stationary neutron slowing down in an infinite medium with non-zero buckling in the multigroup B_L approximation.

Physical description

Same as for Benchmark 2.2.

a) Slowing down: fixed source

```
c sdimmg.dat
c*input file 20**********************************
c
c line 0 case identifier
c
c line 1 bb       buckling
c        lm       highest moment desired (max 5)
c        nor   -1 normalize to area under collision
c                 density
c               1 do not normalize
c        isg      number of groups in source region
c
c line 2 (sg(ig),ig=1,isg):source strength for each source
c                          group.source integral normalized
c                          to one.
c
c**************************************************************
```

a.1) Xsec generation

```
c xsecbl.dat
```

```
c input:***********************************************
c
c line 0: case identifier
c
c line 1:
c  ic      number of scattering species (max=10)
c  lq      number of lethargy edit points in [0,q] and [q,2q]
c  iqq     species number of q for first two intervals
c  lm      xsecs desired for moments (lm.le.5)
c  isf  -1 do not write source file
c        1 write source file
c
c line 2:
c  lu      number of lethargy edit points in [2q,ul]
c  ul      last lethargy point
c
c line 3:
c  isg     number of source groups
c  us      last lethargy of source region
c
c line 4:  enter the following for each of the ic
c          species
c  aa      scattering species atomic mass number
c  an      atom density (units of e-24)
c  sis     microscopic scattering cross section (barns)
c  sia     microscopic absorption cross section (barns)
c  vf      volume fraction
c
c line 5
c ifmt -1  combine format (for therm.for)
c       1  standard multigroup format (for mgim.for
c                                     and sdimmg.for)
c
c if isf .lt. 0 enter for each legendre source moment
c line 6
c  (sg(i,l),i=1,isg):source by group
c*******************************************************
c output for ifmt=-1:combine format*********************
c
c a)file 25:xo0.dat
c line 0  cross section id
c
c line 1  lgm   number of groups
c         lm    number of bl components
c         sigt  total cross section
c
c line 2 moment identifier
c
c line 3 group identifier
c
c line 4  (xss(1,ig,igp),ig=1,lgm):transfer xsec for p0 moment
c         (xss(1,ig,igp),ig=1,lgm):transfer xsec for p1 moment
c
c note:lines 3 and 4 repeated for each group and lines 2-4 repeated
c      for each moment
c
c b)file 29:xot.dat
```

```
c line 1  energy grid identifier
c
c line 2  (e(ig),de(ig),ig=lgm,1,-1):energy grid and widths
c         note:last group first
c
c line 3  total xsec identifier
c
c line 4  ((xsec(i,ig),ig=lgm,1,-1),i=1,2):absorption (i=1) and
c         scattering (i=2) cross sections
c         note:last group first
c*******************************************************
c output for ifmt=1:standard multigroup****************
c
c a)file 25:xo0.dat
c line 0  cross section id
c
c line 1  lgm   number of groups
c         lm    number of bl components
c
c line 2  lethargy grid identifier
c
c line 3  (u(i),i=1,lgm+1):lethargy points
c
c line 4  total xsec identifier
c
c line 5  (xt(ig),ig=1,lgm):tot xsecs
c
c line 6  transfer xsec identifier
c
c line 7  moment identifier
c
c line 8  group identifier
c
c line 9  (xss(ig,igp),igp=1,lgm) for ig=1,lgm:transfer xsecs
c
c note:lines 8 and 9 repeated for each group and lines 7-9 repeated
c      for each moment
c*******************************************************
c
c file 35:sum.dat
c Sums cross sections to give c for each group as a check
c*******************************************************
c
c output for isf=1*************************************
c
c file 30:xos.dat**************************************
c line 1  bo source identifier
c
c line 2  (ig,s0(ig),ig=lgm,1,-1):p0 source by group
c         note:last group source first
c
c line 3  b1 source identifier
c
c line 4  (ig,s0(ig),ig=lgm,1,-1):p1 source by group
c         note:last group source first
c
c*******************************************************
```

```
c
c*******************************************************
c file 22:scratch file
c*******************************************************
```

b) Slowing down: criticality

```
c mgcrit.dat
c input********************************************************
c line 0  Case ID
c
c line 1 nmat     number of materials
c
c line 2 u0       initial lethargy
c        ul       last lethargy
c        ng       number of groups
c        ngt      maximum inelastic group transfers
c
c line 3 bl0      initial BL
c        bl1      final BL
c
c line 4 err      desired error
c
c *************************************************************
c input files
c an1.dat     Material densities (an(im),im=1,nmat)
c             Volume fractions   (vf(im),im=1,nmat)
c abs1.dat    Cross sections (abs,fiss,sce,sci) and nu
c               (xxa(im,ig),ig=1,ng)
c               (xxf(im,ig),ig=1,ng)
c               (xse(im,ig),ig=1,ng)
c               (xsi(im,ig),ig=1,ng)
c               (ana(im,ig),ig=1,ng)
c dwns1.dat   Inelastic scatter transfer cross sections
c               (((dwns(im,igp,ig),im=1,nmat),igp=1,ng),ig=1,ng)
c               note:dwns(im,ig,ig)=0.0d0
c xo0mg.dat   Elastic scatter transfer cross sections
c xsp1.dat    fission spectrum
c               (xsp1(ig),ig=1,ng)
c
c**************************************************************
c output files
c pltxc.dat  cross section and fission spectrum output
c keff.dat   keff vs BL
c dist.dat   normalized flux (ph(0)=1.0d0) and fiss spectrum
c
c**************************************************************
```

Benchmark 2.4: Slowing down and thermalization in an infinite medium/the embedded multigroup approximation

Descriptive title

Neutrons scattering in the thermal energy region below the resonance region in an infinite medium with a non-zero buckling.

Physical description

After neutrons have been slowed down in the fast energy region (5 MeV to 10 KeV) and have survived the resonance region (1 KeV to 1 eV), they enter the thermal region (~0.0253 eV). Here, the neutrons gain and lose energy upon collision depending on the thermal motion of interacting nuclei. Usually, we neglect thermal motion of the nucleus in the fast and resonance regions but cannot at thermal energies. In the multigroup approximation, the scattering matrix becomes full since each group communicates with all other groups. Neutron spatial redistribution is significant at thermal energies; therefore, buckling is included to simulate leakage. The thermalized flux represents a fine-group weighting spectrum, which is essential in producing representative homogenized cross sections.

```
c note1:this code employs the following notation:
c
c        ig=1 is the highest energy (lethargy) group(in combine the
c        lowest energy point)
c        ig=lgm is the lowest energy (lethargy) group(in combine the
c        highest energy point)
c
c note2:when generating xsecs from xsecbl must use ifmt=-1 option
c
c therm.dat
c input file 20:therm1.dat****************************************
c
c line 0  case identifier
c
c line 1  b       geometric buckling
c         an      atomic density (units of 10**24)
c         ixgp -1 multigroup calculation
c               1 point energy calculation (for combine data)
c         nor  -1 do not normalize
c               1 normalize to total integral
c
c line 2  lg1     lower group bound of group range to be evaluated
c         lg2     upper group bound of group range to be evaluated
c
c line 3  ic   -1  read in initial conditions from files 27,28
c               1  initial condition set to zero
c         lk      number of terms in taylor series approximation (15)
c         e0      acceleration parameter for f0 derivative (0.75)
c         e1      acceleration parameter for f1 derivative (0.75)
c
c line 4  err series truncation error (1.0e-04 for 3-place accuracy)
c
c line 5  t0  initial time
c         tl  final time
c         nt  number of time intervals (le 500)
c
```

```
c line 6  iegp number of energy groups to be edited
c         (enter 0 if none desired)
c
c note:next line not entered if iegp=0
c line 7  (ng(ig),ig=1,iegp) groups to be edited (trace)
c
c note: next file can be generated by xsecbl.for with lgmt=-1
c input file 25:xo0*********************************************
c read cross sections (must be prepared for both moments p0 and p1)
c
c line 0  cross setion id
c
c line 1  lgm   number of groups
c         lmmax number of bl components on file
c         sigt  total cross section
c
c line 2  moment identifier
c
c line 3  group identifier
c
c line 4  (xss(1,ig,igp),ig=1,lgm)):transfer xsec for p0 component
c         (xss(2,ig,igp),ig=1,lgm)):transfer xsec for p1 component
c
c lines 3 and 4 repeated for each group (igp=1,lgm)
c lines 2,3 and 4 repeated for each moment (p0,p1 components)
c
c input file 29:xot*********************************************
c line 1  energy grid identifier
c
c line 2  (e(ig),de(ig),ig=lgm,1,-1):energy grid and widths
c          note:read in for last group first
c
c line 3  total xsec identifier
c
c line 4  ((xsec(i,ig),ig=lgm,1,-1),i=1,2):absorption (i=1) and
c         scattering (i=2) cross sections
c         note:read in for last group first
c
c input file 30:xos*********************************************
c line 1  b0 source identifier
c
c line 2  (ig,s0(ig),ig=lgm,1,-1):p0 source by group
c         note:read in last group source first
c
c line 3  b1 source identifier
c
c line 4  (ig,s1(ig),ig=lgm,1,-1):p1 source by group
c         note:read in last group source first
c
c input files 27,28:io0,io1*************************************
c read initial conditions for f0 and f1
c
c on file 27:
c line 1  t0   initial time relative to zero time
c
c line 2  (f0(ig),ig=1,lgm) initial condition
c
```

```
c on file 28:
c line 1  (f1(ig),ig=1,lgm) initial condition
c
c*************************************************************
c
c list of output and input files:
c     file              contents                               name
c      20      edit and numerical method input                  therm1.dat
c      21      energy,ig,f0,f1 er0,er1 by group                 o1.dat
c              where er0,er1 are the relative error
c              estimates wrt stationary solution
c      22      t,f0 for edited groups(trace not normalized)     o2.dat
c      23      t,f1 for edited groups(trace not normalized)     o3.dat
c      24      plot file                                        plotf.dat
c      27      last f0 for initial guess(restart)               io0.dat
c      28      last f1 for initial guess(restart)               io1.dat
c      29      total xsecs                                      xot.dat
c      30      source                                           xos.dat
c
c screen output
c      the beginning of each time step is indicated along with the
c      time step number (it).
c      the number of groups having converged (iu) is also given.
c      the global convergence parameter (cp) which is the sum over
c      all groups at each time is also indicated.
c
c**************************************************************
c diagnostic indicators
c        error 1:taylor series did not converge at time indicated
c                for group ig.the actual relative error is also
c                given as err.
c
c        error in arctan:error in the determination of gam(ig).
c
c**************************************************************
```

Benchmark 3.1: Monoenergetic transport in an infinite medium/the Fourier transform solution

Descriptive title

Neutron transport without energy loss in an anisotropically scattering infinite medium including space dependence.

Physical description

Neutrons, emitted at the center of a homogeneous infinite medium, are restricted to move in one linear dimension defined by a direction (cosine) as shown in Figure 3.1.1. Nuclei of sufficiently high mass scatter neutrons without energy loss and anisotropically. The solution defines the infinite medium Green's function.

```
c ogim.dat
c input*********************************************
c
c input read in free format
```

```
c
c line -1 case identifier
c
c line 0
c ncc =  number of cases
c
c line 1
c ig  =  1 plane geometry
c     =  2 spherical geometry
c     =  3 cylindrical geometry
c isp =  1 delta function source
c     =  2 spatially distributed source (dexp(-sp(1)x) for x>0)
c     =  3 uniformly distributed source(x>0)
c ian =  1 isotropic source
c     =  2 beam source
c ll  =    scattering order(ll<=3)
c jx  = -1 read in spatial grid
c     =  1 read first and last grid points and mesh spacing
c
c line 2
c q0  =    source normalization
c c   =    number of secondaries
c am0 =    incident beam direction dcosine
c
c line 3
c (wb(l),l=0,ll)=scattering coefficients
c
c if jx<0 then enter
c line 4a
c lx   =   number of spatial points to be entered
c
c line 4b
c (xx(ix),ix=1,lx)=spatial grid
c
c if jx>0 then enter
c line 4b
c x00 =    initial grid point
c xl  =    final grid point
c n0  =    number of intervals
c
c line 5
c lj  =    max number of terms in infinite series
c          representation of fourier integrals(<100)
c ien =    number of terms that meet convergence
c          criteria (3)
c ifc =  0 do not consider uncollided flux separately
c     =  1 consider uncollided flux separately
c
c line 6
c err =    relative error for fourier integral
c          evaluation (1.0e-03)
c tol =    relative error for romberg integration (err/10)
c
c line 7
c (sp(i),i=1,5)= parameters in user supplied transform
c                for source
c note:enter a line with floating point zeroes if not used
```

```
c
c note:lines 8 and 9 required for all additional cases(max=20)
c line 8
c (nn(i),in(i),i=1,6) = change fixed pt variables for next case
c                        according to input specification number nn
c                        nn   variable(in)
c                    _____________________
c                        1    ig
c                        2    ian
c                        3    ll
c                        4    lj
c                        5    ien
c                        6    ifc
c note:if no fixed point changes made enter zeroes for both nn and variable
c
c line 9
c (nn(i),an(i),i=1,6) = change floating point variables for
c                        next case according to (note: maximum of 6
c                        variables can be changed)
c
c                        nn   variable(an)
c                    _____________________
c                        1    q0
c                        2    c
c                        3    am0
c                        4    err
c                        5    tol
c                        6    wb(0)
c                        7    wb(1)
c                        8    wb(2)
c                        9    wb(3)
c                       10    wb(4)
c                       11    sp(1)
c                       12    sp(2)
c                       13    sp(3)
c                       14    sp(4)
c                       15    sp(5)
c note:if no floating point changes made enter zeroes for nn and an
c
c************************************************************
```

Benchmark 3.2: Monoenergetic transport in a semi-infinite medium/the Laplace transform solution

Descriptive title

Monoenergetic neutron transport in a homogeneous half-space with isotropic scattering – the albedo problem.

Physical description

Neutrons, uniformly entering the free surface of a homogeneous semi-infinite medium, are restricted move in one linear dimension defined by one direction (cosine) as shown in Figure 3.2.1. Nuclei of sufficiently high mass scatter neutrons without energy loss and isotropically. This is the most basic transport solution to include a boundary.

```
c semi.dat
c*******************************************************************
c input description(free format)
c
c line 0  case identifier
c
c line 1  nc        number of cases(<=20)
c         iv     -1 single and multiple cases for angle of incidence(am0)
c                 1    "    "     "       "    "  number of secondaries(c)
c
c line 2  is     -1 beam source
c                 1 isotropic source
c         q0        source normalization
c
c line 3  lj        number of terms in inversion series (<100)
c         lg        number of iterations of bromwich contour (<10)
c         lm        legendre-gauss quadrature order (<100)
c         ju     -1 specify gt for contour iteration where
c                   gs0 =-1/v0 ,gam0 =gs0+gt/x
c                 1 use supplied limits for contour iteration:
c         inor   -1 normalize to scalar flux at x=0
c                 1 no normalization
c
c line 4  err       desired relative error for inversion series truncation
c
c line 5 note:enter if ju=-1
c         gt        to determine starting contour gam0 (see line 3)
c
c line 6  x0        initial position from surface
c         xl        final       "        "
c         n         number of intervals between x0 and xl (<=50)
c
c line 7 (v(ic),ic=1,nc)
c         a) if iv>0 number of secondaries for nc cases
c         b) if is<0 and iv<0 number of incident directions for nc cases
c
c line 8 note:enter if is<0
c         a) incident direction if iv<0
c         b) number of secondaries if iv>0
c
c +   gs0 is rightmost singularity
c ++  v0 is zero of infinite medium dispersion relation
c *   gam0 is initial contour for contour iteration
c*******************************************************************
c output description
c
c   file 21:scalar flux vs position
c
c   file 22:diagnostic messages:
c        a)error0 h-function iteration did not converge
c        b)error1 search for zero of infinite medium
c                 dispersion relation did not converge
c        c)error2 x=aaaaa err=bbbbb
c           inversion series did not converge at x=aaaaa
c           with error estimate err=bbbbb
c        d)error3 j=iiiii x=aaaaa err=bbbbb
c           romberg integration did not converge ax term j
```

```
c           and x=aaaaa with error estimate err=bbbbb
c        e)error4 x=aaaaa err=bbbbb
c           contour iteration did not converge at x=aaaaa
c           with error estimate err=bbbbb
c
c******************************************************************
```

Benchmark 3.3: Monoenergetic transport in a 1-D slab/the *Fn* solution

Descriptive title

Monoenergetic neutron transport in an isotropically scattering slab (two surfaces) with vacuum boundary conditions and an impinging flux on the left surface.

Physical description

Monodirectional neutrons enter the left surface of a slab and scatter isotopically without energy loss. The slab, embedded in a vacuum, is composed of a single homogeneous region.

```
c oneslab.dat
c***************************************************************
c input description
c
c note:suggested values and limitations in parenthesis
c
c line 0   case identifier
c
c line 1   ncc   number of cases
c          lm3   gauss-legendre integration order for evaluation
c                of integrals over boundary fluxes (<ilm)
c          lit   number of boundary iterations for each slab at
c                each fn iterate (2)
c
c line 2   l1    initial n of fn approximation
c          l2    final n of fn approximation (<np)
c          l12d  increment between approximations (2)
c
c line 3   mm1   number of direction edit points (<imm1)
c          ig    -1 use g-l angular edit points (order mm1)
c                 1 specify uniform angular edit points
c
c note:if ig is 1 line 4 must be entered (a blank line is allowed)
c line 4   an0   first edit direction
c          an1   last edit direction
c
c line 5   err1  desired relative error (1.0e-04)
c
c note:enter lines 6 and 7 for each case
c line 6   am0   source direction
c          s0    intensity of boundary source
c
c line 7   wsr   single scatter albedo
c          dr    slab width
```

```
c          ibr   1 shifted legendre polynomial basis fcns (pl(2*x-1))
c                2 monomial basis fcns (x**(xar*l))
c                3 shifted monomial basis fcns ((2*(x**xar)-1)**l)
c                4 modified legendre polynomial basis fcns
c                  (pl(u),u=2*(x**xar)-1))
c          lmr   g-l quadrature order for matrix elements (<ilm)
c          xar   parameter for basis fcns when ibr is 2 - 4 (0.75)
c          s1r   exponential volume source strength
c          alp1r exponent for volume source
c          nxxr  number of edit points in slab (<npx)
c
c***************************************************************
c output files
c
c file 21 (stored as o1.dat):transmission and reflection
c      slab no. (col1) n (col2) refl. (col 3) trans. (col4)
c
c file 22 (stored as o2.dat):boundary fluxes for each slab
c      mu vs flux for mu<0 (col1) flux for mu >0 (col2)
c
c file 23 (stored as o3.dat):interior edit (nxxr points) by slab
c      mu vs flux for mu<0 (col1) flux for mu >0 (col2)
c
c screen output (also on file 26-stored as o6.dat)
c
c**************************************************************
```

Benchmark 3.4: Monoenergetic transport in a 1-D cylinder/the *Fn* solution

Descriptive title

Monoenergetic neutron transport in an isotropically scattering infinite cylinder (one surface) with vacuum boundary conditions.

Physical description

Monodirectional neutrons enter the surface of a cylinder of infinite longitudinal length and scatter isotopically and monoenergetically. The 1-D infinite cylinder is composed of a single homogeneous region.

```
c dfn.dat
c input*********************************************************
c line 1   Problem ID
c line 2   rr        Radius for fixed source
c          nr        number of edits
c          icrt   -1 criticality read in edit points
c                 -2 criticality full distribution
c                  1 fixed source
c          isrc   -1 normalize to 4pi
c                  1 normalize to 1
c If icrt .lt.0:
c line 3   ref(i),i=1,nr: reference edit points
c Note: For each case (<201) input:
c line 4   c        secandaries
```

```
c          err      error
c          lm0      starting quadrature
c          nn0      starting n of Fn
c          is00     0 call for uncollided
c                   1 do not call for uncollided
c          ich     -1 no acceleration
c                   1 acceleration
c          rr0      initial guess for radius (icrt=-1)
c Note: last case must be -1 0 0 0 0 0 0
c input*********************************************************
c output********************************************************
c file o31.dat: Flux and current profiles for fixed source
c file o33.dat: critical radii
c file o31.dat: critical flux
c output********************************************************
```

Benchmark 4.1: Multigroup transport in infinite media/the Fourier transform solution

Descriptive title

Neutrons slowing down in an infinite medium with spatial dependence in the multigroup approximation.

Physical description

Neutrons, emitted at one energy at the center of an infinite medium, slow down upon collision with stationary nuclei (no upscattering). One spatial dimension and one angle describe the neutron motion after emission. We solve the neutron transport equation in the multigroup approximation in plane and spherical geometries. Upscattering and fission are included for isotropic point source emission in the last example.

a) Fixed source

```
c mgim.dat
c input (file 20)*******************************************
c
c line 0 case identifier
c
c line 1
c ig  =  1 plane geometry
c     =  2 spherical geometry
c     =  3 cylindrical geometry
c idst=  1 delta function source in top group
c isr =  1 isotropic source
c     =  2 beam source
c ll  =    scattering order (set to 0)
c jx  = -1 read in spatial grid
c     =  1 read first and last grid points and mesh spacing
c
c line 2
c q0  =    source normalization
c am0 =    incident beam direction codsine
```

```
c
c if jx<0 then enter
c line 3a
c lx   =   number of spatial points to be entered (<lxx)
c
c line 3b
c (xx(ix),ix=1,lx)=spatial grid
c
c if jx>0 then enter
c line 3c
c x00 =    initial grid point
c xl  =    final grid point
c lx  =    number of intervals
c
c line 4
c lj  =    max number of terms in infinite series
c          representation of fourier integrals(<100)
c ien =    number of terms that meet convergence
c          criteria (3)
c ifc =  0 do not consider uncollided flux separately
c     =  1 consider uncollided flux separately
c
c line 5
c err =    relative error for fourier integral
c          evaluation (1.0e-03)
c tol =    relative error for romberg integration (err/10)
c
c line 6
c lue =    number of groups to be edited
c lxe =    number of spatial points to be edited (file o1.dat)
c
c line 7
c (neu(i),i=1,lue):groups to be edited
c
c line 8
c (nex(i),i=1,lxe):spatial points to be edited
c*********************************************************
c input (file 25)*****************************************
c
c note:file xo0.dat (can be created bt xsecbl.for with
c                    option ifmt=1)
c
c line 0   cross section id
c
c line 1
c lgm =   number of groups (<lgmx)
c i   =   not used
c sigt=   not used
c
c line 2
c identifier to indicate lethargy points to follow
c
c line 3
c (u(i),i=1,lgm+1):lethargy points
c
c line 4
c identifier to indicate total cross sections to follow
```

```
c
c line 5
c (xt(ig),ig=1,lgm):tot xsecs
c
c line 6
c identifier to indicate zeroth moment
c
c line 7
c identifier to indicate transfer cross sections to follow
c
c the following is by group:
c line 8a
c group number
c
c line 8b
c (xss(ig,igp),igp=1,lgm): transfer xsecs
c**********************************************************
c
c output
c
c file o1.dat
c   flux profile for edited groups
c
c file o2.dat
c   diagnostic information
c
c file o3.dat
c   one group summation
c
c file o6.dat
c   flux file for E (or u) vs phi for each x
c
c file o7.dat
c   flux file E (or u) vs x vs phi
c**********************************************************
```

b) Criticality

```
c mgimc.dat
c input******************************************************
c line 0  Case ID
c
c line 1  nmat     number of materials
c
c line 2  u0       initial lethargy
c         ul       last lethargy
c         ng       number of groups
c         ngt      maximum inelastic group transfers
c
c line 3  r0       initial edit point
c         rl       final edit point
c         nr       number of edit intervals
c
c line 4  err      desired error
c         mb       quadrature for Fourier transform inversion (15)
```

```
c
c line 5  (q(ig),ig=1,ng)  Source strengths
c
c line 6a lk               Number of spatial edits for spectral plot
c line 6b (ipt(k),k=1,lk)  Edit point numbers for spectral edit
c
c *************************************************************
c input files
c an1.dat     Material densities (an(im),im=1,nmat)
c             Volume fractions   (vf(im),im=1,nmat)
c abs1.dat    Cross sections (abs,fiss,sce,sci) and nu
c               (xxa(im,ig),ig=1,ng)
c               (xxf(im,ig),ig=1,ng)
c               (xse(im,ig),ig=1,ng)
c               (xsi(im,ig),ig=1,ng)
c               (ana(im,ig),ig=1,ng)
c dwns1.dat   Inelastic scatter transfer cross sections
c               (((dwns(im,igp,ig),im=1,nmat),igp=1,ng),ig=1,ng)
c               note:dwns(im,ig,ig)=0.0d0
c xo0mg.dat   Elastic scatter transfer cross sections
c xsp1.dat    fission spectrum
c               (xsp1(ig),ig=1,ng)
c
c**************************************************************
c output files
c  o1.dat     Mixed macroscopic x-secs
c  plt1.dat   Spatial edit plot by group
c  plt2.dat   Group edit by position
c**************************************************************
```

Benchmark 4.2: Multigroup slab transport/the Green's function method

Descriptive title

Neutrons slowing down in a homogeneous slab medium with spatial dependence in the multigroup approximation.

Physical description

Neutrons of one energy impinging on the surface of a homogeneous slab medium undergo energy loss and gain through scattering. One spatial dimension and one direction describe the neutron motion. We solve the transport equation in the multigroup approximation by the Green's function method (GFM/MG) also called the boundary source method.

```
c gfmmg.dat
c Input*******************************************
c line 0     ID
c
c line 1     mb      Quadrature order for GF
c            err     Desired error
c
c line 2     lm      For integral eqn solutio
c            lm1     Angular edit
```

```
c line 3     am0     Beams inclination
c            cz      Number of secondaries (for random xsecs)
c************************************************
c***Problem input***(xsecgfm.dat)*********************
c line 0     ID
c
c line 1     ng       number of groups
c            jmg     -3 Fast reactor example
c                    -2 Siewert bencchmark
c                    -1 Random xses
c                     1 Read in xsesc
c line 2     ar       Slab thickness
c************************************************
c***Cross section input***************************
c jmg=-3
c input files
c an1.dat     Material densities (an(im),im=1,nmat)
c             Volume fractions   (vf(im),im=1,nmat)
c abs1.dat    Cross sections (abs,fiss,sce,sci) and nu
c               (xxa(im,ig),ig=1,ng)
c               (xxf(im,ig),ig=1,ng)
c               (xse(im,ig),ig=1,ng)
c               (xsi(im,ig),ig=1,ng)
c               (ana(im,ig),ig=1,ng)
c dwns1.dat   Inelastic scatter transfer cross sections
c               (((dwns(im,igp,ig),im=1,nmat),igp=1,ng),ig=1,ng)
c               note:dwns(im,ig,ig)=0.0d0
c xo0mg.dat   Elastic scatter transfer cross sections
c xsp1.dat    fission spectrum
c               (xsp1(ig),ig=1,ng)
c-----------------------------
c jmg=-2   Set in program
c-----------------------------
c jmg=-1   Use cz input above
c-----------------------------
c jmg= 1 From file xsecgfm.dat
c Block 1      (sigt(ig),ig=1,ng)
c Block 2      (sigf(ig),ig=1,ng)
c Block 3      (chi(ig),ig=1,ng)
c Block 4      (anu(ig),ig=1,ng)
c Block 5      ((sigs1(ig,igp),igp=1,ng),ig=1,ng)
c-----------------------------
c************************************************
c**************************************************************
c Output:
c      o1.dat: gf
c      o2.dat: Ref&Trn
c      o3.dat: avg error
c      o4.dat: exiting angular
c      o5.dat: faux angular edit
c      o6.dat: summed exiting angular over gps
c      if jmg.eq.-3: o8.dat for table error comparison
c**************************************************************
```

Benchmark 5.1: Monoenergetic transport in a two-dimensional semi-infinite medium/the searchlight problem (SLP)

Descriptive title

Two-dimensional neutron transport in an isotropically scattering medium with no energy loss upon collision commonly called the searchlight problem, referring to a beam of neutrons illuminating a point on the surface of a semi-infinite medium.

Physical description

Neutrons, tracked in the longitude (z) and the plane radial (ρ) dimensions, impinge at a point on the surface of a semi-infinite homogeneous medium. We assume the nuclei scattering centers to be of sufficiently high mass to scatter neutrons without energy loss. All scattering directions after collision are equally probable (isotropic scattering).

```
***** slp.dat
****************************************************************
***** input description slp.for
****  line 0  case identifier

***** line 1 lm Legendre-Gauss quadrature order (<100)
*****
***** line 2 c      number of secondaries
*****        is = 1 source at rho=0.0
*****             2 ring source at rho=a1
*****             3 gaussian source: s=2(a1^2)exp(-(a1*rho)^2)
*****             4 disc source:     s=2/a1^2 for rho.lt.a1
*****                                s=0.0    for rho.gt.a1
*****        ifc =0 evaluate scalar flux only at z=0
*****             1 evaluate flux and current at z=0
*****        ibi =1 isotropic source
*****             2 normal beam source
*****        iin =1 flux normalized to 1 at z=0 (beam or iso)
*****             2 current normalized to 1 at z=0 (isotropic)
*****        iplt= -1 r few z plot
*****               1 z few r plot
*****
***** line 3 err  relative error for series truncation
*****        lj   maximum number of terms in inversion series
*****        lg   number of contour iterations
*****        nm   legendre-gauss order for small r integrals
*****
***** line 4 gami starting contour
*****        gsi  contour near singularity
*****
***** line 5 r0   initial radial edit point
*****        rl   final radial edit point
*****        nr   number or radial edit points
*****
***** line 6 x0   initial axial edit point
*****        xl   final axial edit point
*****        nx   number of axial edit points
*****
```

```
***** line 7 a1   parameter for distributed sources
*****************************************************************
c output
c****file o1.dat
c      flux or current output (r,z,flux or current,no of terms in fb
c                              series inversion)
c
c****file o2.dat
c      diagnostic information
*****************************************************************
```

Benchmark 5.2: Multigroup transport in a three-dimensional infinite medium/the point kernel method

Descriptive title

Multigroup, multi-dimensional neutron transport in an isotropically scattering/fissioning infinite medium from an isotropically emitting wire source configured in a plane.

Physical description

Neutrons diffuse from a wire source into an isotropically scattering/fissioning infinite medium. Neutrons, emitted isotropically, gain or lose energy through scattering and appear through fission. We assume the multigroup approximation.

```
c mgimpkm.dat
c input*******************************************************
c line 0  Case ID
c
c line 1  jmg             -3    MOX benchmark
c                         -2    artificial x-sesc
c                         -1    Random x-secs
c         ng                    number of groups (<=20)
c         isrc             1    circular source
c                          2    elliptical source
c                          3    spiral source
c         ie                    number of gps to be edited
c                                <0 then ie = ng
c
c line 2  err                   desired error
c         mb                    quadrature for Fourier transform inversion
(15)
c         idff            -1    Output rel error between current
calculation and
c                               that on o51.dat
c
c line 3  (q(ig),ig=1,ng)       Source strengths by group
c
c line 4  (ige(i),i=1,ie)       Groups to be edited (edit all groups if
ie<0)
c
c line 5  cz                    Secondaries when jmg = -2
c
```

```
c line 6  nx                       Spatial edit points on a side in detector
plane
c         xl                       Detector (square) plane dimension
c         z0                       Distance detector plane is from source
plane
c
c line 7  nint                     Number of interpolation points
c         lmt                      Quadrature for point kernel integration
c
c line 8  rs0                      Radius of circle and spiral
c         a0                       Elliptical axis 1
c         b0                       Elliptical axis 2
c         th1                      -----
c         th2                      Source in angular intervals [0,th1],
[th2,2pi] for
c                                  isrc = 1 or 2
c         ne                       Number of turns of spiral source
c
c line 10 xr0                      x-position of detector plane
c         yr0                      y-position of detector plane
c
c line 11 ssa0                     Absorption coefficient for artificial x-
secs
c         ga                       Absorption factor
c         gs                       Scattering factor
c
c line 12 im                  1    full edit
c                            -1    line/gp edit
c***************************************************************
c input files:
c  mox.dat: MOX data
c
c***************************************************************
c output files:
c  plt1.dat   Group flux at interpolation points
c  o5.dat     Group fluxes
c  o7.dat:benchmark table
c  if(im.lt.0)   o8.dat:line/gp contour
c  if(idff.lt.0) o6.dat:relative error between current calculation and
c                        that on o51.dat
c***************************************************************
```

INDEX

AUTHOR BIOGRAPHICAL SKETCH

Barry D. Ganapol is currently Professor in the Department of Aerospace and Mechanical Engineering (AME) at the University of Arizona and a Research Professor in the Department of Nuclear Engineering at the University of Tennessee. He received his PhD from the University of California, Berkeley in 1971 followed by two years at the Swiss Federal Institute for Reactor Research and one year at the Center for Nuclear Studies at Saclay in France. After three years at Argonne National Laboratory, he joined the Department of Nuclear Engineering (NE) faculty at the University of Arizona in 1976. Professor Ganapol has served as Chair of the NE Department and Acting and Associate Chair of the AME Department. His research interests include developing analytical and numerical methods to solve the neutron Boltzmann equation in the pursuit of high quality benchmark solutions. This activity has lead to his broader interest of verification and validation strategies applied to modeling and simulation of nuclear systems. In addition to his nuclear interests, Professor Ganapol has investigated the health of vegetation canopies from first principles of radiative transfer with application to satellite remote sensing. During his 30-year career, Professor Ganapol has held appointments at eleven DoE, NASA and military research laboratories and published over 250 articles. In addition, he is Fellow of the American Nuclear Society and recent recipient of the Gerald C. Pomraning Award from the Mathematics and Computation Division of the American Nuclear Society for his outstanding contributions to transport theory. In 2006, Professor Ganapol received the Da Vinci Award for excellence in overall scholarship, teaching and service from the College of Engineering at the University of Arizona.

OECD PUBLICATIONS, 2 rue André-Pascal, 75775 PARIS CEDEX 16
Printed in France.